INVESTIGATION OF NONLINEAR AEROELASTIC SYSTEMS

A thesis submitted to the University of Manchester
for the degree of Doctor of Philosophy
in the Faculty of Science and Engineering

October 2001

By
Grigorios Dimitriadis
Department of Aerospace Engineering

Contents

List of Tables

List of Figures

Abstract

The investigation of nonlinear aeroelastic phenomena is becoming increasingly important to the aerospace community. The existence of structural and aerodynamic nonlinearities in aircraft has always been acknowledged but, it is only mainly with the advent of modern digital computers that their investigation has become possible. Additionally, aircraft control systems are becoming increasingly nonlinear with the introduction of Active Control Technology. The effects of these nonlinearities on the dynamic response of aircraft have created the need for further research into the modelling, identification and prediction nonlinear aeroelastic systems.

This thesis deals with four aspects of nonlinear aeroelasticity. Firstly, the effect of the common industrial approach to nonlinearity, i.e. that of linearisation, is investigated. Six flutter prediction methods for linear aircraft are tested and compared on linear and nonlinear mathematical models of aeroelastic systems. The performances of the methods on linear systems are evaluated and compared. Subsequently, their predictions predictions when applied to nonlinear systems are assessed.

Secondly, the dynamic response of nonlinear aircraft is investigated by means of the Harmonic Balance method and the direct integration of the nonlinear mathematical model. Emphasis is given to the explanation of the appearance of Limit Cycle Oscillations as Hopf bifurcations and on the control and suppression

of these oscillations by means of a feedback control system. The chaotic vibration of nonlinear aeroelastic systems is also investigated by means of Poincaré diagrams and Lyapunoff exponents.

Thirdly, the identification of nonlinear aeroelastic systems is considered. Identification of aeroelastic systems is important since, especially in the case of structural nonlinearities, it is often not known whether an aircraft is linear or not and what nonlinearities it may contain until it is tested, either on the ground (Ground Vibration Testing) or in the air (Flight Flutter Testing). An existing nonlinear system identification method is compared to an approach developed during the course of the present project. The two techniques are applied to a nonlinear mathematical aeroelastic system and to a set of nonlinear input-output data obtained from an experimental system. Both methods were found to be able to deal with both systems with varying degrees of success.

Finally, the gust response of nonlinear aircraft is investigated with particular emphasis on the calculation of gust design loads. Turbulent gust clearance is a very important part of any airworthiness testing procedure. Until recently, the linear assumption was considered adequate by the requirements however, there is a current shift towards setting new requirements that take into account nonlinear phenomena. Eight gust load prediction methods for nonlinear aircraft(both stochastic and deterministic) are applied to a simple and a more complex nonlinear mathematical aircraft model. The performance of the methods is assessed with respect to both accuracy and computational efficiency.

Declaration

No portion of the work referred to in this thesis has been submitted in support of an application for another degree or qualification of this or any other university or other institution of learning.

Copyright

Acknowledgments

I would like to thank my supervisor Dr J. E. Cooper for his guidance and support throughout this work, my advisor Professor J. R. Wright for his constructive criticism, Dr W. J. Wink for providing a lot of material on gust load response, my friend Pafsanias 'Bob' Ftakas for occasional help with some of the programming, my friend Justin Whitty for too many things to mention and my mother for even more things.

Chapter 1

Introduction

1.1 Flutter, Limit Cycles and Gust Response

Aeroelasticity is the study of the effects of aerodynamic forces on elastic structures. Its purpose is to analyse the mutual interaction of inertial, aerodynamic and structural forces. One of the most important aeroelastic phenomena is flutter, which is an unstable oscillation that can result in structural failure. Flutter is a result of an unfavorable interaction of inertial, aerodynamic and structural forces and occurs at particular airspeeds and configurations, which are different for every aircraft. Generally, flutter is a high-speed phenomenon however, low speed flutter is not uncommon, indeed 'no speed regime is truly immune from flutter' [1].

Flutter is a very dangerous phenomenon since it can cause structural failure and therefore has to be avoided. Consequently techniques for predicting the flutter speed for an aircraft have always been sought. These techniques include aerodynamic and structural modelling, wind tunnel and ground vibration testing and, most importantly, flight flutter testing. The latter is probably the most critical part of the test programme of a prototype aircraft [2] since it investigates the behaviour of the aircraft itself, not of a mathematical or wind-tunnel

model, at a range of flight conditions. The purpose of all these techniques is to demonstrate that the aircraft is flutter-free throughout its design flight envelope. The proof of stability is also governed by airworthiness requirements, for example JAR 25.6.29(1) states that, for civil aircraft, the flutter speed must be at least 1.2 times the design dive speed. For detailed investigations of classical linear flutter see [3] and [4].

With the introduction of Active Control Technology (ACT), aeroelastic effects other than flutter have become of interest to researchers of aeroelasticity and aircraft designers. Aeroservoelasticity [5], which is the study of the interaction of the control system with inertial, elastic and aerodynamic forces has become very important over the last 25 years. ACT has been used to improve stability (flutter suppression), maneuvrability, ride comfort and other flight characteristics but have also introduced the potential to cause aeroservoelastic instabilities. A further side-effect of ACT is the fact that aircraft have been made more nonlinear.

The fact that aircraft structures are nonlinear has been known for a long time. Such nonlinearities can be caused by '... elastic deformations in riveted, screwed and bolted connections as well as in the structural components themselves' [6]. Flight control systems can introduce further nonlinearities, such as pitch stops and rate limiters. The best known effect of nonlinearities on aircraft response is that the modal frequencies are functions of the amplitude of vibration and that the modal dampings are functions of both the frequency and the amplitude of vibration [6]. However, aircraft with nonlinearities are susceptible to a number of other nonlinear aeroelastic effects including Limit Cycle Oscillations (LCO). LCOs are stable periodic vibrations which can be caused by a number of nonlinearities, including bilinear springs, rate limiting and hysteresis, all of which can be found in modern flight control systems. Reference [7] gives a number of examples of LCO occurence in aeronautical applications. Needless to say, LCOs are

undesirable since they compromise the effectiveness of the flight control system and can cause various components to vibrate outside their design range.

A further aeroelastic phenomenon that is of interest is the response of aircraft to atmospheric turbulence. The importance of this phenomenon was recognized very early in the history of aviation [8], with NASA publishing a study of the subject in its very first report. Atmospheric turbulence excites aircraft structures, in such a way as to give rise to a number of considerations including increased loading of the structure, structural fatigue, difficulty in controlling the aircraft and passenger or crew discomfort. There are a number of approaches that attempt to combat the gust response problem. The most straightforward approach is avoidance of severe patches of turbulence. Additionally, gust load alleviation systems are included in the control systems of some modern aircraft to decrease the loads applied on an airplane flying through turbulence. Finally, predictive methods have been developed to determine the design loads on particular aircraft, caused by turbulent patches of prescribed intensity and likelihood. This latter approach is complicated by the presence of nonlinearities in the structure or control system.

1.2 The current state of the art

Three aeroelastic (and aeroservoelastic) problems that are of interest within the aeroelastic community are the prediction of the the flutter velocity of an aircraft from flight flutter test data, the characterisation and suppression of LCOs and the prediction of design gust loads for aircraft flying through turbulence. All of these problems are further complicated by the presence of nonlinearities either in the structure or the control system.

1.2.1 Flutter prediction from flight flutter test results

The most common approach to flight flutter testing is to fly the aircraft at a number of airspeeds and excite it using any number of excitation systems, including control surface pulses and oscillations, thrusters, aerodynamic vanes or atmospheric turbulence [1]. The response of the aircraft is measured at a number of stations on the structure and subsequently analysed to yield the natural frequencies and dampings of all the significant modes. Aircraft generally have a large number of modes however, only two or three of them contribute to flutter and, hence, only these modes are tracked. The flutter speed is mathematically defined as the speed at which the damping becomes zero. The calculated damping values are plotted against airspeed and extrapolated to obtain the flutter condition.

The initial flight test is normally carried out at low altitude and an airspeed equal to half the theoretically predicted flutter speed. Theoretical predictions of the flutter condition can be obtained from finite element and aerodynamic modelling packages. This process effectively guarantees that flutter will not occur during the test. The excitation signal is chosen such that it excites all the significant dynamic characteristics of the aircraft. Typically, responses are measured at 20-30 stations using accelerometers. A number of methods are can be employed to analyse the responses and decide whether aeroelastic stability can be expected at an increased airspeed. These methods include identification of the eigenvalues and mode shapes of the aircraft, estimation of various stability parameters and identification of the equations of motion of the aircraft. More details on these methods are given in Chapter 2.

In practice, all the response analysis tools used during flight flutter tests assume that the aircraft is linear. Recently, identification methods have been developed for nonlinear systems, although as yet none of these methods have been used to analyse flight flutter test data. Identification is necessary in the case where

it is not possible to develop an adequate model of a given system analytically. It can be argued that since a lot of nonlinearities (especially structural) are not designed for but occur inadvertently, identification is always necessary, even in the case where accurate models are available. In other words, a complete description of an aeroelastic structure can only be obtained by testing the structure and using the resulting responses to yield the equations of motion. One of the ultimate goals of nonlinear system identification is flutter and LCO prediction for nonlinear aircraft from flight test data.

1.2.2 Characterisation of nonlinear systems

Currently, the application of nonlinear aeroelastic research in industry is very limited. Most aircraft structures are assumed to be linear, enabling engineers to apply linear flutter prediction methods, as described earlier. However, in the quest for more accurate predictions, which are rapidly becoming a necessity with the introduction of nonlinear control systems in modern aircraft, researchers are concentrating on nonlinear aeroelasticity.

The main aspect of nonlinear aircraft research currently concerns detailed numerical and experimental investigations to characterize simple aeroelastic systems. The need for such investigations arises because very little is known about the behaviour of nonlinear systems. A number of parameters such as the airspeed, the initial conditions, and the nonlinearities present in a system, dictate whether the response of a system will be stable, LCO, flutter, or even chaotic. Mapping the response of a system in a large section of its parameter space [9] can lead to a more thorough understanding of how and when bifurcations from one type of behaviour to another occur and what are their effects on the system's stability. However, this procedure is almost impossible for large systems like aircraft due to the very large number of parameters that dictate the system response. For

example, if a real aircraft can be idealised as a system with 25 degrees of freedom (DOF), then its parameter-space would have 51 dimensions: initial displacement and velocity of each DOF and airspeed. A detailed investigation of the aircraft response at each possible value of each of the 51 parameters would be an extremely expensive undertaking in terms of computational cost, if not impossible.

1.2.3 Gust load response

The investigation of the load response of an aircraft in the presence of a turbulent gust is required by airworthiness regulations. Due to the unpredictable nature of turbulence, gust load prediction is a very demanding task. Most major airworthiness code such as the U.S. Federal Aviation Regulation (FAR) and the European Joint Airworthiness Requirements (JAR) require gust load calculations for both discrete gusts and continuous turbulence. Discrete gusts are isolated turbulent events which are assumed to occur at intervals sufficiently large to allow the aircraft motion to subside between occurrences. Currently both FAR and JAR requirements assume that a discrete gust can be adequately modelled using a 1-cosine function [10]. Continuous turbulence consists of atmospheric fluctuations occurring in patches within which the gust velocity and the aircraft response vary continuously. Continuous turbulence loads can only be described stochastically.

Gust load prediction for linear aircraft is by no means a trivial task however, a number of methods have been developed, able to predict these loads adequately given analytical structural and aerodynamic models of the aircraft under consideration. Nonlinear aircraft present a much greater challenge mainly because the principle of superposition cannot be applied. There already exist a number of gust load prediction methods for nonlinear aircraft, none of which have yet reached a satisfactory combination of accuracy and computational cost.

1.3 Objectives of this work

In this thesis, all three topics mentioned in the previous section are investigated and original contributions are made. Initially, a number of linear flutter prediction methods are compared on linear systems. Subsequently, these methods are employed to test the linearisation approach in an effort to determine how accurate are the results obtained by the use of linear flutter prediction methods on nonlinear aeroelastic systems.

A mathematical model of a simple nonlinear aeroelastic system is used to analyse and categorize all the types of response that can occur. The main object of this part of the work is to determine which are the adverse types of response and to attempt to suppress LCOs.

Nonlinear system identification is approached with the desire to develop a more general identification approach than the ones currently available. Existing methods fail to deliver acceptable system descriptions or are uneconomical for various types of systems e.g. large systems, coupled systems or systems containing discontinuous nonlinearities, depending on the method. An original system identification method is developed which can identify multi-DOF nonlinear systems with any type of nonlinearity.

The final part of the work compares gust load predictions for nonlinear aircraft obtained using a variety of existing methods. The current difficulty in gust research is the existence of a large number of methods none of which has yet managed to become a standard. The methods are compared with respect to the accuracy of their predictions but also with respect to their computational cost and efficiency.

1.4 Summary by chapter

Chapter 2

Five existing flutter prediction methods and one method developed during the course of this work are described and validated by means of an application to two linear aeroelastic mathematical models, one of a simple wing and one of a complete aircraft. The methods are evaluated and compared on the basis of the resulting predictions. Finally, the methods are applied to the simple wing model, this time including a nonlinearity. The effectiveness of the methods when applied to a nonlinear system is assessed.

Chapter 3

The current state of the art in research on the effects of nonlinearities on the behaviour of aeroelastic systems is presented. This includes methods to solve the nonlinear equations of motion, description of nonlinear aeroelastic phenomena such as LCOs, bifurcations, stability and chaotic response, the Harmonic Balance Method for the prediction of the amplitude of limit cycles, energy considerations. This material is combined to show that it is possible to control and, even suppress LCOs by use of a suitable control system.

Chapter 4

An existing nonlinear system identification method, the NARMAX approach, is described and validated on a simple nonlinear system. The technique is enhanced by extending its validity to aeroelastic systems. A new identification method is developed and successfully applied to a number of simulated nonlinear systems, featuring a wide variety of nonlinearities. The approach is also validated on a 2 DOF experimental system with cubic stiffness.

Chapter 5

A detailed description of turbulent gust load research is presented. Subsequently, three continuous turbulence and five discrete gust methods are outlined and applied mathematical models of a simple and a more complete aircraft. The methods are compared to provide criteria by which a future selection of a standard method can be made possible.

Chapter 6

The contents of the previous chapters are summarized and the most important conclusions are drawn out. Some suggestions for further work are presented.

Chapter 2

Flutter Prediction Using Flutter Test Data

2.1 Introduction

This chapter deals with methods for predicting the flutter speed of aircraft from measured flight flutter test results. Flutter is defined as the interaction of inertial, elastic and aerodynamic forces on a structure, which produces unstable oscillations, sometimes leading to structural failure. Flutter occurs most often at high speeds however, low-speed aircraft are also likely to flutter. Since flutter is a very dangerous phenomenon and can occur at any speed regime, a lot of emphasis is placed on predicting the flutter condition for every aircraft and ensuring that this condition does not lie within the normal flight envelope of the aircraft.

During the design stage, the flutter velocity is estimated by producing detailed mathematical and aeroelastic wind tunnel models of the aircraft under design. These estimates have to be complemented by tests of the actual flying aircraft, commonly termed *flight flutter tests*. The earliest form of flight test was to fly the aircraft at its maximum velocity in an attempt to demonstrate its aeroelastic

stability [1]. This procedure, however, does not attempt to determine the flutter speed and is inherently dangerous. Flight flutter tests are much more sophisticated procedures which, in general, consist of flying an aircraft at a range of subcritical airspeeds and applying some form of excitation on the structure. The response of the structure is measured at a number of stations and the data is used to determine the stability at the current flight speed and predict the stability at higher speeds. In practice, the most common response data analysis procedure is to estimate the damping present in the aircraft response and its variation with airspeed. The data are then fitted by a polynomial, or even by hand, to yield the velocity at which the damping becomes zero.

Even in the days of high-speed computers and sophisticated data capturing and analysis tools, flutter testing remains as much an art as a science. Subcritical damping data can not always be safely extrapolated in order to obtain an accurate prediction for the flutter velocity. Nonlinearities in the control system or in the aerodynamics and structure of the aircraft can critically affect its aeroelastic behaviour. Finally, the aeroelastic stability can change from positive to negative with an increase in airspeed of only a few knots and the whole procedure is very dangerous and time-consuming.

There are various methods for analysing response data from flight flutter tests. The purpose of this chapter is to examine a number of existing approaches as well as to introduce a new one. Both the efficiency and quality of the predictions obtained by the methods are compared using simulated systems to provide a comprehensive overview of contemporary flutter prediction procedures. The effectiveness of the methods investigated when applied to systems containing nonlinearities is also considered.

Before any flutter prediction methods are discussed, a new procedure for evaluating the eigenvalues of a system from response data will be introduced. The

procedure will be used in conjunction with a number of the flutter prediction methods investigated in this chapter.

2.1.1 Rational Fraction Polynomial Method

The standard Rational Fraction Polynomial (*RFP*) method [11] attempts to express the Frequency Response Function (*FRF*) of a given system in terms of a polynomial fraction of the form

$$H(\omega) = \frac{b_{nb}(\jmath\omega)^{nb} + b_{nb-1}(\jmath\omega)^{nb-1} + \ldots + b_0}{(\jmath\omega)^{na} + a_{na-1}(\jmath\omega)^{na-1} + \ldots + a_0} \tag{2.1}$$

where $H(\omega)$ is the FRF, b_i, a_i are the coefficients of the polynomials and nb and na are the orders of the polynomials. Then, b_i, a_i are evaluated by rewriting equation 2.1 as

$$\left\{ \begin{array}{c} H(\omega_1)(\jmath\omega_1)^{na} \\ H(\omega_2)(\jmath\omega_2)^{na} \\ \vdots \\ H(\omega_L)(\jmath\omega_L)^{na} \end{array} \right\} = - \left(\begin{array}{cccc} H(\omega_1)(\jmath\omega_1)^{na-1} & H(\omega_1)(\jmath\omega_1)^{na-2} & \ldots & H(\omega_1) \\ H(\omega_2)(\jmath\omega_2)^{na-1} & H(\omega_2)(\jmath\omega_2)^{na-2} & \ldots & H(\omega_2) \\ \vdots & \vdots & \vdots & \vdots \\ H(\omega_L)(\jmath\omega_L)^{na-1} & H(\omega_L)(\jmath\omega_L)^{na-2} & \ldots & H(\omega_L) \end{array} \right) \times$$

$$\left\{ \begin{array}{c} a_{na-1} \\ a_{na-2} \\ \vdots \\ a_0 \end{array} \right\} + \left(\begin{array}{cccc} (\jmath\omega_1)^{nb} & (\jmath\omega_1)^{nb-1} & \ldots & 1 \\ (\jmath\omega_2)^{nb} & (\jmath\omega_2)^{nb-1} & \ldots & 1 \\ \vdots & \vdots & \vdots & \vdots \\ (\jmath\omega_L)^{nb} & (\jmath\omega_L)^{nb-1} & \ldots & 1 \end{array} \right) \left\{ \begin{array}{c} b_{nb} \\ b_{nb-1} \\ \vdots \\ b_0 \end{array} \right\} \tag{2.2}$$

which is equivalent to the form $\mathbf{Y} = -\mathbf{\Phi}_a\mathbf{a} + \mathbf{\Phi}_b\mathbf{b}$. Finally, b_i, a_i are obtained by solving equation 2.2 in a least squares sense using

$$\mathbf{Y} = \left(\begin{array}{cc} -\mathbf{\Phi}_a & \mathbf{\Phi}_b \end{array} \right) \left\{ \begin{array}{c} \mathbf{a} \\ \mathbf{b} \end{array} \right\} \tag{2.3}$$

In general, the coefficients a_i are forced to be real by choosing $na = 2 \times m$, where m is the number of modes in the system. Then, the roots of the

denominator are m complex conjugate pairs and are also the eigenvalues of the system. The problem with this formulation is that it is ill-conditioned, yielding poor estimates. Orthogonal polynomials are often employed to counteract the problem [11].

For the present work, a slightly modified approach is introduced. The coefficients of both the numerator and the denominator are allowed to be complex. In turn, this signifies that the orders of the polynomials are undetermined. Consequently, an optimization procedure is employed to obtain na and nb. The procedure for the RFP technique with complex coefficients (RFP-CC) is:

- The FRF is expressed as in equation 2.3
- The value of na and nb is set to 1.
- Equation 2.3 is solved to yield values for a_i and b_i. Then the root-mean-square (rms) value of the difference between the left-hand-side and the right-hand-side of equation 2.1 is evaluated.
- na is kept fixed while nb is allowed to increase in steps of 1 and the rms value of the difference between the actual FRF and the polynomial fraction is evaluated at each step.
- As nb keeps increasing, when it reaches a certain value, the $\mathbf{\Phi}$ matrix in equation 2.3 will become rank deficient. Then, the value of nb is reset to 1 and that of na is increased by 1.
- The optimization process is terminated when na reaches such a value that at $nb = 1$ the $\mathbf{\Phi}$ matrix is rank deficient. This occurs even when the results are noisy.
- The rms values of the differences between actual FRF and approximation are compared and the best-case combination of na and nb is chosen.

The eigenvalues are, again, given by the roots of the denominator, only, in this approach, the roots are not complex conjugate pairs. There are m roots that approximate the m eigenvalues as well as a number of other roots that describe the shape of the FRF away from the peaks. In this sense, the RFP-CC method approximates the 3-dimensional landscape that is described by the FRF in the real-imaginary-frequency space. Its ability to describe the shape of the FRF away from the peaks means that it copes better with noise than the standard RFP, since the extra roots of the denominator 'absorb' the noise to a certain degree, leaving the numerator and the approximations of the eigenvalues in the denominator to describe the noise-free FRF.

The natural frequencies and dampings are given by

$$\begin{aligned} \omega_{n_i} &= \mid \lambda_i \mid \\ \zeta_i &= \frac{\Re e(\lambda_i)}{\mid \lambda_i \mid} \end{aligned} \tag{2.4}$$

where ω_n are the natural frequencies, ζ are the damping ratios and λ_i are the eigenvalues. The roots that approximate the eigenvalues are separated from the other roots by comparing the natural frequencies obtained from them to where the peaks occur in the FRF.

Figures 2.1 and 2.2 show FRF fits for a three-degree-of-freedom wing system using the RFP-CC method, for a clean and a noisy signal respectively. Note that the fit creates an extra two peaks at high frequencies to accommodate the noise. The 'true' peaks however coincide with the ones in the original FRF.

For a large system, the FRF can not be identified in a single step. Instead, it has to be broken down into smaller regions and each region identified separately. Here, again, the RFP-CC method has an advantage over the standard RFP method. When applying the latter, it has to be decided how many modes exist in each region to be identified. However, each of the FRFs of a large system will not necessarily contain all the modes. Additionally, such a procedure

requires user input, in other words, the regions have to be defined by the user. With the RFP-CC this is not a requirement since the approach does not need the number of modes to be specified. Instead, it will fit the best-case curve through the given data, which will include all the actual modes plus a number of other modes. The latter can be separated from the former easily since they do not lie in the frequency range of interest.

2.2 Flutter Prediction Methods

This section will concentrate on linear flutter prediction methods only. Nonlinear flutter prediction methods are still in their infancy and have not found their way in industrial applications. In section 2.5 these linear methods are applied to a nonlinear simulated aeroelastic system in an attempt to determine whether such an approach can deliver acceptable flutter predictions.

The methods were applied to two different simulated aeroelastic models, one of them modelling a simple, 3-degree of freedom, rectangular wing with control surface, referred to as the Hancock model (see Appendix A) and the other modelling a 4-engined civil transport (see Appendix G), referred to as the Sim-2 model. Figures 2.3 and 2.4 show the variation of natural frequencies and damping ratios for both model. In the case of the Sim-2 model, only some representative modes are plotted. The flutter speeds of the two models were calculated from the equations of motion, using the procedures described in appendices B and C, as

- Hancock model: 44.07 m/s
- Sim-2 model (5000 ft): 398 kts

With both models, and for all the methods, the excitation waveforms used were frequency sweeps. Additionally, all responses were contaminated by 5% rms simulated noise to approximate the effects of experimental uncertainty. Each

method was tested in a variety of velocity ranges, as shown in the result tables. In each of the ranges, a number of tests were performed at increments of 7% of the true flutter speed.

2.2.1 Damping Ratio Variation with Airspeed

Traditionally, the most widely used indicators of the stability of an aeroelastic system are the modal dampings and their variation with free stream velocity. At flutter, the damping in at least one of the modes will be zero, thus causing self-excited oscillations. In the typical flight flutter test the damping ratios for all the significant modes are evaluated at a number of subcritical airspeeds using system identification. Then they are curve-fitted by a polynomial, or by hand, and extrapolated to yield the flutter velocity.

The problem with this approach is that, even though the zero-damping criterion is correct, the subcritical behaviour of the damping ratio is very unpredictable. In the case of hard flutter, the damping drops very abruptly near the critical velocity and therefore flutter can be encountered at what can be mistaken for a safe flying condition. Hence, during the flutter prediction process, a lot of emphasis needs to be given to deciding whether a particular aeroelastic system will undergo hard or soft flutter.

There are numerous system identification methods, both in the time and the frequency domain, that allow the calculation of the eigenvalues and, hence, frequencies and dampings of a vibrating system. Here, the new version of the Rational Fraction Polynomial method detailed in subsection 2.1.1 is used.

Method Validation

The two main considerations with any polynomial extrapolation is the order of the polynomial used and the range of validity of the extrapolation. Figures 2.5

and 2.6 show polynomial fits of damping data for responses without noise and with 5% rms noise respectively for the Hancock model. The solid lines are the fits, the circles the estimated damping ratios and the crosses the actual damping ratios, obtained by solving the equations of motion rather than analyzing the responses. In both cases, although the shape of the polynomial fit is accurate in the high-velocity range, providing good estimates for the actual flutter velocity, the fit is very poor in the lower-velocity range where the damping ratio should go to zero since the system does not contain any structural damping. Furthermore, the best estimate for the flutter depends on the order of the polynomial used. In general, low order polynomials, may fail to fit the data points adequately whereas high order polynomials will fit the data much more accurately but may fail to extrapolate to the critical velocity, i.e. may not have a root near where the flutter speed should be. Figure 2.7 shows the variation of the error in the flutter velocity with increasing polynomial order, again for the Hancock model. This figure as well as figures 2.5 and 2.6 suggest that the best order is around 5 or 6. However, this is by no means a general result. Since, in practice, the flutter speed is not known in advance it is impossible to predict which order of fit will give the best estimate. Table 2.1 shows the best flutter estimates for damping data taken at different velocity ranges and the corresponding orders, for the Hancock model. In this table, and in all the other tables in this section concerning the Hancock model, all speeds are expressed as ratios of true airspeed to true flutter speed.

The table shows that a range of polynomial orders (between 3 and 8) can give the optimal results. Additionally, changing the order by one can give wildly inaccurate results. In general, orders between 3 and 6 are the most suitable choices, however, results can be out by up to 17.5% of the true value. Furthermore, if too high an order is used (typically above 10, depending on how many points are fitted) the matrix used for the polynomial fit becomes rank deficient and the fit

Velocity Range	Best Flutter Speed Estimate	% Error	Best Order of fit
0.23-0.43	50.3983	+14.4	3
0.23-0.57	46.3494	+5.1	3
0.23-0.70	40.0809	-9.1	4
0.23-0.84	44.0199	-0.1	6
0.23-0.98	44.2804	+0.5	8
0.45-0.66	51.7872	+17.5	2
0.45-0.79	43.6776	-0.9	4
0.45-0.93	44.0317	-0.1	5
0.68-0.88	44.1609	+0.2	3

Table 2.1: Flutter Estimates using Damping Fit Method, Hancock Model

itself fails completely.

The sensitivity of the method to noise is governed by the sensitivity of the FRF fit method. The deteriorating quality of the latter with increasing levels of noise affects the flutter prediction negatively, as is seen in figures 2.8 and 2.9, where a FRF fit and a flutter prediction respectively are shown for results with 20% rms noise. The symbols on figure 2.9 are as in figures 2.5 and 2.6 with the addition of the dashed line which denotes a best-case polynomial fit of the actual damping ratio data. A comparison between the latter and the best-case fit of the estimated damping ratios shows that the flutter speed has been overestimated by quite a margin (4.4 %) and also that the estimated subcritical behaviour of the damping curve is wrong.

Table 2.2 shows flutter speed predictions for the Sim-2 model, again using best order polynomials. As with the Hancock model, all velocities are presented as a ratio of the true airspeed to the flutter speed. While a range of orders between 3 and 9 yields the optimal results however, orders of 3 or 4 are most often the best. When flutter tests are carried out close to the flutter speed, the flutter estimates are very accurate. If the maximum test airspeed is 230 kts or less (approximately 40% lower than the critical airspeed) the errors in the flutter speed predictions are quite large.

Velocity Range	Best Flutter Speed Estimate (kts)	% Error	Best Order of fit
0.23-0.43	54.2116	-88.4	3
0.23-0.57	330.7390	-17.0	3
0.23-0.70	361.7980	-9.2	6
0.23-0.84	416.6640	+4.6	6
0.23-0.98	397.1000	-0.3	9
0.45-0.66	409.6763	+2.8	3
0.45-0.79	408.6679	+2.3	4
0.45-0.93	400.4373	+0.5	4
0.68-0.88	409.9488	+2.9	3

Table 2.2: Flutter Speed Estimates using Damping Fit Method, Sim-2 model

In conclusion it has to be stated that fitting the damping ratio variation by a polynomial is not a very reliable way of obtaining flutter predictions, especially since the particular examples presented do not exhibit hard flutter behaviour. Choosing the order of the polynomial fit is a very arbitrary process and noise affects predictions in an undesirable manner. However, it is a very simple and inexpensive way of obtaining estimates for the flutter velocity and, as such, could be employed to confirm results obtained by a more effective flutter prediction method.

2.2.2 Flutter Margin Method

The Flutter Margin Method (*FFM*) was first presented in reference [12]. The basis of the approach is the quest for a more fundamental stability criterion than just tracking the damping present in the system. In its original form, the approach only covers binary flutter however, in [13] an extension of the technique to trinary flutter is presented.

The standard form of the equations of motion for an unforced aeroelastic system is

$$\mathbf{M}\ddot{\mathbf{q}} + \mathbf{C}\dot{\mathbf{q}} + \mathbf{K}\mathbf{q} = \mathbf{0} \tag{2.5}$$

where $\mathbf{M}$ is the generalised mass matrix, $\mathbf{C}$ the generalised damping matrix, $\mathbf{K}$ the generalised stiffness matrix and $\mathbf{q}$ the generalised coordinates. If solutions of the form $\mathbf{q} = \mathbf{q}_0 \exp \lambda t$ are chosen, where λ are the eigenvalues of the system and $\mathbf{q}_0$ arbitrary constants, and substituted in the equations of motion, the characteristic equation of the system is obtained. The equation is polynomial with increasing powers of λ. Routh's stability criterion requires that, for such a system to be stable, all the coefficients of λ along with a number of other coefficients be positive [14]. However, for a two-degree-of-freedom system, for which the characteristic equation is a quartic of the form

$$\lambda^4 + A_3\lambda^3 + A_2\lambda^2 + A_1\lambda + A_0 = 0 \tag{2.6}$$

the stability criterion reduces to

$$\left[A_2\left(\frac{A_1}{A_3}\right) - \left(\frac{A_1}{A_3}\right)^2 - A_0\right] > 0 \tag{2.7}$$

Hence, for a two-degree-of-freedom system there is a quantity described by equation 2.7 which has to be positive for the system to be stable and becomes zero when instability is reached. This quantity is termed the flutter margin and is given by (in slightly modified form)

$$F = \left[A_2\left(\frac{A_1}{A_3}\right) - \left(\frac{A_1}{A_3}\right)^2 - A_0\right] = \left[\left(\frac{A_2}{2}\right)^2 - A_0\right] - \left[\left(\frac{A_2}{2}\right) - \left(\frac{A_1}{A_3}\right)\right]^2 \tag{2.8}$$

The application of the method is quite straightforward. For a two-degree-of- freedom system the response to a known input at a particular (subcritical) airspeed is recorded and the eigenvalues of the system are calculated. These are then used to compute the Flutter Margin according to

$$F = \left[\left(\frac{\omega_2^2 - \omega_1^2}{2}\right) + \left(\frac{\beta_2^2 - \beta_1^2}{2}\right)\right]^2 + 4\beta_1\beta_2\left[\left(\frac{\omega_2^2 + \omega_1^2}{2}\right) + 2\left(\frac{\beta_2 + \beta_1}{2}\right)^2\right] -$$

$$\left[\left(\frac{\beta_2-\beta_1}{\beta_2+\beta_1}\right)\left(\frac{\omega_2^2-\omega_1^2}{2}\right)+\left(\frac{\beta_2+\beta_1}{2}\right)^2\right]^2 \tag{2.9}$$

which is obtained from equation 2.8, after substituting for the two sets of complex conjugate eigenvalues, $\lambda_1, ..., \lambda_4$, such that

$$\lambda_{1,2} = \beta_1 \pm i\omega_1$$

$$\lambda_{3,4} = \beta_2 \pm i\omega_2$$

Using some further derivation [12], it can be shown that the Flutter Margin is a quadratic function of the dynamic pressure, i.e.

$$F = B_2 q^2 + B_1 q + B_0 \tag{2.10}$$

where B_0, B_1 and B_2 are coefficients to be evaluated. Hence, if the flutter margin is known at three different airspeeds, it can be fitted by a second-order polynomial and hence extrapolated. Flutter occurs when $F = 0$. In practice, to counteract the effects of experimental uncertainty, the Flutter Margin is estimated at a wider range of subcritical airspeeds and then fitted in a least squares sense.

The fact that the flutter margin is derived for a two-degree-of-freedom system does not imply that the method cannot be used with larger systems. In fact, the flutter mechanism is usually dependent on two modes only. If it is known beforehand which two modes will cause flutter, the Flutter Margin method can be applied successfully. It will be shown later that the method can be also applied when there is no prior knowledge of the flutter mechanism. For a multi-degree-of-freedom system, a search procedure can be employed to investigate the stability of all possible modal couples.

Some experimental evaluation of the method suggests that using a quadratic fit of the Flutter Margin can yield results that are very sensitive to errors or uncertainty in the experimental data [15]. An alternative is to use linear extrapolation, again in a least squares sense. The rationale behind this approach is that

the variation of the Flutter Margin at intermediate subcritical to critical airspeeds is relatively linear anyway, most of its parabolic characteristics appearing at low speeds.

For the present work, the eigenvalues of the systems investigated were again calculated using the RFP-CC method.

Method Validation

As mentioned earlier, successful application of the Flutter Margin method to a multi-dof aeroelastic system depends upon the knowledge of the flutter mechanism, i.e. which two modes will combine to cause flutter. By applying the technique to these two modes a 'representative' system is analysed. It is interesting to note that Flutter Margins calculated from any combination of modes containing the mode which becomes unstable at flutter will become zero at the flutter velocity. In reference [16] it is shown that equation 2.8 can be re-written as

$$F = \left[1 - \left(\frac{\beta_2 - \beta_1}{\beta_2 + \beta_1}\right)^2\right] \left\{\left(\frac{\omega_2^2 - \omega_1^2}{2}\right)^2 + (\beta_1 + \beta_2)^2 \left[\left(\frac{\omega_2^2 + \omega_1^2}{2}\right) + \left(\frac{\beta_2 + \beta_1}{2}\right)^2\right]\right\} \tag{2.11}$$

It is obvious that if either β_1 or β_2 become zero then,

$$\left[1 - \left(\frac{\beta_2 - \beta_1}{\beta_2 + \beta_1}\right)^2\right] = 0$$

and F also becomes zero. This phenomenon is illustrated in figure 2.10 for the Hancock model whose flutter mechanism includes the wing torsion and control surface torsion modes, the damping of the control surface torsion mode becoming zero at flutter. Figure 2.10 shows flutter margins calculated for all three combinations of modes. In the wing bending- wing torsion case the Flutter Margin never becomes zero. In the other two cases, which contain the control surface torsion

mode, the Flutter Margin becomes zero at flutter. This phenomenon is due to the fact that any system formed of two modes from another system, one of which is unstable, will also be unstable. However, figure 2.10 shows that the variation of the Flutter Margin with airspeed for the wing bending-control surface torsion case is not quadratic. In other words, a number of 'spurious flutter margins', or parameters indicating the stability of a multi-dof system, can be formed using the Flutter Margin methodology but these parameters will not be the Flutter Margin, as defined by Zimmerman et al in [12]. Only if the actual flutter mechanism is used will the Flutter Margin be obtained.

The predictions of the Flutter Margin method are also affected by the number and location of the subcritical test. Table 2.3 shows predictions for the flutter velocity obtained for subcritical tests carried out at various velocity ranges on the Hancock model.

Velocity Range	Flutter Speed Estimate	% Error
0.23-0.43	41.0910	-6.8
0.23-0.57	45.7884	+3.9
0.23-0.70	45.1524	+2.5
0.23-0.84	44.5518	+1.1
0.23-0.98	44.1327	+0.1
0.45-0.66	44.6406	+1.3
0.45-0.79	44.8151	+1.7
0.45-0.93	44.1058	+0.1
0.68-0.88	43.7000	-0.8

Table 2.3: Flutter Speed Estimates by Flutter Margin Method, Hancock model

The table indicates that the best flutter estimates are obtained when at least some of the subcritical tests are carried out near the actual flutter speed. However, predictions obtained away from the critical region are still accurate to within 1% - 3% percent. Only in the case of the first velocity range where only 4 tests are performed at very low speeds does the prediction error increase to about 7%.

As with the damping fit approach, the Flutter Margin method's sensitivity to

noise depends upon that of the RFP-CC. Figures 2.11- 2.12 show the degradation of the flutter velocity predictions with increasing noise in the responses for the Hancock model. In the case of figure 2.11, with 10% rms noise, the flutter velocity estimate is increased to just under $50m/s$ and in figure 2.12, with 20% rms noise, to just under $60m/s$ (the true flutter speed being 44.0749 m/s). It is at these conditions that [15] suggests a linear fit of the Flutter Margin gives better estimates for the flutter velocity. However, figure 2.13 shows that this latter approach would provide worse results than the normal quadratic fit.

The application of the Flutter Margin method to the Sim-2 model was not as straightforward as in the Hancock case. The Sim-2 model contains 23 modes, of which mode 12 becomes unstable at flutter. The flutter mechanism consists of mode 12 and mode 4. The Flutter Margin variation with speed for the actual flutter mechanism is shown in figure 2.14. Notice that the variation is not exactly quadratic since such a variation can only be obtained for systems with no structural damping [13], whereas the Sim-2 model contains structural damping. Unfortunately, mode 4 is highly damped with respect to most of the other modes and hence does not feature prominently in any of the FRFs, even at low speeds. Since, for this work, the eigenvalues were obtained using a frequency domain method, the eigenvalue of mode 4 could not be obtained. As a consequence, an alternative approach was used. The Flutter Margin method was applied to the combination of modes 12 and 3, the latter being a prominent mode in the FRFs. Equation 2.8 was applied to these two modes yielding a 'spurious' flutter margin which did not vary quadratically and had to be curve fitted by higher order polynomials. Nevertheless, since the spurious flutter margin became zero at flutter, it served as a stability parameter. Table 2.4 contains the flutter velocity predictions for the Sim-2 model. Some velocity ranges did not yield a flutter speed at all because of the constraint that the data must be fitted by a second

order polynomial. The noise in the Flutter Margin data caused the polynomial to have the wrong curvature, hence never crossing the airspeed axis.

Velocity Range	Flutter Speed Estimate (kts)	% Error
0.23-0.43	-	-
0.23-0.57	323.6037	-18.8
0.23-0.70	336.6151	-15.5
0.23-0.84	383.4589	-3.8
0.23-0.98	401.7859	+0.8
0.45-0.66	315.4346	-20.8
0.45-0.79	420.3867	+5.5
0.45-0.93	-	-
0.68-0.88	-	-

Table 2.4: Flutter Speed Estimates using Flutter Margin Method, Sim-2 model

2.2.3 Envelope Function

The Envelope Function was originally proposed as a tool to provide an assessment of overall stability to complement standard analysis [17]. However, it has since been used in practice to provide flight flutter clearance of a German high altitude research aircraft.

The method is based on the fact that the impulse response of any damped system is decaying, the shape of the decay in the time-domain being described by the decay envelope. As the damping in a given aeroelastic system decreases, the decay envelope grows wider, eventually becoming a rectangle as the damping becomes zero. By evaluating the position of the centroid of the decay envelope and the way that it shifts on the time axis as the damping decreases, it is possible to assess the stability of the system.

For an aeroelastic system with impulse response $y(t)$, the decay envelope, or envelope function, is given by

$$\text{env}(t) = \sqrt{y(t)^2 + y_H(t)^2} \tag{2.12}$$

where $y_H(t)$ symbolizes the Hilbert transform of the impulse response and is given by

$$y_H(t) = \frac{1}{\pi} \int_{-\infty}^{+\infty} \frac{y(\tau)}{t-\tau} d\tau \tag{2.13}$$

which is a convolution in the time domain. In the frequency domain this convolution can be expressed as

$$Y_H(\omega) = -\jmath \, \frac{\omega}{|\omega|} Y(\jmath\omega) \tag{2.14}$$

where Y denotes the Fourier transform of y. Transforming back into the time domain and noting that only positive frequencies are of interest

$$y_H(t) = F^{-1}(Im(Y(\omega)) - \jmath \, Re(Y(\omega)) \tag{2.15}$$

Im and *Re* denoting imaginary and real part respectively. The time centroid of the decay envelope is given by

$$\bar{t} = \frac{\int_0^{t_{max}} \mathrm{env}(t) t dt}{\int_0^{t_{max}} \mathrm{env}(t) dt} \tag{2.16}$$

The upper limit of integration, t_{max}, serves to define the rectangle within which the integration takes place. In the case of low damping, the response takes a long time to decay and an upper limit other than $+\infty$ is needed in order to make the integration feasible. Additionally, it helps define the flutter condition. For a single-degree-of-freedom system, when the damping is zero, the decay envelope is a rectangle stretching to $t = +\infty$. If that rectangle is truncated at $t = t_{max}$ its time centroid lies at $t = t_{max}/2$. For a multi-degree-of-freedom system, it is suggested that $t = t_{max}/2$ is an adequate approximation for the position of the time centroid [17].

Since $\bar{t}$ tends to increase as the damping drops its inverse is usually employed as the significant shape parameter, i.e.

$$S = \frac{1}{\bar{t}} \tag{2.17}$$

in which case the value of S at the flutter condition is approximately $S \approx 2/t_{max}$.

The envelope function flutter testing procedure is to evaluate S at a number of subcritical airspeeds. The variation of S with airspeed is then curve-fitted using a polynomial, as with the damping method, and extrapolated to the point where $S = 2/t_{max}$, thus yielding the flutter velocity.

Method Validation

The Envelope Function procedure begins with obtaining the impulse response of the system under consideration and then evaluating its decay envelope. Figure 2.15 shows such a decay envelope. Then the centroid of the decay envelope is plotted against velocity and the flutter condition is located at the point where the centroid lies at $2/t_{max}$, as shown in figure 2.16.

The main considerations in the successful application of the method are the number and velocity of subcritical tests, the order of the polynomial fit of the decay envelope centroid, the value of t_{max} and noise. When testing a multi-degree of freedom system a number of responses can be measured, all of which will yield an envelope function and a shape parameter at each airspeed. Hence the shape parameters from every measured response can be curve-fitted to yield an estimate for the flutter velocity. Table 2.5 shows flutter predictions for the Hancock wing with control surface model with variation of the factors mentioned above.

The poor quality of the flutter estimates is caused by the presence of noise. Any noise present in the responses is magnified when the latter are transformed to the frequency domain and then back to the time domain to obtain the impulse

Range	t_{max}	Best Polynomial Order	Best Flutter Speed Estimates	% Error
0.23-0.43	10	2	54.7619	+24.2
	8	2	49.7932	+13.0
	6	2	34.7932	-21.1
0.23-0.57	10	3	43.5895	-1.1
	8	3	43.1423	-2.1
	6	3	44.1552	+0.2
0.23-0.70	10	3	44.2338	+0.4
	8	3	44.3199	+0.6
	6	4	45.1514	+2.4
0.23-0.84	10	5	42.9772	-2.5
	8	5	46.1875	+4.8
	6	4	45.9741	+4.3
0.23-0.98	10	6	44.0838	+0.0
	8	4	44.0438	-0.1
	6	3	43.9444	-0.3
0.45-0.66	10	2	41.2831	-6.3
	8	2	41.0387	-6.9
	6	2	42.6185	-3.3
0.45-0.79	10	3	41.0289	-6.9
	8	3	43.2193	-1.9
	6	3	44.3230	+0.6
0.45-0.93	10	4	44.1043	+0.1
	8	4	44.1887	+0.3
	6	4	44.3050	+0.5
0.68-0.88	10	2	44.4217	+0.8
	8	2	44.2729	+0.4
	6	2	44.6352	+1.3

Table 2.5: Flutter Speed Estimates using Envelope Method, Hancock Model

responses. A demonstration of this is given in figure 2.17. The 5% rms error is magnified to approximately 20% in the impulse response. This magnification, in turn, causes significant scatter in the results for the position of the decay envelope centroid, see figure 2.18.

Additionally, the appropriate order of the polynomial fit of the decay envelope centroid is far from obvious. In table 2.5 very different orders are shown to give the best flutter estimate for each test case. The problem here is, as in the damping curve-fit method, that a single polynomial order can not be chosen to be adequate for a variety of test cases. Finally, the value of t_{max} does not appear to greatly influence the flutter predictions since table 2.5 shows that none of the three values used yields consistently more accurate estimates.

The results presented so far tend to show that the accuracy of the envelope function method is limited. However, when the method is used on more realistic and complex systems, better quality of prediction is obtained. The envelope method was also applied to the Sim-2 aeroelastic model (see Appendix G). Figure 2.19 shows the centroid variation for each of the 17 measuring positions for the case where the aircraft is excited vertically at the wingtip at an altitude of 15,000 ft. Only symmetric modes were considered for this experiment. All the centroids approach the $2/t_{max}$ value at the actual flutter speed. The advantage of applying the method to a large system with many measurement positions is that, even if some of the responses overshoot the decay envelope flutter criterion because of measurement error, on average the criterion is satisfied. This can be seen more clearly in figure 2.20 where the impulse responses were corrupted with 10% rms noise. Hence, the envelope function flutter prediction procedure can be modified to include curve fitting of the shape parameters of all the measured impulse responses as was done in the case of table 2.6

Notice that the polynomial order for all tests in table 2.6 is 6. Since there are

Velocity Range	Best Flutter Speed (kts)	% Error
0.23-0.43	420.4711	+5.5
0.23-0.57	258.5753	-35.1
0.23-0.70	333.9946	-16.2
0.23-0.84	408.3616	+2.5
0.23-0.98	395.8387	-0.7
0.45-0.66	435.9705	+9.4
0.45-0.79	422.5396	+6.0
0.45-0.93	403.5002	+1.3
0.68-0.88	400.4848	+0.5

Table 2.6: Flutter Speed Estimates using Envelope Method, Sim-2 model, $t_{max} = 4$

many shape parameters to curve fit, there is no need to look for the optimum polynomial fit for each one of them. Instead, all of them are fitted with the same polynomial order. As a result, not all of the fits will yield flutter velocities and hence, the maximum number of flutter speed estimates for each test presented was 7 (out of 17 responses and 17 possible estimates). This fact was the factor that determined the use of a polynomial order of 6. Other orders were tried but it was found that they yielded less flutter speed estimates. These estimates can be used to provide a mean estimate for the flutter velocity of the Sim-2 model. As with the Damping and Flutter Margin methods, the Envelope method yields much better flutter speed estimates when the test range is closer to the critical speed.

Figure 2.20 also demonstrates that the existence of noise has a positive effect. Noise will appear in the steady-state responses thus displacing the time-centroid to the right and making the transient response less significant. Hence, apart from the rigid body modes, all the flexible modes in figure 2.20 are relatively flat at subcritical speeds. As flutter is approached, the transient response takes longer to decay and becomes more significant, resulting in a drop in the shape parameters. Hence, flutter is approached when the shape parameters are no longer flat. Thus, subcritical variations in the shape parameter can be ignored, making the detection

of flutter a simpler process. Of course, at high noise levels, this advantage is lost since, the higher the noise amplitude, the more sudden the drop in the shape parameter near flutter.

2.2.4 Nissim & Gilyard Method

The two methods described previously deal with attempting to evaluate the stability of a given aeroelastic system and, hence, the flutter velocity. The Nissim & Gilyard Method (*NG*) [18], [19] adopts a different approach by attempting to identify the whole system, including its aerodynamic variation with free stream airspeed by estimating its equations of motion. Then, the identified system can be solved for different velocities to obtain the flutter speed.

The equations of motion for a forced aeroelastic system are

$$\bar{\mathbf{M}}\ddot{\mathbf{q}} + \bar{\mathbf{C}}\dot{\mathbf{q}} + \bar{\mathbf{K}}\mathbf{q} = \bar{\mathbf{F}}g(t) \tag{2.18}$$

where $\bar{\mathbf{M}}$ is the generalised mass matrix, $\bar{\mathbf{C}}$ is the generalised damping matrix, $\bar{\mathbf{K}}$ is the generalised stiffness matrix, $\bar{\mathbf{F}}$ is the forcing vector, g(t) is the excitation function and $\mathbf{q}$ are the generalised coordinates. If equation 2.18 is transposed to the frequency domain and pre-multiplied by $\bar{\mathbf{M}}^{-1}$ the equations of motion become

$$\left\{-\mathbf{I}\omega^2 + \mathbf{C}\jmath\omega + \mathbf{K}\right\}\mathbf{q}(\omega) = \mathbf{F}g(\omega) \tag{2.19}$$

where

$$\mathbf{C} = \bar{\mathbf{M}}^{-1}\bar{\mathbf{C}}$$
$$\mathbf{K} = \bar{\mathbf{M}}^{-1}\bar{\mathbf{K}}$$
$$\mathbf{F} = \bar{\mathbf{M}}^{-1}\bar{\mathbf{F}}$$

and multiplication by $\jmath\omega$ denotes differentiation. Dividing both sides of equation 2.19 by $g(\omega)$ and re-arranging

$$\mathbf{C}\jmath\omega\mathbf{H}_q(\omega) + \mathbf{K}\mathbf{H}_q(\omega) - \mathbf{F} = \mathbf{I}\omega^2\mathbf{H}_q(\omega) \tag{2.20}$$

where $\mathbf{H}_q(\omega) = \mathbf{q}(\omega)/g(\omega)$. For a m-degree-of-freedom system equation 2.20 can be re-arranged and expanded as

$$\begin{pmatrix} H_{q_1}(\omega_1) & \dots & H_{q_m}(\omega_1) & \jmath\omega_1 H_{q_1}(\omega_1) & \dots & \jmath\omega_1 H_{q_m}(\omega_1) & -1 \\ H_{q_1}(\omega_2) & \dots & H_{q_m}(\omega_2) & \jmath\omega_2 H_{q_1}(\omega_2) & \dots & \jmath\omega_2 H_{q_m}(\omega_2) & -1 \\ \vdots & \vdots & \vdots & \vdots & \vdots & \vdots & \vdots \\ H_{q_1}(\omega_{nf}) & \dots & H_{q_m}(\omega_{nf}) & \jmath\omega_{nf} H_{q_1}(\omega_{nf}) & \dots & \jmath\omega_{nf} H_{q_m}(\omega_{nf}) & -1 \end{pmatrix} \begin{pmatrix} \mathbf{K}^T \\ \mathbf{C}^T \\ \mathbf{F}^T \end{pmatrix} =$$

$$\begin{pmatrix} \omega_1^2 H_{q_1}(\omega_1) & \dots & \omega_1^2 H_{q_m}(\omega_1) \\ \omega_2^2 H_{q_1}(\omega_2) & \dots & \omega_2^2 H_{q_m}(\omega_2) \\ \vdots & \vdots & \vdots \\ \omega_{nf}^2 H_{q_1}(\omega_{nf}) & \dots & \omega_{nf}^2 H_{q_m}(\omega_{nf}) \end{pmatrix} \tag{2.21}$$

where n_f is the number of points used in the identification process. Equation 2.21 is of the form

$$\mathbf{T}\mathbf{X} = \mathbf{B} \tag{2.22}$$

where $\mathbf{X}$ is to be evaluated using a least squares procedure. Strictly speaking, nf only needs to be equal to m for a successful identification, however, to counteract the effect of noise in the responses, usually $nf > m$ and the equation is solved in a least squares sense. Additionally, because matrices $\mathbf{T}$ and $\mathbf{B}$ are complex, noisy results cause large errors in the estimation of the equations of motion. The solution to this problem is to solve separately for the real and imaginary parts, i.e.

$$\begin{Bmatrix} Re(\mathbf{T}) \\ Im(\mathbf{T}) \end{Bmatrix} \mathbf{X} = \begin{Bmatrix} Re(\mathbf{B}) \\ Im(\mathbf{B}) \end{Bmatrix} \tag{2.23}$$

where *Re* denotes real part and *Im* imaginary part. As soon as $\mathbf{X}$ is evaluated, the system is fully identified but only at a particular free-stream velocity.

For increased accuracy, multiple forcing vectors can be applied to the system. This is particularly relevant to the case where the responses include a high level of noise. Then, matrix $\mathbf{F}$ will be of order $m \times n$, where n is the number of forcing vectors and matrix $\mathbf{T}$ will change to

$$\begin{pmatrix}
H^1_{q_1}(\omega_1) & \dots & H^1_{q_m}(\omega_1) & \jmath\omega_1 H^1_{q_1}(\omega_1) & \dots & \jmath\omega_1 H^1_{q_m}(\omega_1) & -1 & 0 & \dots & 0 \\
\vdots & \vdots & \vdots & \vdots & \vdots & \vdots & \vdots & \vdots & \vdots & \vdots \\
H^1_{q_1}(\omega_{nf}) & \dots & H^1_{q_m}(\omega_{nf}) & \jmath\omega_{nf} H^1_{q_1}(\omega_{nf}) & \dots & \jmath\omega_{nf} H^1_{q_m}(\omega_{nf}) & -1 & 0 & \dots & 0 \\
H^2_{q_1}(\omega_1) & \dots & H^2_{q_m}(\omega_1) & \jmath\omega_1 H^2_{q_1}(\omega_1) & \dots & \jmath\omega_1 H^2_{q_m}(\omega_1) & 0 & -1 & \dots & 0 \\
\vdots & \vdots & \vdots & \vdots & \vdots & \vdots & \vdots & \vdots & \vdots & \vdots \\
H^2_{q_1}(\omega_{nf}) & \dots & H^2_{q_m}(\omega_{nf}) & \jmath\omega_{nf} H^2_{q_1}(\omega_{nf}) & \dots & \jmath\omega_{nf} H^2_{q_m}(\omega_{nf}) & 0 & -1 & \dots & 0 \\
\vdots & \vdots & \vdots & \vdots & \vdots & \vdots & \vdots & \vdots & \vdots & \vdots \\
H^n_{q_1}(\omega_1) & \dots & H^n_{q_m}(\omega_1) & \jmath\omega_1 H^n_{q_1}(\omega_1) & \dots & \jmath\omega_1 H^n_{q_m}(\omega_1) & 0 & 0 & \dots & -1 \\
\vdots & \vdots & \vdots & \vdots & \vdots & \vdots & \vdots & \vdots & \vdots & \vdots \\
H^n_{q_1}(\omega_{nf}) & \dots & H^n_{q_m}(\omega_{nf}) & \jmath\omega_{nf} H^n_{q_1}(\omega_{nf}) & \dots & \jmath\omega_{nf} H^n_{q_m}(\omega_{nf}) & 0 & 0 & \dots & -1
\end{pmatrix}$$

superscripts $1 \dots n$ denoting the response for forcing vector $1 \dots n$. Matrix $\mathbf{B}$ will change accordingly.

In order to obtain an identified model of the system at all airspeeds, a second identification needs to take place at a different free-stream velocity. According to [20] the unsteady aerodynamic matrix, $\mathbf{Q}(\jmath\omega)$ for an aeroelastic system is given by

$$\mathbf{Q}(\jmath\omega) = \frac{1}{2}\rho V_\infty^2 \left[\bar{\mathbf{A}}_0 + \bar{\mathbf{A}}_1 \jmath\omega \left(\frac{b}{V_\infty}\right) + \bar{\mathbf{A}}_2 (\jmath\omega)^2 \left(\frac{b}{V_\infty}\right)^2 + \left(\frac{V_\infty}{b}\right) \sum_{n=1}^{n_L} \frac{\bar{\mathbf{A}}_{(n+2)}}{\jmath\omega + (V_\infty/b) b_n} \right] \tag{2.24}$$

where ρ is the air density, V_∞ the free-stream velocity, b a reference length, n_L depends upon the desired accuracy but is usually no more than four and

$\bar{\mathbf{A}}_0 \ldots \bar{\mathbf{A}}_{n_L}$ are matrix coefficients. For a steady, or quasisteady, aerodynamic representation the lag terms are ignored leading to

$$\mathbf{Q}(\jmath\omega) = \frac{1}{2}\rho V_\infty^2 \mathbf{A}_0 + \frac{1}{2}\rho V_\infty \mathbf{A}_1 \jmath\omega - \frac{1}{2}\rho \mathbf{A}_2 \omega^2 \tag{2.25}$$

where $\mathbf{A}_i = b^i \bar{\mathbf{A}}_i$ for $i = 1, 2$, $\mathbf{A}_0$ represents aerodynamic stiffness terms, $\mathbf{A}_1$ aerodynamic damping terms and $\mathbf{A}_2$ aerodynamic inertia terms. The latter are usually very small compared to structural inertia terms and therefore neglected. Hence,

$$\mathbf{Q}(\jmath\omega) = \frac{1}{2}\rho V_\infty^2 \mathbf{A}_0 + \frac{1}{2}\rho V_\infty \mathbf{A}_1 \jmath\omega \tag{2.26}$$

In other words, matrices $\mathbf{C}$ and $\mathbf{K}$ in equation 2.21 can be broken down into structural and aerodynamic part, i.e.

$$\mathbf{C} = \mathbf{C}_s + \frac{1}{2}\rho V_\infty \mathbf{A}_1$$

$$\mathbf{K} = \mathbf{K}_s + \frac{1}{2}\rho V_\infty^2 \mathbf{A}_0$$

subscript s denoting structural terms. If the identification process described earlier is repeated at two distinct velocities, then the structural and aerodynamic matrices can be evaluated separately and the behaviour of the system at any airspeed can be numerically predicted either by integrating the equations of motion or by calculating the system's eigenvalues. Finally, the flutter speed can be obtained by means of a suitable iterative calculation, e.g. evaluating the system damping at increasing speeds until flutter is reached.

It should be noted that the NG method requires modal responses to work. Consequently, if only physical coordinates, $\mathbf{z}$, are available, then the modal matrix, $\mathbf{\Phi}$, should be evaluated and used to obtain the modal coordinates from

$$\mathbf{z} = \mathbf{\Phi}\mathbf{q}$$

Method Validation

The NG modelling of the equations of motion of a system is very accurate for low order models and in the absence of noise in the responses. A sample application of the method to the Hancock wing model yields the following matrices for a velocity of 30 m/s.

$$C_{id} = \begin{pmatrix} 5.1641 & -0.0157 & -0.0192 \\ -54.0986 & 3.0709 & -0.9797 \\ 104.8484 & -11.9187 & 9.1895 \end{pmatrix}, K_{id} = 10^4 \begin{pmatrix} 0.2866 & 0.0014 & -0.0037 \\ -0.3771 & 1.9534 & -0.5034 \\ -5.6567 & -7.7934 & 4.6044 \end{pmatrix}$$

$$F_{id} = \begin{Bmatrix} 2.2666 \\ -35.4727 \\ 85.2259 \end{Bmatrix}$$

where subscript id denotes identified matrix. The actual matrices for the system are

$$C_a = \begin{pmatrix} 5.1640 & -0.0156 & -0.0193 \\ -54.0959 & 3.0728 & -0.9805 \\ 104.8440 & -11.9018 & 9.1815 \end{pmatrix}, K_a = 10^4 \begin{pmatrix} 0.2866 & 0.0014 & -0.0037 \\ -0.3771 & 1.9532 & -0.5034 \\ -5.6566 & -7.7934 & 4.6044 \end{pmatrix}$$

$$F_a = \begin{Bmatrix} 2.2664 \\ -35.4708 \\ 85.2220 \end{Bmatrix}$$

subscript a denoting actual matrices.

The equations of motion for an aeroelastic system, once identified, can be solved by evaluating the eigenvalues and hence natural frequencies and damping ratios at various airspeeds. Figure 2.21 demonstrates this procedure. At the velocity where the damping ratio becomes zero, flutter occurs.

The factors that affect the accuracy of the NG method are the presence of noise and the velocities at which the subcritical tests take place. A further consideration is the number of airspeeds at which tests are carried out. The NG method

only needs two tests at two different velocities in order to provide the complete equations of motion. However, during the course of the present research, the possibility that flutter predictions might improve if more than two velocities are used was examined. The basic premise of this idea is that, if there are measurement errors in the responses used in the identification process, then the identified equations of motion will also contain errors, resulting in less accurate flutter predictions. Hence, if tests are carried out at more than two velocities and the aerodynamic and structural matrices obtained by a least squares procedure, the flutter estimates might improve.

To test this idea, the Hancock model was used, in the 10-30 m/s velocity range (or $0.23V_f - 068V_f$). The first test was carried out with two velocities, one at 10/s and one at 30m/s. The second test was carried out with three velocities, one at 10m/s, one at 20m/s and one at 30m/s. In all, seven tests were carried out with up to eight velocities, all within the same range. The responses in all the tests were contaminated with 10% rms white noise, chosen from a normal distribution with zero mean and unity variance. Each test case was repeated 100 times to provide a large population of flutter speed estimates. The confidence bounds of the mean flutter estimate for each test case were calculated using the Student's T test [21] with a confidence level of 1%. The results are tabulated in table 2.7 and plotted in figure 2.22.

Number of Airspeeds	Flutter Speed Estimate (m/s)
2	44.0761 ± 0.0434
3	44.0931 ± 0.0600
4	44.1506 ± 0.0720
5	44.1208 ± 0.0656
6	44.0532 ± 0.0715
7	44.1218 ± 0.0564
8	44.1468 ± 0.0526

Table 2.7: Flutter estimates by the NG method using different numbers of test speeds

In figure 2.22, the horizontal line is the true flutter speed. It can be seen that the best result, both in terms of mean flutter speed and confidence bounds occurs in the case when only 2 speeds are used. This result is also obvious in table 2.7, since the general tendency is for the confidence bounds to grow with increasing number of test speeds. The conclusion drawn from these results is that there is no advantage in using more than two test speeds to identify a system with NG method.

Since only two tests are needed for a successful identification, the tabulated results for the NG method will, by necessity, slightly differ to those for the previous methods. The velocity ranges will be the same, but there will only be two speeds in each range, one at the start and one at the end. Table 2.8 shows flutter predictions for the Hancock model obtained using the NG method .

Velocity range ($\times V_f$)	Flutter Speed Estimate	% Error
0.23-0.43	42.9950	-2.5
0.23-0.57	46.1450	+4.7
0.23-0.70	44.6420	+1.3
0.23-0.84	44.1040	+0.1
0.23-0.98	44.1100	+0.1
0.45-0.66	43.7340	-0.8
0.45-0.79	43.7810	-0.7
0.45-0.93	44.1420	+0.2
0.68-0.88	44.3750	+0.7

Table 2.8: Flutter Speed Estimates using NG, Hancock model

It can be seen that there is very little variation in the flutter prediction with the velocity range, the only poor estimate occurring when the test were below 60% of the true flutter speed. Despite the presence of 5% rms noise the predictions are very accurate. However, as the noise level increases the quality of identification decreases as can be seen in figure 2.23. The system identified contains no structural damping so that the damping ratios should be zero at zero velocity but the quality of identification in the presence of 10% rms noise is so low that the

predicted dampings at zero velocity are non-zero. The corresponding identified matrices in the equations of motion are

$$C_{id} = \begin{pmatrix} 5.6637 & 0.1748 & -0.0954 \\ -50.7432 & -0.5380 & 0.7206 \\ 60.0906 & -8.3478 & 7.4080 \end{pmatrix} K_{id} = 10^4 \begin{pmatrix} 0.2779 & -0.0207 & 0.0068 \\ -0.4377 & 1.7631 & -0.4132 \\ -4.9510 & -5.8034 & 3.6588 \end{pmatrix}$$

$$F_{id} = \begin{Bmatrix} 2.6217 \\ -31.9403 \\ 48.5328 \end{Bmatrix}$$

the actual matrices being as given earlier. The adverse effects of experimental errors can be overcome by using more than one forcing vectors during identification. With four forcing vectors and with 20% rms noise, for the same test case, the identified matrices are

$$C_{id} = \begin{pmatrix} 5.1643 & -0.0155 & -0.0190 \\ -54.0989 & 3.0712 & -0.9823 \\ 104.8461 & -11.9231 & 9.1805 \end{pmatrix} K_{id} = 10^4 \begin{pmatrix} 0.2866 & 0.0014 & -0.0037 \\ -0.3771 & 1.9533 & -0.5035 \\ -5.6566 & -7.7934 & 4.6042 \end{pmatrix}$$

$$F_{id} = \begin{Bmatrix} 2.2669 \\ -35.4731 \\ 85.2241 \end{Bmatrix}$$

i.e., as accurate as they were in the no noise test case presented earlier.

The NG method was not successfully applied to the Sim-2 model. The large number of modes in the Sim-2 model, coupled with the fact that the equations of motion are 'stiff', i.e. some of the system eigenvalues are orders of magnitude larger than the low frequency eigenvalues, caused matrix T in equation 2.22 to be badly scaled and, hence, nearly singular. As a consequence, the resulting equations of motion were highly inaccurate.

2.2.5 Steady State Identification Method

This method was developed during the course of the present research as a time-domain variation of the NG. It is based on the premise that a linear system can be identified by only looking at its steady-state response to a known forcing function. As a demonstration of this premise consider the following simple, 1-degree-of-freedom, second order system

$$m\ddot{x} + c\dot{x} + kx = A\sin\omega t + B\cos\omega t$$

The steady-state response of this system is of the form

$$x = C_1\sin\omega t + C_2\cos\omega t$$

If the excitation signal and the steady-state response are considered to be known, it is possible to substitute back into the equation of motion and, equating sine and cosine parts, obtain

$$\begin{aligned} -m\omega^2 C_1 - c\omega C_2 + kC_1 &= A \\ -m\omega^2 C_2 + c\omega C_1 + kC_2 &= B \end{aligned}$$

which is a system of two equations with three unknowns, m, c and k. By repeating the excitation at, say, a different frequency and recording the response, a third equation can be generated and the system can be identified.

The Steady State Identification (SSI) method is just an extension of this simple procedure to a large aeroelastic system. The standard equations of motion for such a system with sinusoidal input are

$$\bar{\mathbf{M}}\ddot{\mathbf{q}} + \bar{\mathbf{C}}\dot{\mathbf{q}} + \bar{\mathbf{K}}\mathbf{q} = \bar{\mathbf{F}}A_f\sin(\omega t + \Phi) \tag{2.27}$$

Φ being the phase angle and A_f the amplitude of the excitation signal. Normalizing by $\bar{\mathbf{M}}$

$$\mathbf{I}\ddot{\mathbf{q}} + \mathbf{C}\dot{\mathbf{q}} + \mathbf{K}\mathbf{q} = \mathbf{F}A_f(\sin(\omega t)\cos\Phi + \cos(\omega t)\sin\Phi) \tag{2.28}$$

where

$$\mathbf{C} = \bar{\mathbf{M}}^{-1}\bar{\mathbf{C}}$$
$$\mathbf{K} = \bar{\mathbf{M}}^{-1}\bar{\mathbf{K}}$$
$$\mathbf{F} = \bar{\mathbf{M}}^{-1}\bar{\mathbf{F}}$$

The ith steady-state response is of the form $q_i(t) = A_i \sin\omega t + B_i \cos\omega t$. Substituting back into equation 2.18 gives

$$\left[-\omega^2\mathbf{I}\begin{pmatrix} A_1 & B_1 \\ \vdots & \vdots \\ A_m & B_m \end{pmatrix} + \omega\mathbf{C}\begin{pmatrix} -B_1 & A_1 \\ \vdots & \vdots \\ -B_m & A_m \end{pmatrix} + \mathbf{K}\begin{pmatrix} A_1 & B_1 \\ \vdots & \vdots \\ A_m & B_m \end{pmatrix}\right]\begin{pmatrix} \sin\omega t \\ \cos\omega t \end{pmatrix} =$$

$$\mathbf{F}A_f\begin{pmatrix} \cos\Phi & \sin\Phi \\ \vdots & \vdots \\ \cos\Phi & \sin\Phi \end{pmatrix}\begin{pmatrix} \sin\omega t \\ \cos\omega t \end{pmatrix} \tag{2.29}$$

Re-arranging the equation results in

$$\begin{pmatrix} -\omega B_1 & \dots & -\omega B_m & A_1 & \dots & A_m & -A_f\cos\Phi \\ \omega A_1 & \dots & \omega A_m & B_1 & \dots & B_m & -A_f\sin\Phi \end{pmatrix}\begin{pmatrix} \mathbf{C}^T \\ \mathbf{K}^T \\ \mathbf{F}^T \end{pmatrix} =$$

$$\omega^2\begin{pmatrix} A_1 & \dots & A_m \\ B_1 & \dots & B_m \end{pmatrix} \tag{2.30}$$

Again, equation 2.30 is a system of $2m$ equations with $(2m+1)m$ unknowns. Hence, nf more responses need to be obtained by exciting the system at nf different frequencies (where n_f is the number of frequencies). Since $(2m+1)m$ is not divisible by $2m$, either some of the $2m \times nf$ equations need to be omitted or the resulting system of equations needs to be solved in a least squares sense.

The latter approach is much more advisable since it minimizes the effect of noise in the measured responses. Equation 2.30 becomes

$$\begin{pmatrix} -\omega_1 B_1(\omega_1) & \dots & -\omega_1 B_m(\omega_1) & A_1(\omega_1) & \dots & A_m(\omega_1) & -A_f \cos\Phi \\ \vdots & \vdots & \vdots & \vdots & \vdots & \vdots & \vdots \\ -\omega_{nf} B_1(\omega_{nf}) & \dots & -\omega_{nf} B_m(\omega_{nf}) & A_1(\omega_{nf}) & \dots & A_m(\omega_{nf}) & -A_f \cos\Phi \\ \omega_1 A_1(\omega_1) & \dots & \omega_1 A_m(\omega_1) & B_1(\omega_1) & \dots & B_m(\omega_1) & -A_f \sin\Phi \\ \vdots & \vdots & \vdots & \vdots & \vdots & \vdots & \vdots \\ \omega_{nf} A_1(\omega_{nf}) & \dots & \omega_{nf} A_m(\omega_{nf}) & B_{nf}(\omega_{nf}) & \dots & B_m(\omega_{nf}) & -A_f \sin\Phi \end{pmatrix} \times$$

$$\begin{pmatrix} \mathbf{C}^T \\ \mathbf{K}^T \\ \mathbf{F}^T \end{pmatrix} = \begin{pmatrix} \omega_1^2 A_1(\omega_1) & \dots & \omega_1^2 A_m(\omega_1) \\ \vdots & \vdots & \vdots \\ \omega_{nf}^2 A_1(\omega_{nf}) & \dots & \omega_{nf}^2 A_m(\omega_{nf}) \\ \omega_1^2 B_1(\omega_1) & \dots & \omega_1^2 B_m(\omega_1) \\ \vdots & \vdots & \vdots \\ \omega_{nf}^2 B_1(\omega_{nf}) & \dots & \omega_{nf}^2 B_m(\omega_{nf}) \end{pmatrix} \tag{2.31}$$

The amplitudes A_i and B_i are obtained by curve-fitting the steady-state responses in the time-domain. The transient response is allowed to decay away and then as much of the steady-state response as possible is fitted by a sum of one sine and one cosine in a least squares sense. This approach is very powerful in the case of noisy results since the sinusoidal curve-fit can eliminate a lot of the noise. In general, if the expected shape of the response is known, it is easier to separate if from noise.

Once the matrices **C**, **K** and **F** are known, the identification procedure is repeated at a different velocity and the aerodynamic matrices of the system are evaluated as in the case of the NG method described earlier.

Method Validation

A sample application of the SSI method is presented here, again using the 3-dof wing system as the aeroelastic system to be identified. Using four forcing vectors of different frequencies the identified matrices at a speed of 21 m/s, and in the absence of any noise, are

$$C_{id} = \begin{pmatrix} 5.1639 & -0.0156 & -0.0193 \\ -54.0361 & 3.0691 & -0.9808 \\ 104.9539 & -11.9081 & 9.1809 \end{pmatrix} K_{id} = 10^4 \begin{pmatrix} 0.1120 & 0.0038 & -0.0022 \\ -0.1471 & 1.4847 & -0.4256 \\ -2.2093 & -5.9786 & 3.8761 \end{pmatrix}$$

$$F_{id} = \begin{Bmatrix} 0.1133 \\ -1.7735 \\ 4.2611 \end{Bmatrix}$$

the actual matrices being

$$C_a = \begin{pmatrix} 5.1640 & -0.0156 & -0.0193 \\ -54.0959 & 3.0728 & -0.9805 \\ 104.8440 & -11.9018 & 9.1815 \end{pmatrix} K_a = 10^4 \begin{pmatrix} 0.1120 & 0.0038 & -0.0022 \\ -0.1473 & 1.4847 & -0.4256 \\ -2.2096 & -5.9786 & 3.8761 \end{pmatrix}$$

$$F_a = \begin{Bmatrix} 0.1133 \\ -1.7735 \\ 4.2611 \end{Bmatrix}$$

For best results the frequencies of the forcing vectors need to lie within the frequency range of the actual system's natural frequencies. In the absence of noise in the responses no more forcing vectors are needed than necessary to obtain enough equations for the number of unknowns. Then the flutter velocity can be obtained as shown earlier in the case of the NG method. Figure 2.24 shows the damping ratio variation with velocity as obtained from the identified equations of motion.

A further advantage of the sinusoidal curve-fit is that it decreases the method's sensitivity to experimental errors. Figure 2.25 shows that the identification of responses containing 20% rms noise is still very accurate using only the four necessary forcing vectors. Higher levels of noise do cause degradation, as seen in figure 2.26, but that can be rectified by the use of more forcing vectors, figure 2.27. The true flutter speed for the system in figures 2.24- 2.27 is $42.6290 m/s$.

As with the NG method, only two tests at two airspeeds are required for a successful identification. More than two airspeeds were tried but no improvement in the accuracy of the flutter predictions was obtained. Hence, each of the results presented in table 2.9 were obtained for the Hancock model using two tests; one at the start of the velocity range, and one at the end.

Velocity range ($\times V_f$)	Flutter Speed Estimate	% Error
0.23-0.43	43.0600	-2.3
0.23-0.57	44.4142	+0.8
0.23-0.70	44.2872	+0.5
0.23-0.84	44.5370	+1.0
0.23-0.98	44.2410	+0.4
0.45-0.66	43.4520	-1.4
0.45-0.79	43.9870	-0.2
0.45-0.93	43.8520	-0.5
0.68-0.88	44.0920	+0.0

Table 2.9: Flutter Speed Estimates using SSI method, Hancock model

The flutter speed is consistently calculated with considerable accuracy, the highest percentage error being 2.3 % and occurring when the two tests are carried out at low speeds, very close to each other.

It has to be noted that any application of the SSI method at low-damping conditions is likely to present difficulties since the method depends upon identifying the steady state response of a system. If the transient response takes a long time to decay, it is likely that some of it will still be present in the signal used for identification, hence affecting the sinusoidal curve fit. This means that the

method delivers the best and fastest results away from the critical regions, unlike the FFM approach discussed earlier.

The main disadvantage of the SSI method is that it is very expensive both in experimental and computational terms. As discussed earlier, the more degrees of freedom in the system under investigation, the more forcing vectors are needed for a successful identification. For a 10-dof system, 11 forcing vectors are needed, more if there are high levels of noise present in the data.

As with the NG method, the SSI method could not be successfully applied to the Sim-2 model. Because of the stiffness in the Sim-2 equations, the left-hand-side matrix in equation 2.31 was found to be badly scaled and nearly singular. Using additional forcing vectors did not solve the problem.

2.2.6 ARMA-based method

Let there be a linear 1-dof dynamical system described by the equation

$$m\ddot{y} + c\dot{y} + ky = u(t) \tag{2.32}$$

where m is the mass, c is the damping, k is the stiffness and $u(t)$ is the excitation function. Using the following expressions for the acceleration and velocity in the equation of motion

$$\ddot{y}_i = \frac{y_{i+1} - y_i + y_{i-1}}{\Delta t^2}$$

$$\dot{y}_i = \frac{y_{i+1} - y_{i-1}}{2\Delta t}$$

the finite difference representation of the equation of motion (using central differences, see Appendix D) is obtained;

$$\left(\frac{m}{\Delta t^2} + \frac{c}{2\Delta t}\right) y_{i+1} + \left(k - \frac{m}{\Delta t^2}\right) y_i + \left(\frac{m}{\Delta t^2} - \frac{c}{2\Delta t}\right) y_{i-1} = u_i \tag{2.33}$$

where Δt is the time-step (or the inverse of the damping frequency).

Thus, the equation of motion can be expressed as a sum of the value of the response of the system at three consecutive time instances equal to the value of the forcing function at the current time instance. This is the basis of the representation of dynamical systems by ARMA (Auto-Regressive, Moving-Average) models where the AR part denotes the terms containing y and the MA part denotes the white noise excitation terms.

For a multi-dof system, the general form of a ARMA is [22]

$$\sum_{m=0}^{2J} b(m)y(i+m) = \sum_{m=0}^{2J-1} a(m)u(i+m) \tag{2.34}$$

where i denotes the ith time instance, a and b are coefficients and J is the order of the model which can be equal to the number of modes of the system to be modelled (as in the simple case presented above) but, in the presence of experimental noise, it is usually taken to be greater than the number of modes.

In order to identify a given dynamical system, the ARMA equation is applied to a set of single-input single-output sampled data. The unknown coefficients, a, b and J are evaluated using a parameter estimation algorithm, the simplest of which is the least squares procedure. This evaluation can be simplified by dividing the ARMA equation throughout by $b(2J)$, so that the leading AR coefficient is always 1 and need not be calculated.

If equation 2.34 is evaluated at instances $i = 1, \ldots, k$ then the coefficients can be obtained using

$$\begin{pmatrix} y(2J) & \dots & y(1) & u(2J) & \dots & u(1) \\ y(2J+1) & \dots & y(2) & u(2J+1) & \dots & u(2) \\ \vdots & \vdots & & \vdots & \vdots & \\ y(2J+k-1) & \dots & y(k) & u(2J+k-1) & \dots & u(k) \end{pmatrix} \times \begin{Bmatrix} b(2J-1) \\ \vdots \\ b(0) \\ a(2J-1) \\ \vdots \\ a(0) \end{Bmatrix} = - \begin{Bmatrix} y(2J+1) \\ y(2J+2) \\ \vdots \\ y(2J+k) \end{Bmatrix} \tag{2.35}$$

This matrix equation can be solved using any number of schemes, such as those described in [23] and [24]. The eigenvalues of the system can be obtained by forming the characteristic polynomial [24]

$$G(\mu) = \mu^{2J} + b(2J-1)\mu^{2J-1} + \ldots + b(1)\mu + b(0) = 0 \tag{2.36}$$

and, subsequently, evaluating its roots

$$\mu_{1,2} = \exp\left((-\zeta\omega \pm j\omega\sqrt{1-\zeta^2})\Delta t\right) \tag{2.37}$$

where ζ is the damping ratio and ω is the natural frequency.

The choice of J is very important. In the case were there is no noise (experimental or numerical) in the data used in equation 2.35 J can be equal to the number of modes, thus yielding the finite difference coefficients.

The ARMA method, as described up to now is a system identification technique. Matsuzaki [22] suggests a procedure for using an ARMA representation of an aeroelastic system as a means of predicting the flutter velocity. The basis of the approach is the Jury Determinant method for evaluating the stability of a discrete-time system, which is very similar to the Routh-Hurwitz criterion for continuous-time systems (used in conjunction with the Flutter Margin method). The Jury stability criterion applies to the characteristic polynomial,

equation 2.36, as follows:

$$G(1) > 0, \quad G(-1) > 0 \tag{2.38}$$

and

$$F^{\pm}(l) = |X_l^* \pm Y_l^*| > 0, \quad \text{for } l = 1, 3, \ldots, 2J-1 \tag{2.39}$$

where X^*_{2J-1} and Y^*_{2J-1} are $(2J-1) \times (2J-1)$ matrices defined as

$$X^*_{2J-1} = \begin{pmatrix} b(2J) & b(2J-1) & \ldots & \ldots & b(3) & b(2) \\ 0 & b(2J) & b(2J-1) & \ldots & b(4) & b(3) \\ 0 & 0 & b(2J) & \ldots & b(5) & b(4) \\ \vdots & & \vdots & & \vdots & \\ 0 & \ldots & \ldots & \ldots & \ldots & b(2J) \end{pmatrix} \tag{2.40}$$

$$Y^*_{2J-1} = \begin{pmatrix} b(2J-2) & b(2J-3) & \ldots & \ldots & b(1) & b(0) \\ b(2J-3) & b(2J-4) & \ldots & \ldots & b(0) & 0 \\ b(2J-4) & b(2J-5) & \ldots & b(0) & 0 & 0 \\ \vdots & & \vdots & & \vdots & \\ b(0) & 0 & \ldots & \ldots & \ldots & 0 \end{pmatrix} \tag{2.41}$$

Consequently, the flutter condition is defined as the first airspeed at which any of the criteria $G(1)$, $G(-1)$, $F^{\pm}(l)$ becomes zero. As a consequence, the system can be identified at a range of velocities, the values of the criteria plotted against airspeed and then curve fitted by a polynomial to yield the points were they intersect the velocity axis and hence the flutter velocities. This particular implementation of the Jury stability criterion is disadvantageous compared to the Flutter Margin method in that the criteria do not vary in a predictable manner with velocity. Instead, if polynomial fitting is attempted, the order will not be

known and will have to be adjusted so that it gives the best result, as with the damping fit and Envelope methods.

Method Validation

The MA (Moving Average) part of a ARMA model implies white noise excitation however, since all the other methods were evaluated using frequency sweep excitation signals, an ARMAX (Auto-Regressive Moving Average with eXogenous inputs) model was used instead of ARMA to ensure a fair comparison of the methods. The term exogenous inputs refers to inputs other than white noise.

The first difficulty in the implementation of the method is the evaluation of the ARMAX coefficients. In the absence of noise, this evaluation can be accomplished quite successfully even using a simple least squares procedure with $J=$ number of modes. Then, the response of the ARMAX model to a given signal is almost identical to that of the actual system, as was found when the procedure was applied to the Hancock model. In figures 2.28 and 2.29 all the stability criteria are plotted for a range of velocities up to the flutter velocity for the noise-free case. Criterion F_5^- goes negative at an airspeed very close to the actual flutter velocity. However, it can be seen that the drop in the value of F_5^- is very abrupt. If a curve-fit of the criterion were attempted at low subcritical speeds, it would fail to predict flutter. References [22] and [25] suggest a linear curve-fit very close to the flutter velocity however, such a procedure would carry considerable risks in the case of an experimental test, be it in the wind-tunnel or in the air.

When the responses contain noise, the evaluation of an accurate ARMA representation of an aeroelastic system becomes very difficult. A number of parameter estimation schemes were used in the application of the method to the Hancock wing with control surface model with 5% rms noise in the response. These included standard Least Squares, Instrumental Matrix with Delayed Observations,

Double Least Squares, [24] and the Recursive Filtering Method [23]. Figures 2.30 and 2.31 show the estimated stability criteria for a best-case application using Double Least Squares and J = number of modes. Despite the noise, F_5^- is correctly identified as the first criterion to go negative however, the curves are obviously very rugged and would not admit a successful polynomial curve fit. The flutter velocity was identified accurately but only after tests were performed at a high subcritical speed. For $J = 5$ (number of modes +2) the resulting criteria are worse (figures 2.32 and 2.33). The authors of [22] and [25] suggest a Maximum Likelihood approach for the estimation of the coefficients however, they do not mention any applications of that approach to the case were there are measurement errors in the responses in either of these references.

The best results were obtained when using J = number of modes with Double Least Squares. The response results were decimated, i.e. the time-step was increased because when the time-step is very small the curve-fit is more sensitive to corruption [24]. Table 2.10 shows flutter predictions using this approach for the Hancock model.

Velocity Range	Best Flutter Speed Estimate	% Error	Best Order of fit
0.23-0.43	23.7299	-46.2	2
0.23-0.57	36.3818	-17.5	2
0.23-0.70	34.8338	-21.0	6
0.23-0.84	37.2929	-15.4	9
0.23-0.98	43.9580	-0.3	7
0.45-0.66	33.6654	-23.6	2
0.45-0.79	40.2583	-8.7	2
0.45-0.93	43.3815	-1.6	5
0.68-0.88	41.4045	-6.1	3

Table 2.10: Flutter Estimates using ARMAX Method, Hancock Model

The flutter predictions in table 2.10 are worse than those obtained from all the other methods. Even when the ARMAX coefficients are calculated successfully, the tests have to be carried out at very high subcritical speeds to yield an accurate

flutter velocity.

For the Sim-2 model, the best ARMAX fits were obtained using normal least squares and $J=$ number of modes. It was found that small amounts of noise improved the fits. Figure 2.34 shows a sample fit. The agreement between ARMAX model and the Sim-2 results is very good. The performance of the ARMAX method is generally better for the Sim-2 model than for the Hancock model. This is due to the fact that, because of the high number of modes, there are many more $F^{\pm}(l)$ stability criteria. Figure 2.35 shows the $F^{+}(l)$ and figure 2.36 shows the $F^{-}(l)$ criteria for a sample application (criteria $G(1)$ and $G(-1)$ do not go negative). The critical criterion is $F^{-}(45)$ since it assumes negative values first. Hence, the flutter velocities in table 2.11 were obtained by polynomial curve-fits of $F^{-}(45)$.

Velocity Range	Best Flutter Speed Estimate	% Error	Best Order of fit
0.23-0.43	186.091	-53.3	3
0.23-0.57	267.351	-32.9	3
0.23-0.70	372.563	-6.5	7
0.23-0.84	363.819	-8.7	5
0.23-0.98	394.513	-1.0	4
0.45-0.66	266.028	-12.1	2
0.45-0.79	350.197	-8.7	5
0.45-0.93	407.393	+2.2	4
0.68-0.88	390.476	-2.0	4

Table 2.11: Flutter Estimates using ARMAX Method, Sim-2 Model

2.3 Simulated Flutter Test

Simulated flutter tests were performed for both models using all the flutter prediction methods. The procedure for all approaches (apart from the Nissim & Gilyard technique) was as follows:

1. The response of each model was first obtained at a low subcritical speed, equal to 22.7% of the actual flutter speed. In the case of the Sim-2 model the response also depends on the flight altitude which was fixed at 5000ft. The responses were analysed to provide estimates for the damping ratios, Flutter Margin, envelope function shape parameter and ARMA-based stability criteria.

2. The flight speed was increased by an increment equal to 7% of the actual flutter speed and estimates of the of the four stability parameters mentioned in step 1 were obtained.

3. The flight speed was increased again by the same increment of the actual flutter speed and estimates of the four stability parameters were obtained. Each of the parameters was fitted with respect to flight speed by a second-degree polynomial whose roots were subsequently obtained. Any roots which were complex, lower than the current flight speed, or occurred at points of positive curvature were ignored. The remaining roots provided the first estimates for the flutter speed, a maximum of one estimate for each stability parameter. Subsequently, checks were performed to ensure that the next flight speed would not be within 20% of any of the flutter speed estimates. At this early stage in the testing procedure, all methods indicated stability for the next test point.

4. The flight speed kept being increased by the same increment, new estimates for the stability parameters being obtained and added to the curve fitting procedure. With each new estimate, higher orders of polynomial curve fits were possible. The Flutter Margin was only fitted by 2nd order polynomials but the other three stability parameters were fitted by polynomials of all possible orders, the new estimate for the flutter speed being calculated as

the mean of all the acceptable roots. After all the new estimates were obtained, stability checks were performed for the next test speed.

5. The simulated flight test was ended at the test speed at which all methods predicted that the next test speed would be within 20% of the latest flutter speed estimates. For each of the methods, the final flutter speed estimate was taken to be the first estimate at which the stability check failed.

For the Nissim & Gilyard method, the procedure was slightly different. At each test point, only the current and initial responses were used to provide a flutter estimate. Additionally, the NG and SSI methods were only applied to the Hancock model flutter tests for the reasons explained in the previous section.

All results were obtained for responses contaminated by 5% rms white noise. The noise was simulated by taking the inverse Fourier transform of a frequency signal with constant amplitude and random phase. The simulated flutter test procedure was repeated 30 times and the mean flutter speed prediction and 5% confidence interval was calculated for each method. The results are tabulated in tables 2.12 and 2.13.

Method	Mean Flutter Speed Estimate (m/s)	Mean Error (%)
Damping Fit	43.73 ± 1.054	-0.8
Envelope	46.00 ± 1.093	+4.4
Flutter Margin	45.34 ± 0.251	+2.9
ARMAX-based	24.50 ± 2.176	-44.4
Nissim & Gilyard	44.13 ± 0.142	+0.1
SSI	44.10 ± 0.098	+0.1

Table 2.12: Flutter predictions for the Hancock model, simulated flutter test

2.4 Comparison between the methods

From the discussion already presented, it should be clear that all the flutter prediction methods investigated here can yield accurate predictions under certain

Method	Mean Flutter Speed Estimate (kts)	Mean Error (%)
Damping Fit	394.15 ± 5.88	-1.0
Envelope	386.82 ± 2.47	-2.8
Flutter Margin	432.82 ± 5.38	+8.8
ARMAX	164.08 ± 9.87	-58.8

Table 2.13: Flutter predictions for the SIM-2 model, simulated flutter test

circumstances. The crucial consideration that divides the techniques is how wide is this set of circumstances for each one of them. A further consideration is the ease of use and the speed of the calculations involved. During a flight flutter test it is often very important to know as soon as possible whether proceeding to the next test point is safe.

The methods can be separated into two categories:

- **Category 1**: Methods that identify the equations of motion. This category contains the NG and SSI methods, both of which require the degree of freedom or modal responses. The identification requires only two tests at two different velocities. The equations of motion can then be solved to yield the flutter speed.

- **Category 2**: Methods that only require one set of measured response data. This category contains the rest of the methods (Damping Fit, FM, Envelope and ARMA-based). They all calculate a parameter which characterizes the stability of a system at each test velocity. The parameter variation with airspeed is curve-fitted by a polynomial and then extrapolated to the condition for instability, to yield the flutter velocity.

To facilitate the assessment of the methods, tables 2.14 and 2.15 summarize the results presented in the previous section. Errors in the estimated flutter predictions are tabulated against speed range of the test, which is presented as a ratio of the true flutter velocity.

Velocity Range	Damping Fit	Flutter Margin	Envelope	NG	SSI	ARMAX
0.23-0.43	+14.4	-6.8	+13.0	-2.5	-2.3	-46.2
0.23-0.57	+5.1	+3.9	-2.1	+4.7	+0.8	-17.5
0.23-0.70	-9.1	+2.5	+0.6	+1.3	+0.5	-21.0
0.23-0.84	-0.1	+1.1	+4.8	+0.1	+1.0	-15.4
0.23-0.98	+0.5	+0.3	-0.1	+0.1	+0.4	-0.3
0.45-0.66	+17.5	+1.3	-6.9	-0.8	-1.4	-23.6
0.45-0.79	-0.9	+1.7	-1.9	-0.7	-0.2	-8.7
0.45-0.93	-0.1	+0.1	+0.3	+0.2	-0.5	-1.6
0.68-0.88	+0.2	-0.8	+0.4	+0.7	+0.0	-6.1

Table 2.14: Errors in Flutter Estimates using all methods, Hancock Model

As far as the accuracy of prediction and the range of parameters under which high accuracy is maintained is concerned, the equation-of-motion-identification methods are best, as indicated by the Hancock model results. Both the NG and the SSI method provide consistently high quality predictions even when the subcritical tests are carried out at relatively low velocities and under high levels of noise. Their accuracy is derived from the fact that a number of responses to different inputs are employed in the calculations.

On the other hand, it was found that category 1 methods could not be successfully applied to the Sim-2 model. Only category 1 methods could provide results for that model, the Damping Fit approach being by far the most successful, followed by the Envelope Method. However, category 2 methods require polynomial curve-fitting and, except in the case of the Flutter Margin method, the order of the polynomial is unknown. One way of determining which order of polynomial is best, is to obtain a preliminary value for the flutter velocity. This can be provided either by using a mathematical model of the system under consideration or from earlier flight flutter tests. Additionally, with the exception of the Envelope method, category 2 methods are 'complementary', i.e. they all require a knowledge of the eigenvalues of the system. Once these have been evaluated for a particular test-case, flutter predictions can be obtained very quickly

and inexpensively. Hence, the Damping fit, Flutter Margin and ARMA methods could conceivably be applied simultaneously at each test-case.

It should be noted that the present research indicates that, for large systems, the Damping Fit method is the most effective. This method also happens to be the most widely used approach in practical flight flutter tests. In a purely academic sense, category 1 methods are preferable to the Damping Fit technique because they provide a fuller picture of the dynamics of a given system. Nevertheless, in real applications category 1 methods are confronted by a number of practical problems like the choice of the number of modes or the need for modal responses, as well as mathematical problems, like 'stiff' systems. The Damping Fit method does not suffer from any of these difficulties. Any aeroelastic system, no matter how complex, will yield damping data and will have zero damping at the flutter speed.

Velocity Range	Damping Fit	Flutter Margin	Envelope	ARMAX
0.23-0.43	-88.4	-	+5.5	-53.3
0.23-0.57	-17.0	-18.8	-35.1	-32.9
0.23-0.70	-9.2	-15.5	-16.2	-6.5
0.23-0.84	+4.6	-3.8	+2.5	-8.7
0.23-0.98	-0.3	+0.8	-0.7	-1.0
0.45-0.66	+2.8	-20.8	+9.4	-12.1
0.45-0.79	+2.3	+5.5	+6.0	-8.7
0.45-0.93	+0.5	-	+1.3	+2.2
0.68-0.88	+2.9	-	+0.5	-2.0

Table 2.15: Errors in Flutter Estimates using all methods, Sim-2 Model

A final note should be made on the ARMA-based method. Its performance in both the stand-alone tests and the simulated flutter tests was much poorer than the performance of any of the other methods. The Jury stability criteria, which are employed to pinpoint the flutter velocity have a very indifferent low subcritical variation, i.e. flat and noisy, as seen in figures 2.35 and 2.36. Only

near flutter does the variation become significant. Hence, any polynomial curve-fit that uses low subcritical values of the stability criteria will yield large errors. In essence, the present research into the ARMA-based method sheds doubts on the suitability of the Jury stability criteria for the analysis of flight flutter test data.

In terms of computational effort, category 1 methods require more data, especially if multiple excitation vectors are used, but less test speeds than category 2 methods. As table 2.16 shows, category 1 methods are less expensive than category 2 methods, mainly because of the smaller number of tests. The computational time and number of flops (floating point operations) data were obtained for a speed range of 10-43 m/s for the Hancock model. Category 2 method tests took place every 3 m/s in that range (a total of 12 m/s). Category 1 methods were applied with four excitation vectors each. Of course, these results should only be seen as indicators of comparative computational costs, not as absolute assessments of the computational efficiency of each method.

Method	Time (s)	Flops
ARMA	103.9080	58279907
Damp	119.0050	580848971
FM	93.4040	420815792
Envelope	58.6300	111513021
NG	19.2780	16367706
SSI	23.3440	24874321

Table 2.16: Comparative computational costs

2.5 Flutter prediction for nonlinear systems using linear methods

In recent years there has been a shift in the aeroelastic community towards investigating the effects of nonlinearities on the response of aircraft. It is now

recognized, especially with the advent of active control systems, that aircraft are in general nonlinear structures and hence, that using linear methods to evaluate their aeroelastic behaviour may be incorrect. The purpose of this section is to assess exactly how inaccurate the flutter predictions obtained by linear methods for nonlinear systems are.

First, a short overview of the effects of nonlinearities on aeroelastic systems will be presented. A more thorough discussion of the subject will be presented in the next chapter. Here only some basic facts will be mentioned. Nonlinearities, in general change many of the characteristic features of a dynamic system. However, their main effect is to alter to stability of the system. In a linear aeroelastic system the stability is positive until the free stream velocity reaches a certain value at which the stability becomes negative and the system is said to flutter. A nonlinear system may become critically unstable without fluttering for a wide range of airspeeds. The system simply undergoes non-diverging self-excited oscillations which are termed limit-cycle oscillations (LCOs). Whether LCOs will appear or not depends on a wide range of parameters including airspeed, amplitude of excitation and initial conditions. For an exhaustive survey of the parameter-space of a simple aeroelastic model see [9]. Nevertheless, at a given airspeed higher than the LCO airspeed range the system will flutter irrespective of the other parameters.

Another serious effect of nonlinearities on aeroelastic systems is the distortion they cause on the FRF of the system. The FRF of a linear system will demonstrate a number of peaks equal to the number of modes in the system. FRFs of nonlinear systems include additional higher harmonics as in the case of figures 2.37- 2.38, for the the Hancock wing with a slightly bilinear control surface pitch spring. Even though the system described in these figures has only three modes there are at least 9 visible peaks in the FRF, the last one appearing at a

frequency exceeding 200 Hz. The extra peaks are caused by the bilinear spring, i.e. they are the frequencies of the Fourier series approximating the bilinear response. Additionally, since the response of the nonlinear spring changes when it is worked at different excitation amplitudes, its Fourier series also changes. Hence, it is found that the extra peaks in the FRF change frequency with excitation amplitude. A further difficulty is that, if the FRF is taken during a LCO, the time response will be necessarily truncated and will introduce leakage in the FRF, as in figure 2.39.

Finally, the flutter velocity itself is changed by a nonlinearity introduced to a linear system. There is as yet no general method for predicting that change and whether the flutter velocity will increase of decrease. One procedure that can accomplish this prediction is the Harmonic Balance method ([26],[27]) but its applicability is limited to systems with nonlinearities in only one mode.

The applicability of the linear flutter prediction methods presented in the previous section on nonlinear systems will be assessed using two nonlinear versions of the simple 3-dof wing system used earlier. The nonlinear versions are identical to the linear version apart from featuring nonlinear control surface stiffnesses. The first nonlinear version has a bilinear control surface spring (see figure 3.6) with $K_1 = 0.5K_2 = 0.5K_{linear}$ while the second has a freeplay control surface spring (see figure 3.8) with $K = K_{linear}$ and is therefore highly nonlinear. The bilinear system will be referred to as slightly nonlinear (since it causes less distortion in the FRF) and the freeplay system will be referred to as highly nonlinear. The flutter velocities of the two nonlinear systems were obtained by repeated integrations as

- Bilinear: 43.50 m/s
- Freeplay: 43.65 m/s

As with the linear case, all simulations where carried out with 5%rms noise

corruption in the responses, at test points separated by 7% of the true flutter speed and at various velocity ranges.

2.5.1 Damping Fit method

As in the linear case, the accuracy of the Damping Fit method depends on the performance of the RFP-CC procedure and the order of the polynomial fit. The problem with using the RFP-CC is that, as shown earlier, the FRF of the non-linear systems includes higher harmonics that describe the nonlinearity. If the RFP-CC is instructed to look for only three modes then it will identify the three higher peaks in the FRF, irrespective of whether they are real modes or harmonics. Overspecification will lead to a fit of all the real modes and some of the harmonics which will give a larger number of damping ratios whose variation needs to be investigated with velocity.

Table 2.17 shows flutter predictions obtained by the damping fit method for the bilinear system. The table shows that reasonable flutter predictions can be obtained as long as some test are carried out to within 30% of the flutter speed. Additionally, the best polynomial order is in most cases 2, although this may be a system-specific result.

Velocity Range	Best Flutter Speed Estimate	% Error	Best Order of fit
0.23-0.43	53.9334	+24.0	3
0.23-0.57	35.6001	-18.2	4
0.23-0.70	44.9294	+3.3	2
0.23-0.84	43.0155	-1.1	2
0.23-0.98	43.6665	+0.4	4
0.45-0.66	40.3442	-7.3	2
0.45-0.79	44.2339	+1.7	2
0.45-0.93	43.4231	-0.2	2
0.68-0.88	40.1717	-7.7	2

Table 2.17: Flutter Estimates using Damping Fit Method, Bilinear Hancock Model

Table 2.18 shows flutter predictions obtained by the damping fit method for the freeplay system. The quality of the flutter predictions is worse than in the bilinear case. Acceptable results were only obtained when tests were performed within 15% of the flutter speed. Figures 2.40 and 2.41 show damping results for the bilinear and freeplay systems, respectively. It can be seen that the damping data for the latter are much more scattered. This scatter is caused by the fact that the freeplay system exhibits limit cycle behaviour from speeds of 15 m/s up to the flutter speed. The LCO causes increased distortion of the FRFs, thus affecting the damping ratio estimates. Of course, as table 2.18 shows, despite the LCO, it is possible to obtain some acceptable predictions for the flutter speed if tests are carried out sufficiently close to the critical speed. This possibility however, depends on whether the linear modes have been accurately curve-fitted by the RFP-CC method and on the effect that the nonlinearity has on the flutter behaviour of the system. Both the bilinear and freeplay nonlinearities investigated in this section were chosen to cause small changes in the flutter velocity. In any case the wisdom of testing an aircraft and measuring responses during a LCO is questionable.

Velocity Range	Best Flutter Speed Estimate	% Error	Best Order of fit
0.23-0.43	18.6243	-57.2	3
0.23-0.57	33.3280	-23.6	5
0.23-0.70	49.1489	+12.6	3
0.23-0.84	44.7340	+2.5	2
0.23-0.98	43.0773	-1.3	8
0.45-0.66	19.9272	-54.3	3
0.45-0.79	38.3586	-12.1	4
0.45-0.93	44.2416	+1.4	5
0.68-0.88	39.0851	-10.5	2

Table 2.18: Flutter Estimates using Damping Fit Method, Freeplay Hancock Model

It was found that changing the amplitude of excitation changes the frequencies of the harmonics in the FRF but it does not affect the flutter velocity. This

observation is supported by Price et. al. in [28], [9] where the flutter boundary is always described as a straight line in every 2D cut-away of parameter space in which one of the variables is velocity.

2.5.2 Flutter Margin Method

Most of the findings of the previous section also holds for the Flutter Margin method since the RFP-CC is still used to obtain the eigenvalues. Figure 2.42 shows the flutter prediction by the FM method for the bilinear system. The actual flutter speed of 43.50 m/s is predicted inadequately. The flutter prediction in figure 2.43 is for the freeplay system. The predicted value of 52 m/s is quite poor compared to the actual flutter speed of 43.65 m/s.

Table 2.19 shows flutter predictions obtained by the FM method for the bilinear system. Compared to the results in table 2.17 obtained by the damping fit method, the Flutter Margin method predictions are less accurate. This inaccuracy is caused by the fact that the FM method uses two of the system eigenvalues to obtain the Flutter Margin. If there are significant errors in both these eigenvalues (which there will be due to the FRF distortion effect discussed previously), then the error in the Flutter Margin data will be squared, causing increased in accuracy in the flutter predictions.

Velocity Range	Flutter Speed Estimate	% Error
0.23-0.43	141.5129	+225.3
0.23-0.57	115.5411	+165.6
0.23-0.70	47.5366	+9.3
0.23-0.84	41.3696	-4.9
0.23-0.98	42.1239	-3.2
0.45-0.66	49.6976	+14.2
0.45-0.79	40.7760	-6.3
0.45-0.93	41.5856	-4.4
0.68-0.88	41.1209	-5.5

Table 2.19: Flutter Estimates using Flutter Margin Method, Bilinear Hancock Model

Table 2.20 shows flutter predictions obtained by the FM method for the freeplay system. The table shows that the high sensitivity of the method to errors in the eigenvalues is further increased by the limit cycle behaviour causing unacceptable flutter predictions.

Velocity Range	Flutter Speed Estimate	% Error
0.23-0.43	20.7732	-52.4
0.23-0.57	25.3656	-41.9
0.23-0.70	29.1133	-33.3
0.23-0.84	33.0474	-24.3
0.23-0.98	35.4283	-18.8
0.45-0.66	29.9543	-31.4
0.45-0.79	34.4903	-21.0
0.45-0.93	39.3358	-9.9
0.68-0.88	38.4398	-11.9

Table 2.20: Flutter Estimates using Flutter Margin Method, Freeplay Hancock Model

2.5.3 Envelope Function

The Envelope function method requires that the impulse response function be obtained. This is usually accomplished not by directly applying an impulse to the system but by obtaining the response to another type of forcing function that excites all of the system's natural frequencies (e.g. sine sweep or white noise with prescribed frequencies) and then taking the inverse Fourier Transform of the resulting FRF. The distortions in a system's FRF caused by the presence of a nonlinearity mean that this latter approach can cause inaccuracies. Figure 2.44 shows the estimated impulse response for the bilinear system. The early response is reasonable however, after about 5 seconds, a second burst of activity occurs. This second burst is termed 'non-causal response', occurs because of the nonlinearity and can be omitted by a suitable choice of t_{max}.

Nonetheless, flutter predictions for the bilinear system are reasonably accurate, as shown in figure 2.45. This fact is also demonstrated in table 2.21, where flutter predictions for the bilinear system are presented. For $t_{max} = 8$, the entire impulse response is used for the shape parameter calculations, including the non-causal response. For $t_{max} = 6$, only part of the non-causal section is used and for for $t_{max} = 5$, only the causal part is used. The astonishing result is that there are no striking differences in the accuracy of the flutter speed predictions for the three cases. In fact, the $t_{max} = 8$ case appears to yield slightly more accurate estimates than the others. A possible explanation for this phenomenon might be that, despite the presence of the non-causal response, the centroid of the envelope function is still displaced towards the $+\infty$ direction of the time axis as the velocity increases.

The freeplay case is very similar to the bilinear case, with respect to the accuracy of flutter predictions by the Envelope method. Figure 2.46 shows the shape parameters calculated for the freeplay system during a sample test run. Unlike the Damping fit and Flutter Margin methods, the accuracy of the Envelope approach does not suffer in the presence of limit cycles caused by the freeplay nonlinearity, as demonstrated by table 2.22.

2.5.4 Nissim & Gilyard Method

In the presence of nonlinearities, any attempt to identify the system equations of motion will come up against considerable obstacles due to the fact that the coefficients of the equations are not all going to be constants but some of them will be nonlinear functions. This difficulty is augmented by the fact that, in the Nissim & Gilyard method, the equations are pre-multiplied by the mass matrix. Hence, if in the original equations a nonlinearity appeared in only one of the modes, it will now appear in all modes. The variability of the equation of motion

Range	t_{max}	Best Polynomial Order	Best Flutter Speed Estimates	% Error
0.23-0.43	8	2	34.0114	-21.8
	6	2	35.4595	-18.5
	5	2	31.2331	-28.2
0.23-0.57	8	2	43.9944	+1.1
	6	2	38.0047	-12.6
	5	3	43.9234	+1.0
0.23-0.70	8	6	43.4246	-0.2
	6	6	37.1113	-14.7
	5	4	42.2149	-3.0
0.23-0.84	8	4	43.1871	-0.7
	6	3	42.5797	-2.1
	5	2	42.2447	-2.9
0.23-0.98	8	2	43.4597	-0.1
	6	8	43.5849	+0.2
	5	8	43.3586	-0.3
0.45-0.66	8	3	37.5291	-13.7
	6	2	41.3359	-5.0
	5	3	43.0901	-0.9
0.45-0.79	8	3	42.5898	-2.1
	6	2	42.3383	-2.7
	5	2	42.9123	-1.4
0.45-0.93	8	3	43.2756	-0.5
	6	3	43.7678	+0.6
	5	3	43.3487	-0.4
0.68-0.88	8	2	42.2305	-2.9
	6	2	41.6514	-4.2
	5	2	40.6735	-6.5

Table 2.21: Flutter Speed Estimates using Envelope Method, Bilinear Hancock model

Range	t_{max}	Best Polynomial Order	Best Flutter Speed Estimates	% Error
0.23-0.43	8	2	26.0415	-40.3
	6	2	24.3134	-44.3
	5	2	40.2719	-7.7
0.23-0.57	8	2	36.7491	-15.8
	6	4	28.2307	-35.3
	5	3	29.3971	-32.7
0.23-0.70	8	2	46.0160	+5.4
	6	4	44.4519	+1.8
	5	7	42.2397	-3.2
0.23-0.84	8	4	44.1062	+1.0
	6	2	43.2799	-0.8
	5	3	42.3283	-3.0
0.23-0.98	8	11	43.5648	-0.2
	6	11	43.2500	-0.9
	5	6	43.7425	+0.2
0.45-0.66	8	3	38.4883	-11.8
	6	3	29.5659	-32.3
	5	2	38.0893	-12.7
0.45-0.79	8	3	43.6241	-0.1
	6	3	41.1697	-5.7
	5	2	43.8365	+0.4
0.45-0.93	8	5	43.8605	+0.5
	6	6	43.0260	-1.4
	5	5	42.5838	-2.4
0.68-0.88	8	5	42.5838	-2.4
	6	3	38.2303	-12.4
	5	2	42.5367	-2.6

Table 2.22: Flutter Speed Estimates using Envelope Method, Freeplay Hancock model

coefficients means that every time a different set of response data is used to identify the matrix coefficients different matrices will be obtained. In this respect using multiple forcing vectors is not recommended.

Nevertheless, for a slightly nonlinear system, such as the bilinear Hancock model used here, the Nissim & Gilyard method can still deliver reasonable flutter predictions, by identifying a linear system . Figure 2.47 shows the flutter prediction for the bilinear system. One of the damping ratios goes negative straight away, even at very low airspeeds. However, another damping ratio goes unstable at 49 m/s which is close enough to the actual flutter speed of 47 m/s.

Table 2.23 shows flutter predictions obtained by the NG method for the bilinear system. The flutter estimates are acceptable, as long as one test is made at an airspeed higher than 80% of the true flutter velocity.

Velocity Range	Flutter Speed Estimate	% Error
0.23-0.43	40.9814	-5.8
0.23-0.57	41.0540	-5.6
0.23-0.70	41.4280	-4.8
0.23-0.84	43.0097	-1.1
0.23-0.98	43.5192	+0.0
0.45-0.66	42.6110	-2.0
0.45-0.79	42.6073	-2.1
0.45-0.93	42.8100	-1.6
0.68-0.88	40.1717	-7.7

Table 2.23: Flutter Estimates using NG Method, Bilinear Hancock Model

The bilinear system does not limit cycle and, consequently, causes less difficulties in the identification process than the freeplay system, which does flutter. If the NG method is applied to the freeplay Hancock model at a limit cycle, the model will be identified as a fluttering linear system. Hence, the flutter velocity will always be the velocity at which the tests take place. This effect can be observed in figure 2.48. The figure depicts the natural frequency and damping ratio variation of a NG model of the freeplay system. Two tests were carried

out, one at 21m/s and one at 41m/s. The resulting model is unstable at every airspeed, but the damping of all three modes becomes zero at the test speeds. This difficulty can be overcome by using data from the low frequency part of the spectrum. The NG method only requires a relatively small amount of data in order to perform the identification, hence choosing low-frequency points only is not a problem. Figure 2.49 shows the spectrum of one of the responses at 41 m/s. The nonlinear behaviour is concentrated in the higher frequency part (above 40Hz), as witnessed by the numerous harmonics. The low frequency part (below 40Hz) is mainly linear. Consequently, if only the low frequency part is used in the identification process, the method is tricked into thinking that the system does not limit cycle and into identifying it as a stable linear system. Figure 2.50 shows, the result of using this trick. Table 2.24 shows flutter predictions obtained by the NG method for the freeplay system. The errors in the flutter predictions are, on average, a lot higher than in the bilinear case.

Velocity Range	Flutter Speed Estimate	% Error
0.23-0.43	30.0426	-31.2
0.23-0.57	34.3394	-21.3
0.23-0.70	39.7054	-9.0
0.23-0.84	42.7253	-2.1
0.23-0.98	44.0280	+0.9
0.45-0.66	39.5310	-9.4
0.45-0.79	42.2920	-3.1
0.45-0.93	44.7946	+2.6
0.68-0.88	44.6930	+2.4

Table 2.24: Flutter Estimates using NG Method, Freeplay Hancock Model

2.5.5 Steady State Identification Method

Even though the Steady State Identification method also attempts to evaluate the matrices of the equations of motion, it does not suffer in the presence of nonlinearities to the same extent that the Nissim & Gilyard method does. This

is due to the sinusoidal excitation and subsequent sinusoidal fit of the system response. By fitting the system steady-state response by a sine function the nonlinearity is linearised, i.e. represented by its base harmonic. The frequency of this base harmonic is assumed to be equal to the frequency of excitation as in the case of the Harmonic Balance method and consequently, multiple forcing vectors can be used. To illustrate this consider a single dof system with nonlinear stiffness described by

$$m\ddot{x} + c\dot{x} + f(x) = A\sin(\omega t + \Phi) \tag{2.42}$$

where $f(x)$ is a nonlinear function. Both the NG and the SSI methods will attempt to fit this equation by a linear equation of the form

$$m\ddot{x} + c\dot{x} + kx = A\sin(\omega t + \Phi) \tag{2.43}$$

where m, c and k are to be evaluated. Since the original equation is nonlinear, its solution, x, can be represented by a Fourier series of the form

$$x(t) = \frac{A_0}{2} + \sum_{n=1}^{\infty} [A_n \cos n\omega t + B_n \sin n\omega t] \tag{2.44}$$

The NG method will use this latter function, or rather its Frequency domain representation, in its calculations. The SSI method however, will use the simpler, linearised, function

$$x(t) = A_1 \cos \omega t + A_2 \sin \omega t \tag{2.45}$$

i.e. it will ignore all the higher harmonics. The end result is that the NG method attempts to fit nonlinear data to a linear model whereas the SSI method will fit linearised data to a linear model. Hence, the resulting k value will be compliant with the equivalent stiffness definition of the Harmonic Balance method.

The identified matrices are not identical to those of the nonlinear system but they approximate those of an equivalent linearised system. For the freeplay system the identified matrices were

$$C_{id} = \begin{pmatrix} 5.2668 & -0.0375 & -0.0168 \\ -39.1687 & 1.8634 & -0.8452 \\ -25.6382 & -0.8822 & 7.9868 \end{pmatrix} K_{id} = 10^4 \begin{pmatrix} 0.1035 & 0.0029 & -0.0039 \\ -0.5703 & 1.4907 & -0.4897 \\ 1.7941 & -5.9696 & 4.4864 \end{pmatrix}$$

$$F_{id} = \begin{Bmatrix} 0.1170 \\ -1.5883 \\ 2.5081 \end{Bmatrix}$$

The actual matrices were

$$C_a = \begin{pmatrix} 4.9974 & -0.0151 & -0.0186 \\ -52.3509 & 2.9737 & -0.9489 \\ 101.4620 & -11.5178 & 8.8853 \end{pmatrix} K_a = 10^4 \begin{pmatrix} 0.1120 & 0.0030 & f_1(\beta) \\ -0.1473 & 1.4950 & f_2(\beta) \\ -2.2096 & -6.0041 & f_3(\beta) \end{pmatrix}$$

$$F_a = \begin{Bmatrix} 0.1133 \\ -1.7735 \\ 4.2611 \end{Bmatrix}$$

where $f_i(\beta)$ are nonlinear functions of the control surface angle, β. Notice that the larger differences occur on the third row of the matrices which is the control surface equation and contains the nonlinearity. Figure 2.51 shows the flutter prediction for the bilinear system (47 m/s exactly like the actual flutter speed) and figure 2.51 shows the prediction for the freeplay system. The quality of the latter is worse, 46 m/s as opposed to the actual value of 43 m/s, the reason being that, in the case of a limit cycle caused by sinusoidal excitation, the steady state response includes elements of both the excitation and the limit cycle, thus corrupting the results to a degree.

The SSI method is very similar to the Harmonic Balance method except, since only one amplitude of excitation is considered, limit cycle oscillations can not be

Velocity Range	Flutter Speed Estimate	% Error
0.23-0.43	45.0780	+3.6
0.23-0.57	44.8780	+3.1
0.23-0.70	45.0350	+3.5
0.23-0.84	44.6260	+2.6
0.23-0.98	43.2870	-0.5
0.45-0.66	44.7430	+2.9
0.45-0.79	45.1100	+3.7
0.45-0.93	44.4480	+2.2
0.68-0.88	43.7820	+0.6

Table 2.25: Flutter Estimates using the SSI Method, Bilinear Hancock Model

Velocity Range	Flutter Speed Estimate	% Error
0.23-0.43	33.3500	-23.3
0.23-0.57	36.3973	-16.3
0.23-0.70	40.5630	-6.8
0.23-0.84	42.7150	-1.8
0.23-0.98	41.6230	-4.3
0.45-0.66	38.4320	-11.7
0.45-0.79	41.2120	-5.3
0.45-0.93	43.4360	-0.1
0.68-0.88	43.8420	+0.8

Table 2.26: Flutter Estimates using SSI Method, Freeplay Hancock Model

predicted. If multiple excitation amplitudes were used the SSI would be identical to the Harmonic Balance method. None of the other methods presented here have been found to have the potential to predict LCO's.

Flutter predictions for both the bilinear and freeplay Hancock systems, using the SSI method, are tabulated in tables 2.25 and 2.26.

2.5.6 ARMA-based method

As with the linear application of the ARMA-based method, the best results were obtained when J =number of modes. Table 2.27 shows flutter predictions for the bilinear Hancock model. Table 2.28 shows flutter predictions for the freeplay Hancock model.

Velocity Range	Best Flutter Speed Estimate	% Error	Best Order
0.23-0.43	23.4421	-46.1	2
0.23-0.57	36.2552	-16.7	2
0.23-0.70	58.1532	+33.7	6
0.23-0.84	47.0706	+8.2	2
0.23-0.98	43.5104	+0.0	2
0.45-0.66	31.6086	-27.3	2
0.45-0.79	35.6286	-18.1	3
0.45-0.93	42.0931	-3.2	2
0.68-0.88	41.3428	-5.0	2

Table 2.27: Flutter Estimates using the ARMA Method, Bilinear Hancock Model. Noise: 5% rms. Actual flutter speed: 43.50 m/s

Velocity Range	Best Flutter Speed Estimate	% Error	Best order
0.23-0.43	18.9017	-56.7	3
0.23-0.57	34.3395	-21.3	3
0.23-0.70	36.9073	-15.4	3
0.23-0.84	46.5775	+6.7	2
0.23-0.98	43.0043	-1.5	9
0.45-0.66	29.6683	-32.0	2
0.45-0.79	35.7788	-18.0	3
0.45-0.93	41.3884	-5.3	4
0.68-0.88	39.0266	-10.6	2

Table 2.28: Flutter Estimates using ARMA Method, Freeplay Hancock Model. Noise: 5% rms. Actual flutter speed: 43.65 m/s

In both cases the predictions are of poor accuracy. In fact, the better predictions are due to the fact that polynomials of varying degrees can interpret results in a very indeterminate manner, such that there will often be at least one polynomial which has one root close to the true flutter speed.

2.6 Figures

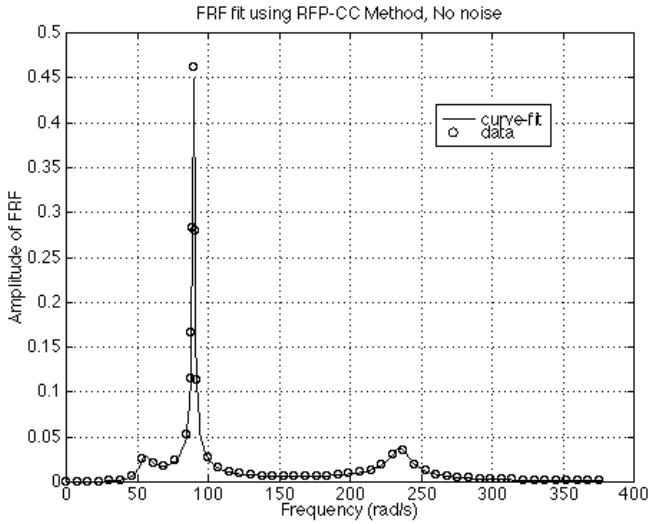

Figure 2.1: FRF fit by the RFP-CC Method; no noise

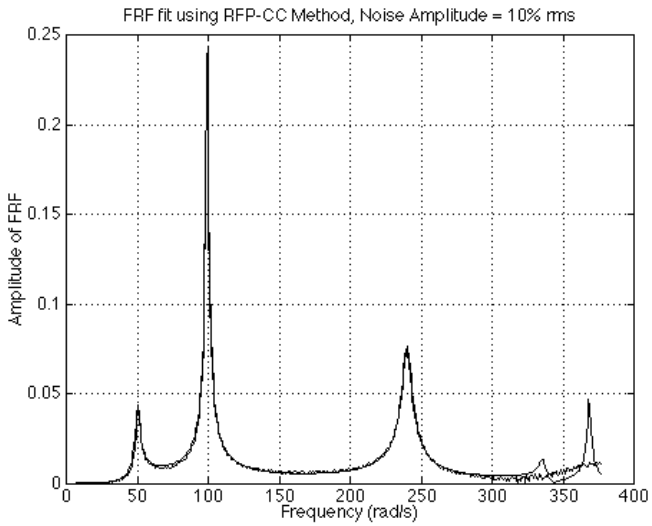

Figure 2.2: FRF fit by the RFP-CC Method; 10% rms noise

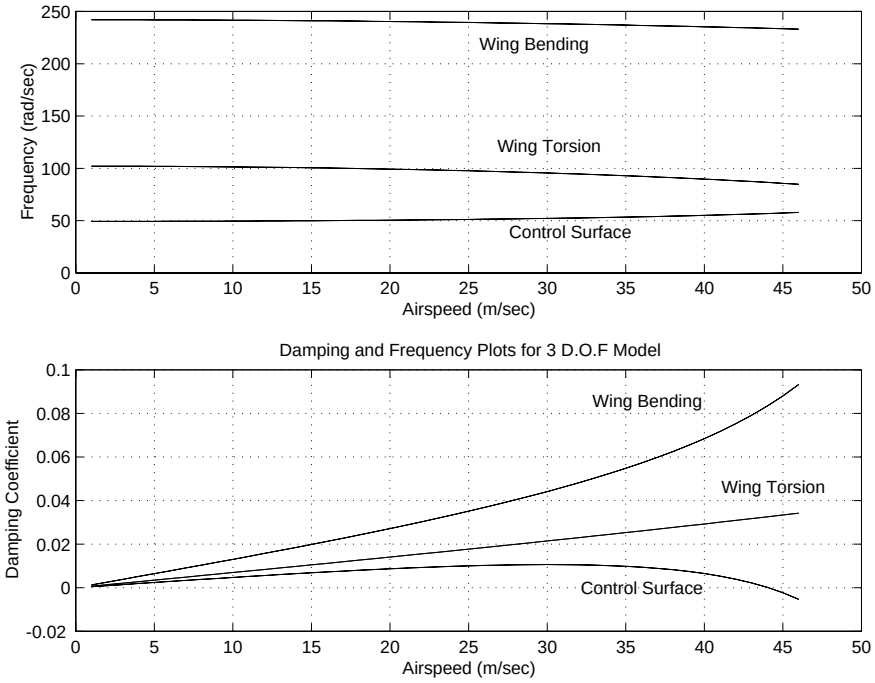

Figure 2.3: Variation of natural frequencies and dampings with airspeed, Hancock model.

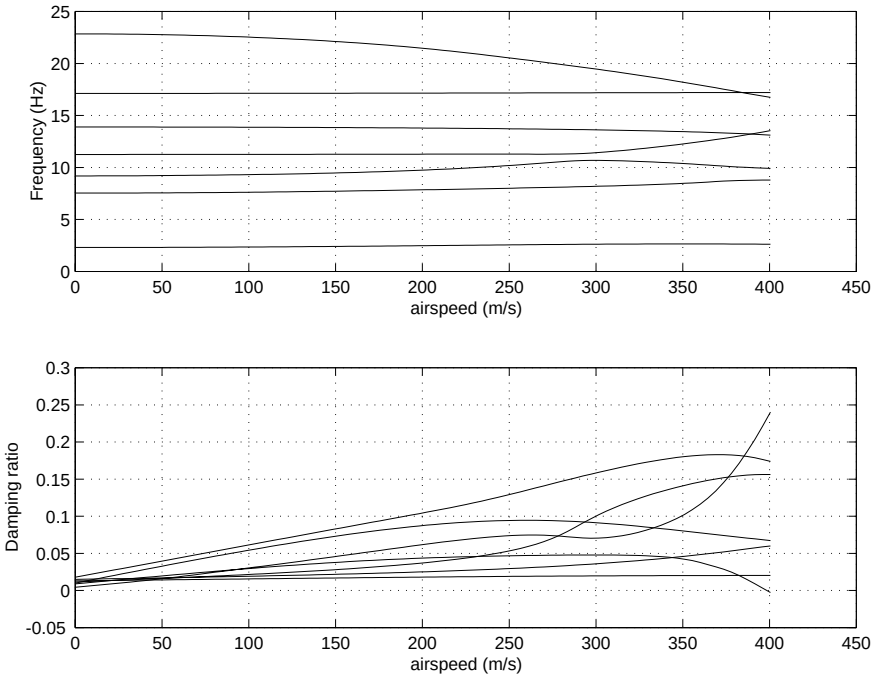

Figure 2.4: Variation of natural frequencies and dampings with airspeed, Sim-2 model.

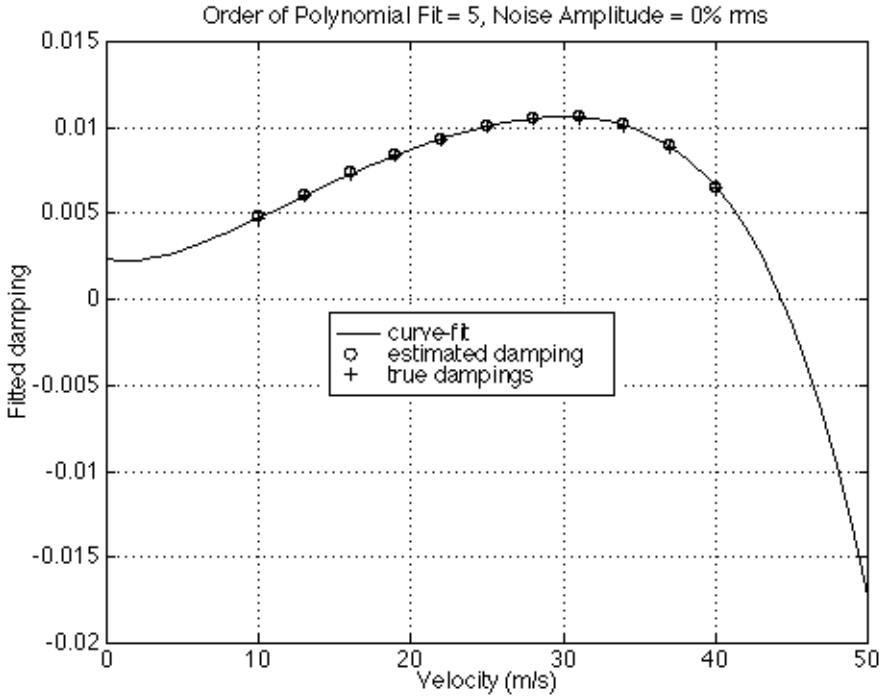

Figure 2.5: Flutter prediction using damping fit; no noise

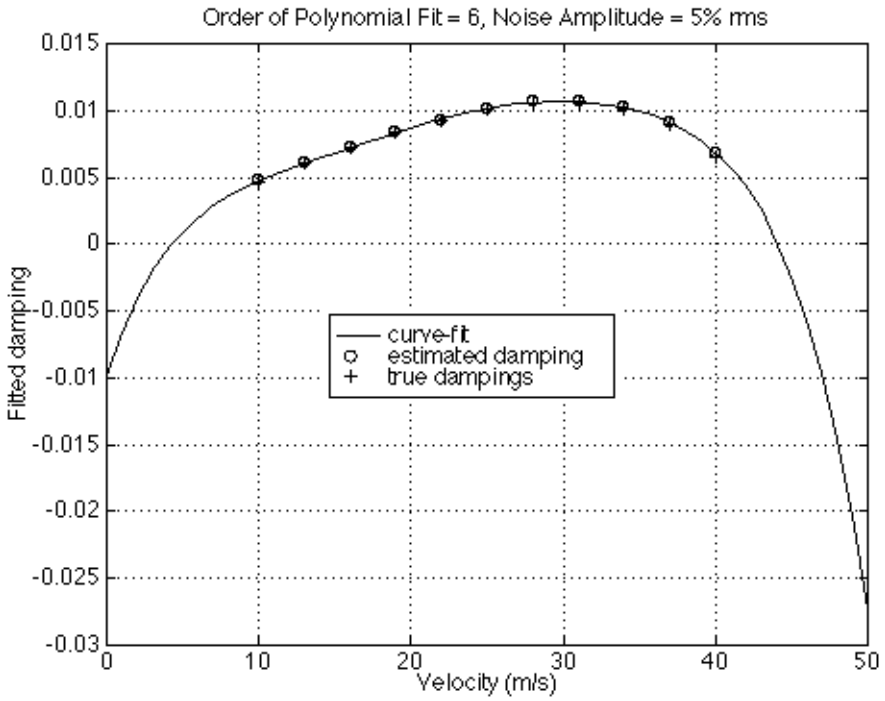

Figure 2.6: Flutter prediction using damping fit; 5% rms noise

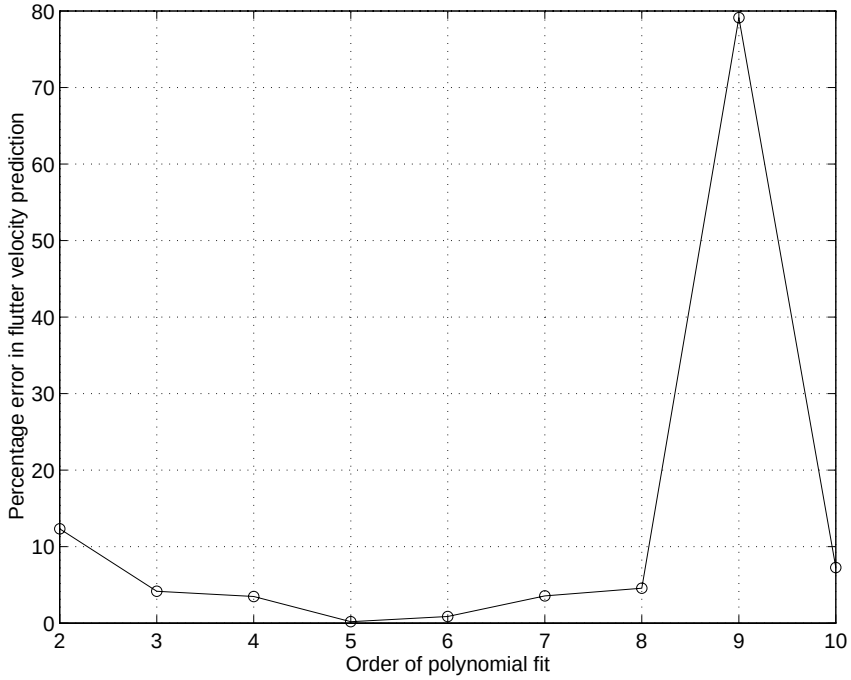

Figure 2.7: Variation of percentage error in flutter velocity prediction with increasing polynomial order.

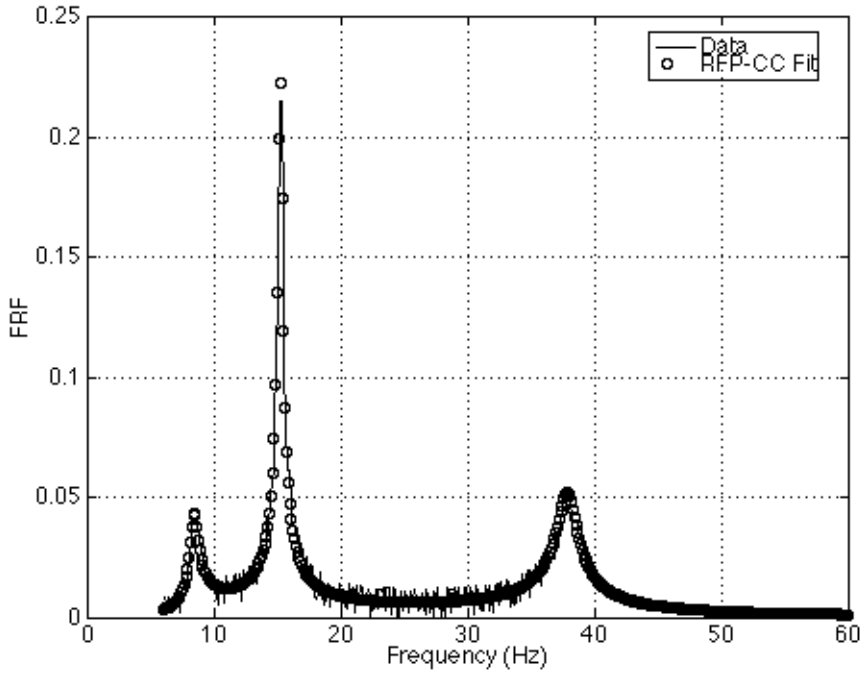

Figure 2.8: FRF fit by the RFP-CC Method; 20% rms noise

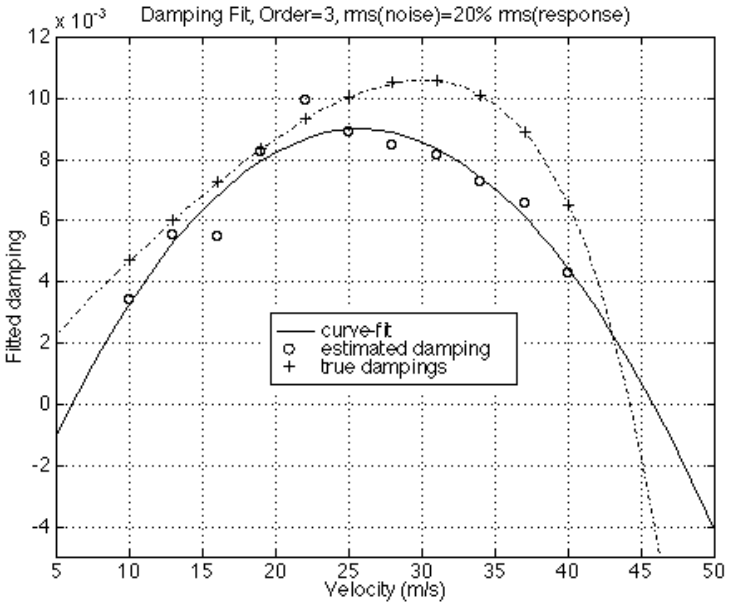

Figure 2.9: Flutter prediction using damping fit; 20% rms noise

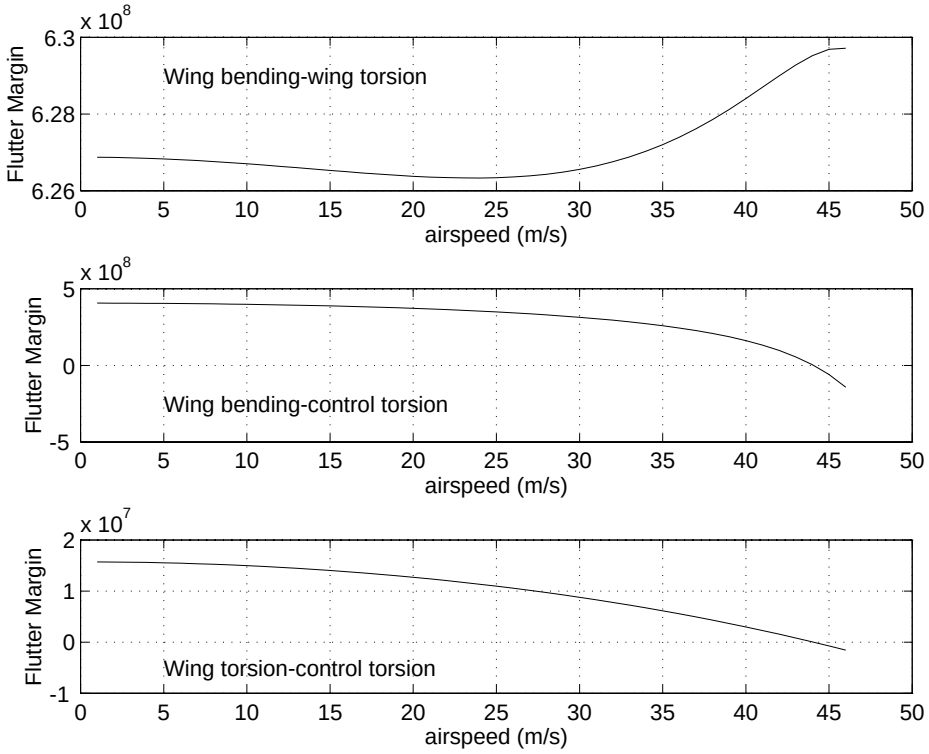

Figure 2.10: Flutter Margin variation for the three possible flutter mechanisms, Hancock model

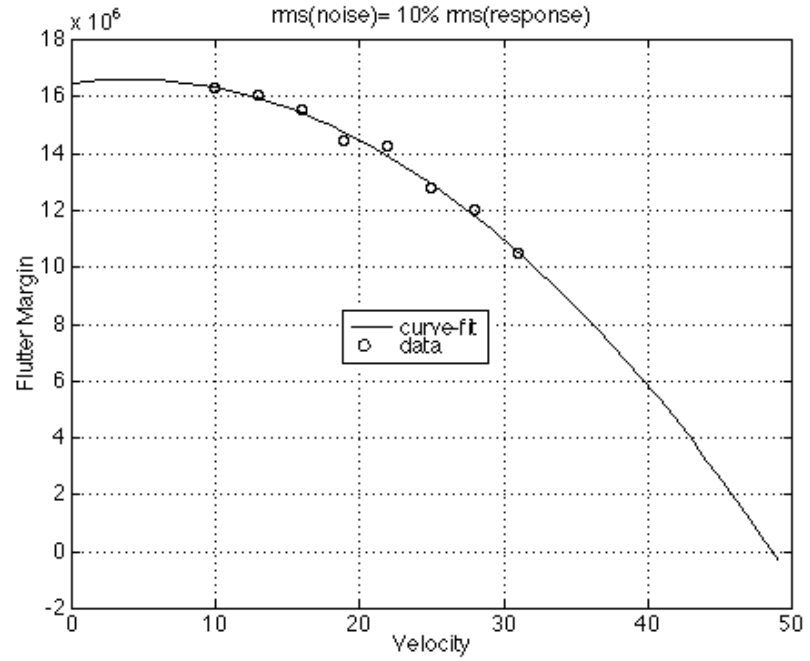

Figure 2.11: Flutter Margin variation with velocity, 10% rms noise

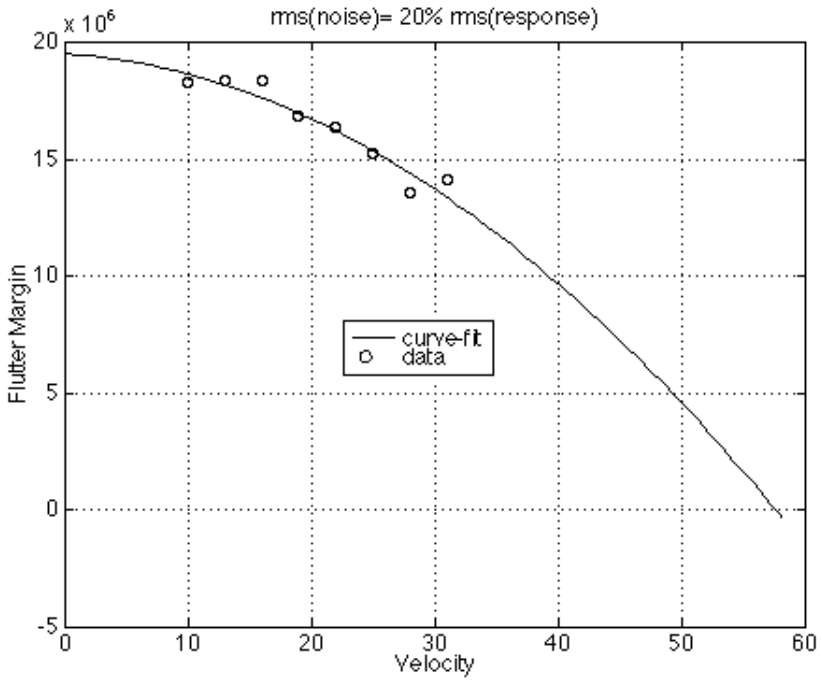

Figure 2.12: Flutter Margin variation with velocity, 20% rms noise

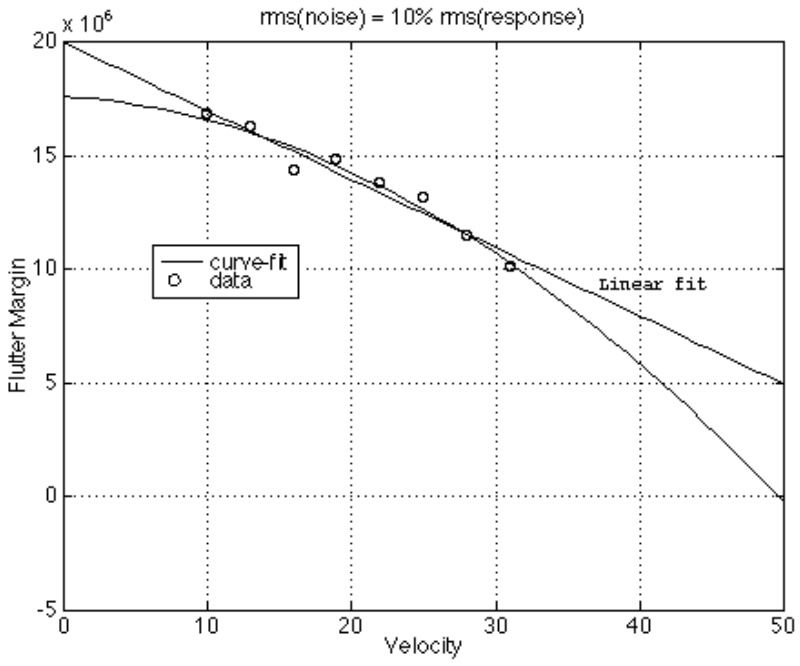

Figure 2.13: Flutter Margin variation with velocity, 10% rms noise, with linear fit

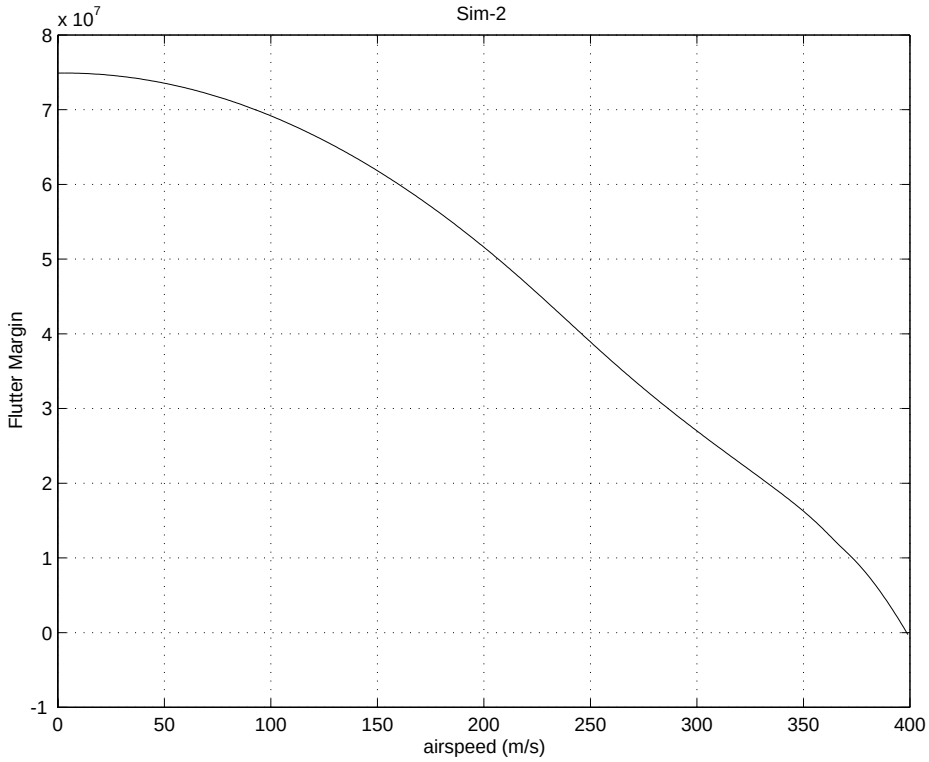

Figure 2.14: True Flutter Margin variation with airspeed, Sim-2 model

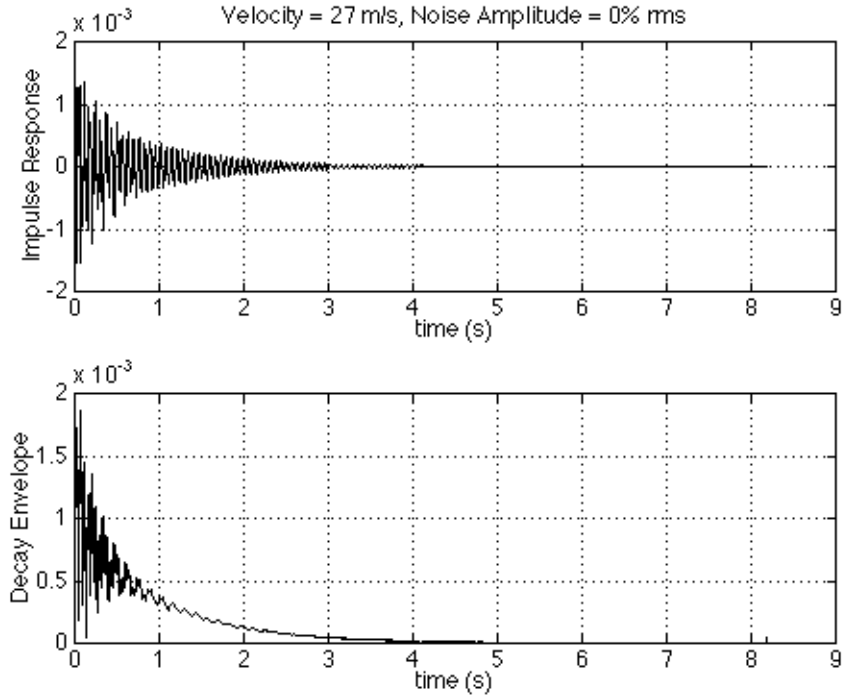

Figure 2.15: Impulse decay envelope

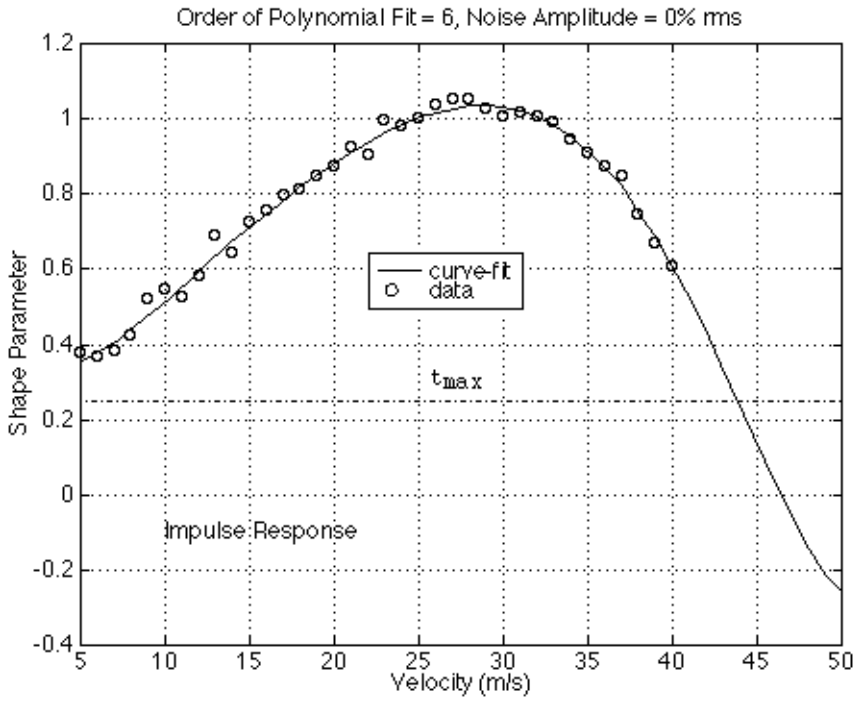

Figure 2.16: Decay Envelope centroid variation with velocity

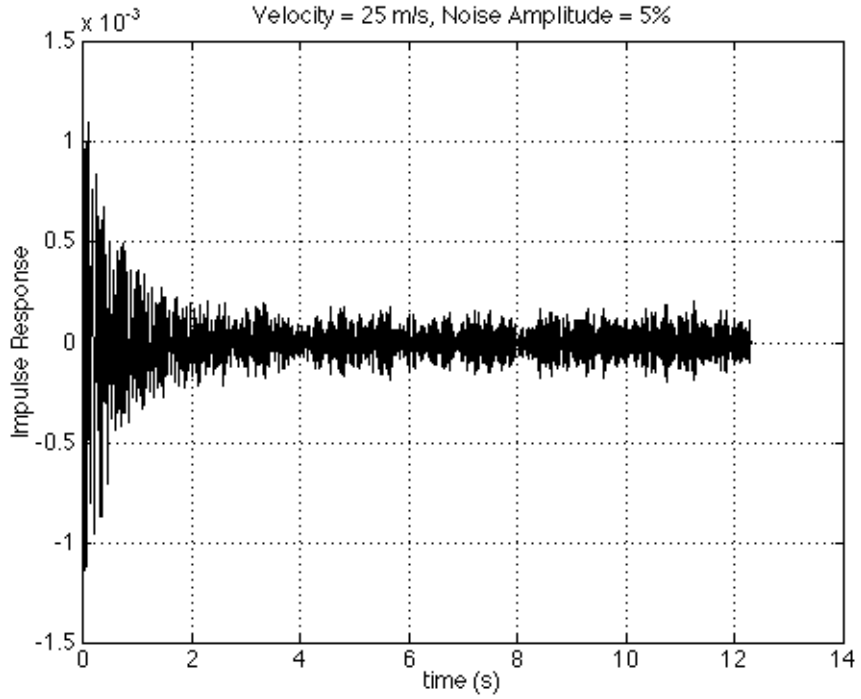

Figure 2.17: Impulse response, 5% rms noise

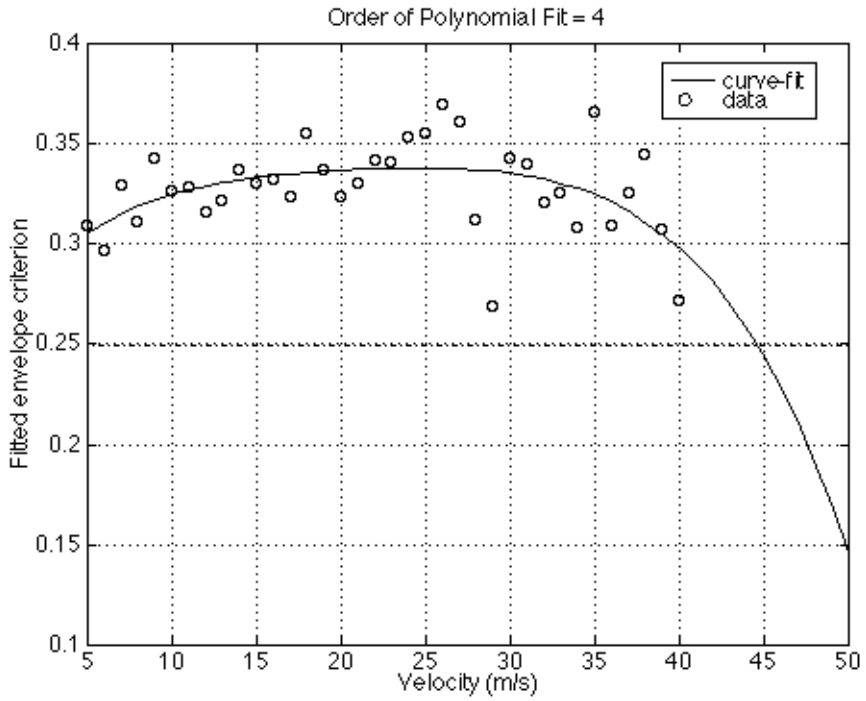

Figure 2.18: Decay Envelope centroid variation with velocity, 5% rms noise

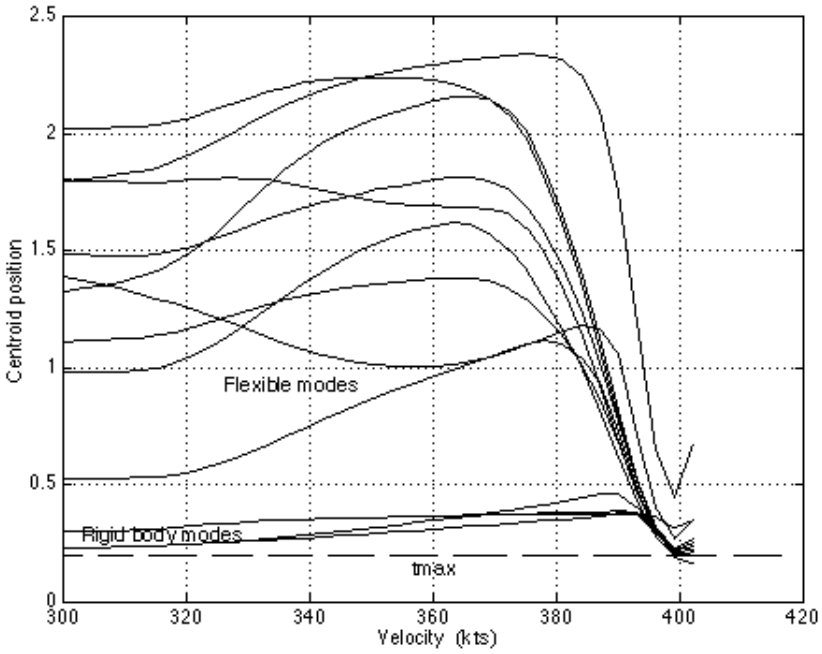

Figure 2.19: Decay envelope variation of Sim-2 symmetric modes. No noise. Actual flutter speed: 398 kts

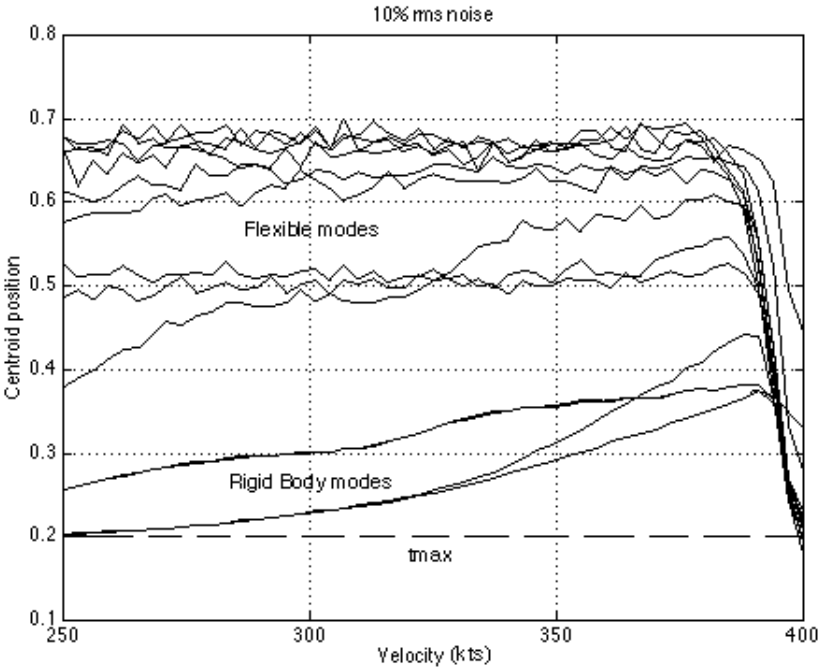

Figure 2.20: Decay envelope variation of Sim-2 symmetric modes. 10% rms noise. Actual flutter speed: 398 kts

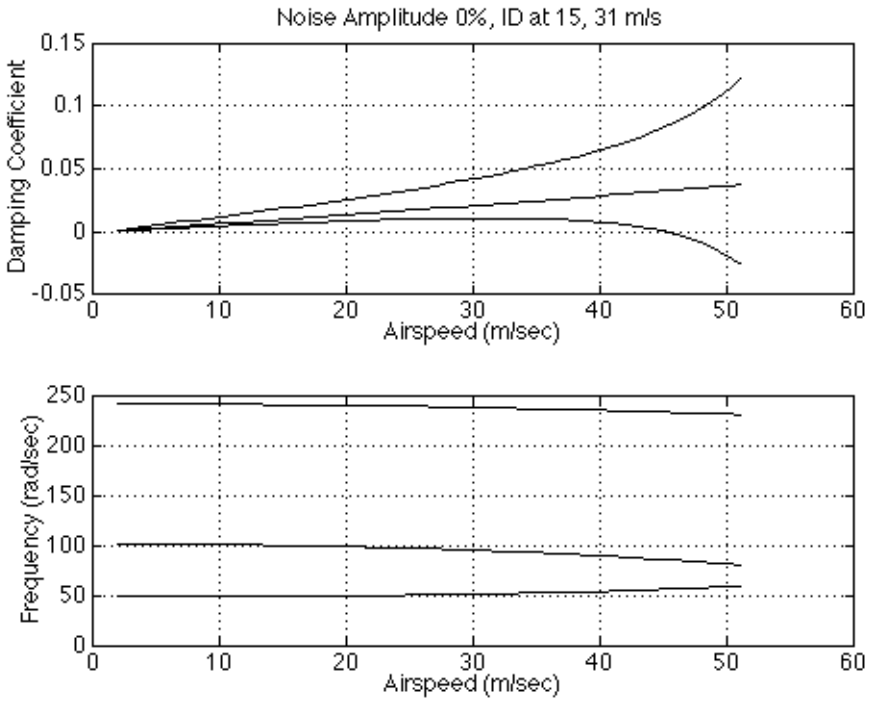

Figure 2.21: Damping and natural frequency by the NG method

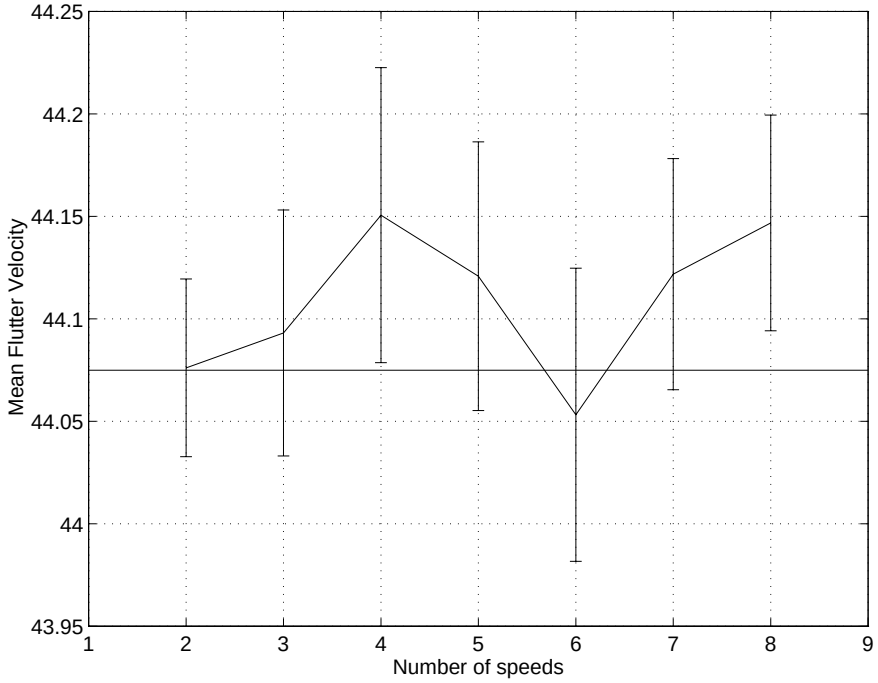

Figure 2.22: Accuracy of flutter estimate variation with number of speeds, NG method

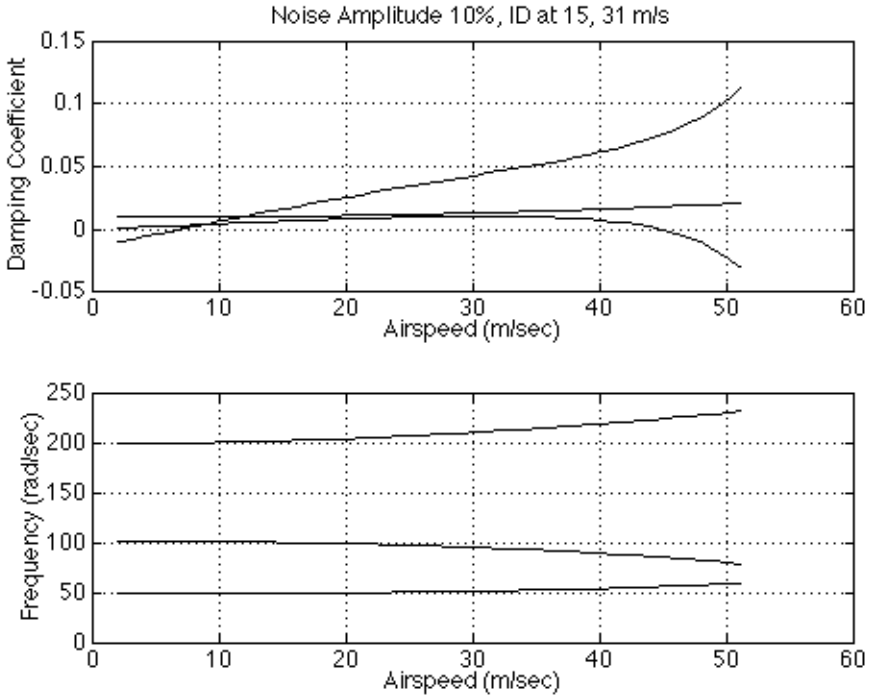

Figure 2.23: Damping and natural frequency by the NG method, 10% rms noise

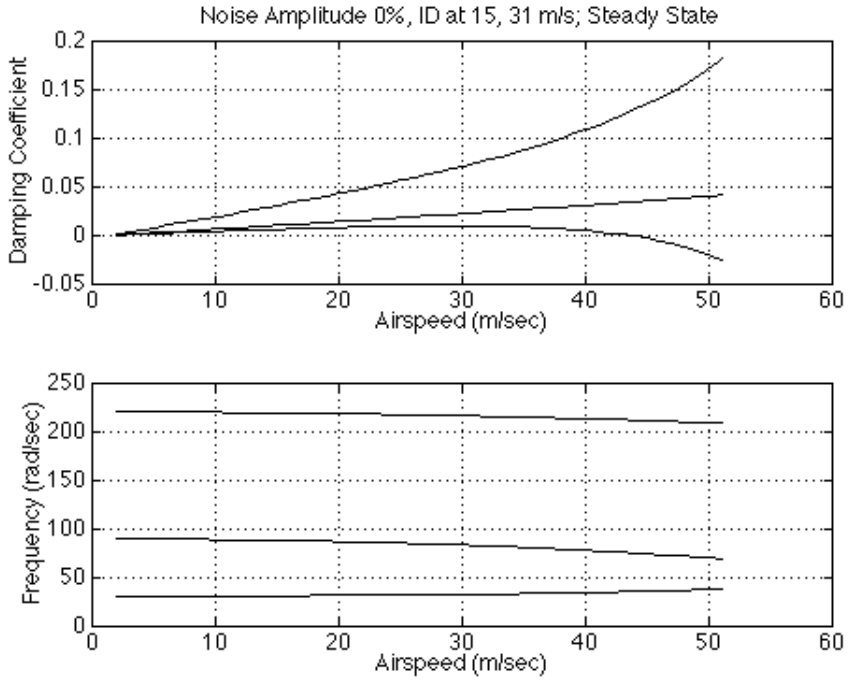

Figure 2.24: Damping and natural frequency by the SSI method

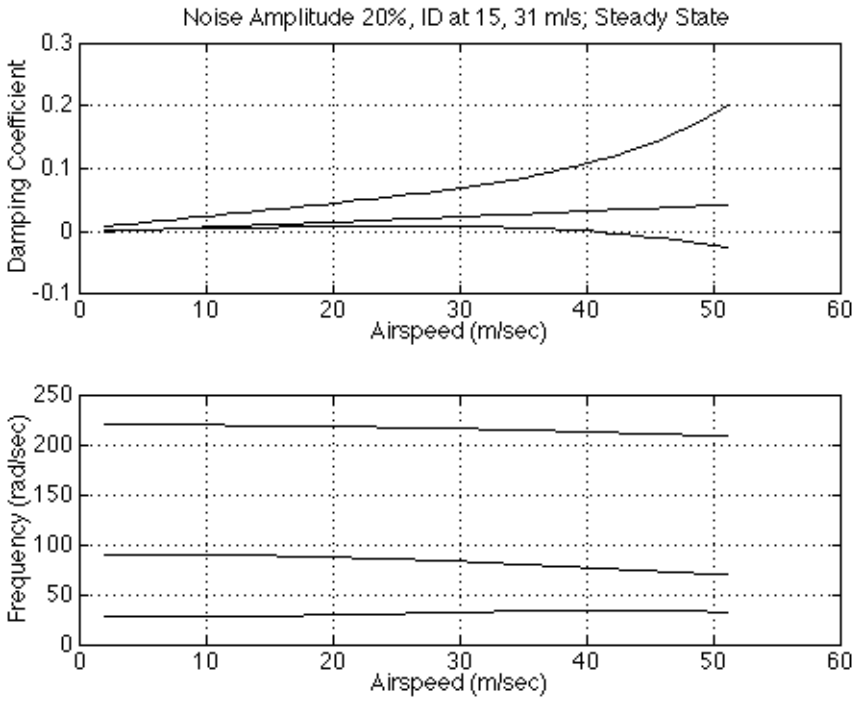

Figure 2.25: Damping and natural frequency by the SSI method, 20% rms noise

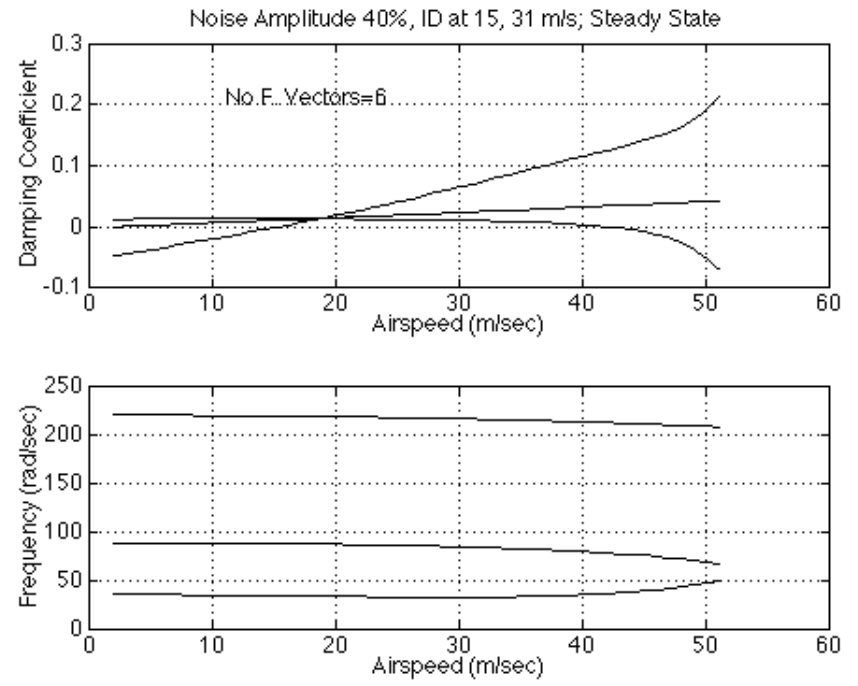

Figure 2.26: Damping and natural frequency by the SSI method, 40% rms noise, 6 forcing vectors

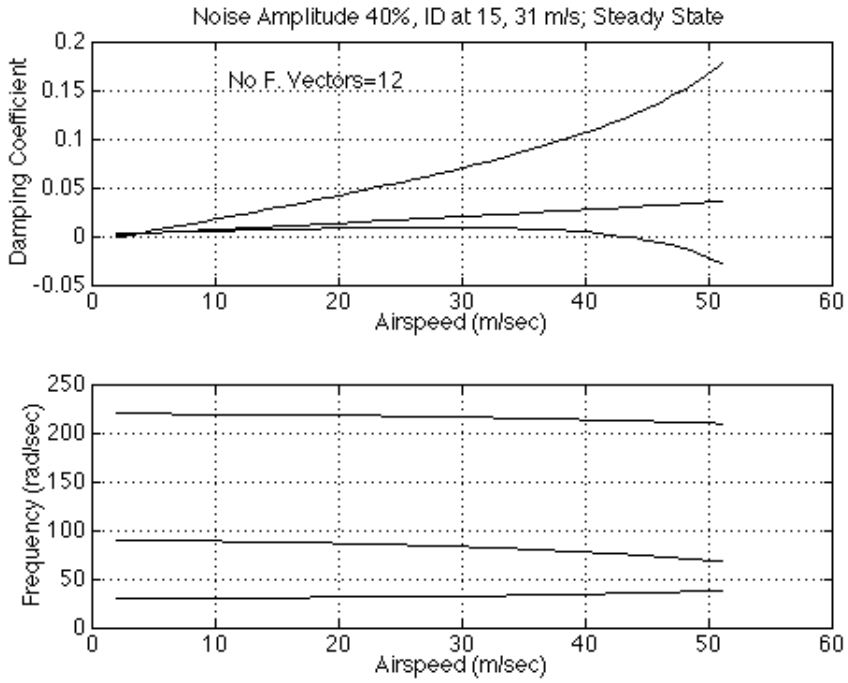

Figure 2.27: Damping and natural frequency by the SSI method, 40% rms noise, 12 forcing vectors

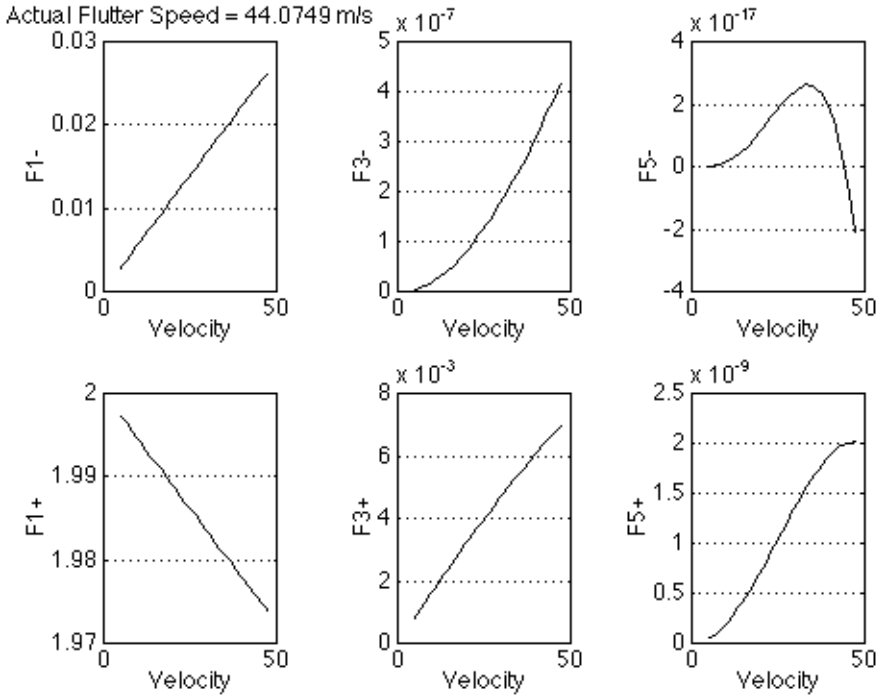

Figure 2.28: F stability criteria using ARMA method, no noise

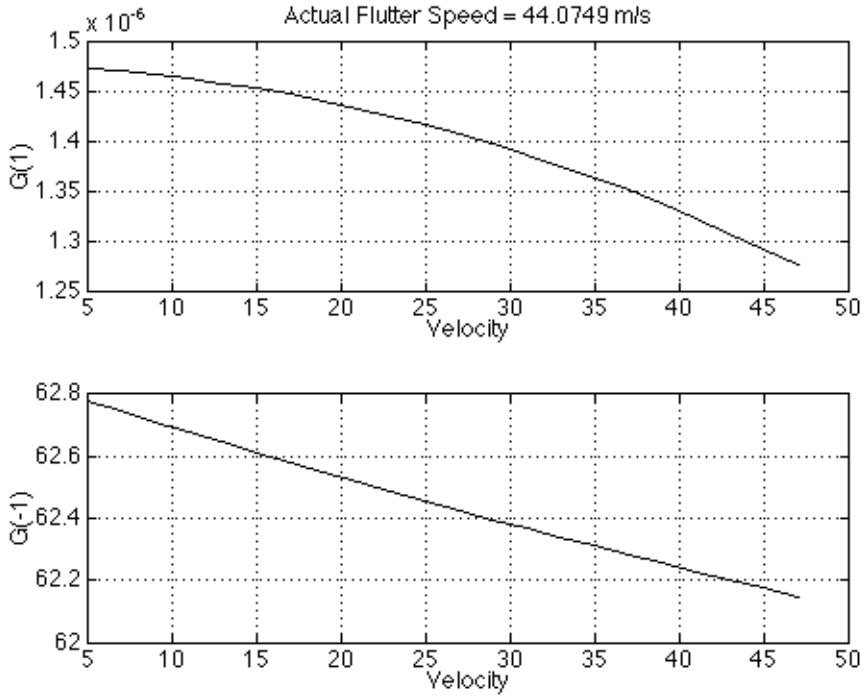

Figure 2.29: G stability criteria using ARMA method, no noise

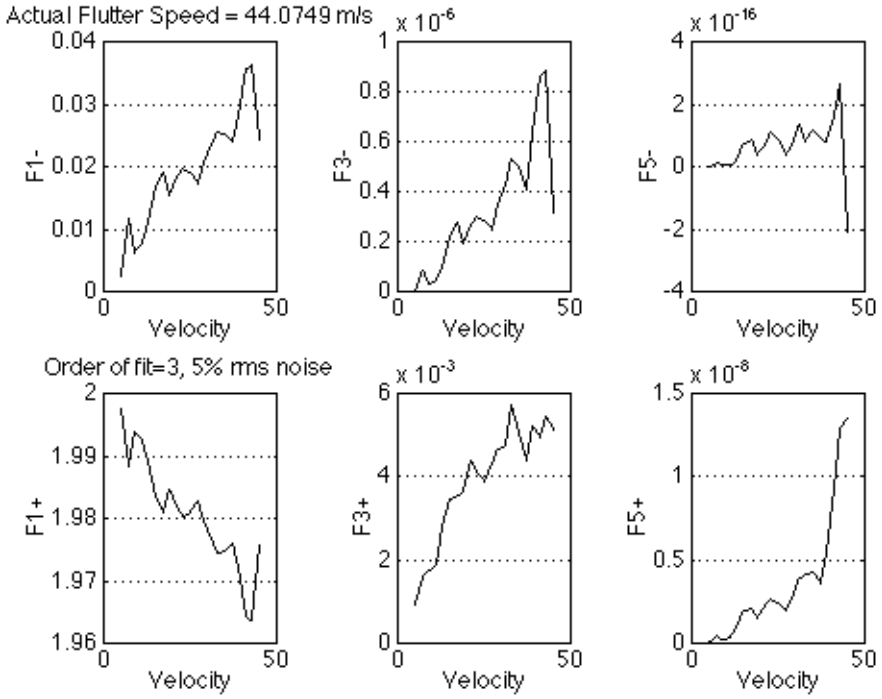

Figure 2.30: F stability criteria using ARMA method, 5% noise, 3d order model

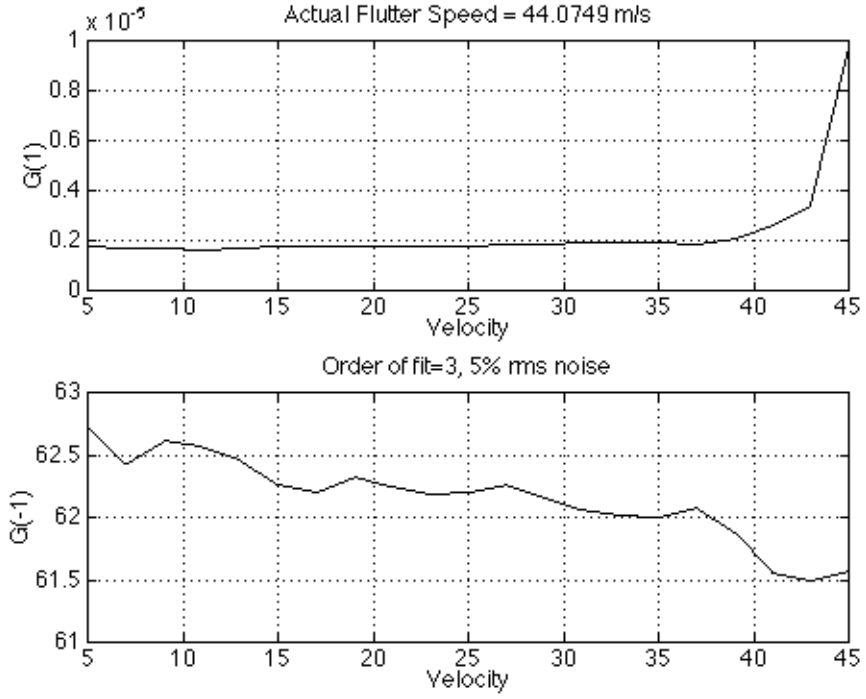

Figure 2.31: G stability criteria using ARMA method, 5% noise, 3d order model

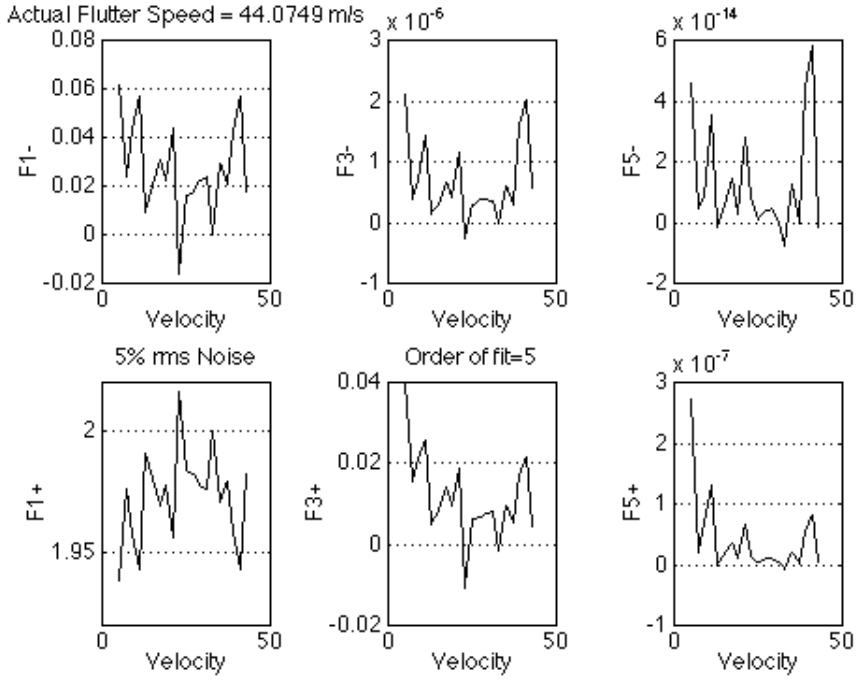

Figure 2.32: F stability criteria using ARMA method, 5% noise, 5th order model

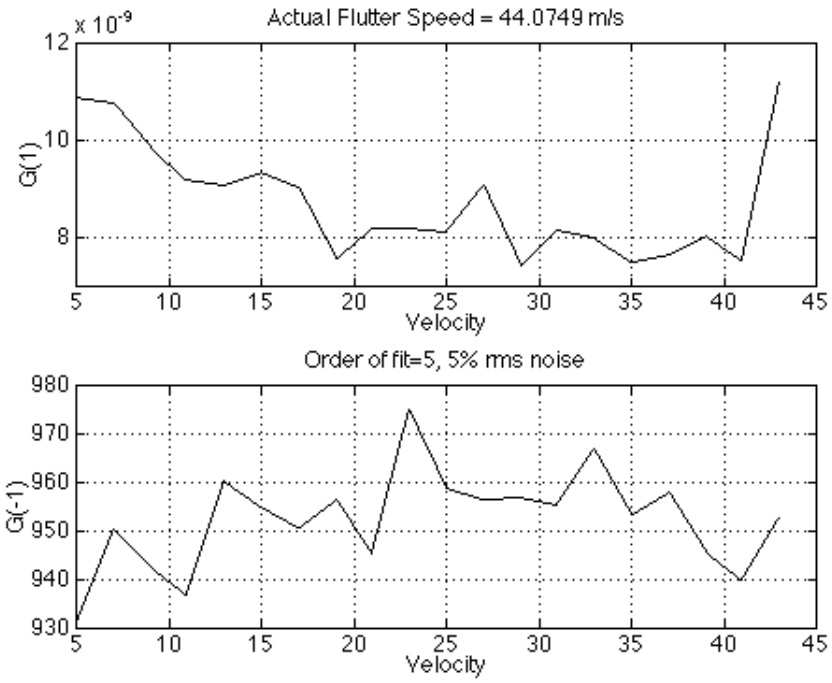

Figure 2.33: G stability criteria using ARMA method, 5% noise, 5th order model

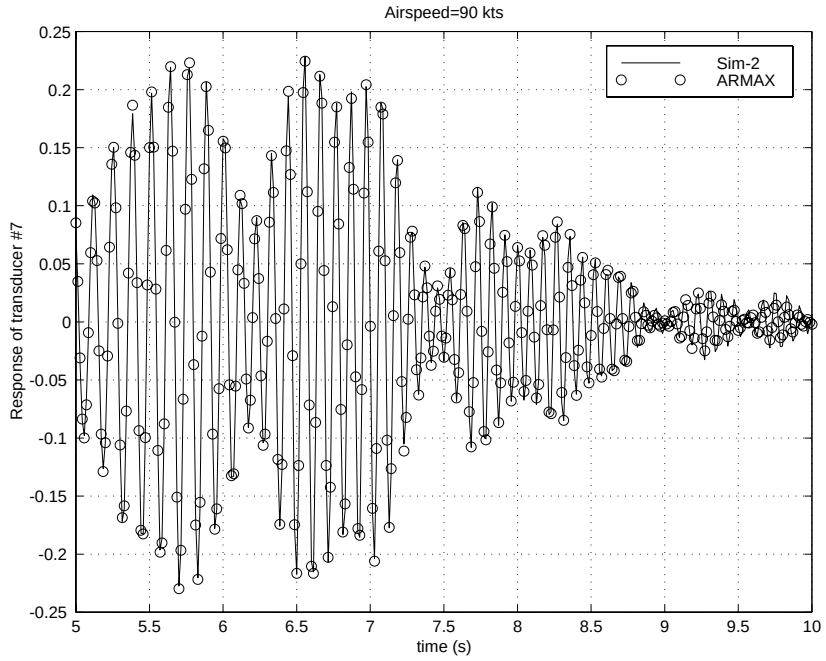

Figure 2.34: A sample ARMAX fit of the Sim-2 model response to chirp input

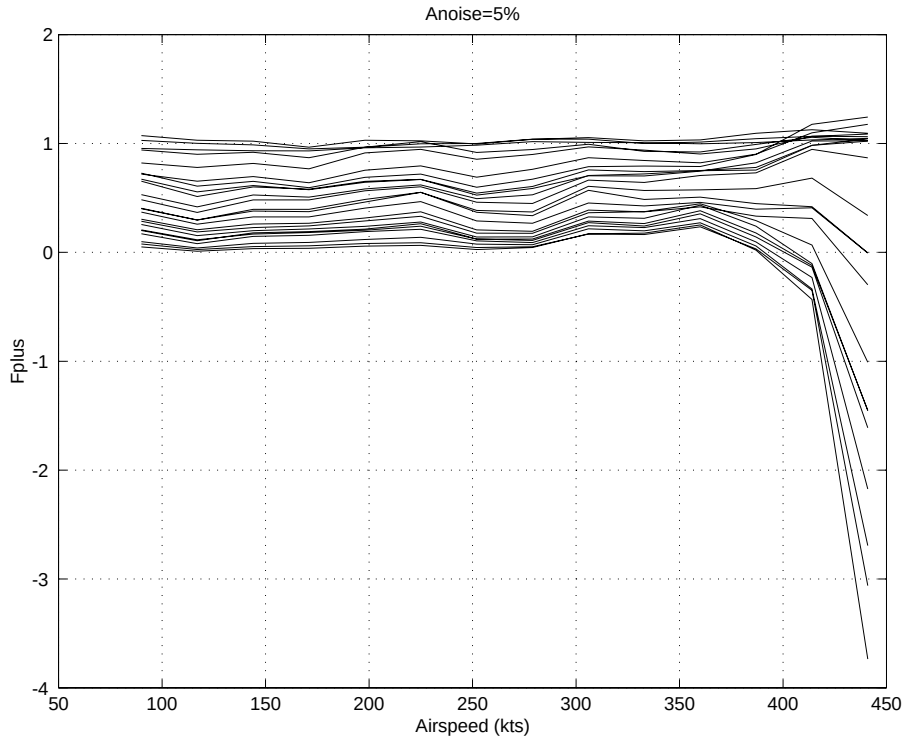

Figure 2.35: $F^{+}(l)$ stability criteria variation with airspeed for Sim-2 model

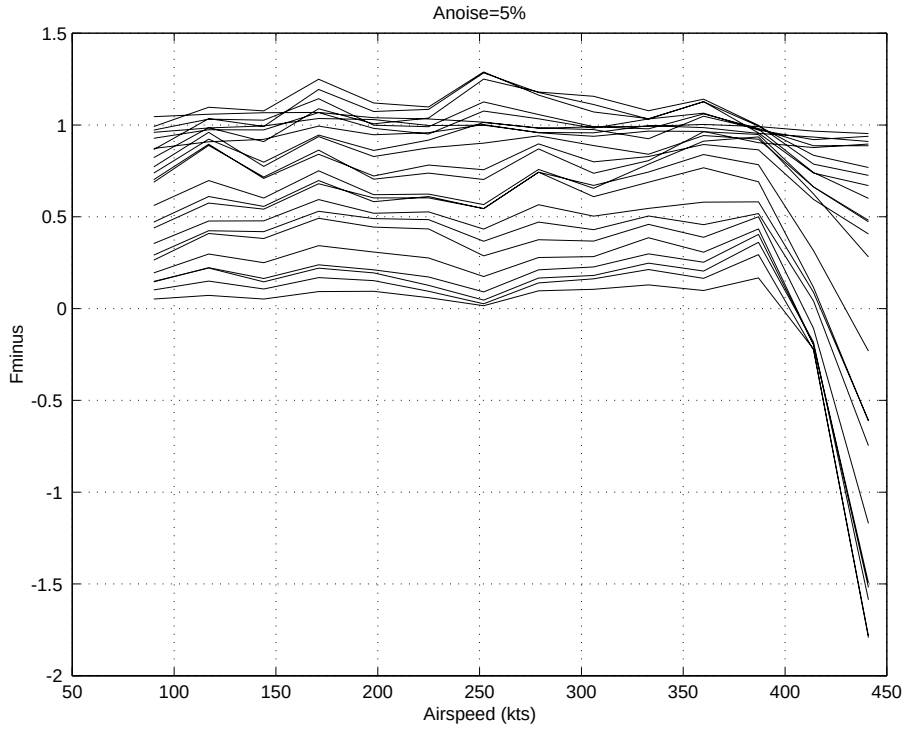

Figure 2.36: $F^{-}(l)$ stability criteria variation with airspeed for Sim-2 model

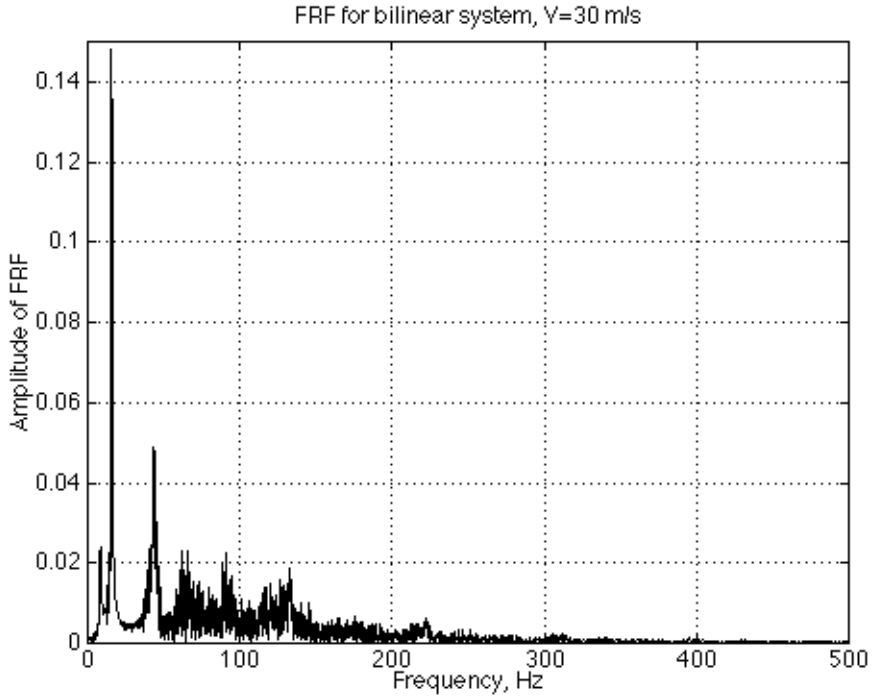

Figure 2.37: FRF for a system with bilinear stiffness, intermediate velocity

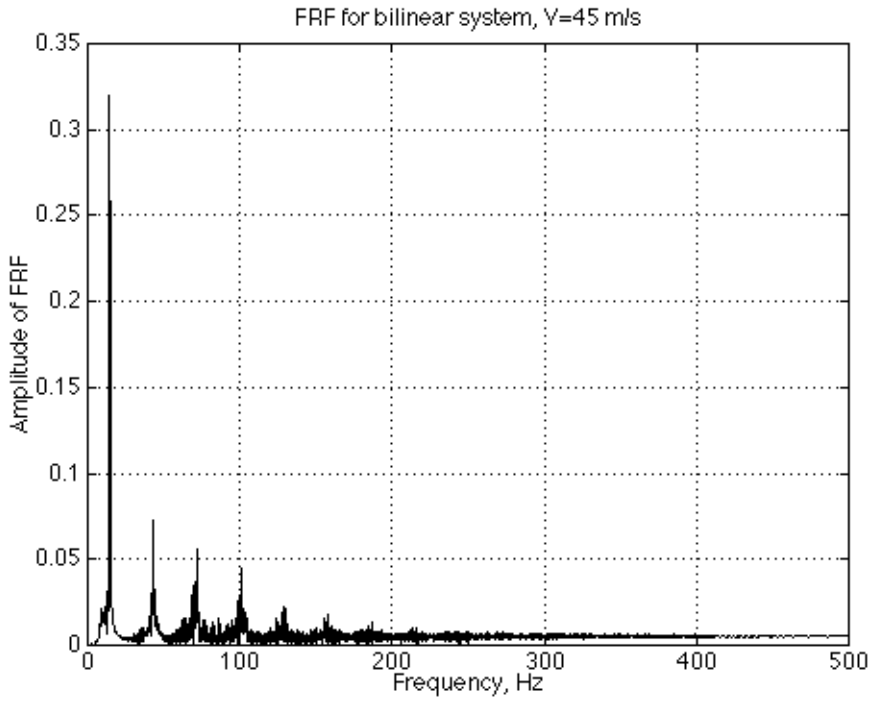

Figure 2.38: FRF for a system with bilinear stiffness, near flutter velocity

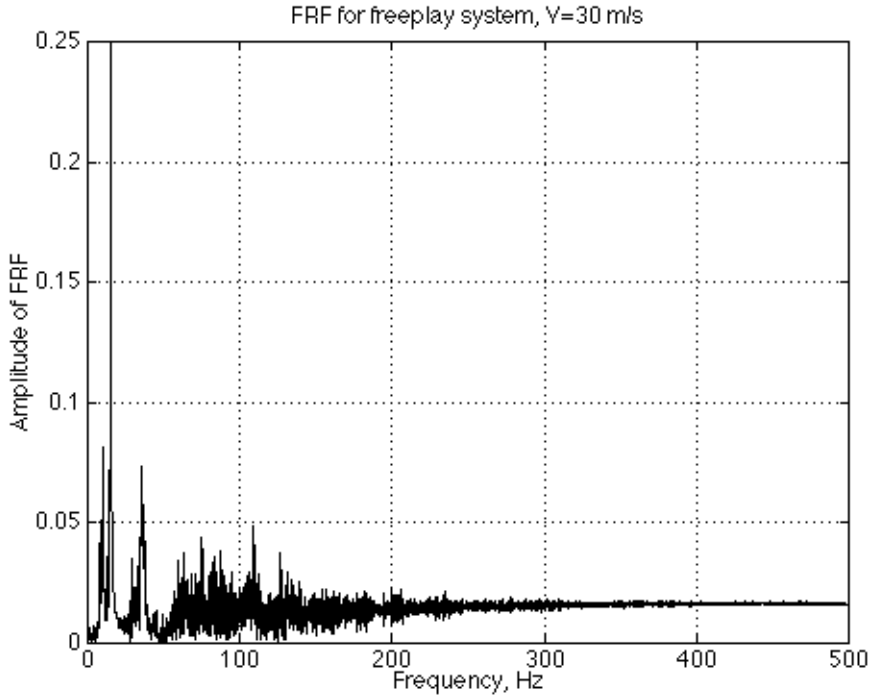

Figure 2.39: FRF for a system with freeplay stiffness, LCO velocity

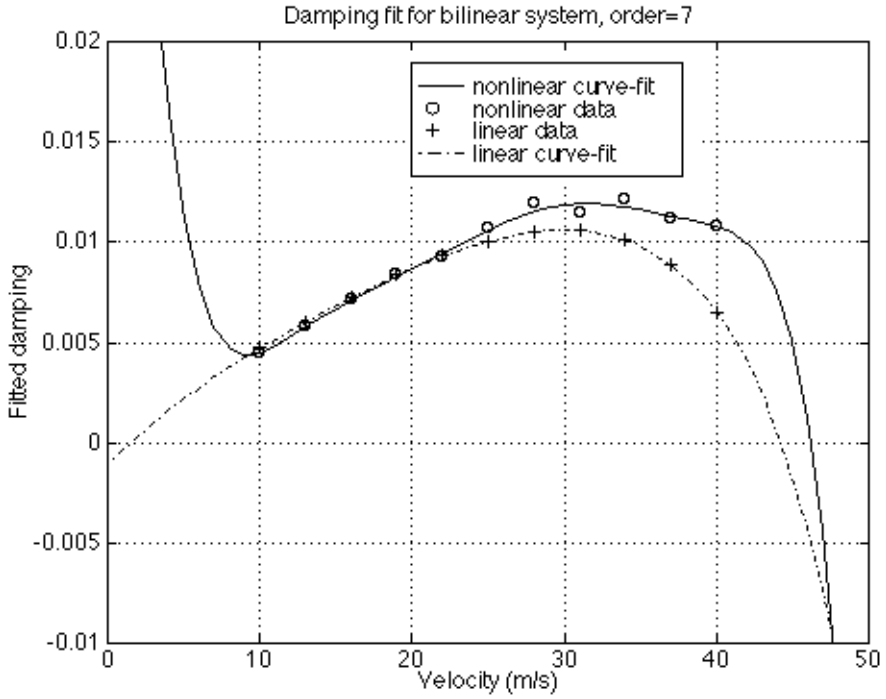

Figure 2.40: Damping Fit flutter prediction for bilinear system

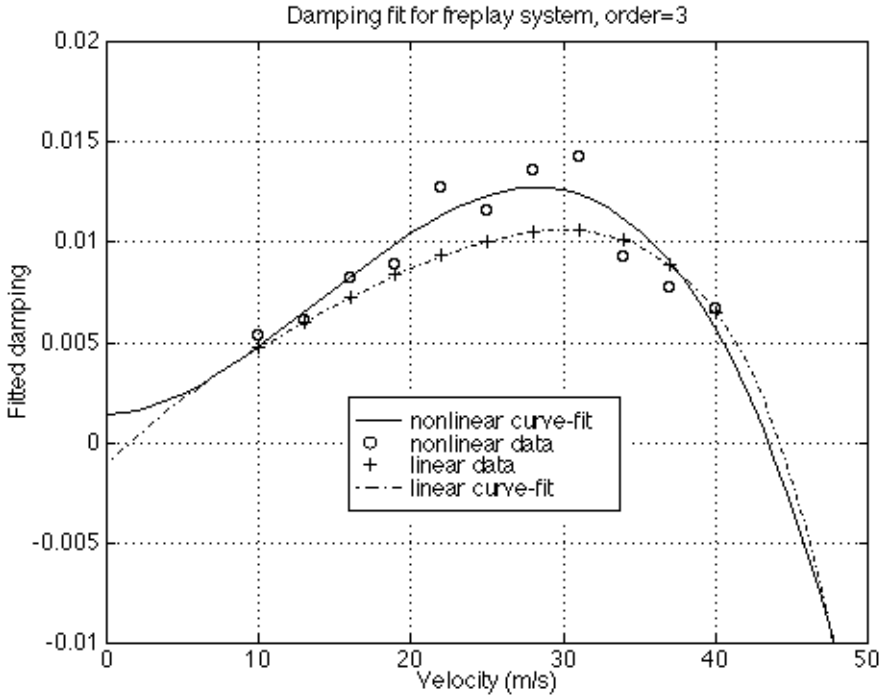

Figure 2.41: Damping Fit flutter prediction for freeplay system

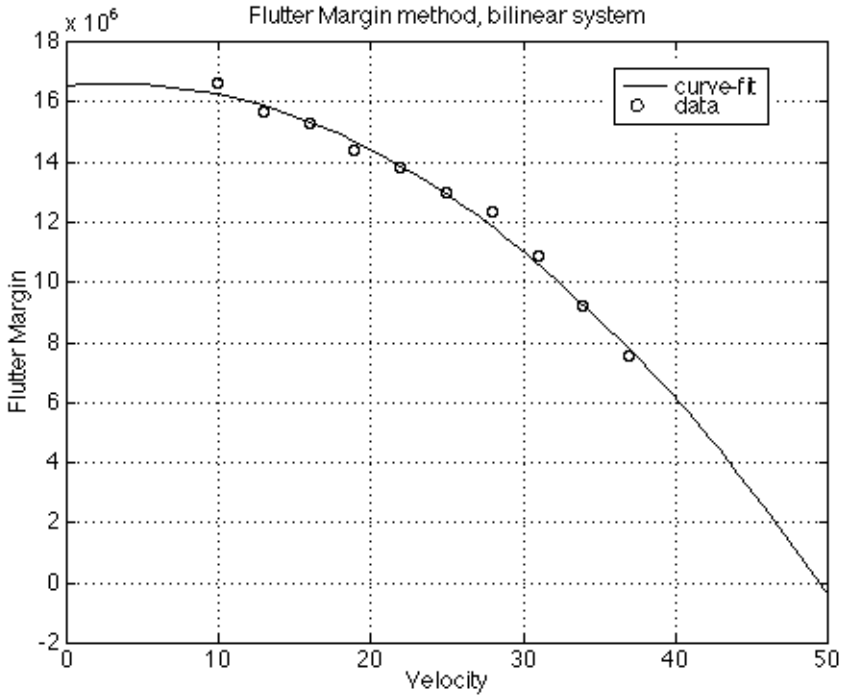

Figure 2.42: Flutter Margin flutter prediction for bilinear system

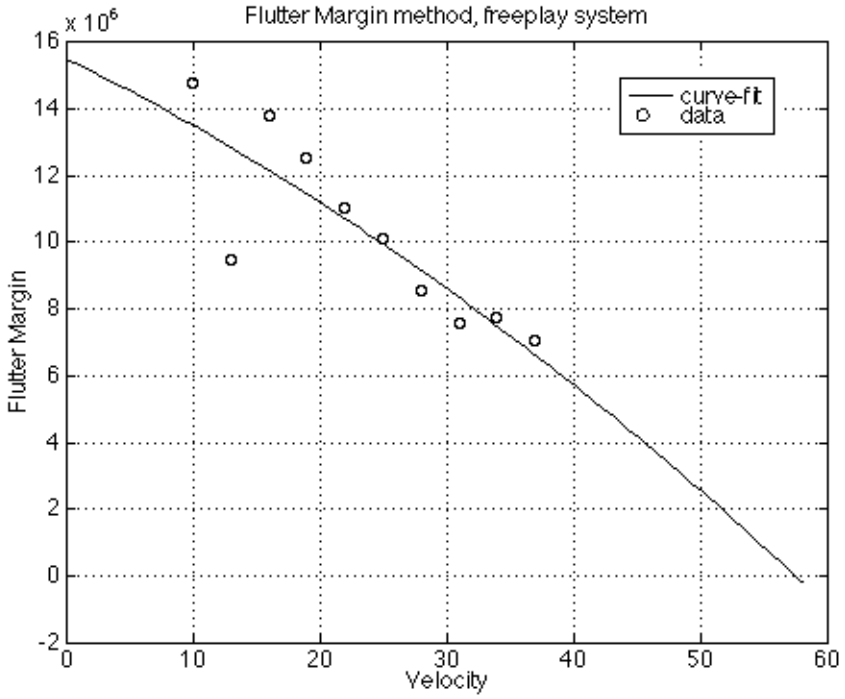

Figure 2.43: Flutter Margin flutter prediction for freeplay system

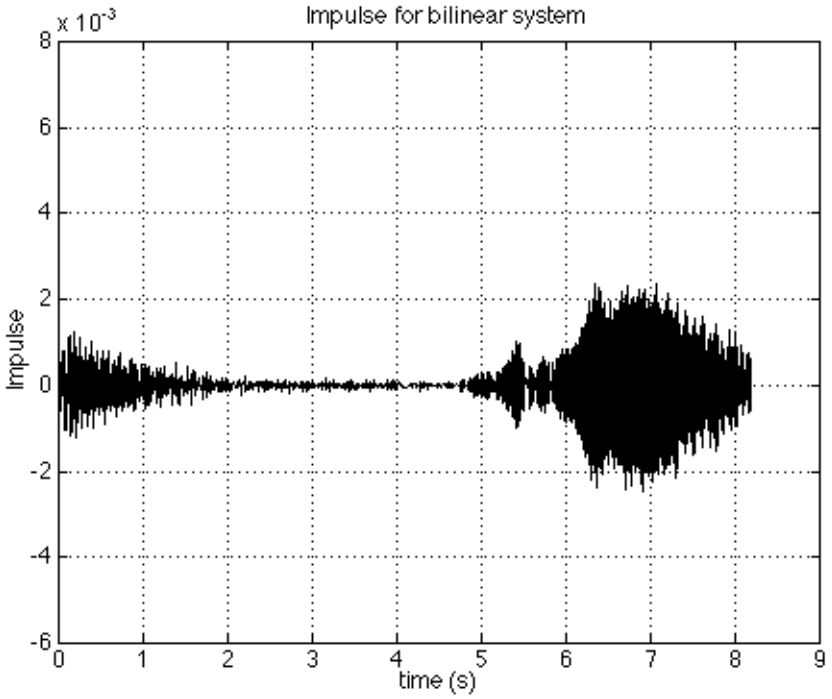

Figure 2.44: Estimated impulse response for bilinear system

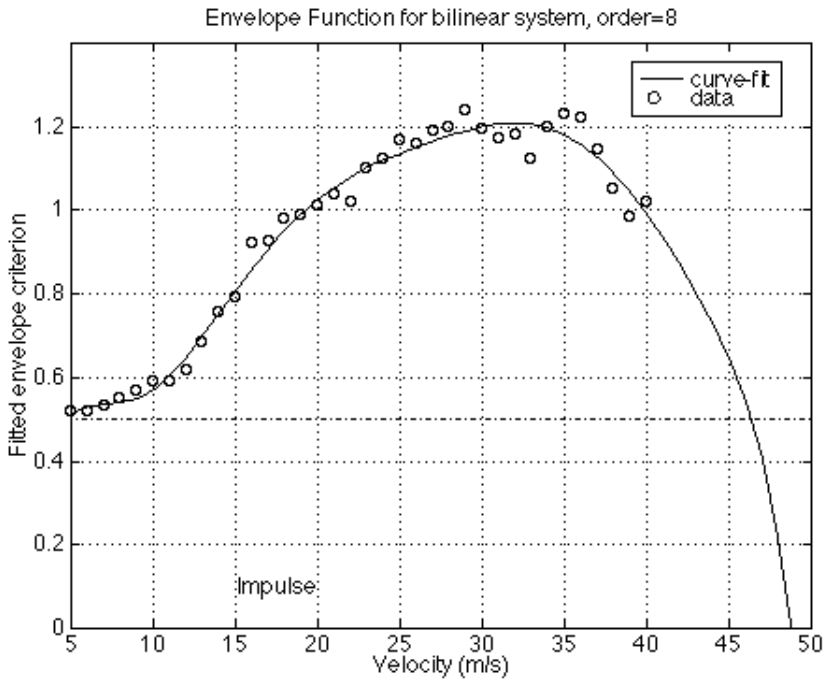

Figure 2.45: Envelope Function flutter prediction for bilinear system

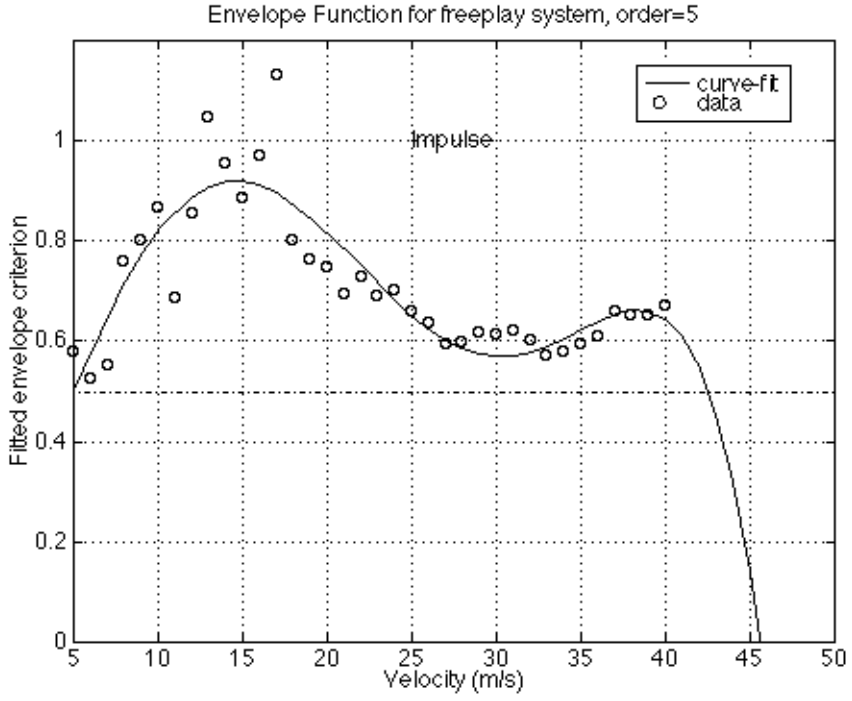

Figure 2.46: Envelope Function flutter prediction for freeplay system

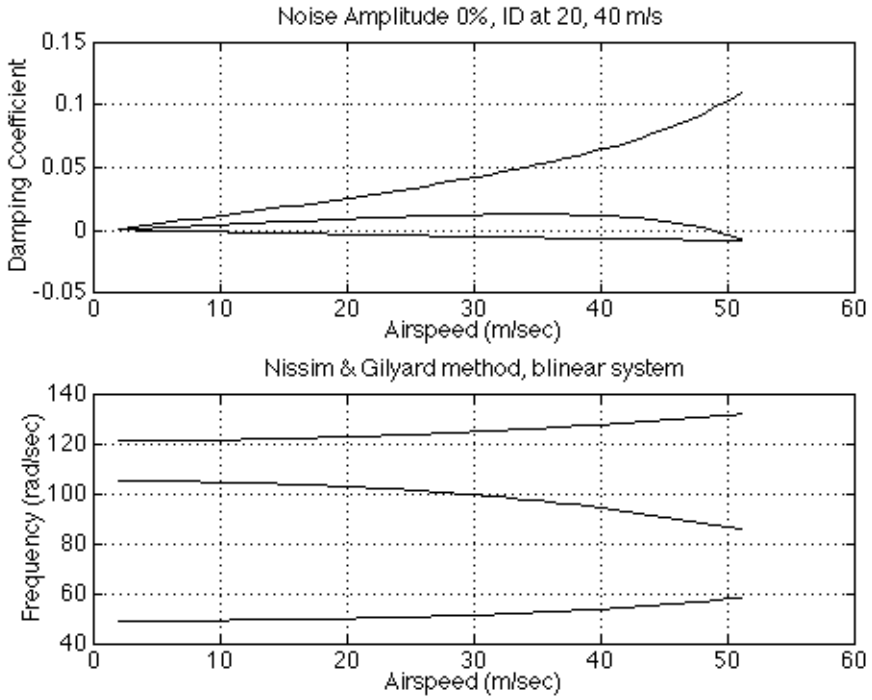

Figure 2.47: Nissim & Gilyard flutter prediction for bilinear system

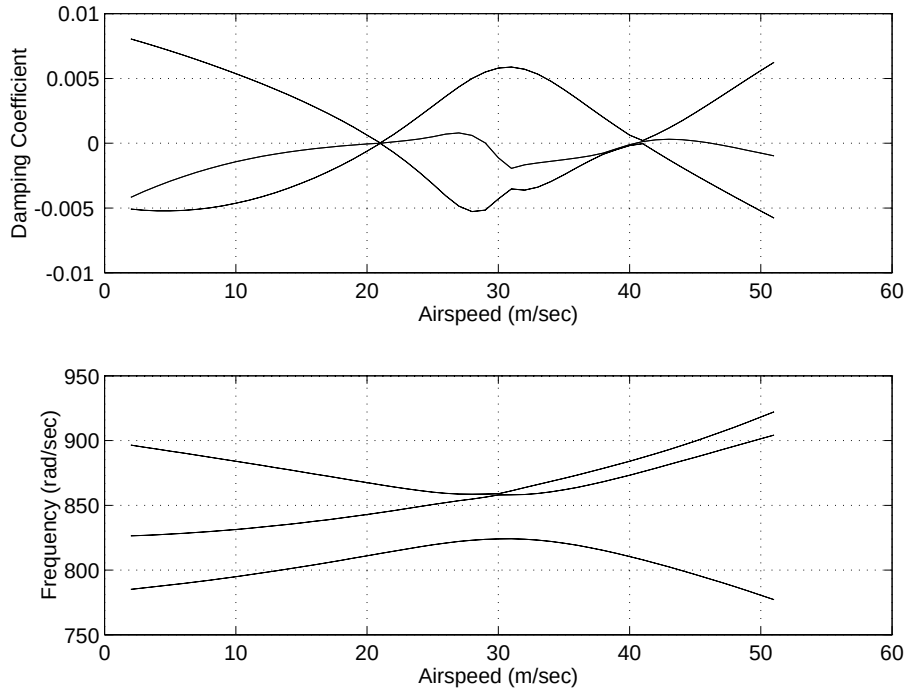

Figure 2.48: Nissim & Gilyard flutter prediction for freeplay system, high frequencies

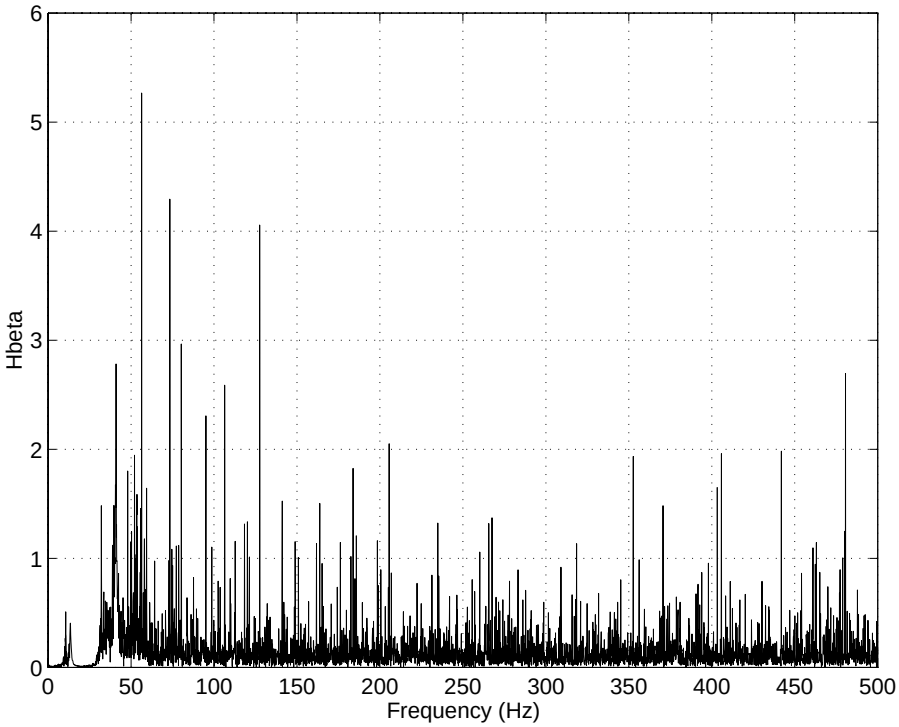

Figure 2.49: Spectrum of the Freeplay Hancock system, 41 m/s

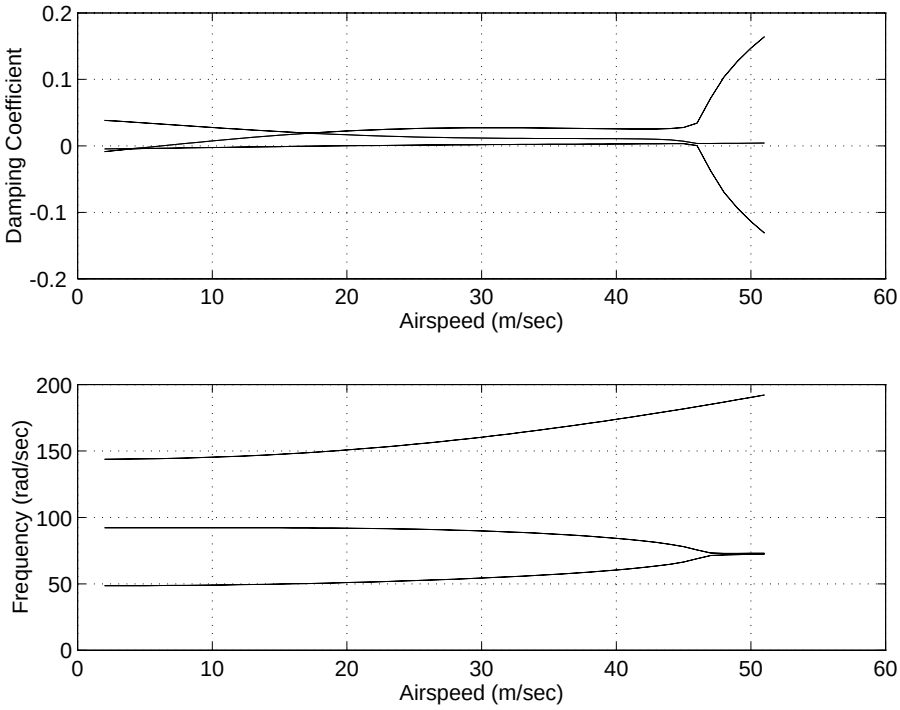

Figure 2.50: Nissim & Gilyard flutter prediction for freeplay system, low frequencies

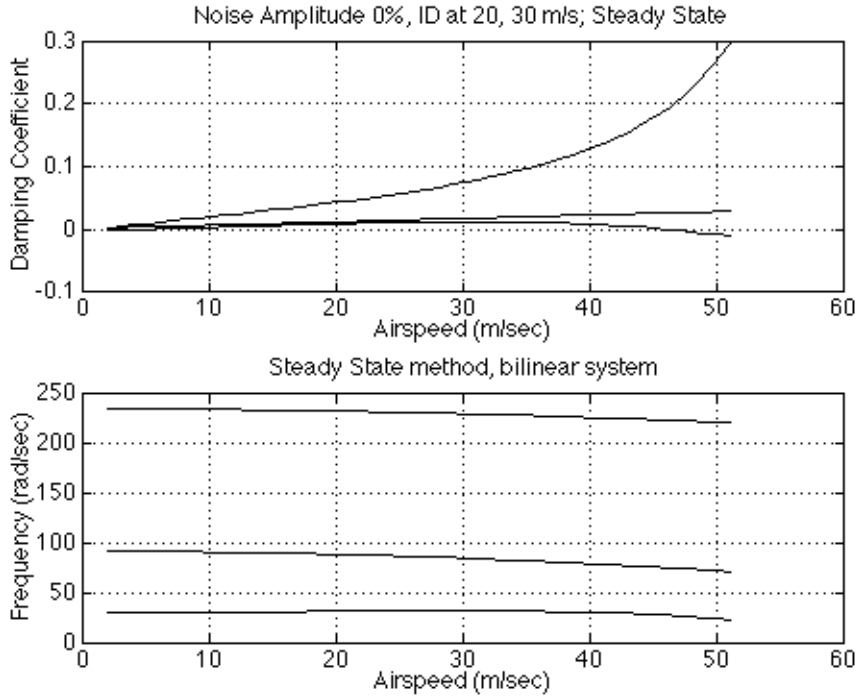

Figure 2.51: Steady State flutter prediction for bilinear system

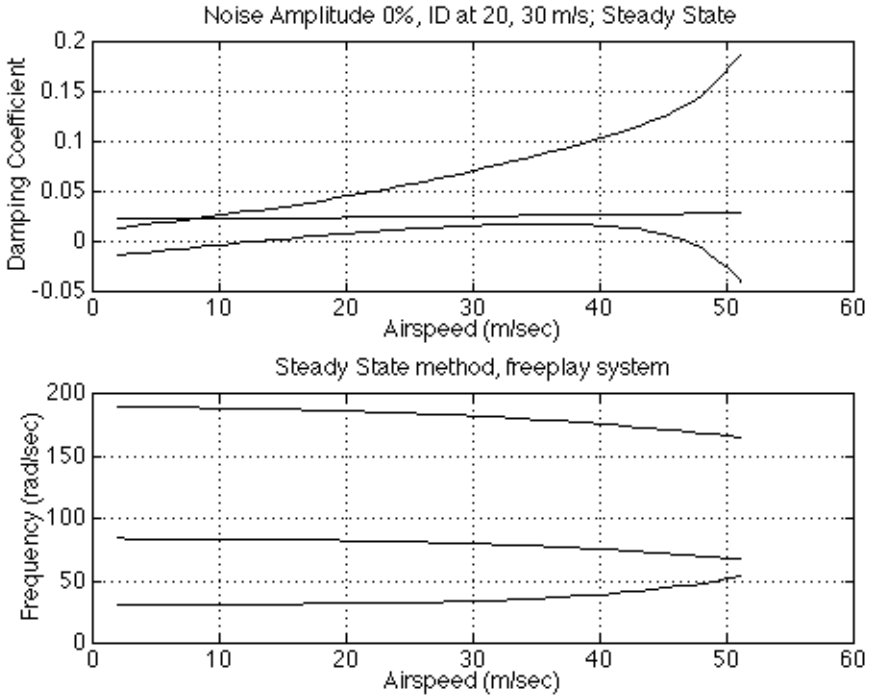

Figure 2.52: Steady State flutter prediction for freeplay system

Chapter 3

Nonlinear Aeroelastic Systems

3.1 Introduction

In this chapter the behaviour of nonlinear aeroelastic systems is analysed, starting with a summary of research on the subject to date. Limit cycles and Limit Cycle Oscillations are defined and explained. One of the most widely used approaches for predicting the existence and the amplitude of LCOs, the Harmonic Balance method is detailed and demonstrated and its limitations are discussed. The ability of the method to predict both stable and unstable limit cycles is suggested and indicated by means of total energy variation with time graphs.

By use of numerical integration of a simple nonlinear aeroelastic system, the evolution of the system from low velocity to flutter is presented as a series of bifurcations which can induce a variety of nonlinear behaviors, such as LCOs and chaotic motion. The existence of multiple limit cycles at a single velocity is demonstrated, as well as the possibility that the system response can switch from one particular limit cycle to another given the right excitation. This limit cycle switching effect is taken advantage of to propose a simple approach for LCO control and even suppression.

Finally, the chaotic behaviour of nonlinear aeroelastic systems is discussed.

Methods to indicate and prove the existence of chaotic oscillations are presented and demonstrated, and a rudimentary explanation for the occurance of these oscillations is attempted.

3.2 Literature Review

Some of the earliest investigations of nonlinear aeroelastic systems were those by Woolston et al [29], [30] and Shen [26]. Despite the lack of modern computing facilities (most of the calculations were carried out on analogue computers) these works established some of the basic nonlinear effects and methodologies that are still researched today. Woolston et al determined the importance of initial conditions in establishing the type of response of a nonlinear system and identified a new nonlinear phenomenon which they termed "self-limited flutter", more commonly known as Limit Cycle Oscillations (LCO). Limit cycles were already known from the work of Poincaré and others as bounded, unforced oscillations, which appear as closed line-singularities in the phase-plane [31].

Shen applied the Kryloff & Bogoliuboff (harmonic balance) method [32] to nonlinear aeroelastic problems and showed that this method could provide results that agreed with their analog computer integrations of simple and multi-dof systems (for more details on the harmonic balance method see the relevant section later in this chapter). Both pieces of research centred around structural nonlinearities that are still of interest today, mainly freeplay (flat spot), freeplay with preload, hysteresis and cubic stiffness.

Approximately 20 years later Breitbach [6] summarized some of the main nonlinear structural effects that had been encountered up to then in aircraft. He classified structural nonlinearities into concentrated and distributed nonlinearities. The first category contained such effects as freeplay in the linkage elements of control systems, solid friction in control cable and push rod ducts, kinematic

limitation of control surface deflection (pitch-stops) and spring tab systems. The second category contained nonlinear effects arising from elastic deformations in rivets, screws, bolts and structural components. The term 'distributed' is due to the fact that, because of the large number of rivets, screws and bolts, these nonlinearities can be assumed to be distributed throughout the aircraft structure. Breitbach found that the most common effect of all these nonlinearities was to cause variations in the natural frequencies and dampings of a structure with increasing amplitude of excitation (and, hence, response).

With the advent of the high-speed digital computer, new impetus was given to nonlinear aeroelastic research. In [33], a mathematical model of a missile control surface with freeplay root stiffness is investigated using both numerical integration and the harmonic balance method. The results of the integration serve to validate the harmonic balance results and to indicate the tendency of the system to limit cycle. The main achievement of that particular piece of research, though, was the fact that the system investigated incorporated two interacting nonlinearities. McIntosh [34] et al produced a set of high quality experimental response data from a wind tunnel model of a 2-dof wing, the first of many such investigations to come. Dowell [35] numerically integrated the equations of motion of a buckled plate in supersonic flow, demonstrating that chaotic motion can occur in aeroelastic systems. He employed Poincaré plots to indicate the existence of chaos.

A few years later Lee [36] developed an iterative method for extending the harmonic balance technique to systems with multiple structural nonlinearities. His approach was based on aligning the amplitude of oscillation in each spring with the harmonic balance prediction of stiffness before computing the final stability characteristics. The method could predict accurately the amplitude of limit cycles of large aeroelastic systems as well as the initial conditions necessary to

cause the limit cycle oscillations. Reference [37] offers another attempt to extend the capabilities of the harmonic balance method, this time by applying an asymptotic expansion to the load-displacement relationship of a nonlinear spring. The harmonic balance method uses a single-term Fourier expansion. The increased accuracy of the method in [37] arises from the fact that the asymptotic expansion allows the inclusion of higher harmonics in the representation of the nonlinearity.

In reference [27] Yang and Zhao tested an experimental, two degree-of-freedom, wing in a wind tunnel in conjunction with numerical integration and harmonic balance analysis of a mathematical model of the same wing. Their main discovery was that certain aeroelastic systems can undergo two or more limit cycle oscillations of different amplitudes at the same airspeed. Furthermore, they determined that the harmonic balance method can predict all of these limit cycles as well as additional unstable limit cycles, which do not appear in the experimental or numerical integration results.

Brase & Eversman [38] developed a new approach for setting up and solving mathematical models of multi-dof aeroelastic systems in three-dimensional compressible flow. In general the unsteady aerodynamic forces are written in terms of Theodorsen' s function which is, in turn, a function of the frequency of oscillation. Therefore, since the frequency can not be known before the equations are solved and the aerodynamic forces can not be evaluated before the frequency is obtained, various iterative schemes are usually applied. However, it is suggested in [38] that Theodorsen' s function can be written as a combination of a second order polynomial and a finite series of simple poles. If this is then transformed from the frequency to the Laplace domain, and then to the time domain, the dependence on frequency can be eliminated. The result is then substituted back into the equations of motion, direct integration of which can yield the complete time history of the system response. Additionally, the authors of [38] observed that

some of the solutions they obtained using their method demonstrated a "jump phenomenon", which could be associated with chaotic response.

Zhao & Yang also observed chaotic behaviour with their 2-dof wing in a later paper [39]. The chaotic motion occurred only when the airspeed was higher than the linear divergence speed. In references, [40], [41] chaos is defined as a "nonperiodic oscillation consisting of a multitude of frequencies and amplitudes". Intermittent chaotic response was encountered during wind-tunnel tests of a 2-dof wing. The chaos was indicated by phase-plane and frequency domain plots of the response. The authors concluded that chaos cannot be obtained from a system with a single nonlinearity however, this has been disputed since, especially in [28]. A helicopter blade with nonlinear hinge and nonlinear aerodynamics was investigated in [42]. Chaotic motions were observed both as a result of the structural and the aerodynamic nonlinearities. In this paper parameter-space sections were used to indicate the various types of response possible depending on airspeed and initial conditions.

A further variation on the harmonic balance was proposed in [43]. By reducing the equations of motion to a set of nonlinear algebraic equations, the linear and nonlinear parts can be handled separately and matched using an iterative procedure. The method is mainly used for the prediction of the fundamental harmonic response of a system.

Another investigation of a mathematical model of a simple 2-dof wing with root-pitch freeplay nonlinearity is described in [28]. Very detailed parameter sections were used to describe as large a portion of the response spectrum of the system as possible. Additionally, the authors of [28] used bifurcation diagrams to analyse the transition from one type of response to another. Limit cycle oscillations with more than one period were observed and explained as results of bifurcations en-route to chaos via period-doubling. In a later paper [9], a similar

analysis was carried out on the same wing with bilinear and cubic nonlinearities. Additionally, Lyapunoff exponents [44] were used to prove the existence of chaos in the response of the wing with cubic stiffness. Contrary to [39], it was found that chaotic motion can occur at speeds lower than the linear static divergence speed. This contradiction is explained in [9] as a consequence of the different aerodynamic models used in the two pieces of research.

Holden et al [45] observed experimentally the same phenomenon that Zhao & Yang reported in [27] concerning multiple limit cycles with different amplitudes existing at the same airspeed. The authors of [45] found that, by repeating an excitation sequence on their wind tunnel model after the model had gone into limit cycle oscillations, they could induce the system to jump to a limit cycle with higher amplitude. The system reverted to the original limit cycle some time after the end of the second excitation sequence.

Further evidence of chaotic response of aeroelastic systems is given in [46] and [47]. By employing a modelling method similar to that of [38], a finite element-doublet lattice model of a flexible wing with freeplay in the root pitch spring is solved. The usual types of response are encountered as well as "chaotic jumps" around two equilibrium positions in a double-well potential manner, similar to those described in [38]. Reference [48] describes wind tunnel and numerical tests of a 3-dof wing with control surface. Special significance is given to the agreement of theory and experiment as well as to the importance of initial conditions in determining the response of the system. One interesting phenomenon that the authors of [48] reported was that, at the instances were the numerical results predicted chaotic motion, the wind tunnel model exhibited non-chaotic but irregular motion with high levels of noise.

A further effect of nonlinearity in aeroelastic systems, internal resonance, is investigated in reference [49]. Internal resonance is the phenomenon whereby a

higher harmonic of a nonlinear element in a structure coincides with the natural frequency of one of the linear modes, causing resonance. The authors of [49] built a nonlinear wind-tunnel model in order to investigate this and other effects, however, the model failed to demonstrate internal resonance.

Most of the current research is still at the stage of reporting results in the attempt to gain a deeper understanding of the effects of nonlinearities to the response of aeroelastic systems. As will be demonstrated in later sections, a number of useful tools have been employed to this effect which, even though not new, had not been used by aeroelasticians in the past. These tools include bifurcation diagrams, Poincaré plots, parameter-space sections, Lyapunoff exponents and asymptotic expansions. Nevertheless, there is still a lack of basic understanding in how to combine these tools and the results that have been produced into a more coherent theory of nonlinear aeroelasticity.

Another common pattern in the research carried out up to now on nonlinear aeroelasticity, is the search for a more effective version of the Harmonic Balance method. This method is the only one available that can predict the response of a system over a wide range of conditions without the need to carry out time-consuming numerical integrations hence, it is used as the basis for other, more general, limit-cycle prediction methods. Despite this effort, each new version of the method only improves on of the aspects of the original approach. Thus, a procedure has been developed that can be applied to systems with multiple nonlinearities, another one improves the accuracy of the method by using higher harmonics, etc, but no method will achieve all of the above.

3.3 Limit Cycle Oscillations

A Limit Cycle Oscillation (LCO) is a bounded, unforced oscillation around a limit cycle, which is a closed line-singularity in the phase-plane [31]. Hence, the

terms LCO and limit cycle should not be confused since the former is a physical motion of the system whereas the latter is a feature of the phase plane. There are three types of limit cycle

- Stable limit cycle
- Unstable limit cycle
- Half-stable limit cycle

Figure 3.1 shows a stable limit cycle in the phase plane. The system motion (or trajectory) approaches the limit cycle both from the inside and outside. The initial conditions for trajectory A are inside the limit cycle and those for trajectory B are outside but in both cases Limit Cycle Oscillations ensue. Note that a trajectory can not cross the limit cycle.

Figure 3.2 shows an unstable limit cycle. Both trajectories A and B move away from the limit cycle. Trajectory A, which lies inside the limit cycle, winds away resulting in a decaying oscillation. Trajectory B, which lies outside the limit cycle, also winds away resulting in an unstable oscillation. Again, the limit cycle can not be crossed. The unstable limit cycle can only be reached as time runs backwards towards $-\infty$ although, of course this is not physically possible.

Finally, figure 3.3 demonstrated a half-stable limit cycle. Trajectory A, which lies inside the limit cycle, also lies on the stable side of the limit cycle and approaches it resulting in LCO. Trajectory B lies outside the limit cycle and on its unstable side and hence moves away from it. Hence this particular half-stable limit cycle is unstable on the outside and stable on the inside. Half-stable limit cycle that are stable on the outside and unstable on the inside also exists. In both cases, the limit cycle can not be crossed. A half-stable limit cycle can be visualized as a composite of a stable and an unstable limit cycle that lie very close together.

It follows that LCOs can only occur around certain types of limit cycle i.e. stable limit cycles and the stable sides of half-stable limit cycles. The mechanism by which limit cycles dictate the motion of the system is energy-related. Around a stable limit cycle, only a certain amount of energy is drawn from the free stream. As a result, when a system undergoing such a LCO is displaced to a higher energy state, it cannot maintain its energy level and winds back on the limit cycle. If the system is at a lower energy state, it receives more energy than is dissipated by the damping and moves up to the limit cycle. On the limit cycle, the rate of energy input from the free-stream is equal to the rate of energy dissipation, resulting in a stable periodic motion. An unstable limit cycle is characterized by the fact that, if a system's response is outside its orbit in the phase-plane, the system continuously receives more energy than it can dissipate and diverges whereas, if the system response lies inside the limit cycle, energy is drawn out of the system and into the free-stream resulting in a decaying oscillation.

Limit cycles result directly from system bifurcations as a parameter is varied [50]. In the case of aeroelastic systems, this parameter is the free-stream velocity. In classical examples of bifurcation theory [31], the system initially has only one singularity in its phase-plane, a stable equilibrium point. As the controlling parameter is varied, the system bifurcates, i.e. the equilibrium point becomes unstable and a stable limit cycle grows around it (see figure 3.4). A typical example of this behaviour is the rotating pendulum. This type of bifurcation results in soft self-excitation behaviour [51], which is characterized by the fact that any infinitesimal departure from the unstable equilibrium point will result in LCO motion. A different type of bifurcation will result in the so-called hard self-excitation behaviour. Here, the equilibrium point remains stable but an unstable limit cycle forms around it, followed by a stable limit cycle of a larger radius, so that finite excitations have to be applied to the system in order to move it from

rest onto the stable limit cycle (see figure 3.5). As will be shown later, both types of bifurcation can be observed in aeroelastic systems.

Depending on the complexity of a given system (number of degrees of freedom, number and type of nonlinearities), a large number of limit cycles can exist in its phase-plane. However, their stability needs to be alternating, i.e. an unstable limit cycle needs to lie between two stable limit cycles, or a stable limit cycle and a stable equilibrium point.

3.4 Harmonic Balance Method

The harmonic balance method is used for a variety of nonlinear problems to provide estimates of the stability of systems. It was first presented in the west in reference [32] but the formulation presented here is based on references [27] and [34]. As mentioned earlier, the crux of the harmonic balance method is to assume that the system admits a limit cycle which is caused by a nonlinear spring. In other words it is assumed that the displacement x of the nonlinear spring is sinusoidal with amplitude A, i.e.

$$x = A \sin t \tag{3.1}$$

Consider a bilinear spring characterized in figure 3.6. Inside the freeplay region (of size δ), the stiffness is K_1 and outside, it is K_2.

Define x as being the input to the spring and F, the force in the spring as the output. If $A < \delta$, then the response of the spring is linear. If $A > \delta$, then the force in the spring is determined by whether x is larger or smaller than δ. Consider figure 3.7, it can be seen that, in the time domain, five distinct regions are defined within one period, from $t = 0$ to t_1, from t_1 to $\pi - t_1$, from $\pi - t_1$ to $\pi + t_1$, from $\pi + t_1$ to $2\pi - t_1$ and from $2\pi - t_1$ to 2, where

$$t_1 = \arcsin \frac{\delta}{A} \tag{3.2}$$

The force, F, in the spring is given in terms of the displacement by

$$F = \begin{cases} K_2 x + (K_1 - K_2)\delta & \text{if } x \geq \delta \\ K_1 x & \text{if } -\delta \geq x \geq \delta \\ K_2 x + (K_2 - K_1)\delta & \text{if } x \leq -\delta \end{cases} \tag{3.3}$$

Substituting for x in 3.3 and taking the first term of the Fourier expansion of $F(t)$ (taking into account the fact that $F(t)$ is an odd function and therefore only the sine term exists in the expansion) gives

$$F(t) = \frac{A}{\pi}(K_2 - K_1)\left\{\frac{K_2}{K_2 - K_1}\pi - 2t_1 - \sin 2t_1\right\}\sin t \tag{3.4}$$

But, since $Asint = x$,

$$F = \hat{K}x$$

where,

$$\hat{K} = \frac{K_2 - K_1}{\pi}\left\{\frac{K_2}{K_2 - K_1}\pi - 2t_1 - \sin 2t_1\right\} \tag{3.5}$$

This is the equivalent linearized stiffness for the bilinear stiffness case. Equivalent linearized stiffnesses for other types of non-linearities are given by

- Freeplay (see figure 3.8)

$$\hat{K} = \frac{K}{\pi}\{\pi - 2t_1 - \sin 2t_1\} \tag{3.6}$$

  where t_1 is as defined before and K is the linear stiffness.

- Cubic (see figure 3.9)

  Defined as $F = Kx + ex^3$, where K is the linear slope and e is a constant.

$$\hat{K} = \frac{3eA^2}{4} + K \tag{3.7}$$

These relationships between the equivalent linearized stiffness and the amplitude of the limit cycle can prove very useful if they are combined with graphs of the flutter (or critical) velocity of the linear model as a function of the same stiffness. The end result is a plot of the possible amplitudes of limit cycles at various critical velocities and is achieved by mapping the equivalent stiffness-amplitude graph onto the critical velocity- equivalent stiffness graph.

The process of building up a Harmonic Balance plot can be seen in figure 3.10. Three plots can be seen in the figure:

1. Quadrant A contains the Equivalent Stiffness vs Amplitude plot for bilinear stiffness, obtained from equation 3.5.

2. Quadrant B contains the Equivalent stiffness vs Flutter Velocity for the system under investigation, obtained from solving the equations of motion with the particular equivalent stiffness.

3. Quadrant D contains the Limit Cycle Amplitude vs Velocity plot, obtained from combining the plots in quadrants A and B.

Quadrant C contains a straight line with slope 1 and intercept zero. The procedure is as follows.

1. A particular value of limit cycle amplitude is chosen, which gives a value of the equivalent stiffness in quadrant A (point A1).

2. The value for the equivalent stiffness is used to give a value for the limit cycle velocity from quadrant B (point B1).

3. The amplitude value from step 1 is used in quadrant D (rotated by 90 degrees at point C1) along with the values of the limit cycle velocity from step 2 to define point D1 in quadrant D.

When enough points have been drawn in quadrant D, the limit cycle velocity vs limit cycle amplitude graph is complete. The velocity-amplitude graph is useful in two ways. Firstly, it shows at which airspeed onwards the system is expected to admit a limit cycle. Below that particular airspeed the response dies down with time and the system is stable. In the case of figure 3.10 that speed is approximately 35 m/s. The graph can also show which is the top speed at which a limit cycle is expected. Above that speed flutter occurs. In the case of figure 3.10, bilinear stiffness dictates that as the amplitude approaches infinity, the equivalent stiffness approaches the outer stiffness K_2 (see figure 3.6), which is 3000 N/m. Hence, the top speed at which a limit cycle is possible is the flutter speed of the equivalent linear system with a stiffness of 3000 N/m. Secondly, it gives all the possible amplitudes of limit cycles taking place in between these two speeds. This last result is approximate, especially for high amplitudes when the linearisation starts to break down, but is a very useful guide as to what tests (on either computer or actual models) have to be performed in order to obtain more accurate results.

3.4.1 Harmonic balance results

Applying the harmonic balance scheme to the model of the wing with control surface (see appendix A) confirms the claim in [36] and [34] that it is possible to obtain two different amplitudes of limit cycles at the same velocity.

In figure 3.10 points D1 and D3 occur at the same speed but at different amplitudes. Figure 3.11 shows how, in the case of freeplay stiffness in the wing pitching spring, it is possible to obtain three different limit cycle amplitudes at

the same speed in the velocity region between 35 and 45 m/sec and two in the region 70-85 m/sec. Figure 3.12 depicts the effects of bilinear stiffness in wing pitch. Since bilinear stiffness is a 'more linear' freeplay case there are less possible amplitudes at one single velocity but it is still possible to obtain two of them in the region 70-85 m/sec. The important thing to note is that all these amplitudes are possible because of the particular shape of the critical velocity- wing pitch stiffness plot. If the graph was monotonically increasing only one amplitude would be possible at every speed.

In the case of nonlinearities in the control pitching spring, the number of amplitudes at one particular velocity, as well as the number of regions were multiple amplitudes are possible, is lower because the velocity-stiffness plot has only one turning point. Only freeplay yields such behaviour, at low equivalent stiffnesses (see figure 3.13). For bilinear stiffness to do the same, the inner stiffness has to be so low that the bilinearity almost disappears and is replaced by freeplay behaviour (see fig 3.14).

In references [27], [9] it is theorized, without proof, that some of the limit cycles predicted by the Harmonic Balance method at a single airspeed are stable and some of them unstable. The next section investigates this possibility

3.4.2 Stable and Unstable Limit Cycle Prediction

The Harmonic Balance Method does not distinguish between stable and unstable limit cycles. As a consequence, it predicts both types, as has been already demonstrated. Figure 3.15 shows harmonic balance results (dotted line) for the Hancock wing with control surface, superimposed over a section of the parameter space (obtained from integration of the equations of motion), on which the LCO-no LCO boundary has been plotted. The y-axis for the Harmonic balance

results is amplitude of LCO and for the LCO boundary control surface pitch initial condition (the nonlinearity is freeplay in the control surface). The parameter space section was obtained by means of system integration using the Runge-Kutta scheme (see appendix D). The dotted line defines two sets of limit cycles, one set of high amplitude and one of low. The reason why these results were included in the same graph as the parameter space section is to indicate that the low amplitude limit cycles are unstable since they correspond to the inner LCO/no-LCO boundary, inside of which no LCO is possible. This observation was also made in [9] without proof.

A further indication that the Harmonic Balance method predicts unstable as well as stable limit cycles is the fact that there is a qualitative difference between high and low amplitude limit cycles predicted by the method. This difference concerns the way that the energy of the system varies during LCOs. As mentioned earlier, the energy of a limit cycling system is constant. However, if only the kinetic and potential energy are considered, their sum oscillates around a constant value. This is demonstrated in figure 3.16, where total energy refers to the sum of the kinetic and potential energies. The same phenomenon can be observed in linear systems that flutter, as depicted in figure 3.17. In both the linear and nonlinear cases, the frequency of oscillation of the total energy is twice the frequency of the periodic motion, reflecting the fact that the potential and kinetic energies are 90 degrees out of phase.

The qualitative difference between low and high amplitude limit cycles predicted by the Harmonic Balance method lies in the energy oscillation of the respective equivalent linearized systems. Figure 3.18 shows the control surface response of the low amplitude linearized system and its energy oscillation. The total energy reaches its minima near the zero positions of the system response. Conversely, figure 3.19 shows that, for the high amplitude linearized system, the

total energy reaches its *maxima* at the zero position of the system response. Hence, an unstable limit cycle, as predicted by the Harmonic Balance method, is one for which the periodic variation of the total energy of the equivalent linearized system reaches its minimum near the zero position of the system response and vice versa, i.e. for a stable limit cycle the total energy reaches its maximum near the zero position of the response. This phenomenon can also be observed in the nonlinear system. Figure 3.20 shows a stable limit cycle and the corresponding total energy variation. The latter, again, reaches its maximum at the zero position of the limit cycle. A similar plot for a nonlinear limit cycle could not be produced since unstable limit cycles can only be reached at time $t = -\infty$, which poses severe numerical difficulties.

To finish off with the discussion of the Harmonic Balance method, it should be mentioned that the end of the unstable LCO branch predicted by the method (figure 3.21) corresponds to the point were no more low amplitude periodic solutions are possible and coincides with the bifurcation to soft self-excitation. Hence, the Harmonic Balance can predict both hard and soft self-excitation bifurcations. The accuracy of the method suffers in the presence of bifurcations to chaotic behaviour at speeds lower than 18 m/s. Accuracy also suffers at amplitudes higher than 0.08 rad as seen in figure 3.21 which shows limit cycle amplitude vs air-speed obtained by direct integration of the system and also by the Harmonic Balance method.

3.5 Bifurcation to flutter

As mentioned earlier, in the case of hard self-excitation, the response of a system, i.e. whether it will limit-cycle or not, is dependent on the initial conditions. Therefore, a complete picture of the system's behaviour can only be obtained if the whole of its parameter-space is investigated. The parameter-space is defined

by the system's initial conditions (velocities and displacements) and the free-stream air-speed. In the case of the Hancock wing with control surface, the parameter-space is 7-dimensional (three displacements, three velocities and the air-speed). Consequently, the investigation of the complete parameter-space is extremely computationally expensive and, for larger systems, becomes impossible. However, a useful description of the system behaviour can be obtained by looking at 2-dimensional sections of the parameter-space, as first demonstrated in [39].

To demonstrate this approach the special case of the Hancock wing with freeplay in the control surface pitch will be investigated. The freeplay in the control surface implies the existence of two linear systems which will influence the behaviour of the nonlinear system.

- *Inner Stiffness Linear System*: This system (corresponding to low amplitude responses of the nonlinear system) has zero control surface structural stiffness.

- *Outer Stiffness Linear System*: This system (corresponding to high amplitude responses of the nonlinear system) has control surface structural stiffness equal to the outer stiffness in the freeplay region.

Figure 3.22 shows a 2-dimensional section of parameter-space. The two dimensions that are considered to be variables are the initial value of the control surface pitch and the air-speed. The other initial conditions are all set to zero. The section was obtain by direct integration of the equations of motion. Figure 3.23 is a bifurcation diagram for the same system. A bifurcation diagram is obtained by plotting at each airspeed the values of one of the state variables at points where another state variable is held fixed. In the case of figure 3.23 the control surface pitch position is plotted at points where the control surface pitch velocity is zero. The diagram shows whether limit cycles occur and how complex

the limit cycle motion is, over a range of airspeeds. The degree of complexity is demonstrated by the number of distinct points in the bifurcation diagram at a single velocity.

- One point means that there is no limit cycle motion and the system is stable.
- Two points denote a simple closed loop (also termed Period-1) limit cycle, an example of which is given in figure 3.24. This figure was produced using the Hancock model with control surface and bilinear stiffness in the wing pitch spring.
- Four points denote a Period-2 limit cycle, demonstrated in figure 3.25 This figure was produced using the Hancock model with freeplay in the control surface spring.
- More points denote higher complexity (Period-3, Period-4, etc). Note that, since the bifurcation diagram is symmetric around the airspeed axis there is always an even number of points at each airspeed where a limit cycle is possible. The phenomenon of bifurcations to higher order period limit cycles is called *Period Doubling*.
- After consecutive bifurcation to higher complexity limit cycles, the system response can become chaotic.

In figures 3.22 and 3.23 three types of bifurcation are observed. Under 15 m/s no limit cycle occurs, the response decays to its equilibrium position. At a free-stream airspeed of just over 16 m/s, the first bifurcation occurs. It is a bifurcation to chaotic behaviour which lasts up to approximately 17 m/s and causes the irregular LCO/no-LCO boundary. It should be noted that the response

in this region is chaotic irrespective of whether a LCO occurs or not, i.e. even the transient decay response is chaotic.

At 17 m/s a second bifurcation occurs leading to hard self-excitation behaviour. As a result, the equilibrium point is still stable, and a pair of limit cycles appears around it, the inner one unstable and the outer one stable. The wing only exhibits LCO behaviour if the initial condition is high enough to place the response outside the unstable limit cycle.

At 27.3 m/s a third bifurcation occurs, this time inducing soft self-excitation behaviour. The equilibrium point is now unstable and there is only one, stable, limit cycle. At this speed, the inner stiffness linear system flutters, hence the instability of the equilibrium point. Even infinitesimal displacements will cause diverging response until the stable limit cycle is reached, at which point the response becomes periodic.

At 43.5 m/s, another chaotic bifurcation occurs, which gives rise to chaotic pockets. Finally, at 45 m/s flutter behaviour begins to appear. Initially, flutter does not occur for every value of the initial condition. At 46.16 m/s however, there remains no initial condition at which the response is stable. The stable limit cycle completely vanishes, leaving only the unstable equilibrium point. The wing's response diverges irrespective of the initial conditions, i.e. flutter occurs. It is interesting to note that the outer stiffness linear system flutters at 44.07 m/s. Generally for this particular system, as seen in table 3.1, the flutter velocities of the outer stiffness linear system and the nonlinear system are very similar.

Thus, the variation of the behaviour of an aeroelastic system with airspeed is governed by a series of bifurcations, eventually leading to flutter. A corollary of this statement is that flutter itself is also a bifurcation phenomenon [44]. Figure 3.26 shows the frequency content of the response of the nonlinear wing model near flutter. It is obvious that none of the natural frequencies approach

Heave (Hz) Stiffness	Pitch (Hz) Stiffness	Freeplay (Hz) Stiffness	Other Parameters	Linear (m/sec) Flutter Speed	Nonlinear (m/sec) Flutter Speed
2	5	15	t=0.03	28.5780	27.5
2	5	15		16.5416	16.5
15	25	15		27.3930	29.0
15	25	30		51.9839	50.5
7	15	25		41.1552	43.5
9	22	25		52.3069	51.0
9	22	30		57.2150	61.4
5	12	30		38.1639	38.5
5	12	30	ha=0.85	37.6082	34.6
5	12	30	ha=0.70	38.8710	39.5
5	12	30	c=0.5	49.3901	49.6
5	12	30	t=0.02	53.8739	54.5

Table 3.1: Comparison of Linear and Nonlinear Flutter Speeds. (t = thickness of wing, c = chord-length of wing, ha = position of hinge axis in percent of chord)

or coalesce (which characterizes the linear flutter mechanism). Instead there is a basic frequency (10.94 Hz) and 4 multiples of it (3×10.94, 5×10.94, 9×10.94 Hz), which is typical of a nonlinear system. The lowest frequency is very close to the natural frequency of the two modes that merge to cause flutter in the outer stiffness linear system.

3.6 Limit Cycle Switching and LCO control and suppression

Limit cycle switching refers to forcing an aeroelastic system to jump from one limit cycle to another, at the same airspeed, by applying a suitable excitation force, as described in [45]. The authors of that paper observed limit cycle switching when they re-applied an excitation signal after a LCO had been initiated. The phenomenon was reproduced for the present work using the aeroelastic system described earlier. Figures 3.27 and 3.28 show limit cycle switching and the shape of the initial and final limit cycles in the phase-plane (Hancock wing with freeplay

in the control surface). In fact, it was observed that the response of the system could be changed from decaying to LCO by re-applying an excitation signal which, on its own, would not be sufficient to cause LCO (see figure 3.29).

In the light of the previous analysis, the phenomenon can be explained in energy terms. The application of the excitation signal supplies the system with enough energy to raise its response to a higher energy (and hence amplitude) limit cycle. In the case of figure 3.29, the small levels of response that are the result of the first excitation sequence contain enough energy to push the system response outside the unstable limit cycle and cause a LCO when the excitation is re-applied. The corollary from this analysis is that, since a general excitation signal is more likely to add energy to the motion, it is only possible to move the response of a system to a higher energy level limit cycle (or from decaying to LCO). In order to cause the system to jump to a lower level limit cycle (or to decaying response), an energy-extracting excitation signal has to be applied. Hence, the signal needs to contain elements of the system itself, i.e. to be the result of a feedback mechanism rather than a standard function.

The easiest way of creating a feedback-type excitation signal that will extract energy from the motion is to increase the effective damping of the system. Hence, the signal consists of a velocity term fed back into the system, i.e.

$$F(t) = -F_A\dot{\beta} \tag{3.8}$$

where $F(t)$ is the excitation signal and F_A is a constant to be determined. The negative sign serves to force the excitation signal to act as additional damping since $F(t)$ will appear on the right-hand-side of the equations of motion. In the context of the computer simulation, the feedback was not instantaneous but lagged by one time-step. This should not have a significant effect if the period of the motion is much larger than the time-step. The signal was constructed by

means of a control system whose basic functions were:

1. Detect the LCO
2. Calculate the amplitude of β and $\dot{\beta}$ during the LCO
3. Calculate F_A according to

$$F_A = \frac{amp(\dot{\beta})}{amp(\beta)} \tag{3.9}$$

   where $amp(\beta)$ denotes the amplitude of β

4. Form $F(t)$ and feed it into the control surface
5. When the response levels have dropped stop the feedback

The scaling of equation 3.9 was found to be appropriate after a certain amount of experimentation. In general F_A can be higher than this value but, if it is too high it can cause numerical instability.

An application of this procedure to the Hancock wing with control surface nonlinearity system can be seen in figure 3.30. The first excitation signal is a standard chirp of sufficient amplitude to cause a LCO. The second signal is applied through the control system. An interval of 2 seconds between the detection of the LCO and the application of the signal was imposed in order to make the process clear.

It should be noted that, if the system is in a state of soft self-excitation, it is impossible to bring it back into equilibrium. As soon as the excitation signal stops the response will increase again, as seen in figure 3.31. In such a case the procedure outlined in this section could only ensure that the system's response lies on the lowest amplitude limit cycle (if more than one limit cycles exist).

3.7 Chaotic behaviour

To begin to investigate the reasons why chaotic motion occurs in aeroelastic systems, consider the Hancock wing with freeplay in the wing pitch degree of freedom. In the absence of a continuous restoring force in the freeplay region, it is evident that $\theta = 0$ (see equation A) becomes an unstable equilibrium point. If the stiffness outside the freeplay region is high enough to prevent divergence, the points $\theta = \pm\delta$ become stable equilibrium points, since the stiffness is driving the wing towards them from outside the freeplay region and the lift from inside it. Hence, the system changes to a double-well potential type of problem. A direct consequence of this fact is the existence of many possible limit cycles centering around any of the three equilibrium points, a few of which are shown in figure 3.32.

A further consequence is the existence of regions in parameter-space where the behaviour is chaotic. The double-well potential problem has been identified as a paradigm for chaotic behaviour of simple deterministic systems, as demonstrated in reference [44]. In short, if the momentum in the motion is such that it brings the wing near the edges of the freeplay region often, the system cannot decide which point it is going to limit cycle around and, as a result, its oscillations jump from the $+\delta$ to the $-\delta$ positions in an unpredictable fashion. These jumps are exactly the same with those reported in [38] and [46]. The authors of [38] attempted to explain them as the onset of flutter since, in their tests, the phenomenon occurs just prior to flutter. However, this is not a general case since it was found in this work that chaotic behaviour can be encountered in both stable limit cycles (narrow band chaos) as in figure 3.33 and decaying motions as in figure 3.34 (intermittent chaos), i.e. far away from the flutter speed. In fact the presence of the freeplay nonlinearity implies that there are two types of instability in the system. The first type is the standard classical flutter and the second is static divergence inside the freeplay region, caused by the fact that the stiffness inside

the freeplay region is zero. It is this second type of instability that causes the chaotic motion when combined with an aerodynamic instability.

Another effect which is closely associated with chaos is period doubling, which has been identified as a route to chaos, a transitional effect [44], [52]. Period doubling occurs when, by systematic variations in the value of a control parameter, (in the aeroelastic case, it is usually the free stream airspeed) the number of harmonic component motions (and their period) in a certain limit cycle doubles with each variation. After a certain amount of increases in the number of periods, the behaviour becomes chaotic. This type of behaviour was encountered in the response of the Hancock wing with control surface model (as shown in figure 3.35, where each loop in the phase-plane is a component motion) and was also reported in [38].

The analysis presented above does not explain the occurance of chaos in every aeroelastic system. The Hancock wing with freeplay in the control surface pitch system will not become a double-well-potential-type problem. It will still exhibit chaotic behaviour though, as seen in section 3.5. Furthermore, the chaotic region lies at lower speeds than the divergence speed of the inner linear system. This behaviour is explained in terms of *inverse* period doubling. As mentioned in [9], there exist period doubling routes to chaos in the direction of both increasing and decreasing airspeed. The bifurcation diagram of figure 3.23 demonstrates this fact. Whether the period-doubling route will be in the increasing or decreasing airspeed direction depends on the type and position of the nonlinearity in the system.

3.7.1 Indicators and proof of chaotic response

The proof of chaos itself is a very delicate process. Moon [44] identifies two indicators of chaos and one rigorous proof. These are

Chaos indicators

- A large number of apparently random peaks in the spectrum of the response of a system.
- Fractal structure of the Poincaré diagram.

Rigorous proof of chaos

- Positive Lyapunov exponents

The first indicator is the least rigorous one. The peaks have to lie within a wide frequency band and have a wide range of amplitudes. This phenomenon, though, can also be observed in laminar (non-chaotic) systems as well as in systems whose measured response contains high levels of noise. Hence, this indicator should not be used on its own.

A Poincaré plot is a phase-plane plot where only sampled points of velocity vs displacement are plotted. As such, any phase-plane plot is a Poincaré plot since the points plotted, whether experimental or numerical, are always sampled. However, if all the points sampled from a chaotic response are included in the diagram, the result is an amorphous mass of points. If only points selected according to a certain criterion are plotted then the result is a so-called *strange attractor* (to distinguish it from sources, sinks, saddle points, limit cycles and other normal attractors) whose main characteristic is fractal structure, i.e. that it keeps the same essential structure at any magnification of the plot. For a single dof system, the simplest criterion by which the points to be included in the diagram are selected is to plot the system's displacement vs velocity every time the phase of the excitation signal assumes a given value [44]. For a non-chaotic system undergoing a period-1 limit cycle the result is one single point, for a period-2 limit cycle two points and so forth. The Poincaré diagram of a system undergoing chaotic oscillations is a fractal strange attractor. The selection

criterion for multi-dof systems is more complicated than that for single-dof. Moon suggests to sample each mode at a vastly different sampling frequency. This procedure however, has only been validated for 2-dof systems and only when the system is experimental. In the case of a mathematical model, sampling at frequencies which differ by orders of magnitude poses significant problems of numerical stability. Reference [42] suggests a much simpler and more effective sampling criterion. One of the displacements or velocities of one of the degrees of freedom is plotted when the displacement of another degree of freedom is zero. Figure 3.36 shows a strange attractor obtained from the chaotic response of the Hancock wing with freeplay stiffness in the control surface using this criterion, in this case β vs $\dot{\beta}$ was plotted when $\gamma = 0$. Figure 3.37 is a Poincaré diagram of θ vs $\dot{\theta}$ for the same system when $\gamma = 0$. Fractal structure of the Poincaré diagram is not a rigorous proof of chaos, however, since there are no known laminar systems that will display fractal structure, it is considered a very safe indicator.

Lyapunov exponents show how fast nearby orbits in phase-space converge or diverge [53]. An orbit in phase-space describes a system's evolution from time zero (when all the state variables of the system have their initial conditions) to time t when the data sequence stops. For example, figure 3.38 shows the time domain variation and phase-space orbit of a system undergoing a limit cycle oscillation but whose initial conditions lie outside the limit cycle in the phase plane. Orbits 1 and 2 in figure 3.38 show the evolution of the system from very similar initial conditions. The two orbits are very close together and merge on the limit cycle. This would not happen in the case of a system undergoing chaotic oscillations. Instead, the two orbits would diverge very quickly. For any system, the existence of a positive Lyapunov exponent denotes rapid divergence of initially close orbits and, hence, chaotic motion. Lyapunov exponents can also detect the existence of any type of attractor, from limit cycles to strange attractors but

without providing any quantitative details on these attractors and, hence, their use in nonlinear system analysis is limited to the detection of chaos. Reference [53] details numerical methods for obtaining Lyapunov exponents both from the equations of motion of a system and from measured time data. It has been pointed out though [28], that these methods fail in the presence of non-analytic nonlinear functions such as bilinear or freeplay stiffness. The algorithm included in [53] was used on the Hancock model with cubic stiffness in the control surface pitch to prove that the system for which the Poincaré diagram is shown in figures 3.36 and 3.37 is indeed chaotic.

3.7.2 The relevance of chaotic motions in aeroelastic systems

Chaotic response is the least worrying of all nonlinear phenomena associated with aeroelastic systems. Even though there is ample evidence that chaos can appear in aeroelastic mathematical and wind tunnel models, it has not been reported in practical aeroelastic applications (at least not to this author's knowledge). In fact, early reports of chaotic motion in wind tunnel models ([40] and [41]) were not accompanied by rigorous attempts to prove chaos. Instead, only the multiple frequency and amplitude criterion was used. In a more recent paper [48] where the possibility of chaotic motions in wind tunnel tests of a simple wing was reported, it was found that the Poincaré diagrams did not depict strange attractors but amorphous blobs, consistent with the existence of high levels of noise.

As such, it could be argued that chaos in aeroelastic systems is much more of a mathematical phenomenon, occurring during integrations of the equations of motion, than a physical one. However, on an academic level and for the sake of completeness, studies of nonlinear systems usually include a certain level of chaotic analysis, if only to indicate the fact that chaos is very rarely of serious

concern.

3.8 Figures

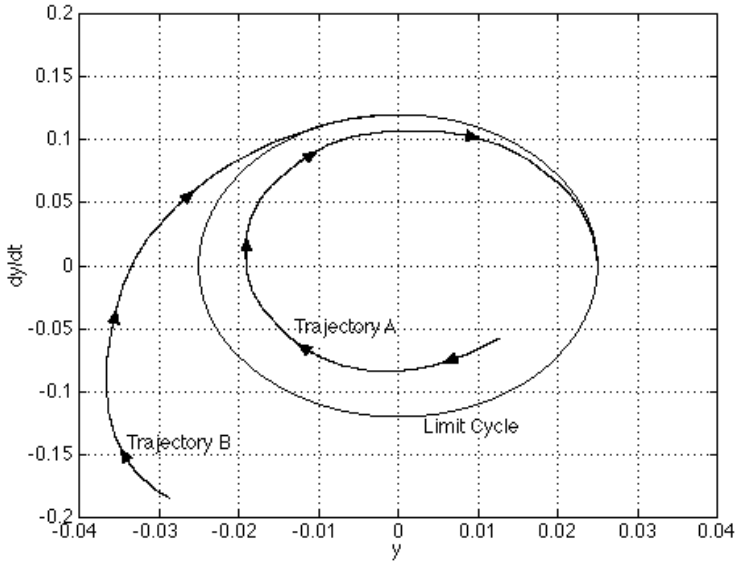

Figure 3.1: Stable limit cycle

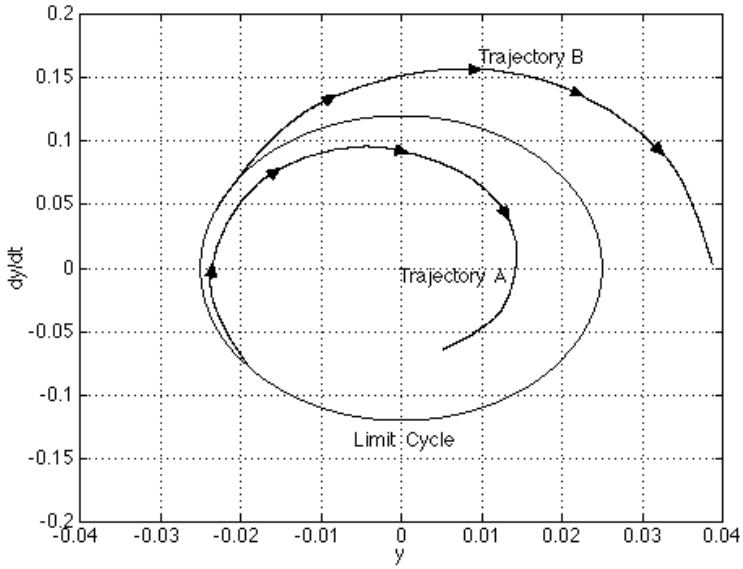

Figure 3.2: Unstable limit cycle

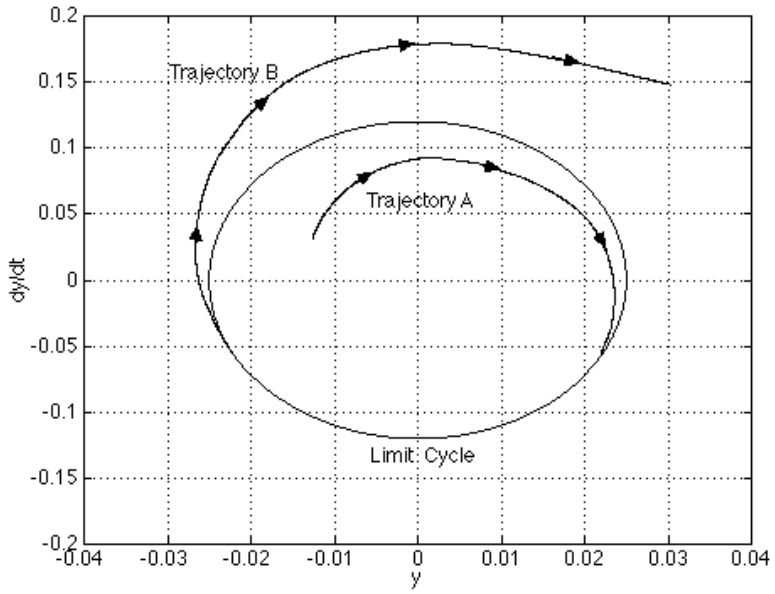

Figure 3.3: Half-stable limit cycle

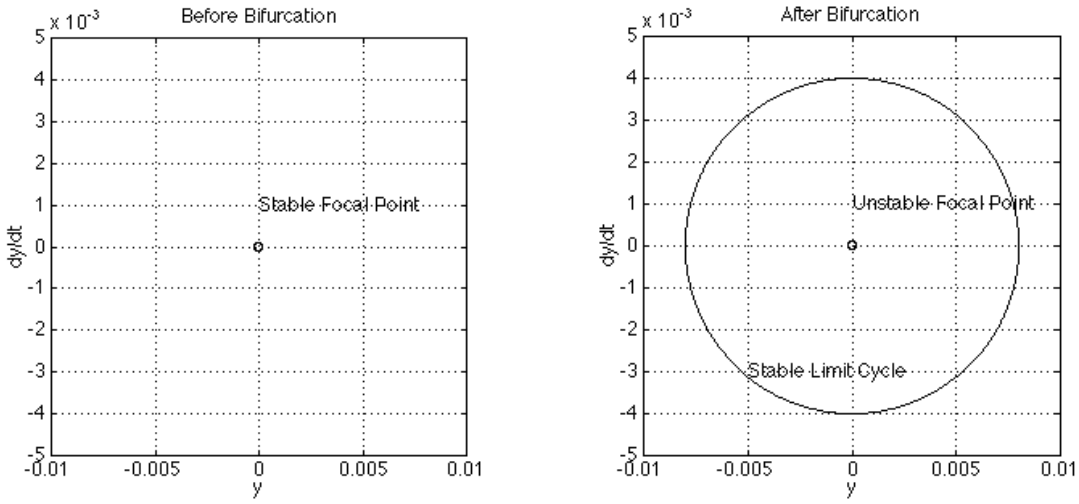

Figure 3.4: Bifurcation to soft self-excitation

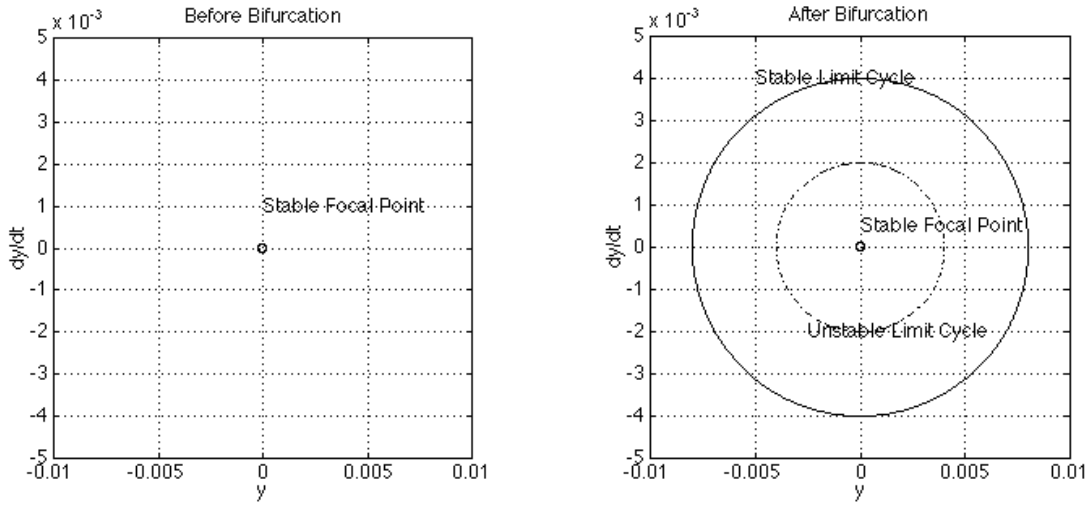

Figure 3.5: Bifurcation to hard self-excitation

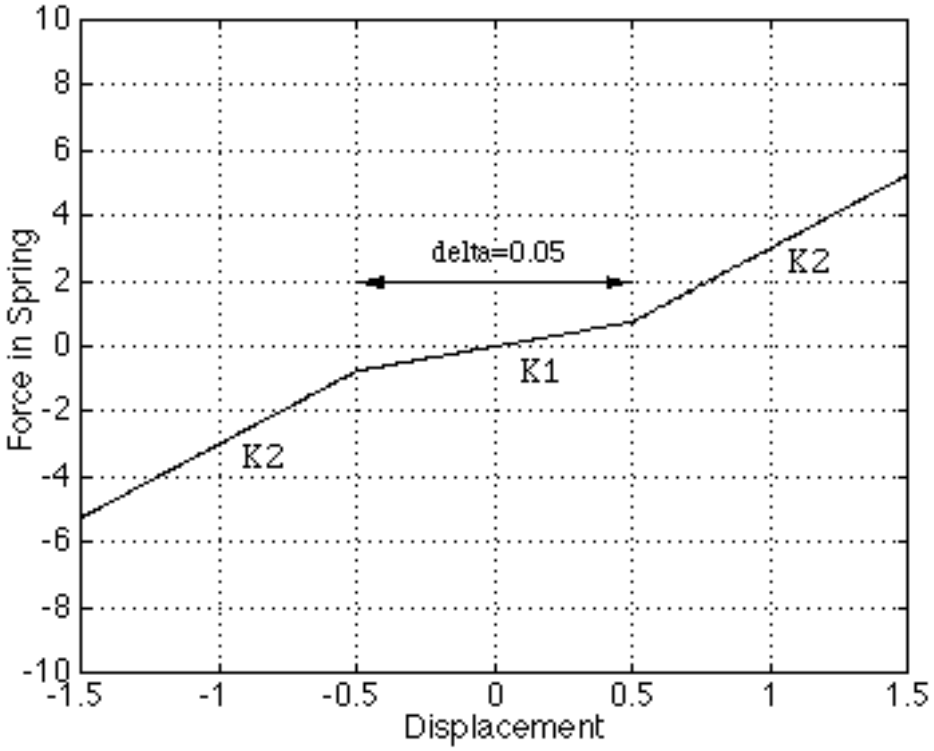

Figure 3.6: Bilinear stiffness versus displacement

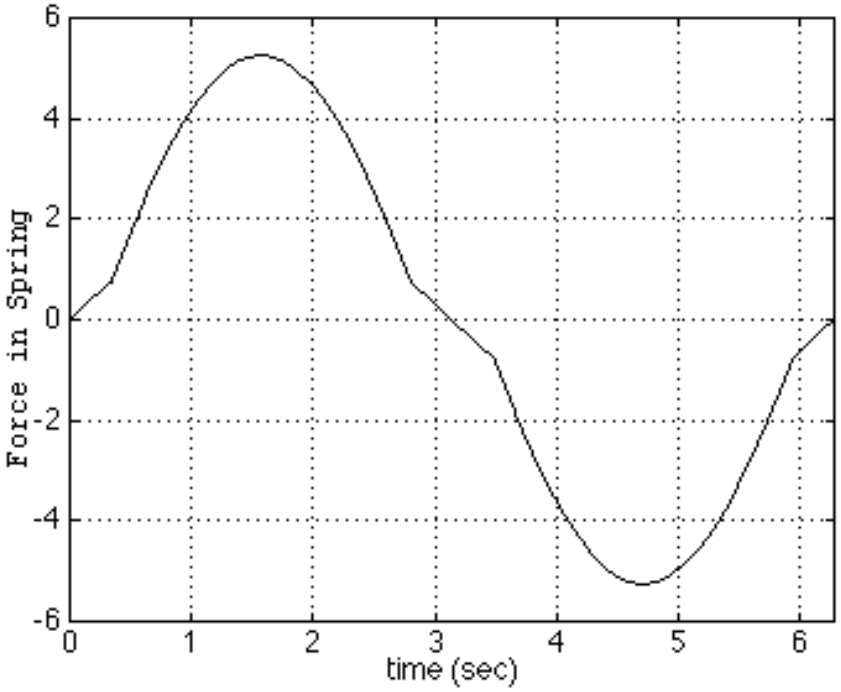

Figure 3.7: Bilinear stiffness vs time

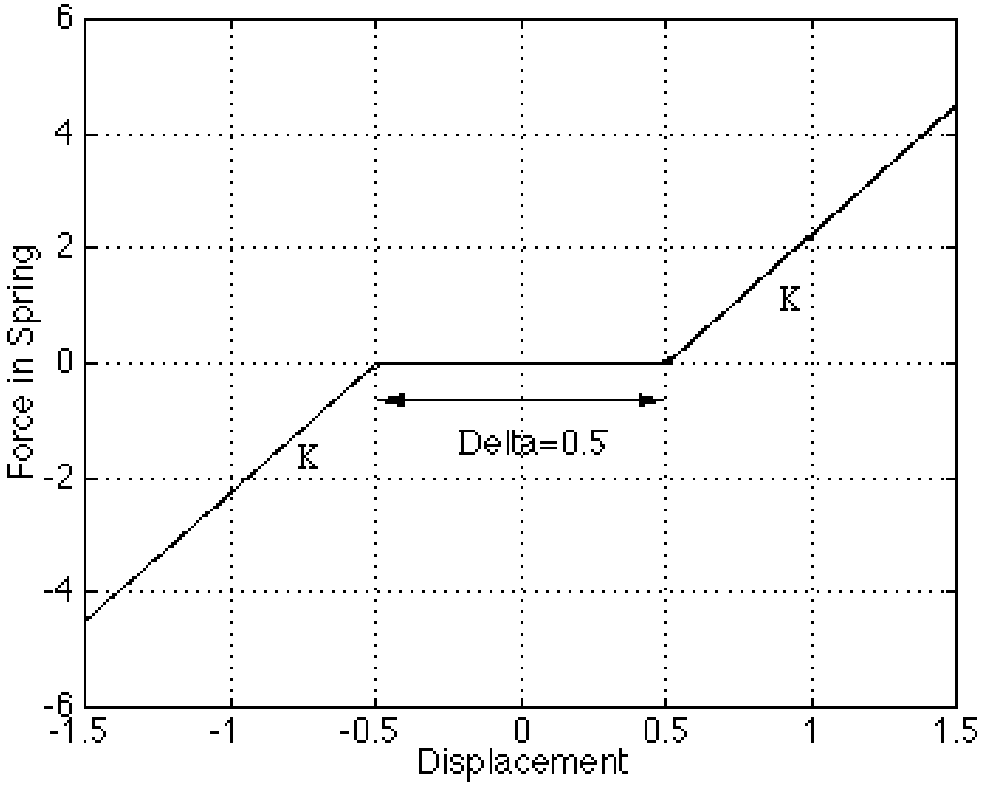

Figure 3.8: Freeplay stiffness versus displacement

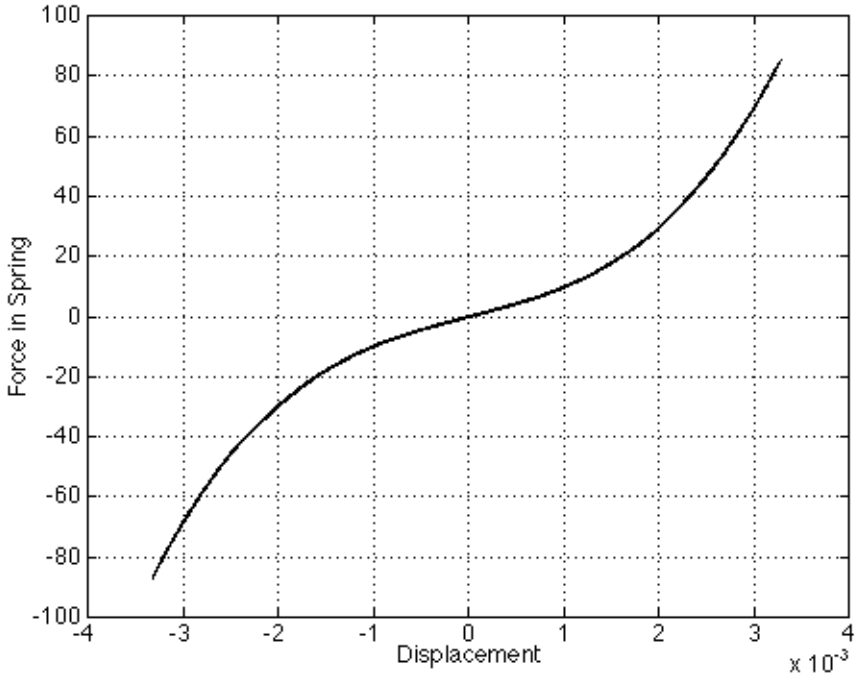

Figure 3.9: Cubic stiffness versus displacement

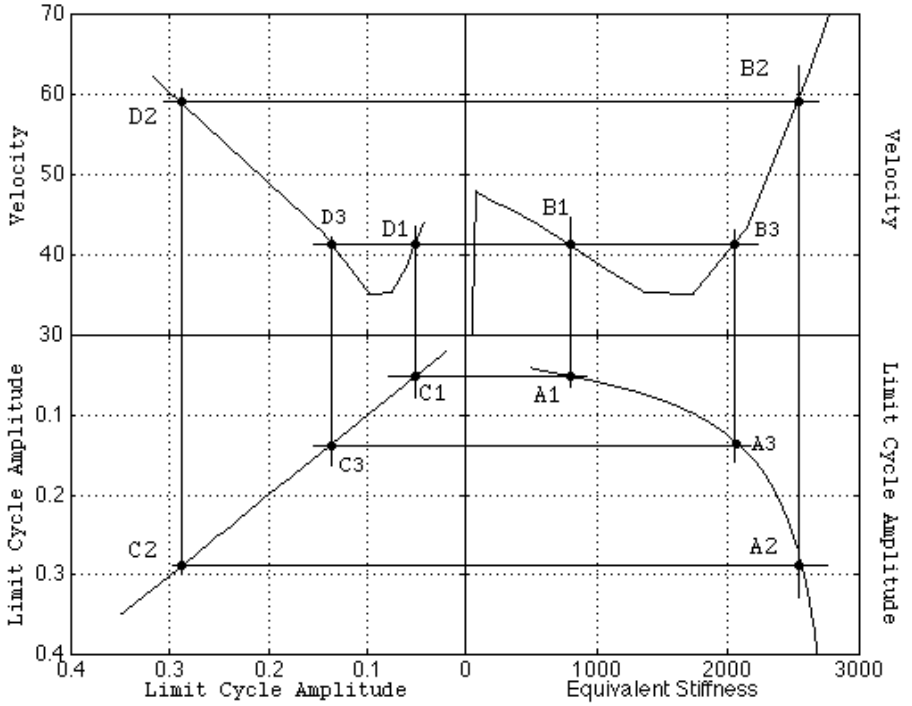

Figure 3.10: Harmonic balance scheme

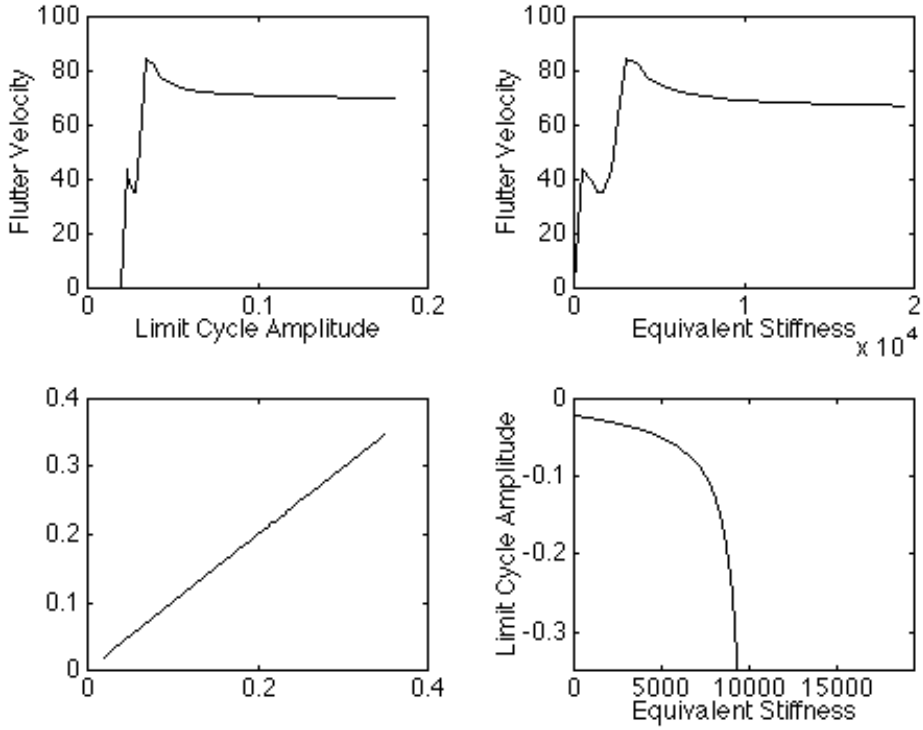

Figure 3.11: Harmonic balance scheme for freeplay in wing pitch spring

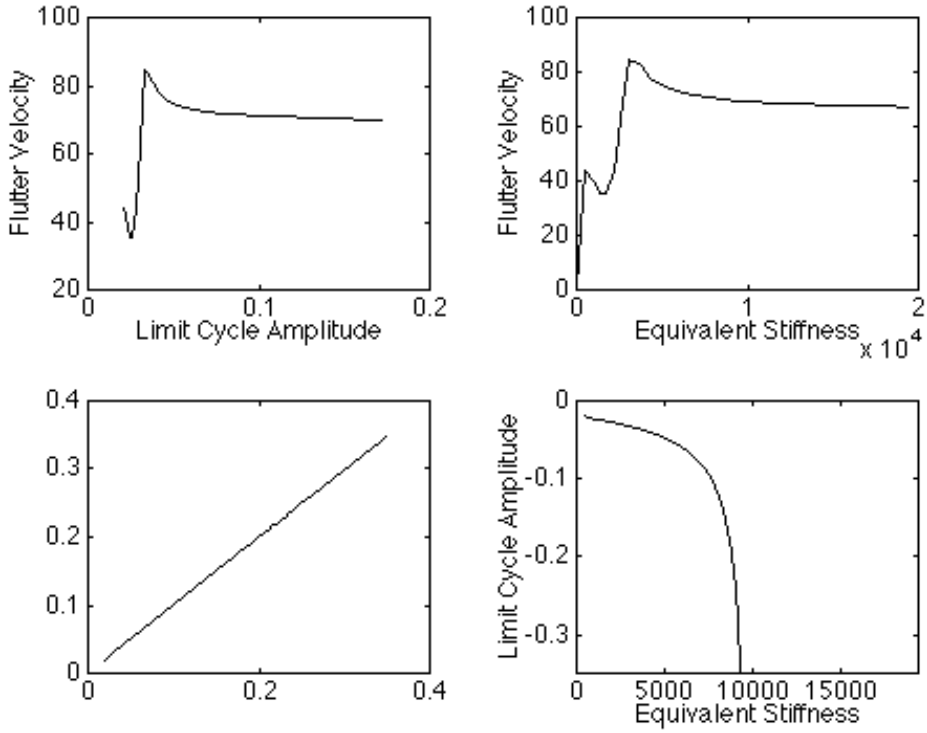

Figure 3.12: Harmonic balance scheme for bilinear wing pitch spring

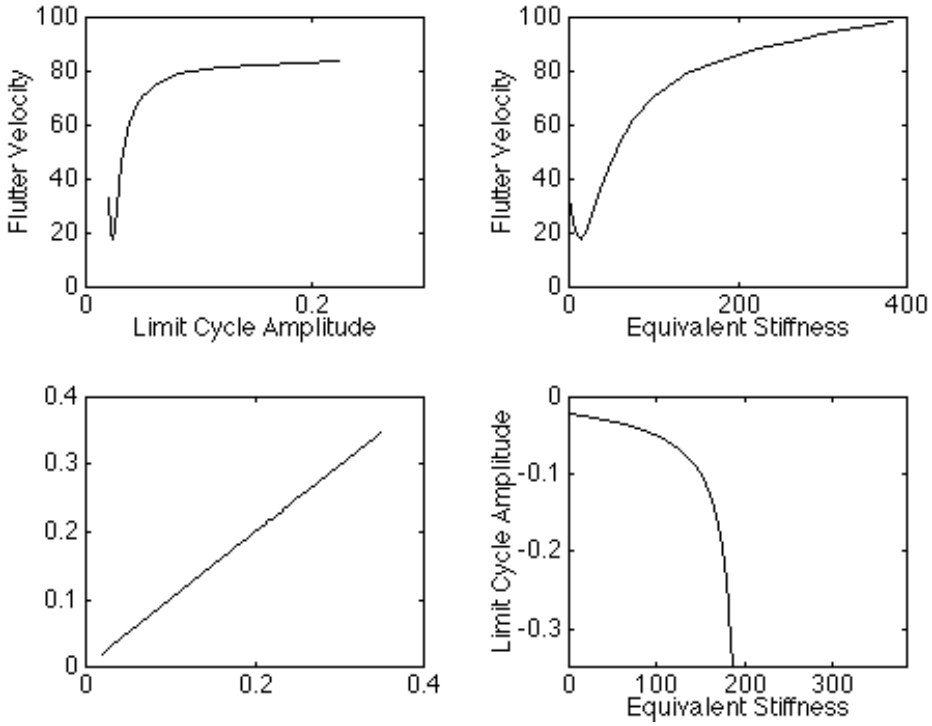

Figure 3.13: Harmonic balance scheme for freeplay in control surface pitch spring

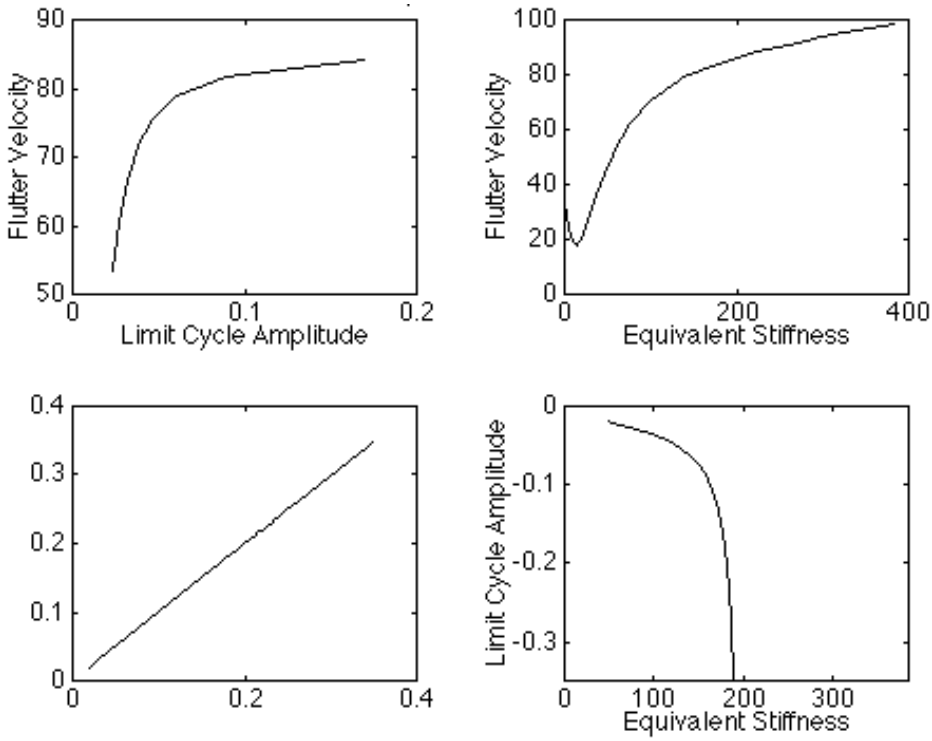

Figure 3.14: Harmonic balance scheme for bilinear control surface pitch spring

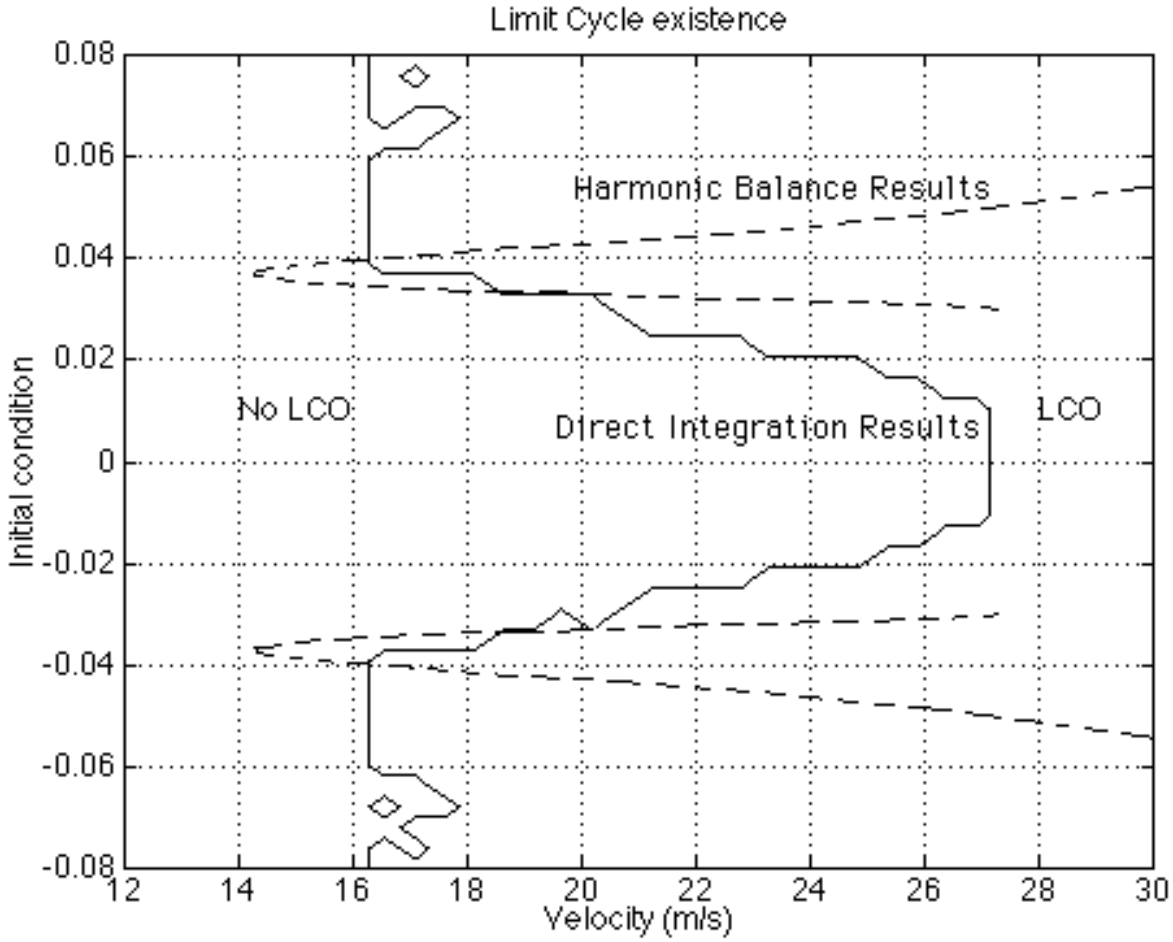

Figure 3.15: 2-D Parameter-Space section with Harmonic Balance results

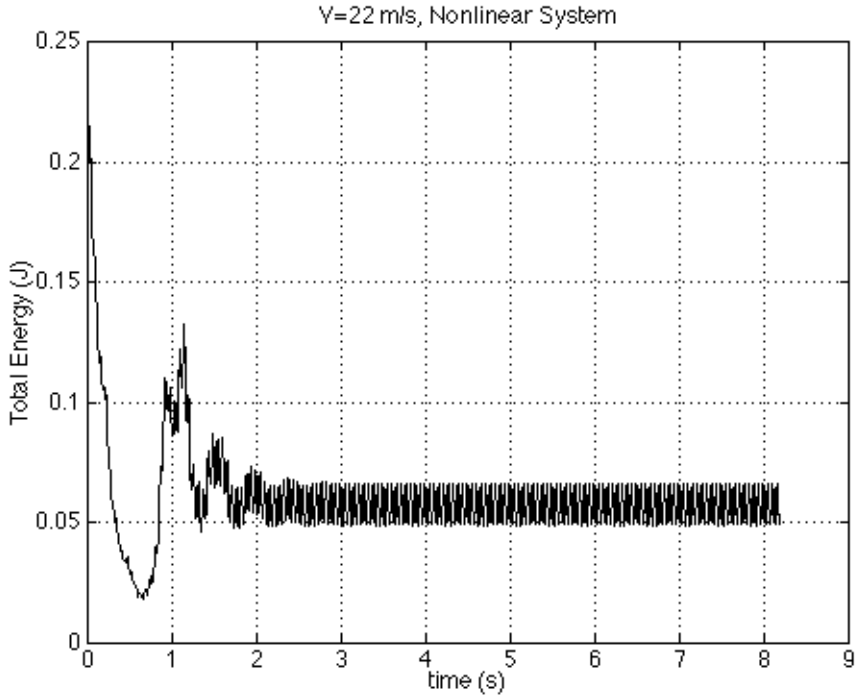

Figure 3.16: Total energy variation with time for nonlinear system during LCO

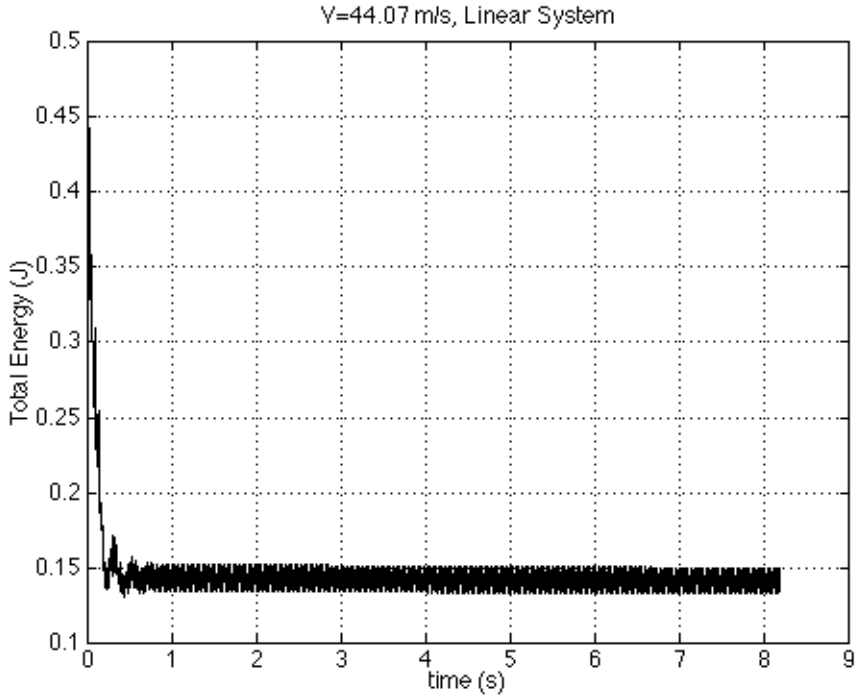

Figure 3.17: Total energy variation with time for linear system during flutter

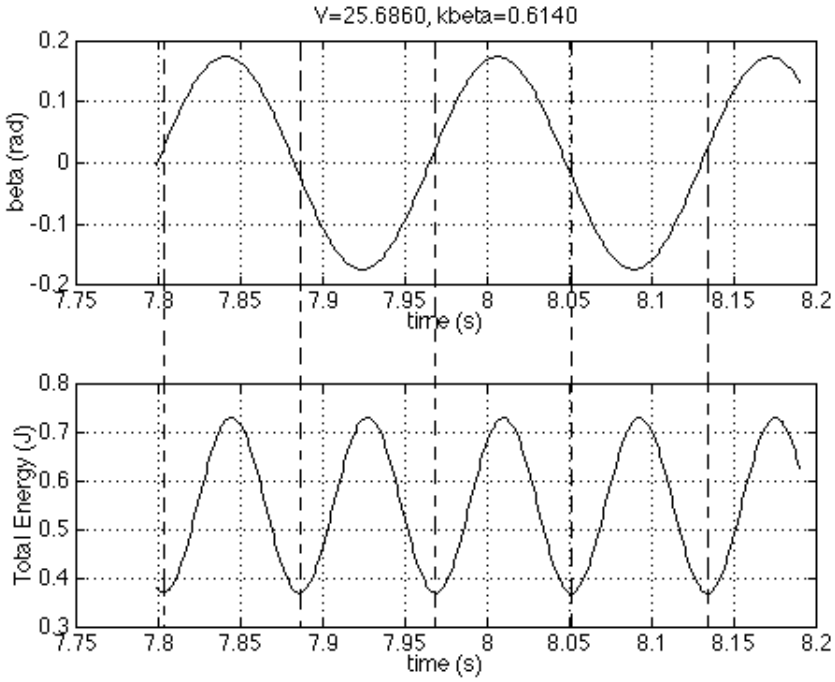

Figure 3.18: Comparison of response and total energy variation for equivalent linearized system, low amplitude

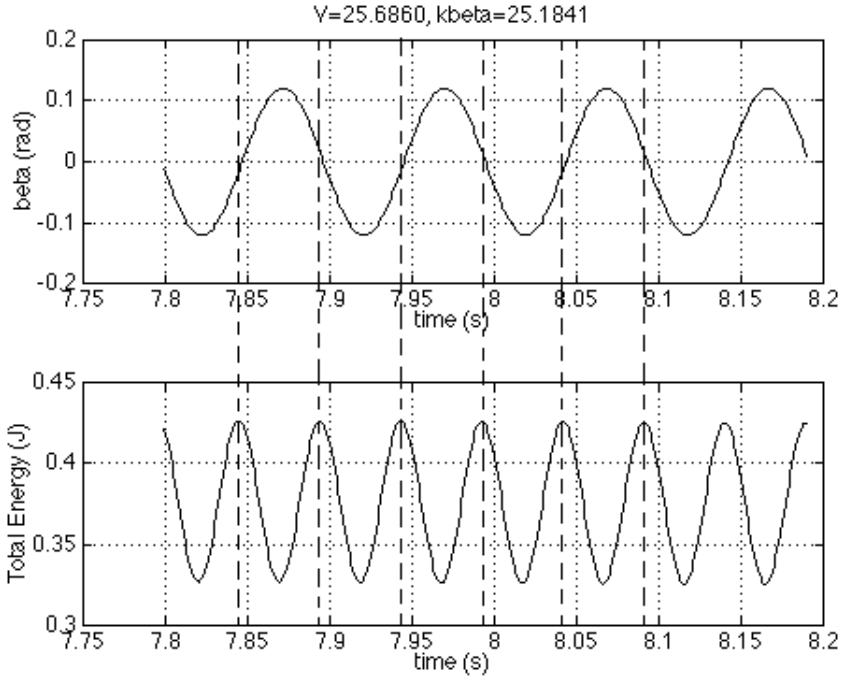

Figure 3.19: Comparison of response and total energy variation for equivalent linearized system, high amplitude

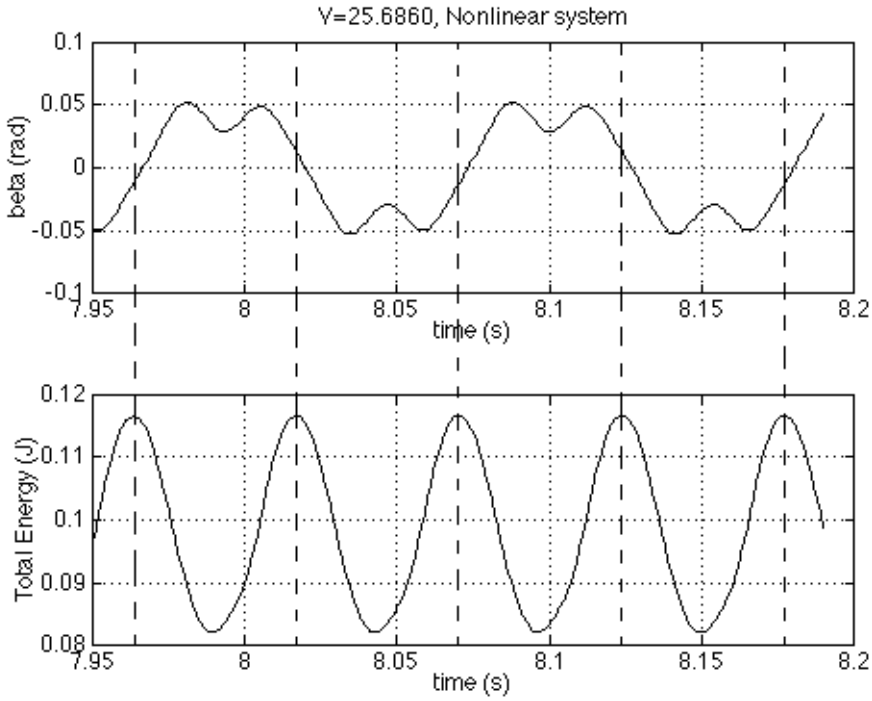

Figure 3.20: Comparison of response and total energy variation for nonlinear system, stable LCO

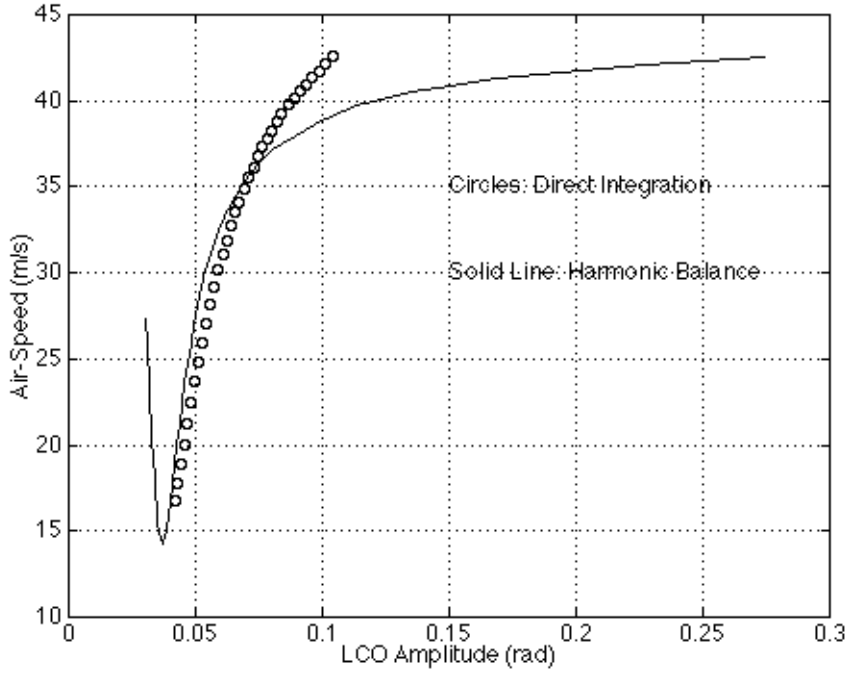

Figure 3.21: LCO Amplitude vs air-speed by Harmonic Balance and Integration

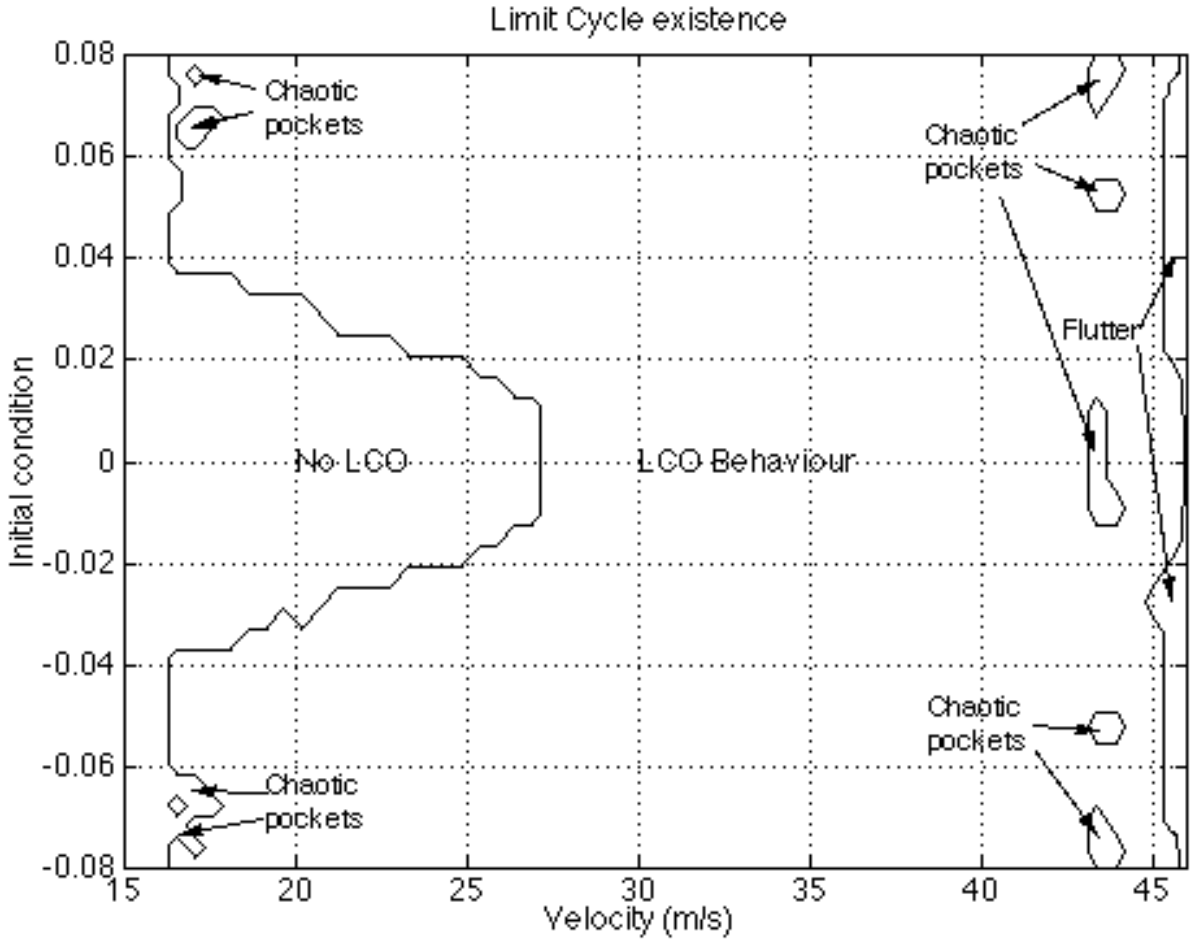

Figure 3.22: 2-D Parameter-Space section

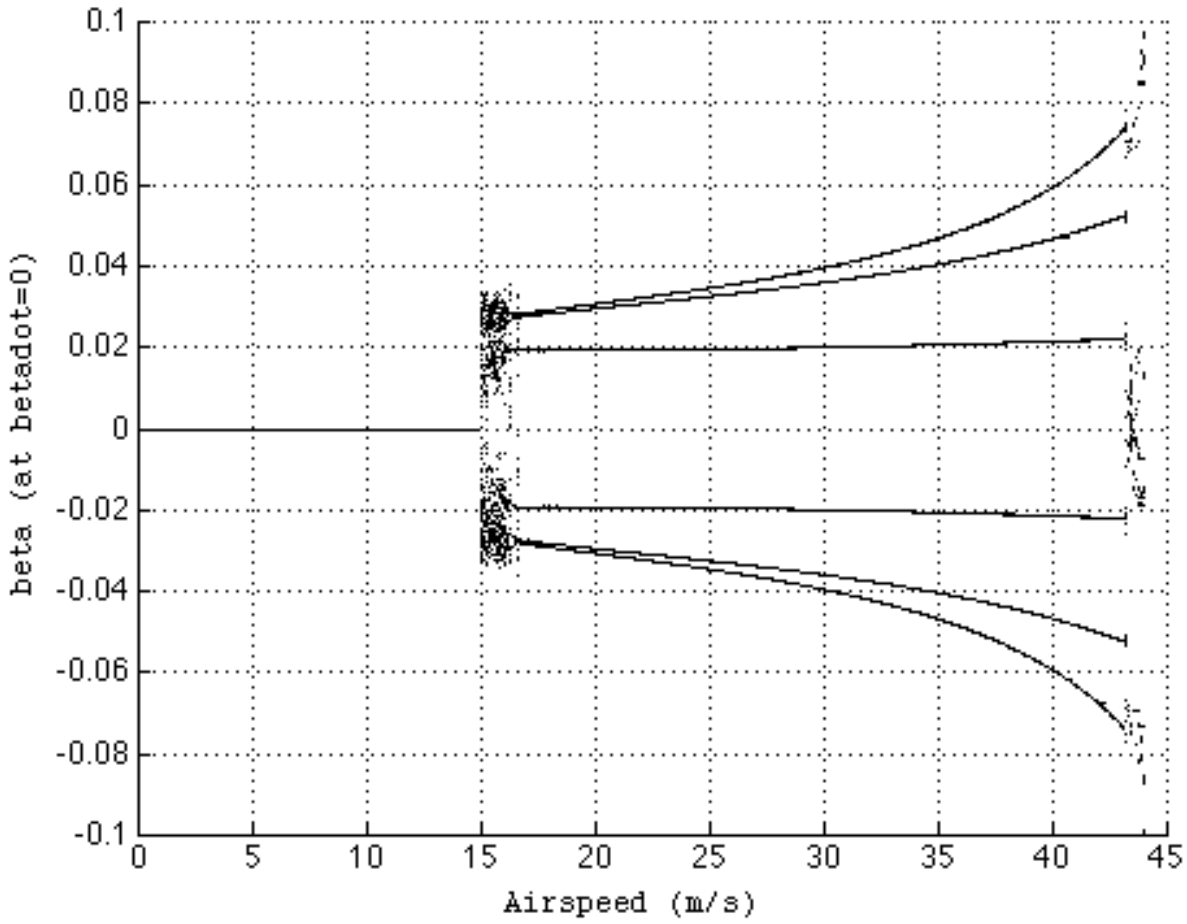

Figure 3.23: 2-D Parameter-Space section

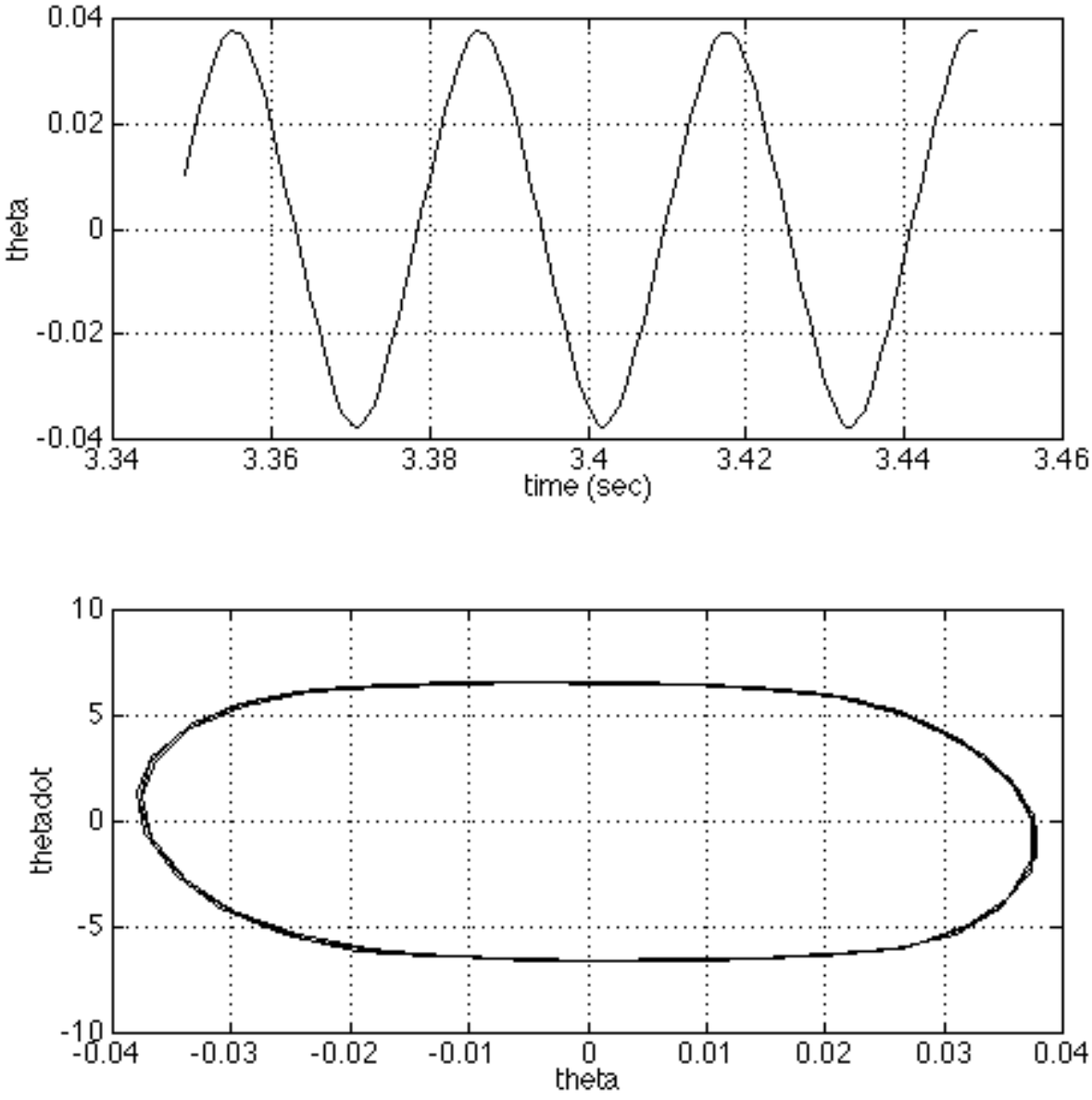

Figure 3.24: Period-1 Limit Cycle (time domain and phase plane)

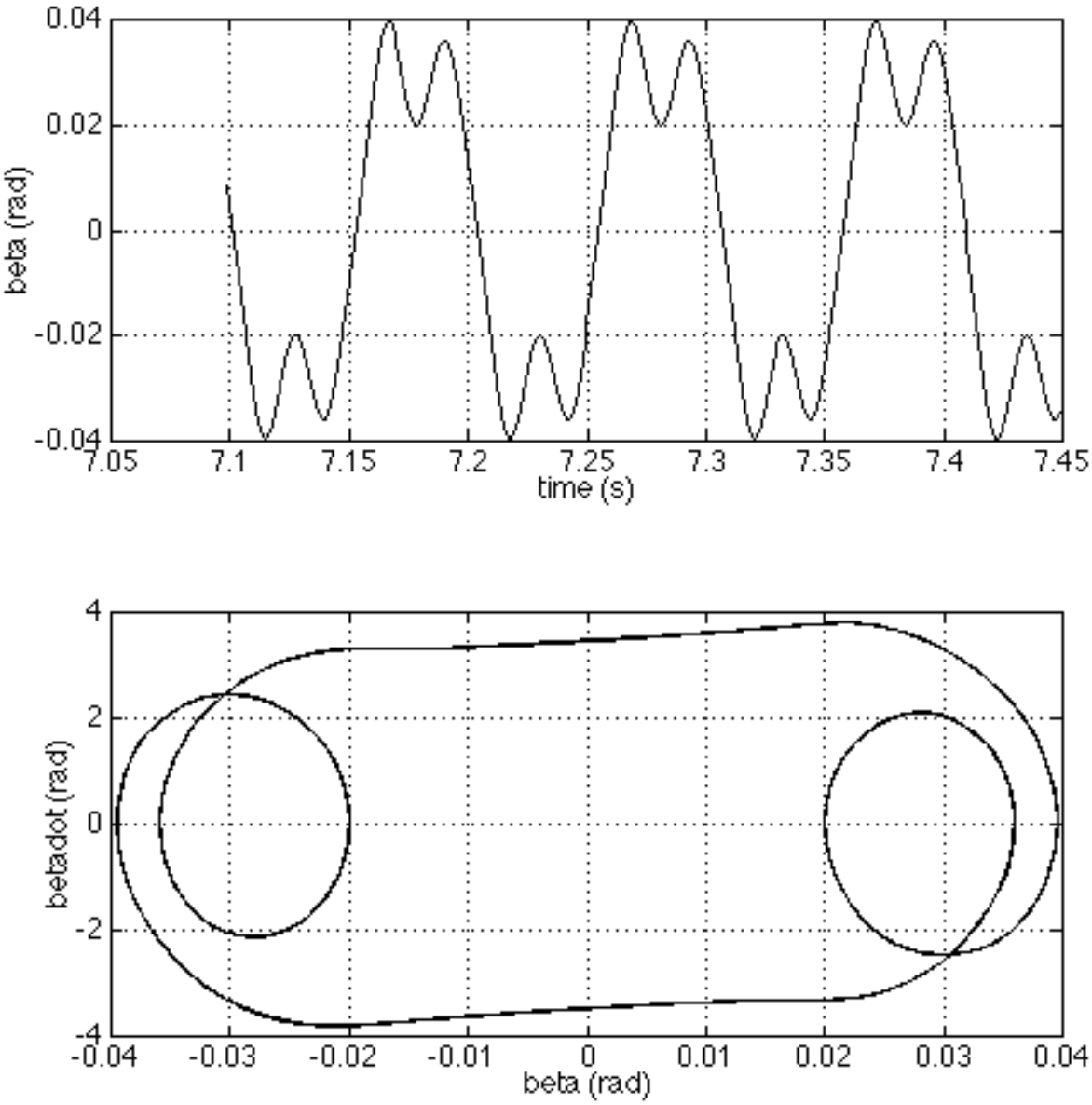

Figure 3.25: Period-2 Limit Cycle (time domain and phase plane)

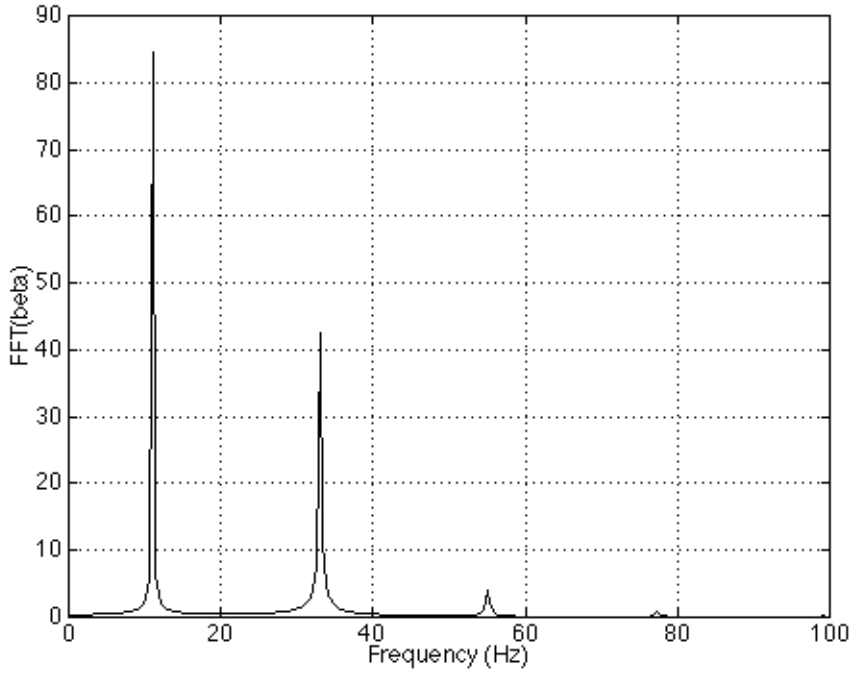

Figure 3.26: Frequency domain representation of response near flutter

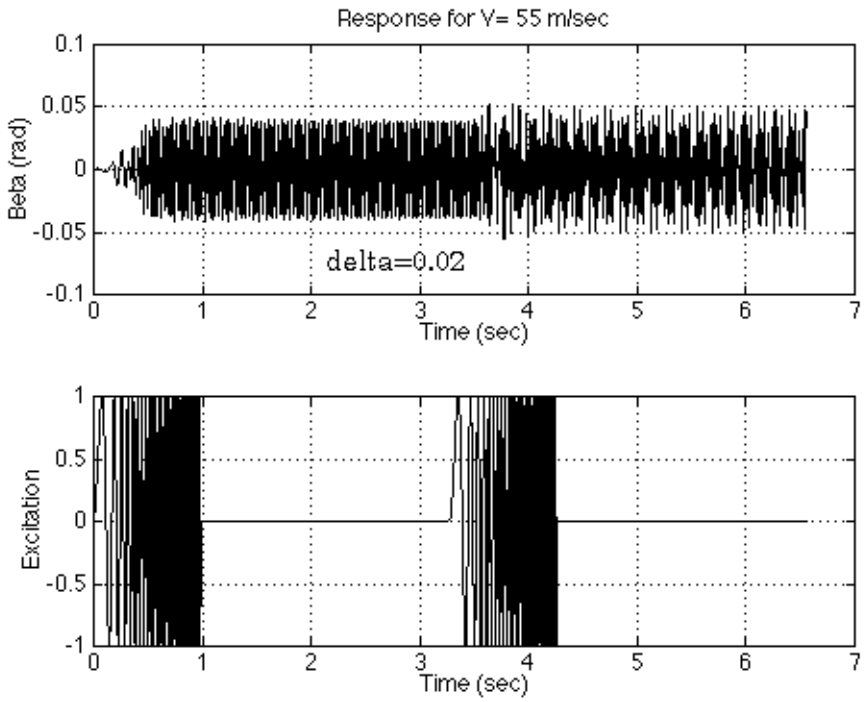

Figure 3.27: Jump from one limit cycle to another after second application of excitation

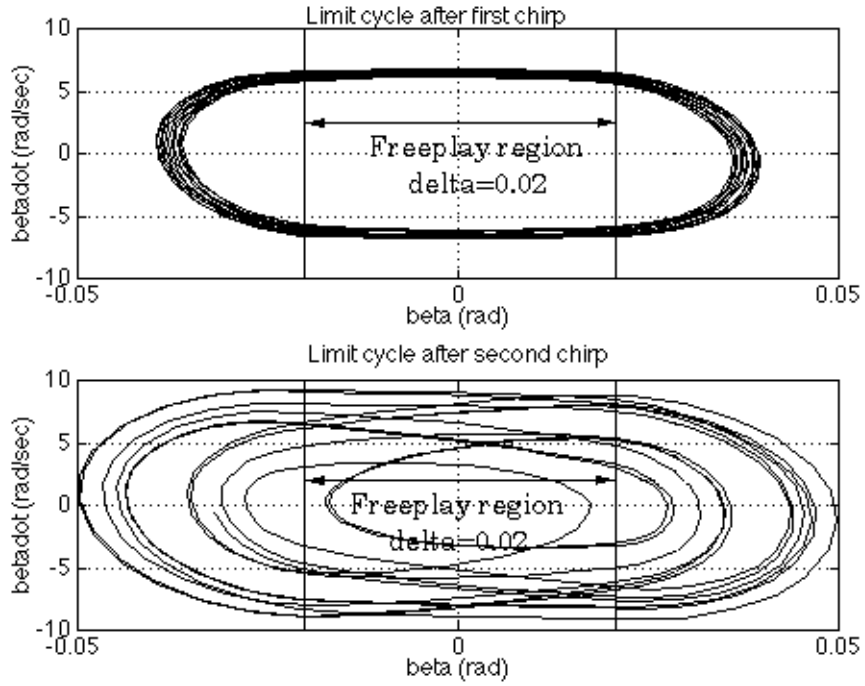

Figure 3.28: Initial and final limit cycles

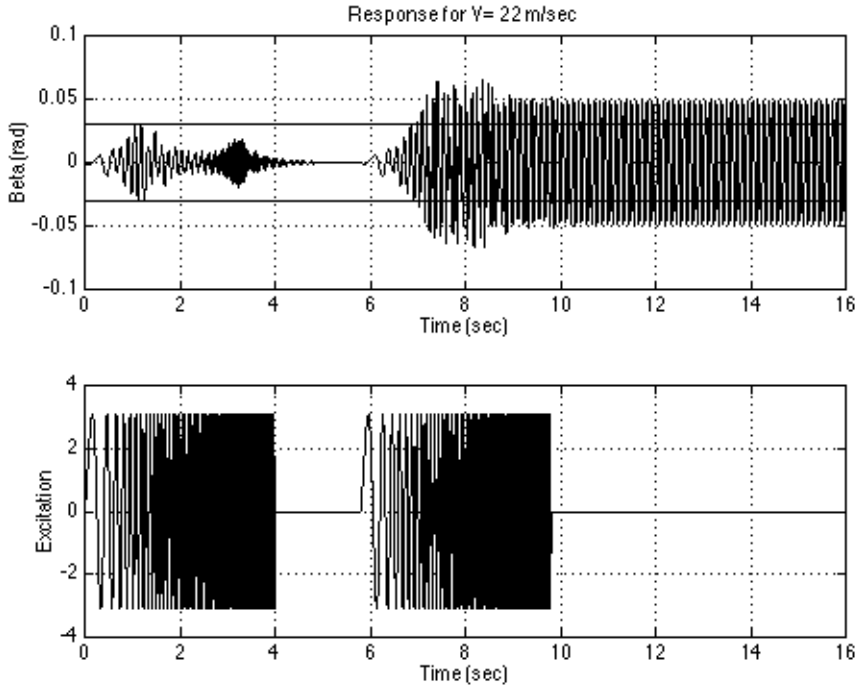

Figure 3.29: Jump from decaying response to LCO after second application of excitation

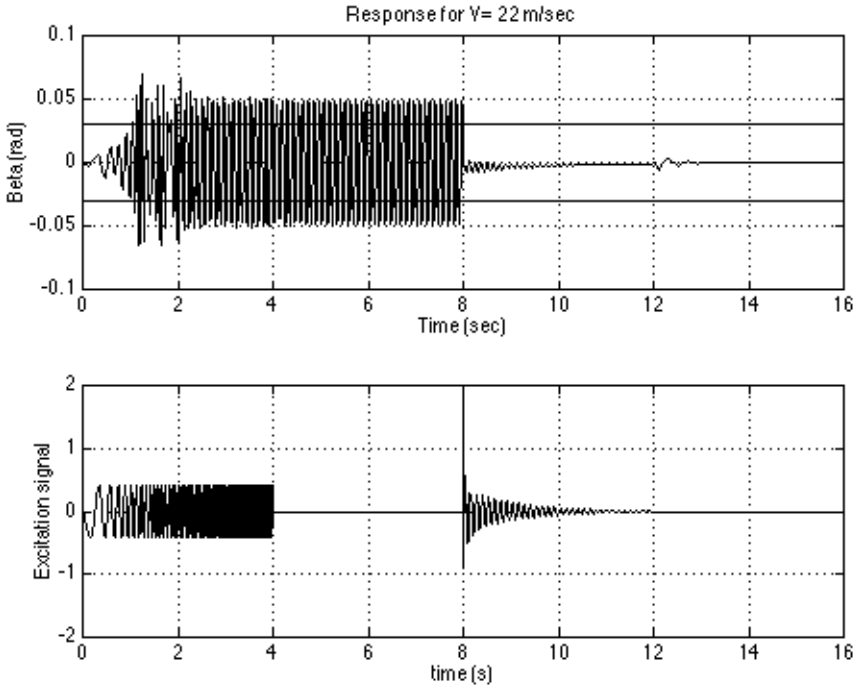

Figure 3.30: LCO suppression by feedback excitation signal

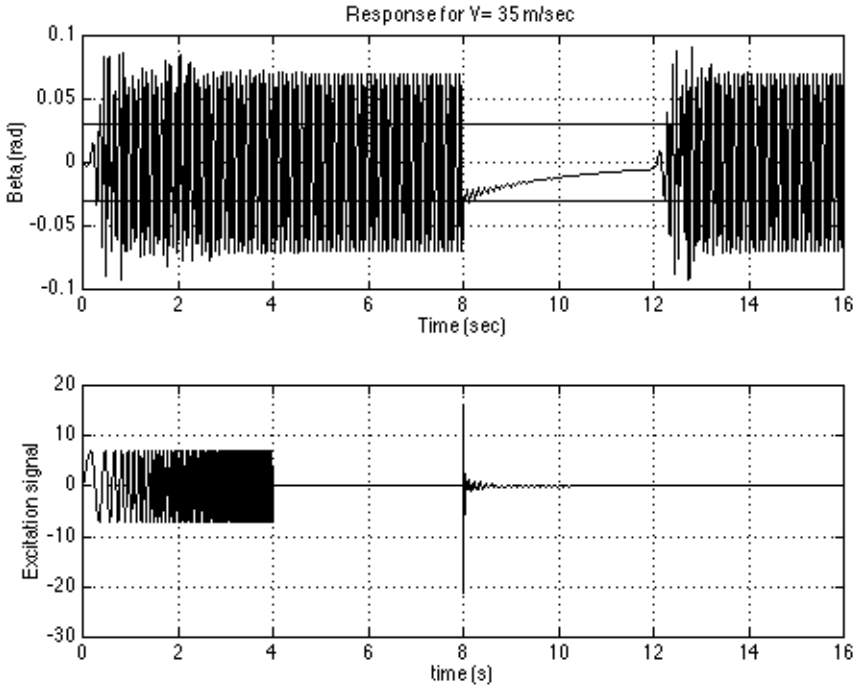

Figure 3.31: Failure of LCO suppression for system in soft self-excitation conditions

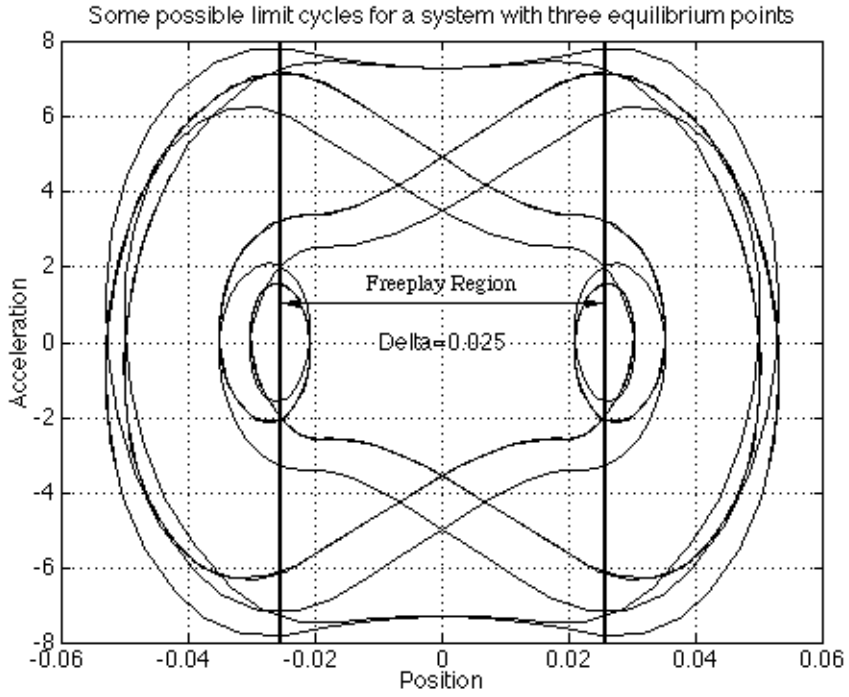

Figure 3.32: Possible limit cycles in phase-plane

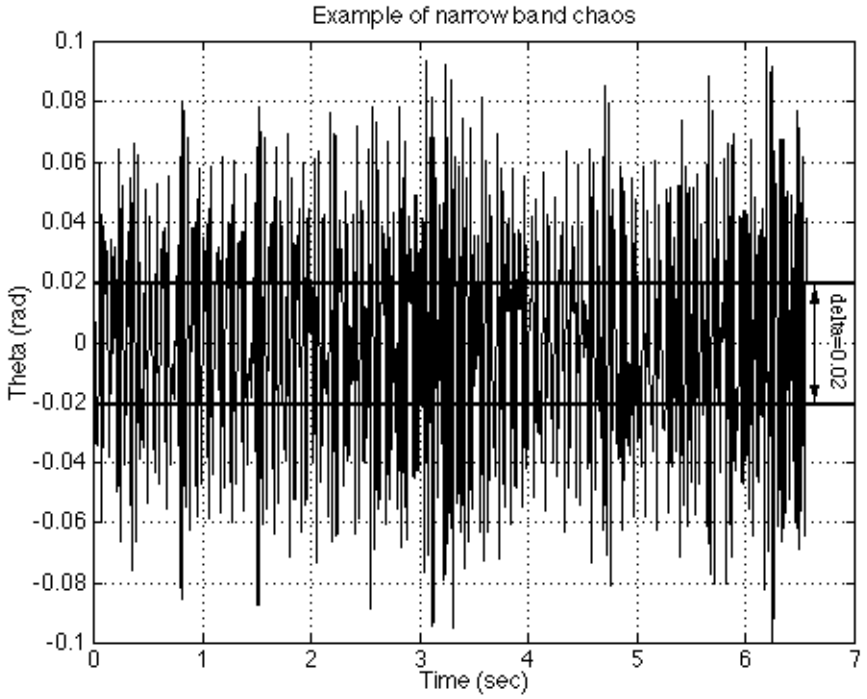

Figure 3.33: Narrow band chaos, wing pitch nonlinearity case

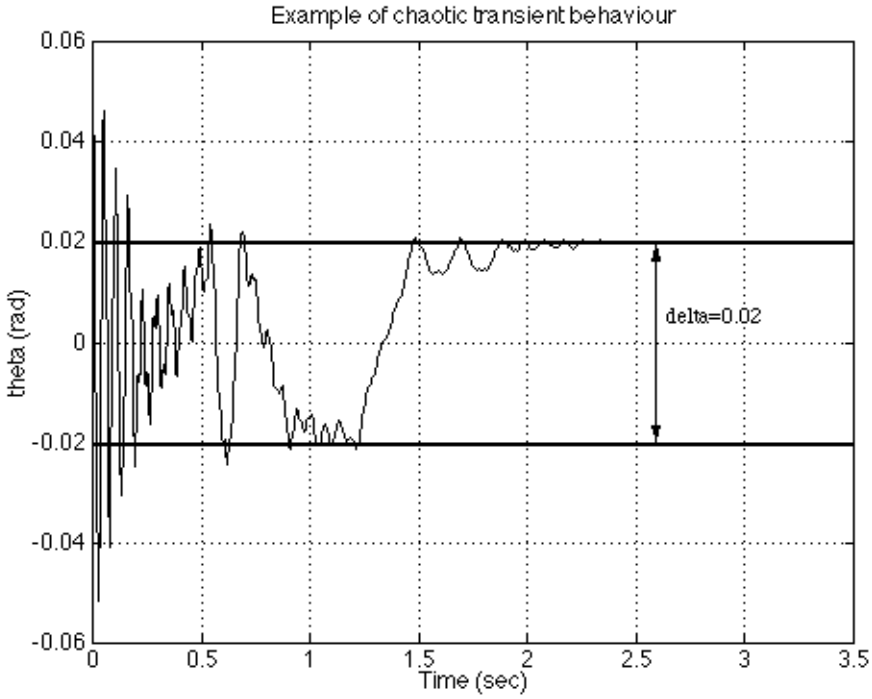

Figure 3.34: Intermittent chaos, wing pitch nonlinearity case

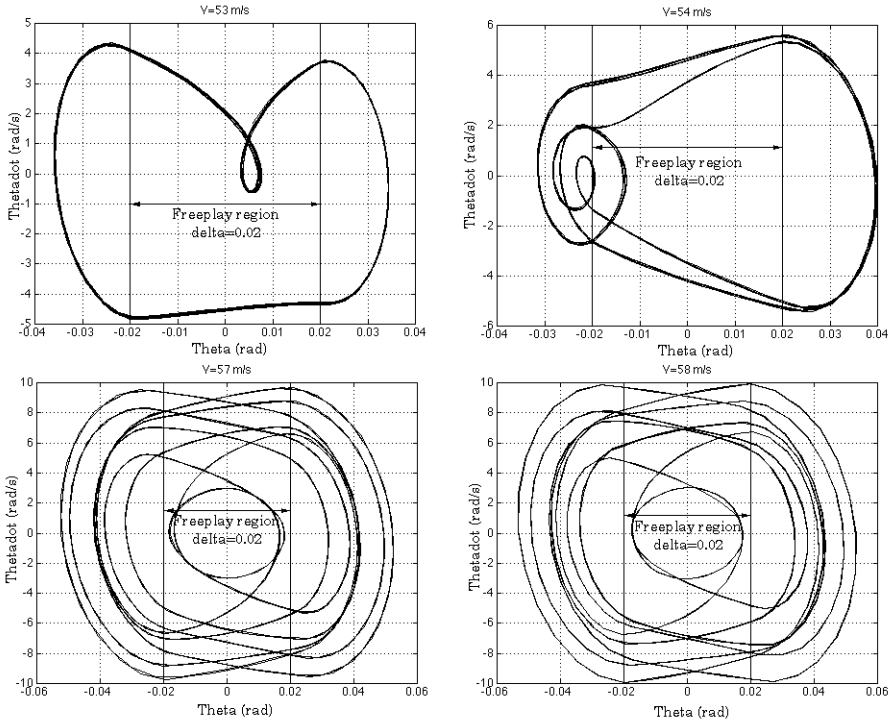

Figure 3.35: Progression of period doubling with increasing airspeed

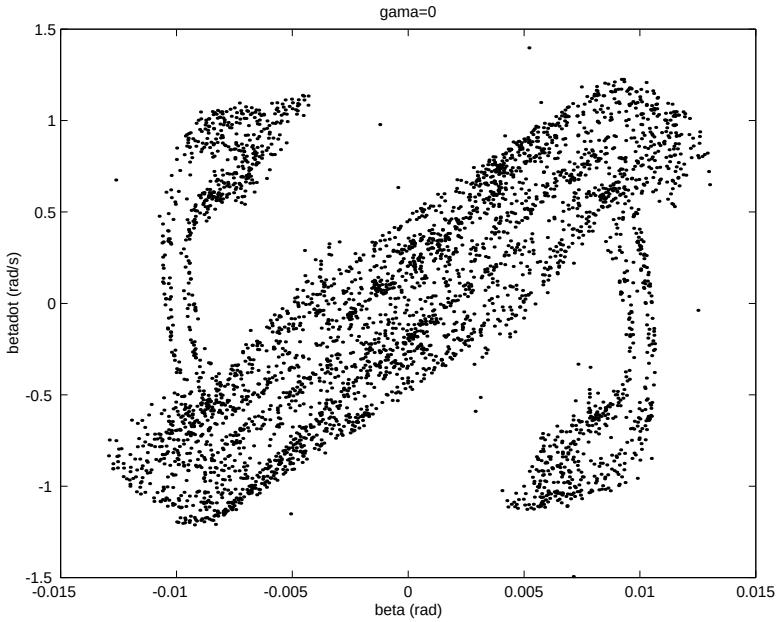

Figure 3.36: Poincaré diagram of β for $\gamma = 0$

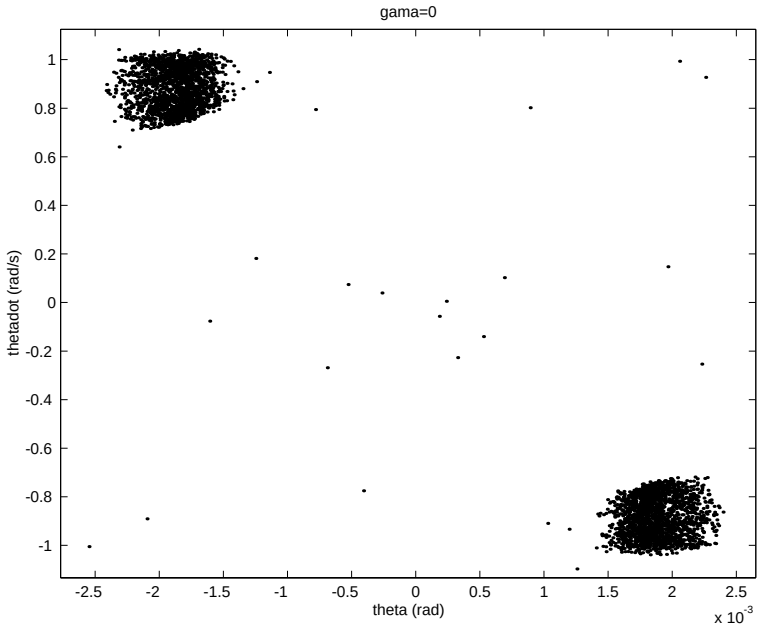

Figure 3.37: Poincaré diagram of θ for $\gamma = 0$

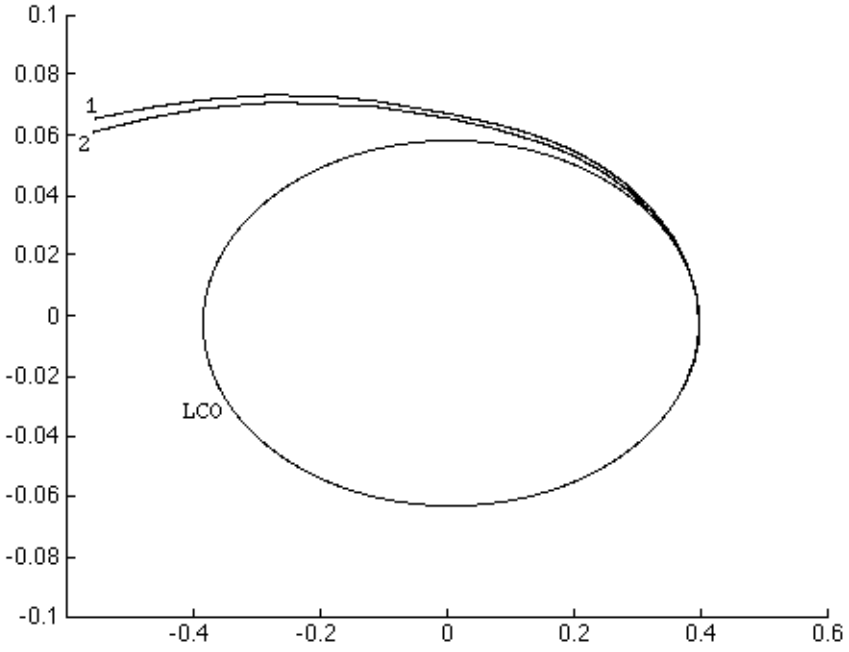

Figure 3.38: Evolution of close orbits in non-chaotic system

Chapter 4

Nonlinear System Identification Methods

4.1 Overview of Nonlinear System Identification

The use of system identification methods to identify frequencies, dampings and mode shapes is commonplace in the aerospace industry. Such methods are used to analyse ground vibration test data in order to validate finite element models, and also during flight flutter testing to track the stability of aircraft as the flight envelope is expanded. There is a vast literature related to the identification of linear systems and a wide range of methods have been implemented in the aerospace field. However, the identification of systems that contain non-linearities is not yet at a stage where an accurate model of a real full-sized structure, e.g. an aircraft, could be estimated.

There already exist methods like the NARMAX model [54] [55], higher order spectra [56] and the restoring force method which can identify nonlinear aeroelastic systems given the inputs and outputs. However, these methods have still not

reached the level of maturity necessary to allow their application to general aeroelastic systems. Both NARMAX and the higher order spectra method are very inefficient when it comes to identifying systems with discontinuous nonlinearities, such as bilinear stiffness or freeplay, which are common in aeroelastic systems. The restoring force method does not share this limitation, but its application to multi degree of freedom systems is still problematic.

A further consideration that must be taken into account is whether the identification process is parametric. The analysis of an identified system is much simpler when the terms in the model resulting from the identification process are parametric, i.e. model explicitly the non-linearities present in the system. However, both NARMAX and the restoring force method yield better results when using non-parametric as well as parametric terms. Hence the resulting model contains terms without any physical meaning.

The effects of structural, aerodynamic and, in particular, control system nonlinearities upon the aeroelastic behaviour of aircraft is becoming of increasing concern. Recent emphasis has been devoted to the study and prediction of limit cycle oscillations (LCO). Although unsteady computational fluid dynamics (CFD) codes are being developed to model non-linear aeroelastic behaviour, their efficient use is a long way off, and for the foreseeable future there will be a requirement to estimate the parameters of non-linear systems.

This part of the work examines one of the most popular nonlinear system identification techniques, NARMAX and introduces a new method, developed by the author, Constant Level Identification.

4.2 NARMAX

In section 2.2.6 the ARMA representation of a linear aeroelastic system was outlined. Here, it will be shown that this representation can be extended to

include nonlinear systems. Consider a single degree of freedom system with a cubic stiffness non-linearity (Duffing Oscillator), whose equation of motion is given by

$$m\ddot{y} + c\dot{y} + k_1 y + k_2 y^3 = u(t) \tag{4.1}$$

By applying the central difference expressions for the first and second derivatives (see Appendix D) equation 4.1 becomes

$$\left(\frac{m}{\Delta t^2} + \frac{c}{2\Delta t}\right) y_{i+1} + \left(k_1 - \frac{m}{\Delta t^2}\right) y_i + \left(\frac{m}{\Delta t^2} - \frac{c}{2\Delta t}\right) y_{i-1} + k_2 y_i^3 = u_i \tag{4.2}$$

where Δt is the time increment and i denotes a time instance. By re-arranging equation 4.2 and regressing all the terms by one time step the following relation is obtained

$$y_i = \left(\frac{m - k_1\Delta t^2}{m + \frac{c\Delta t}{2}}\right) y_{i-1} + \left(\frac{\frac{c\Delta t}{2} - m}{m + \frac{c\Delta t}{2}}\right) y_{i-2} + \left(\frac{-k_2\Delta t^2}{m + \frac{c\Delta t}{2}}\right) y_{i-1}^3 + \left(\frac{\Delta t^2}{m + \frac{c\Delta t}{2}}\right) u_{i-1} \tag{4.3}$$

Equation 4.3 is, in essence, the NARMAX representation of the Duffing Oscillator. It contains all the terms of the ARMA model of the linear case plus a cubic order term. A more general representation of equation 4.3 would be [57]

$$y_i = F^{(3)}(y_{i-1}, y_{i-2}; u_{i-1}) \tag{4.4}$$

where $F^{(3)}$ denotes a function of up to third order combinations of the terms in brackets, i.e. terms of the form

$$y_{i-1}, y_{i-2}, u_{i-1}, y_{i-1}^2, y_{i-1}y_{i-2}, y_{i-1}u_{i-1}, \ldots, y_{i-1}^3, y_{i-1}y_{i-2}^2, y_{i-1}^2 u_{i-1}, \ldots$$

Of course, if it is known that the nonlinearity in the system is, say, cubic, then only the y_{i-1}^3 term need be retained. For the case of a general multi-dof

system with any number of general nonlinearities, the NARMAX representation becomes

$$y_i = \alpha + F^{(l)}(y_{i-1}, \ldots, y_{i-n_y}; u_{i-1}, \ldots, u_{i-n_u}) \tag{4.5}$$

where α is a constant, l is the order of nonlinearity n_y is the maximum regression in y and n_u is the maximum regression in u. This polynomial representation has been shown to adequately describe a wide variety of nonlinear systems [55], even though F can be any nonlinear function. Usually the term NARMAX model defines a model of the type in equation 4.5 with the minimum n_y, n_u and l values that can accurately describe the original system [54].

4.2.1 Noise model

The NARMAX description presented in the previous section is only suitable for application on perfect response data. As with the ARMA method (section 2.2.6), NARMAX modelling suffers in the presence of measurement errors. To overcome this problem, Billings has suggested the estimation of a noise model, a procedure to be carried out simultaneously with the estimation of the NARMAX model. The noise model proposed by Billings [54] is of the form

$$y_i = \alpha + F^{(l)}(y_{i-1}, \ldots, y_{i-n_y}; u_{i-1}, \ldots, u_{i-n_u}; \varepsilon_{i-1}, \ldots, \varepsilon_{i-n_\varepsilon}) + \varepsilon_i \tag{4.6}$$

where ε_i is the prediction error sequence, defined by

$$\varepsilon_i = y_i - \hat{y}_i$$

$\hat{y}_i$ being the estimate of y_i obtained by using the first estimates of the NARMAX model terms. Due to the nonlinearity of the system the noise can be both additive and multiplicative and, hence, it is included in the linear and nonlinear terms.

The noise model is defined as the collection of terms containing ε. What remains is the actual NARMAX model, also termed the *process* model.

4.2.2 Calculation of terms and coefficients

The simplest way of calculating the NARMAX model would be to choose the order of nonlinearity, l, as well as the regressions n_y, n_u and n_ε and then to apply equation 4.6 to measured data of input and output using a least squares procedure. This is not recommended for two reasons. Firstly, the object of a NARMAX identification should be to determine which terms should be included in the model as well as to determine the coefficients. For example, equation 4.4 contains many more terms than is necessary to describe the Duffing oscillator (equation 4.3). An efficient NARMAX estimation algorithm should be able to exclude all these unnecessary terms. Secondly, errors can become arbitrarily large if the least squares matrix is close to singular, which can occur if unnecessary terms are included [57].

The estimation method used throughout the present work is the forward regression orthogonal least squares algorithm detailed in [58] and [54]. The forward regression is used to evaluate which terms are needed in the NARMAX expansion of a given system and the orthogonal least squares are used to prevent the large errors described in the previous paragraph. The basic features of the algorithm will now be described. Equation 4.6 can be written as the sum of all the NARMAX terms

$$y(i) = \sum_{k=1}^{n_\theta} p_k(i)\theta_k + \varepsilon(i) \tag{4.7}$$

where the constant dc term, α, has been neglected, $p_k(i)$ are the NARMAX coefficients, θ_k are the NARMAX terms and n_θ is the total number of terms. The simple least squares solution can be obtained by solving equation 4.7 for

$i = 1, 2, \ldots, n_i$, where n_i is the number of data points used in the modelling process. The orthogonal least squares solution can be obtained by solving the equivalent equation

$$y(i) = \sum_{k=1}^{n_\theta} g_k w_k(i) + \varepsilon(i) \tag{4.8}$$

where $w_k(i)$ are orthogonal. The forward regression algorithm begins with the estimation of process terms only. All process terms $p_k(i)$ are considered as candidates to be the first term in the NARMAX expansion. For $k = 1, \ldots, n_\theta$ the following quantities are calculated

$$\begin{aligned} w_1^k(i) &= p_k(i) \\ \hat{g}_1^k &= \frac{\sum_{i=1}^{n_i} w_1^k(i) y(i)}{\sum_{i=1}^{n_i} (w_1^k(i))^2} \\ \varepsilon RR_1^k &= \frac{(\hat{g}_1^k)^2 \sum_{i=1}^{n_i} (w_1^k(i))^2}{\sum_{i=1}^{n_i} (y(i))^2} \end{aligned} \tag{4.9}$$

where $w_1^k(i)$ is the kth candidate for $w_1(i)$, $\hat{g}_1^k$ is the estimated coefficient of $w_1^k(i)$ and εRR_1^k is the *error reduction ratio* for $w_1^k(i)$, i.e. a quantity expressing the reduction in error caused by the inclusion of term $w_1^k(i)$ to the model. The error reduction ratios for each candidate term are calculated and the term with the highest εRR is chosen to be the first term, $w_1(i)$. All the remaining terms are again considered as candidates to be the second term, $w_2(i)$, and subsequent terms. When choosing the tth term, the following quantities are evaluated for each remaining candidate

$$w_t^k(i) = p_k(i) - \sum_{\lambda=1}^{t-1} \alpha_{\lambda k} w_\lambda(i), \quad \text{where} \quad \alpha_{\lambda k} = \frac{\sum_{j=1}^{n_i} w_\lambda(j) p_k(j)}{\sum_{j=1}^{n_i} (w_\lambda(j))^2}$$

$$\hat{g}_t^k = \frac{\sum_{i=1}^{n_i} w_t^k(i) y(i)}{\sum_{i=1}^{n_i} (w_t^k(i))^2}$$

$$\varepsilon RR_t^k = \frac{(\hat{g}_t^k)^2 \sum_{i=1}^{n_i} (w_t^k(i))^2}{\sum_{i=1}^{n_i} (y(i))^2} \tag{4.10}$$

Again, the term yielding the highest error εRR_t^k is chosen to be term $w_t(i)$. The forward regression algorithm is terminated when the highest error reduction ratio is less than a chosen limit, i.e.

$$\max(\varepsilon RR_t^k) \leq C_d$$

In that case, there is no tth term, the total number of terms being $t-1$. The limit value C_d is chosen according to the peculiarities of the data under investigation. Typical values suggested by Billings et al are $0.001 \leq C_d \leq 0.5$. The forward regression algorithm determines which of the n_θ terms included in the original model, equation 4.7, are necessary to model a given set of response data. It also provides estimates of the coefficients, $\hat{g}_k$, of the orthogonal terms $w_k(i)$. The first estimate of the errors contained in the NARMAX model is given by

$$\hat{\varepsilon}(i) = y(i) - \sum_{k=1}^{n_\theta} g_k w_k(i) \tag{4.11}$$

The values of $\hat{\varepsilon}(i)$ are used to apply the forward regression algorithm to the noise model and determine which terms should be included in the model. The selected terms are added to the model and equation 4.11 is used to recompute the residuals

only, this time the summation is from $k = 1$ to $n_\theta +$ number of noise terms. Then, the orthogonal estimator is re-applied for each of the noise terms and the process is repeated until the parameters converge to constant values.

The NARMAX methodology is very sensitive to a number of factors. These are

- The choice of order of nonlinearity, l. The total number of terms in the model of equation 4.5 increasing combinatorially with increasing order of nonlinearity. It follows that it is advantageous to know what the order of the nonlinearity to be identified is in order to avoid unnecessary calculations. A further corollary is that nonlinearities that do not admit an exact polynomial fit can not be identified by a NARMAX model. Discontinuous functions such as pitch stops or functions with discontinuities in slope such as bilinear and freeplay stiffness require a large number of polynomial terms to be fitted exactly and, hence, NARMAX identification becomes impractical.

- The choice of regressions n_y, n_u and n_ε. Again, the larger the regressions the larger the number of terms that need to be investigated. Billings et al [54] suggest that it is possible to obtain a first estimate of the order of regressions by attempting a linear NARMAX fit first (i.e. with $l = 0$).

- The choice of C_d. This strongly depends on the time step (or sampling frequency) of the measured data. Generally, the smaller the time step, the smaller C_d needs to be. However, C_d also depends on the properties of the system under investigation.

- The number of data points used in the identification. This number should generally be between 500 and 1000 points. In the experience of this author, increasing the number of points to more than 1000 does not alter the

resulting NARMAX fit.

4.2.3 Application of a NARMAX model to aeroelastic systems

The damping and stiffness of aeroelastic systems varies with free-stream airspeed. Consequently, identifying an aeroelastic model at a particular velocity using a NARMAX polynomial is inadequate, since the system will change at a different velocity. In order to demonstrate the application of NARMAX to such a system, the system in equation 4.1 will be modified. An aeroelastic system contains stiffness and damping contributions by aeroelastic forces and systems which depend on velocity. Aerodynamic damping is proportional to the velocity and aerodynamic stiffness is proportional to the square of the velocity. Hence, an aeroelastic form of equation 4.1 would be

$$m\ddot{y} + c(1+\alpha_1 V)\dot{y} + k_1(1+\alpha_2 V^2)y + k_2 y^3 = u(t) \tag{4.12}$$

where V is the velocity and α_1, α_2 are coefficients. Using the analysis detailed previously, the discrete-time difference representation of the system is given by

$$\begin{aligned} y_{i+1} \;=\; & \left(\frac{2 - \dfrac{\Delta t^2 k_1 (1+\alpha_2 V^2)}{m}}{1 + \dfrac{c(1+\alpha_1 V)\Delta t}{2m}} \right) y_i + \left(\frac{\dfrac{c(1+\alpha_1 V)\Delta t}{2m} - 1}{1 + \dfrac{c(1+\alpha_1 V)\Delta t}{2m}} \right) y_{i-1} \\ & - \left(\frac{\dfrac{\Delta t^2 k_2}{m}}{1 + \dfrac{c(1+\alpha_1 V)\Delta t}{2m}} \right) y_i^3 + \left(\frac{\dfrac{\Delta t^2}{m}}{1 + \dfrac{c(1+\alpha_1 V)\Delta t}{2m}} \right) u_i \end{aligned} \tag{4.13}$$

In other words, each coefficient is a fraction of polynomials of the form

$$\theta_i = \frac{1 + \alpha V + \beta V^2}{\gamma + \delta V} \tag{4.14}$$

where the unity in the numerator is a result of normalisation with the denominator.

The identification process for such a system must be repeated at four different velocities, in order to estimate the coefficients in the polynomial fraction. More velocities can be used to minimise any errors using a least squares process. However, as the velocity is varied, new characteristics of the system may become evident in the measured output data requiring different terms in the NARMAX expansion for successful identification. In this case the final model should include all the terms that appear at all four velocities, even if some of these terms are negligible at particular velocities.

In essence, the NARMAX model of an aeroelastic system is not a set of coefficients and their corresponding significant terms but many sets of coefficients of polynomial fractions and the corresponding significant terms.

As an example, the following system was tested to validate the algorithm presented in this section

$$\ddot{y} + 5(1 + 1.4V)\dot{y} + 500(1 + 0.8V^2)y + 1600y^3 = u(t)$$

with $V = 1, 2, 3, 4$ and a time step, $dt = 0.001$. The input used was a 75% burst chirp , with frequencies between 1 and 10 Hz. The resulting coefficients are tabulated in table 4.1.

	term	α	β	γ	δ
True	y_i	0	-0.0002	0.5014	0.0018
Estimated	y_i	0.0000	-0.0002	0.5014	0.0018
True	y_{i-1}	-0.0035	0	-1.005	-0.0035
Estimated	y_{i-1}	-0.0038	0.0000	-1.0050	-0.0032
True	y_i^3	0	0	-626.5625	-2.1875
Estimated	y_i^3	0.0006	-0.0000	-626.5625	-2.2832
True	u_i	0	0	1.0025×10^6	3.5×10^4
Estimated	y_i	0.0003	-0.0001	1.0025×10^6	3.2757×10^4

Table 4.1: True and estimated parameters of NARMAX coefficients

Subsequently, the coefficients of the NARMAX model were evaluated for $V = 5$ and the response calculated. Figure 4.1 shows the agreement between the model and actual system responses for $V = 5$. It should be noted though that the variation of the system with airspeed causes some difficulties with the NARMAX methodology. As noted already, the various parameters used in the NARMAX estimation procedure are strongly dependent upon the particular system and set of data. Changes in the system under investigation can necessitate changes in these parameters. For the simple example presented above it was found that, for high airspeeds, the value of C_d had to be decreased.

4.3 Constant Level Identification method

This section presents a method developed during the course of the present research for the identification of non-linear multiple degree of freedom (DOF) systems with any type of non-linearity [59]. Although the method is general, the application described here and in [59] is suited particularly to the identification of aeroelastic systems. A number of simulated examples, as well as an experimental application, are employed to demonstrate the effectiveness of the method. Reference [60] gives details of the application of the method in conjunction with gust load prediction techniques.

4.3.1 A simple application

Consider the Duffing Oscillator and assume that the position and type of the non-linearity, and also the number of modes (one) are known. The equation of motion for this system is

$$m\ddot{y} + c\dot{y} + k_1 y + k_2 y^3 = u_g(t) \tag{4.15}$$

where m is the mass, c is the damping coefficient, k_1 is the linear stiffness coefficient and k_2 is the non-linear stiffness coefficient. Since it is known that the non-linear term depends on y, the identification process begins with isolating time-instances where y assumes a certain value, as shown in figure 4.2. At this level, the non-linear term has a constant value due to its dependence on y. Thus, the equation of motion for the system can be written as

$$\begin{pmatrix} \ddot{y}(t_1) & \dot{y}(t_1) & 1 \\ \ddot{y}(t_2) & \dot{y}(t_2) & 1 \\ \vdots & \vdots & \vdots \\ \ddot{y}(t_n) & \dot{y}(t_n) & 1 \end{pmatrix} \begin{Bmatrix} m \\ c \\ N \end{Bmatrix} = \begin{Bmatrix} u_g(t_1) \\ \vdots \\ u_g(t_n) \end{Bmatrix} \tag{4.16}$$

where $N = k_1 y + k_2 y^3$ and $t_1, \ldots, t_n$ are the instances in time that correspond to the chosen response level. Notice that y itself does not appear in the equations since, having a constant value, it would render the left hand side matrix singular. Equation 4.16 can be solved using a least squares process to give m, c and N.

The equation of motion can then be re-arranged in the form

$$N(t) = -m\ddot{y} - c\dot{y} + u_g(t) \tag{4.17}$$

to give the values of N at all time-steps.

The result of the identification process is the values of the mass and damping coefficient as well as the stiffness for all time-steps. A characteristic of this approach, that differs from others, is that the linear and non-linear parts of the stiffness have been merged together in one function, N. The response of the system to any other input can be found through the use of this combined function.

However, should the elements of N need to be determined, N can be re-written as

$$N = k_1 y + \hat{N}$$

Then, if the type of nonlinearity in $\hat{N}$ is known, the linear and non-linear parts can be separated by means of curve-fitting. For instance, if for the present example it is known that the nonlinear term is cubic then it will also be known that

$$N(t) = k_1 y(t) + k_2 y(t)^3$$

Discretizing for the jth level,

$$N_j = k_1 y_j + k_2 y_j^3$$

and, expanding for nj levels,

$$\left\{ \begin{array}{c} N_1 \\ N_2 \\ \vdots \\ N_{nj} \end{array} \right\} = \left(\begin{array}{cc} y_1 & y_1^3 \\ y_2 & y_2^3 \\ \vdots & \vdots \\ y_{nj} & y_{nj}^3 \end{array} \right) \left\{ \begin{array}{c} k_1 \\ k_2 \end{array} \right\}$$

which can be solved to find the unknowns, k_1, k_2.

Alternatively, if the nonlinear function, $\hat{N}$, is unknown but differentiable then it can be split into the linear and nonlinear part by differentiating it twice with respect to y, which eliminates the linear part. If the result is then integrated while setting the constants of integration to zero, the purely nonlinear part of N is obtained, i.e.

$$\hat{N} = \int \int \frac{d^2 N}{dy^2} dy dy \tag{4.18}$$

Subtracting $\hat{N}$ from N gives the linear stiffness variation and a linear curve fit will yield the linear stiffness coefficient. It should be noted though, that differentiation and integration introduce additional numerical errors.

To illustrate the complete procedure numerically, the excitation force, $u_g(t)$, was taken to be a sine sweep and the system parameters were set at $m = 1.2$, $c = 0.7$, $k_1 = 5.8 \times 10^3$ and $k_2 = 1.16 \times 10^9$. Figure 4.2 shows the constant level

displacement points that were used to start the analysis. Parameter estimates of $m = 1.199988$, $c = 0.700016$, $k_1 = 5.799974 \times 10^3$ and $k_2 = 1.159989 \times 10^9$ were found. Figure 4.3 shows the true and estimated cubic stiffness values. It can be seen that for this simple case, very good quality estimates (accurate to 4 decimal places) were obtained.

4.3.2 Procedure

The previous example demonstrated the rationale behind the proposed method however, in order to apply it to more realistic systems, various refinements are needed. The first crucial refinement is to multiply the equations of motion throughout by the inverse of the mass matrix, which has the effect of ensuring that the excitation term appears in all the equations of motion and also reduces the sensitivity to noise and increases the speed of the computation by reducing the number of unknowns that need to evaluated. Thus the equations become

$$\ddot{\boldsymbol{q}} + \mathbf{M}^{-1}\mathbf{C}\dot{\boldsymbol{q}} + \mathbf{M}^{-1}\mathbf{K}\boldsymbol{q} = \mathbf{M}^{-1}\boldsymbol{F} \tag{4.19}$$

where $\mathbf{M}$, $\mathbf{C}$ and $\mathbf{K}$ are the mass, damping and stiffness matrices respectively, $\boldsymbol{q}$ is the displacement vector and $\boldsymbol{F}$ is the excitation force vector, but now $\mathbf{M}^{-1}\boldsymbol{F}$ must also be treated as an unknown. The only term in equation 4.19 which is completely known is the acceleration $\ddot{\boldsymbol{q}}$. As a consequence, equation 4.16 is replaced by

$$\begin{pmatrix} \dot{q}_1(t_1) & \dots & \dot{q}_m(t_1) & q_1(t_1) & \dots & q_m(t_1) & f_x(t_1) & 1 \\ \dot{q}_1(t_2) & \dots & \dot{q}_m(t_2) & q_1(t_2) & \dots & q_m(t_2) & f_x(t_2) & 1 \\ \vdots & \vdots & \vdots & \vdots & \vdots & \vdots & \vdots & \vdots \\ \dot{q}_1(t_n) & \dots & \dot{q}_m(t_n) & q_1(t_n) & \dots & q_m(t_n) & f_x(t_n) & 1 \end{pmatrix} \times \begin{Bmatrix} \hat{C}_{i1} \\ \vdots \\ \hat{C}_{im} \\ \hat{K}_{i1} \\ \vdots \\ \hat{K}_{im} \\ \hat{F}_i \\ N_i \end{Bmatrix} = \begin{Bmatrix} \ddot{q}_i(t_1) \\ \vdots \\ \ddot{q}_i(t_n) \end{Bmatrix} \tag{4.20}$$

for $i = 1, \dots, m$, where m is the number of modes. $\hat{K}_{ii}, \hat{C}_{ii}, \hat{F}_i$ are the various elements of the matrices $\hat{\mathbf{K}} = \mathbf{M}^{-1}\mathbf{K}$, $\hat{\mathbf{C}} = \mathbf{M}^{-1}\mathbf{C}$ and $\hat{\boldsymbol{F}} = \mathbf{M}^{-1}\boldsymbol{F}$. In this example $\boldsymbol{N}$ is a vector containing all the nonlinearities in the system. Any nonlinear terms from the damping or stiffness matrices are moved to $\boldsymbol{N}$ together with their associated linear terms (as in the previous case of $N = k_1 y + \hat{N}$), so that all the elements in the matrices are linear or zero.

In equation 4.16, y was not included at all to avoid rendering the equations singular. This should also be the case in equation 4.20, however, since the position of the non-linearity and the variable it depends on are not known, it is impossible to pre-determine which of $q_1, \dots, q_m, \dot{q}_1, \dots, \dot{q}_m$ should be kept constant and excluded. Even the number of modes ,m ,is unknown for a real system, however, preliminary analysis would give an indication via Frequency Response Function (FRF) plots.

The number and types of non-linearities present in each mode are not known, hence the procedure becomes speculative at this point. It is first assumed that there is a non-linearity depending on, say, q_1 (i.e. a stiffness non-linearity or Coulombic friction). Then points where q_1 has a constant value are identified in the output. Assuming that enough such points have been identified in the output

of the system, each of equations 4.20 is solved using a least squares process, each yielding the elements of one line of the mass, structural damping and structural stiffness matrices as well as the value of the nonlinear term. When all the sets of equations are solved, the equivalent of equation 4.17

$$\boldsymbol{N} = -\ddot{\boldsymbol{q}} - \hat{\mathbf{C}}\dot{\boldsymbol{q}} - \hat{\mathbf{K}}\boldsymbol{q} + \hat{\boldsymbol{F}} \tag{4.21}$$

(where the column associated with q_1 in $\hat{\mathbf{K}}$ is made up of zeros) is employed to calculate the values of the nonlinear terms for every instant in time, since all the other matrices are now known.

Since the equations of motion have been multiplied throughout by the inverse of the mass matrix there will be non-linear terms in each of the m equations 4.21, even if there is only one non-linearity in one mode. The non-linear terms, N_i, are then plotted against q_1. If the plots are single-valued functions of q_1, as in figure 4.4, then the non-linearity was assumed to depend on the correct variable and the mode has been identified correctly. If the curve has a phase-plot-type shape, as in figure 4.5, then it means that the non-linearity depends on some other variable and, hence, the procedure needs to be repeated from the beginning, keeping another one of $q_2, \ldots, q_m, \dot{q_1}, \ldots, \dot{q_m}$ constant until a successful identification is obtained. Finally, after the nonlinear terms have been evaluated for all instants in time, they can be curve-fitted to yield continuous functions. Alternatively, the location of the nonlinearity can be obtained using a Hilbert transform approach [61].

In order for the identification process to succeed, the input and output data need to be interpolated to obtain a set of instances in time where the desired variable has exactly the same value. This value needs to be near the equilibrium level so that enough such points can be obtained. Cubic interpolation has been found quite adequate, yielding sets of points that are almost exact solutions to

the equations to the equations of motion. The excitation force also needs to be such that it excites all the important features of the systems, including the non-linearity. Sine-sweep or banded random excitation are suitable since they allow several frequencies of excitation to be applied to the system in one test.

A further consideration regarding the proposed method concerns the effect of performing the identification procedure at various levels and not just the one. This was tried for a few very simple test cases but was not found to improve the accuracy of the resulting system estimates. However, in the case where a significant amount of noise is present in the response data, it is suggested that using a large number of levels would have a beneficial effect, since it would reduce the effect of the noise.

Finally, it should be noted that the method will only identify systems which contain non-linearities dependent upon one variable. For instance, it will identify a wing with friction and freeplay in the wing-root pitch degree of freedom, however it will not identify a system with freeplay both in the wing-root pitch and the wing-root heave degree of freedom. This limitation comes from the fact that the equations of motion are identified as if they had been multiplied throughout by the inverse of the mass matrix. Hence, every non-linearity that exists in the system appears in the equation for every mode. Since the method works on the assumption that it is possible to keep the non-linear term in each equation constant, two or more non-linear terms that depend on two different variables will cause it to fail. To make the application of the method clearer, the algorithm is presented in graphical form in figure 4.6.

4.3.3 A more complex application

The method is here demonstrated by applying it to the Hancock model with bilinear control surface stiffness. The fact that the system is numerical implies

that there is no measurement error, however, numerical errors are introduced by the process of differentiation of the response (introduction of higher derivatives), by interpolation and other effects. In order to apply the identification routine usefully, the time step needs to be sufficiently small. The input used here was a sine sweep. The first step is to choose the number of modes. Because the model is simple, wing heave, γ, wing pitch, θ and control surface pitch, β are the three DOF required for a successful identification.

According to the procedure outlined in the previous subsection, the next step is to assume that there is a non-linearity which appears in every equation. The search procedure is applied and results in the location of the nonlinearity in the control surface pitch degree of freedom. Equations 4.20 are solved and the resulting identified damping matrix was

$$\hat{\mathbf{C}}_{id} = \begin{bmatrix} 0.0381 & -0.0700 & 0.0100 \\ -0.1665 & 0.1293 & -0.0387 \\ 0.2000 & -0.2763 & 0.1159 \end{bmatrix}$$

compared to the actual damping matrix of

$$\hat{\mathbf{C}} = \begin{bmatrix} 0.0381 & -0.0700 & 0.0100 \\ -0.1665 & 0.1292 & -0.0387 \\ 0.2000 & -0.2763 & 0.1158 \end{bmatrix}$$

The identified stiffness matrix was

$$\hat{\mathbf{K}}_{id} = \begin{bmatrix} 16.7993 & -12.2321 & 0.0000 \\ -74.6637 & 225.4430 & 0.0000 \\ 74.6637 & -481.9899 & 0.0000 \end{bmatrix}$$

and the actual stiffness matrix was

$$\hat{\mathbf{K}} = \begin{bmatrix} 16.7994 & -12.2321 & 0.0259 \\ -74.6637 & 225.4430 & 0.0738 \\ 74.6637 & -481.9898 & -0.3048 \end{bmatrix}$$

The two sets of matrices are virtually identical apart from the last column of $\hat{\mathbf{K}}$ which is zero in the identified case. This is due to the fact that the non-linearity appears in all three elements of that column and the identification process merges the linear and nonlinear parts of these elements, as in the earlier example where $N = k_1 y + k_2 y^3$. However, unlike the case of cubic stiffness, the bilinear function is discontinuous and, therefore, can not be differentiated. Additionally, since it is linear in parts, N_i cannot be fitted by least squares as the sum of a linear and a bilinear function. Hence, separating the linear and nonlinear parts of N_i is not as straightforward as in the previous example.

The problem can be partly solved by considering the fact that the linear part of N_i is made up of a structural and an aerodynamic term. Aerodynamic stiffness terms depend on the square of the free stream velocity [18]. Hence

$$N_i(V, \beta) = (k_s + k_a V^2)\beta + \hat{N}_i(\beta) \tag{4.22}$$

where V is the free-stream velocity, k_s is the structural contribution and k_a is the aerodynamic contribution. Since the purely nonlinear term is structural, $\hat{N}_i$ does not depend on V. By performing identifications at two different airspeeds, k_a can be evaluated, however the linear and nonlinear structural terms will remain merged in a new nonlinear function equal to $k_s\beta + \hat{N}_i(\beta)$. Consequently, it is possible to isolate the aerodynamic contribution to the linear part of the system's stiffness but not the structural one.

The best test of the accuracy of the method is to use the new matrices, together with the nonlinear terms obtained to solve the identified model and compare its response to that of the actual system. The nonlinear terms are handled as lookup tables since their discontinuities prohibit the use of large scale interpolation or curve-fitting.

Figure 4.7 shows the percentage error in the identification of the control surface pitch response. The peaks occur where the response is very close to zero, otherwise the error is small. The comparison between the actual nonlinear term in wing heave and that produced by the identification method can be seen in figure 4.8 which shows excellent agreement. Figure 4.9 shows the nonlinear surface for the same degree of freedom, i.e. an equivalent of the restoring force surface given by the restoring force method [62]. In figures 4.10 and 4.11 the agreement between true and identified freeplay terms and the freeplay nonlinear surface are plotted, respectively, again showing very good comparison.

4.3.4 Identifying hysteresis-type nonlinearities

Hysteresis is characterized by the fact that the response lies on one path while increasing and on another one while decreasing [29]. Hence, hysteresis-type nonlinearities can be easily identified by the proposed method with a slight modification. When isolating response levels, only points in the response which lie on the level but have also got a first derivative with respect to time of the same sign can be used. This is demonstrated in figure 4.12.

The simple single-degree-of-freedom system presented earlier but with hysteretic stiffness was identified successfully using the proposed method. For a particular test case, the values of the parameters were $m = 1.2$, $c = 0.7$ and $k = 5.8 \times 10^3$. The identified values were $m = 1.203944$, $c = 0.709445$ and $k = 5.813631 \times 10^3$. The accuracy of these results should be compared to the accuracy of the results at the end of section 4.3.1. The errors in the hysteresis case are larger because the identification process is split in two parts, one part using constant level points with positive first derivative and one part using points with negative first derivative. Figure 4.13 shows the hysteretic stiffness variation with y both for the actual system and the identified one. Figure 4.14 shows the

percentage error.

4.3.5 Identification of large systems

A real system will contain a large number of modes and the identification of the entire system will be difficult to perform accurately. So, it is of interest to determine whether the proposed method could deliver acceptable results when less modes are used in the identification procedure than there are in the real system.

A second mathematical model of a wing was developed, this time without a control surface but with a multi-mode Rayleigh-Ritz series modelling the vibration of the wing. The two wing-root rigid modes (wing-root pitch and heave) were retained as a mechanism of introducing nonlinearities. Since in order to identify a nonlinear system the modes that contain the nonlinearities need to be identified, the two rigid modes always need to appear in the identification process.

The results presented in figure 4.15 are for a 5 degree-of-freedom rectangular wing with bilinear stiffness in wing-root pitch. The Rayleigh-Ritz series contains two bending and one torsional mode. The system was identified using models of increasing complexity from 2 degrees of freedom to 5. Figure 4.15 clearly shows that the quality of the identification deteriorates with decreasing disparity between the number of modes in the actual system and the number of modes used in the identification process. However, even in the 2-mode case, the type and location of the nonlinearity were identified accurately.

4.3.6 Dealing with noise

It has been shown that the proposed identification method yields accurate results when applied to systems containing various types of nonlinearity and with

varying numbers of degrees of freedom. However, all the systems used to validate the method were mathematical models and, hence, their measured response signals were noise-free. In order to obtain a successful identification using results corrupted with noise a further refinement has to be applied to the method. The identification process has to be simultaneously performed at a number of response levels so that errors incurred at one level due to noise corruption can be counteracted. Hence equation 4.20 becomes

$$\begin{pmatrix} \dot{q}_1(t_{11}) & \dots & \dot{q}_m(t_{11}) & q_1(t_{11}) & \dots & q_m(t_{11}) & f_x(t_{11}) & 1 & 0 & \dots & 0 \\ \vdots & \vdots & \vdots & \vdots & \vdots & \vdots & \vdots & \vdots & \vdots & \vdots & \vdots \\ \dot{q}_1(t_{n1}) & \dots & \dot{q}_m(t_{n1}) & q_1(t_{n1}) & \dots & q_m(t_{n1}) & f_x(t_{n1}) & 1 & 0 & \dots & 0 \\ \dot{q}_1(t_{12}) & \dots & \dot{q}_m(t_{12}) & q_1(t_{12}) & \dots & q_m(t_{12}) & f_x(t_{12}) & 0 & 1 & \dots & 0 \\ \vdots & \vdots & \vdots & \vdots & \vdots & \vdots & \vdots & \vdots & \vdots & \vdots & \vdots \\ \dot{q}_1(t_{n2}) & \dots & \dot{q}_m(t_{n2}) & q_1(t_{n2}) & \dots & q_m(t_{n2}) & f_x(t_{n2}) & 0 & 1 & \dots & 0 \\ \vdots & \vdots & \vdots & \vdots & \vdots & \vdots & \vdots & \vdots & \vdots & \vdots & \vdots \\ \dot{q}_1(t_{1l}) & \dots & \dot{q}_m(t_{1l}) & q_1(t_{1l}) & \dots & q_m(t_{1l}) & f_x(t_{1l}) & 0 & 0 & \dots & 1 \\ \vdots & \vdots & \vdots & \vdots & \vdots & \vdots & \vdots & \vdots & \vdots & \vdots & \vdots \\ \dot{q}_1(t_{nl}) & \dots & \dot{q}_m(t_{nl}) & q_1(t_{nl}) & \dots & q_m(t_{nl}) & f_x(t_{nl}) & 0 & 0 & \dots & 1 \end{pmatrix} \times \begin{Bmatrix} \hat{C}_{i1} \\ \vdots \\ \hat{C}_{im} \\ \hat{K}_{i1} \\ \vdots \\ \hat{K}_{im} \\ \hat{F}_i \\ N_{i1} \\ \vdots \\ N_{il} \end{Bmatrix} = \begin{Bmatrix} \ddot{q}_i(t_1 1) \\ \vdots \\ \ddot{q}_i(t_n 1) \\ \vdots \\ \ddot{q}_i(t_1 l) \\ \vdots \\ \ddot{q}_i(t_n l) \end{Bmatrix} \tag{4.23}$$

where l is the number of levels used.

Multi-level identification in the absence of noise gives equally acceptable results to single-level identification, as shown in figure 4.16. However, in the presence of significant amounts of noise, single-level identification fails. The noisy

case was simulated by corrupting the responses of the Hancock model with random noise with a normal distribution. The identification process was then applied at 20 levels yielding an identified system. The agreement between the responses of the identified and the actual (noise-free) system was acceptable, as indicated by figure 4.17, where the identified and true nonlinear terms compare favorably. The identified system was obtained from data containing noise levels of 5% rms(signal)/rms(noise).

4.3.7 Identifying systems with more than one nonlinearity

Systems with more than one nonlinearity can be identified using the Constant Level method with one major modification. The equations of motion can not be identified as having been multiplied throughout by the inverse of the mass matrix, since such an operation introduces more than one nonlinear function in each of the equations. Hence, the mass matrix has to be identified separately. This calculation can be accomplished using the method in [63]. The approach was applied to the Hancock model with freeplay nonlinearities in all three degrees of freedom. Figure 4.18 shows all three actual and identified nonlinearities.

4.4 Experimental validation

The Constant Level and NARMAX identification methods were tested on a simple experimental system with two degrees of freedom, shown in figure 4.19. Each mass was independently supported by a couple of cantilever steel plates. The two masses were attached to each other by a coupling spring. The nonlinearity was cubic stiffness, approximated by a steel ruler attached to mass 2. Each mass was independently excited by means of a shaker driven by a signal generator, the excitation signal being measured by means of a force gauge. One accelerometer

on each mass measured the acceleration.

The excitation signals used for the experiment were random with wide frequency content. This choice was governed by the limitation of the data acquisition software which could not generate chirp signals without significant programming effort from the part of the user. A number of preliminary tests were performed at low excitation amplitudes and wide frequency bands. The FRFs of the system revealed two natural frequencies, at 22.8 Hz and 25.9 Hz. This initial series of tests also revealed that the system was substantially linearised at low excitation levels.

4.4.1 Identification by the CL method

The Constant Level identification method was applied to the low excitation data. The first step was to idealize the steel ruler in figure 4.19 as a massless spring, which is a valid simplification since the mass of the ruler was much lower than that of Mass 1 or Mass 2. The acceleration data was integrated in the frequency domain to yield the velocities and displacements. It was known that the nonlinearity was attached to mass 2, hence, for the initial application of the method, the displacement of mass 2 was held constant. This approach yielded linearised nonlinear terms, as seen in figures 4.20 and 4.21. The identified matrices were:

$$C_{id} = \begin{pmatrix} 5.8437 & -0.5241 \\ -0.3438 & 4.4409 \end{pmatrix} K_{id} = 10^4 \begin{pmatrix} 2.3726 & 0 \\ -0.3121 & 0 \end{pmatrix}$$

$$F_{id} = \begin{Bmatrix} 2.8331 \\ 2.7560 \end{Bmatrix}$$

When the CL method is applied to linear (or almost linear) systems, the choice of which of the responses to keep constant is not important; the system will be identified correctly either way. To investigate this property, the method was reapplied, this time keeping the mass 1 displacement constant. The nonlinear terms

were again identified as linear and the identified matrices were:

$$C_{id} = \begin{pmatrix} 5.7420 & -0.5065 \\ -0.3717 & 4.4824 \end{pmatrix} K_{id} = 10^4 \begin{pmatrix} 0 & -0.3139 \\ 0 & 2.3568 \end{pmatrix}$$

$$F_{id} = \begin{Bmatrix} 2.8364 \\ 2.7660 \end{Bmatrix}$$

i.e., almost identical to the previous case. The validity of the identified model was tested by calculating its response to the same excitation signals that were used on the experimental system. Figures 4.22 and 4.23 show good agreement between true and identified accelerations.

In order to obtain visibly nonlinear results from the experimental system, the excitation amplitude was increased to the limits allowed by the instrumentation and the excitation frequency band was reduced to between 20 and 30 Hz, so that more of the excitation energy affected the two modes. The sampling interval was decreased to 0.001 s in order to increase the quality of the data. The CL identification was carried out at many levels, as described in section 4.3.6. Table 4.2 shows the percentage errors in predicted and measured acceleration obtained with increasing number of levels. The percentage errors were obtained as $e = 100 \times \text{rms}(a_i)/\text{rms}(a_e)$, where e denotes the error, a_i is the acceleration predicted by the identified model, a_e is the experimental acceleration signal and rms denotes root-mean-square value.

Number of levels	% Error in Acceleration	
	Mass 1	Mass 2
1	4.44	4.60
2	3.73	3.94
4	3.76	3.85
6	3.77	3.92
8	3.76	3.94

Table 4.2: rms errors in prediction of response by CL method

Hence, the 4-level case was chosen. Figures 4.24 and 4.25 show the identified

nonlinear term variation plotted against the displacement of mass 2. The curve in figure 4.24 is still linear but figure 4.25 shows a slightly cubic variation. The identified matrices were:

$$C_{id} = \begin{pmatrix} 5.5302 & -0.4777 \\ -0.4023 & 4.1891 \end{pmatrix} K_{id} = 10^4 \begin{pmatrix} 2.2825 & 0 \\ -0.3093 & 0 \end{pmatrix}$$

$$F_{id} = \begin{Bmatrix} 1.5603 \\ 2.7629 \end{Bmatrix}$$

Despite the more pronounced nonlinearity of the data, the damping matrix and the first column of the structural matrix are still linear and should be almost identical to the results presented earlier. The small deviations are due to the lower levels of uncertainty in the second set of results, brought about by the lower time step. The fact that the 'nonlinear' term in mass 1 is still linear (figure 4.24) is due to the diagonality of the mass matrix. The system was identified as if it had been pre-multiplied by the inverse of the mass matrix but, since the inverse is also diagonal, the nonlinearity did not appear in the equation for mass 1. The linear part of the stiffness matrix was shown to be nearly symmetrical during the low excitation tests. This fact was corroborated by curve-fitting the curve in figure 4.24 by a 1st degree polynomial. The resulting polynomial was

$$f(y_2) = -0.3081 \times 10^4 y_2 - 0.0184$$

Substituting the slope of the polynomial in the stiffness matrix yields the completed equations of motion.

$$\begin{pmatrix} 1 & 0 \\ 0 & 1 \end{pmatrix} \begin{Bmatrix} \ddot{y_1} \\ \ddot{y_2} \end{Bmatrix} + \begin{pmatrix} 5.5302 & -0.4777 \\ -0.4023 & 4.1891 \end{pmatrix} \begin{Bmatrix} \dot{y_1} \\ \dot{y_2} \end{Bmatrix} +$$

$$10^4 \begin{pmatrix} 2.2825 & -0.3081 \\ -0.3093 & 0 \end{pmatrix} \begin{Bmatrix} y_1 \\ y_2 \end{Bmatrix} + \begin{Bmatrix} 0 \\ f_n(y_2) \end{Bmatrix} = \begin{Bmatrix} 1.5603 f_1(t) \\ 2.7629 f_2(t) \end{Bmatrix} \quad (4.24)$$

where y_1, y_2 are the displacements of mass 1 and mass 2, respectively, $f_1(t)$ and $f_2(t)$ are the excitation sequences applied to masses 1 and 2 and $f_n(y_2)$ is the nonlinear function. The latter can be estimated by curve-fitting figure 4.25 by a cubic polynomial:

$$f_n(y_2) = 1.3036 \times 10^9 y_2^3 - 5.7977 \times 10^5 y_2^2 + 2.2555 \times 10^4 y_2 - 0.1069 \qquad (4.25)$$

Note that the first order term in the expression for f_n is approximately equal to term $K(1,1)$, signifying that all the linear stiffness on mass 1 is provided by the cantilever spring. The displacement y_2 is of order $O(10^{-3})$ and f_n is of order $O(10)$. The terms in equation 4.25 are of order:

$$\begin{aligned} y_2^3 &: \quad O(1) \\ y_2^2 &: \quad O(10^{-1}) \\ y_2^1 &: \quad O(10) \\ y_2^0 &: \quad O(10^{-1}) \end{aligned}$$

Hence, since the 0th and 2nd order terms can be neglected and the 1st order term is due to the linear cantilever springs, the cubic stiffness caused by the steel ruler is given by $K_{cubic} = 1.3 \times 10^9 y_2^3$, and the equations of motion can be re-written as

$$\begin{pmatrix} 1 & 0 \\ 0 & 1 \end{pmatrix} \begin{Bmatrix} \ddot{y_1} \\ \ddot{y_2} \end{Bmatrix} + \begin{pmatrix} 5.5302 & -0.4777 \\ -0.4023 & 4.1891 \end{pmatrix} \begin{Bmatrix} \dot{y_1} \\ \dot{y_2} \end{Bmatrix} +$$

$$10^4 \begin{pmatrix} 2.2825 & -0.3081 \\ -0.3093 & 2.2555 \end{pmatrix} \begin{Bmatrix} y_1 \\ y_2 \end{Bmatrix} + \begin{Bmatrix} 0 \\ 1.3036 \times 10^9 y_2^3 \end{Bmatrix} = \begin{Bmatrix} 1.5603 f_1(t) \\ 2.7629 f_2(t) \end{Bmatrix} \qquad (4.26)$$

This equation was verified by calculating its response to the same excitation signals that were used on the experimental system, see figures 4.26 and 4.27, which compare the identified and actual accelerations. The comparison is very

good, the rms error being 3.76% for mass 1 and 3.85% for mass 2, as already shown in table 4.2.

4.4.2 Identification by NARMAX

The experimental system of figure 4.19 is a multi-input, multi-output (MIMO) system. However, to the knowledge of this author, there is no MIMO version of NARMAX. Hence, in order to apply the NARMAX technique to the system, exciter 1 in figure 4.19 was disconnected. The acceleration of mass 2 was taken as the system response.

Since the experimental system had 2 degrees of freedom, the regression order of the NARMAX model was chosen to be $2 \times dof = 4$. Additionally, since by this time it was known that the nonlinearity was cubic, the nonlinear order was chosen to be 3. Consequently, the list of possible terms included $y_{i-1}, \ldots, y_{i-4}$ and $u_{i-1}, \ldots, u_{i-4}$ and 2-term and 3-term combinations thereof. The forward regression algorithm was run with three values for c_d, $c_d = 0.001, 0.0001, 0.00001$. The percentage root-mean-square errors obtained for each value are tabulated in table 4.3

c_d	% error
0.001	10.3121
0.0001	3.2407
0.00001	6.3200

Table 4.3: rms errors in prediction of response by NARMAX method

Consequently, $c_d = 0.0001$ was chosen. It should be noted that, because the time-step of 0.001 s was too small for successful identification by the NARMAX technique, the data were decimated, i.e. some data-points were neglected. It was found necessary to neglect 9 in every ten data-points, thus effectively increasing the time-step by a factor of ten. For this case, the process terms retained, as well as their NARMAX coefficients and error reduction ratios are shown in table 4.4.

Term	Coefficient	eRR
y_{i-1}	0.0189	0.0941
y_{i-2}	-2.6111	96.2361
y_{i-4}	-2.3237	3.4149
y_{i-6}	-0.7029	0.2131
u_{i-6}	0.0214	0.0095
u_{i-2}	-0.7560	0.0203
u_{i-3}	0.2772	0.0052
$y_{i-3}y_{i-4}$	0.0065	0.0014
y_{i-5}	-0.0220	0.0005
$y_{i-1}u_{i-5}$	0.0016	0.0004
$y_{i-3}y_{i-6}$	0.0029	0.0004
$y_{i-1}y_{i-2}y_{i-5}$	-0.0001	0.0003
$y_{i-2}u_{i-6}$	-0.0028	0.0002
$y_{i-1}y_{i-1}$	0.0005	0.0002
u_{i-4}	-0.5424	0.0003
$y_{i-1}y_{i-5}$	-0.0004	0.0002
$y_{i-3}y_{i-5}u_{i-2}$	-0.0001	0.0002
$y_{i-2}y_{i-5}$	-0.0020	0.0001
$y_{i-1}y_{i-4}$	0.0015	0.0002
$y_{i-2}u_{i-5}u_{i-5}$	0.0016	0.0001
$y_{i-1}u_{i-3}u_{i-5}$	0.0057	0.0001
$y_{i-5}u_{i-3}u_{i-5}$	-0.0060	0.0003
u_{i-1}	0.2362	0.0001
u_{i-5}	0.2120	0.0002

Table 4.4: Preliminary NARMAX model for 2DOF experimental system

Subsequently, the noise model was applied. Convergence was fast, despite the relatively large number of terms, and the final coefficients are shown in table 4.5.

The response of the NARMAX model is compared to the response of the actual system in figure 4.28. Figure 4.29 shows a comparison of absolute error in the estimation of the acceleration by the two methods. It can be seen from the figure, as well as the rms errors in tables 4.2 and 4.3 that the NARMAX errors are slightly lower than the CL errors. In conclusion, it can be said that, when applied to an experimental system, the CL method is not as accurate as NARMAX however, it provides the user with a better understanding of the system under investigation. The NARMAX terms in table 4.5 do not give any physical

Term	Coefficient
y_{i-1}	0.0198
y_{i-2}	-2.7212
y_{i-4}	-2.2877
y_{i-6}	-0.7219
u_{i-6}	0.0219
u_{i-2}	-0.7487
u_{i-3}	0.2996
$y_{i-3}y_{i-4}$	0.0063
y_{i-5}	-0.0218
$y_{i-1}u_{i-5}$	0.0012
$y_{i-3}y_{i-6}$	0.0034
$y_{i-1}y_{i-2}y_{i-5}$	-0.0001
$y_{i-2}u_{i-6}$	-0.0023
$y_{i-1}y_{i-1}$	0.0005
u_{i-4}	-0.5443
$y_{i-1}y_{i-5}$	-0.0003
$y_{i-3}y_{i-5}u_{i-2}$	-0.0001
$y_{i-2}y_{i-5}$	-0.0023
$y_{i-1}y_{i-4}$	0.0019
$y_{i-2}u_{i-5}u_{i-5}$	0.0015
$y_{i-1}u_{i-3}u_{i-5}$	0.0061
$y_{i-5}u_{i-3}u_{i-5}$	-0.0056
u_{i-1}	0.2453
u_{i-5}	0.2019

Table 4.5: Final NARMAX model for 2DOF experimental system

picture of the system or the nonlinearity contained in it. In fact, in order to obtain the NARMAX model, knowledge of the order of nonlinearity was used, which was first obtained using the CL method. The latter can provide a much clearer understanding of a system under investigation including position and type of nonlinearity as well as the full equations of motion.

4.5 Figures

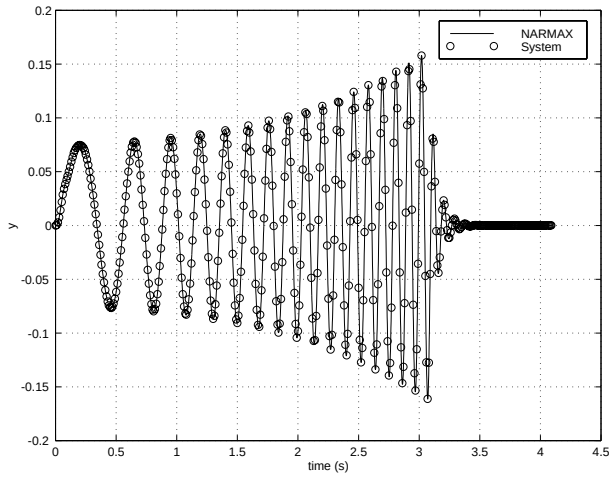

Figure 4.1: Comparison between true and NARMAX responses for airspeed-variable system

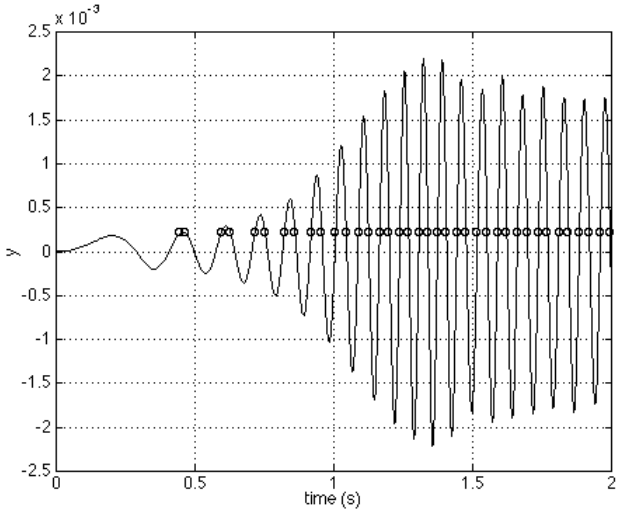

Figure 4.2: Constant level response points used in identification process

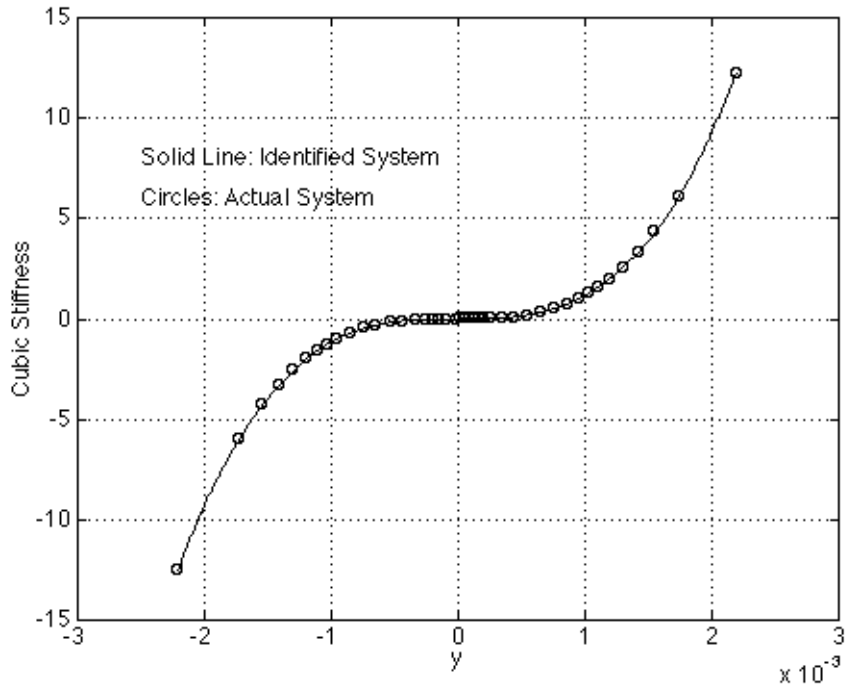

Figure 4.3: True and estimated cubic stiffness

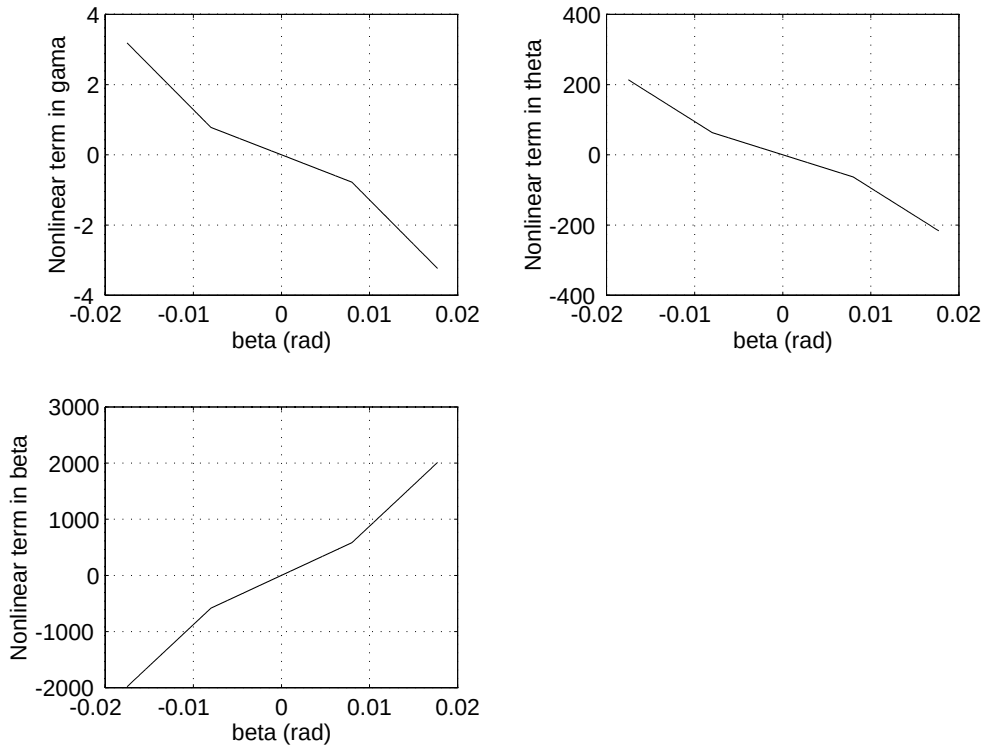

Figure 4.4: Example of successful identification by the CL method

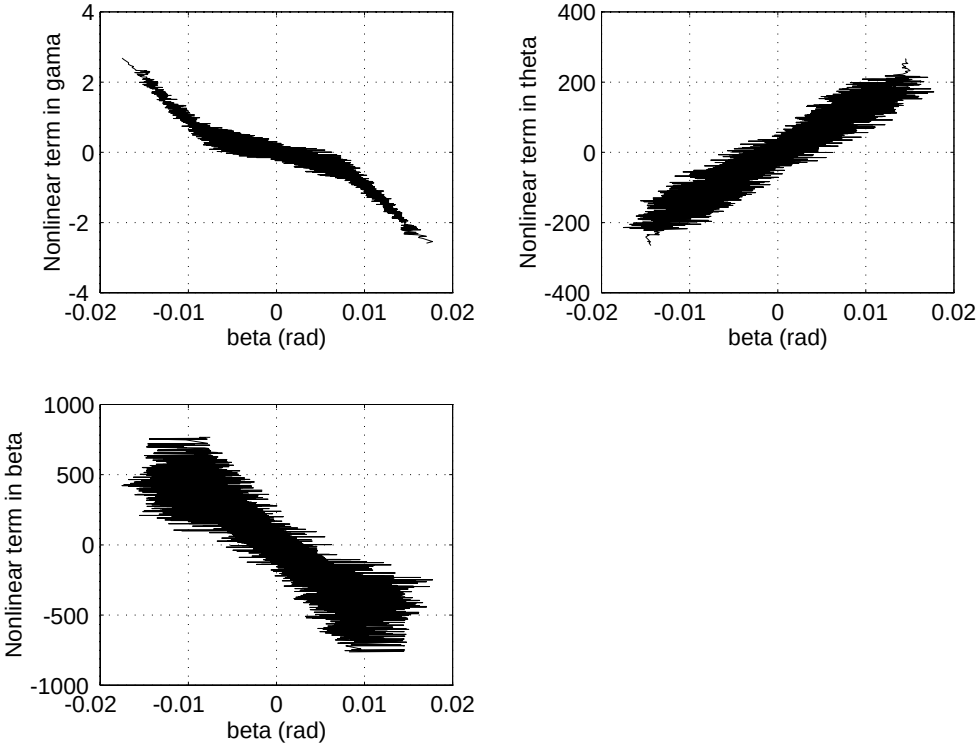

Figure 4.5: Example of failed identification by the CL method

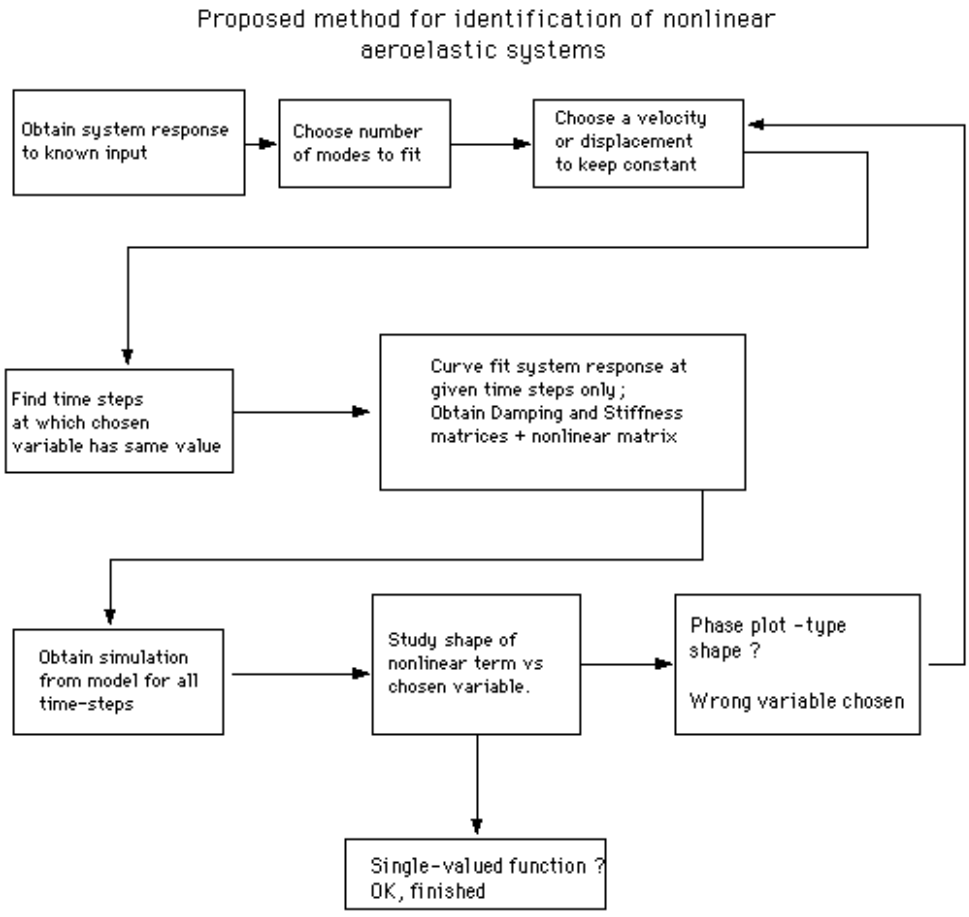

Figure 4.6: System identification algorithm

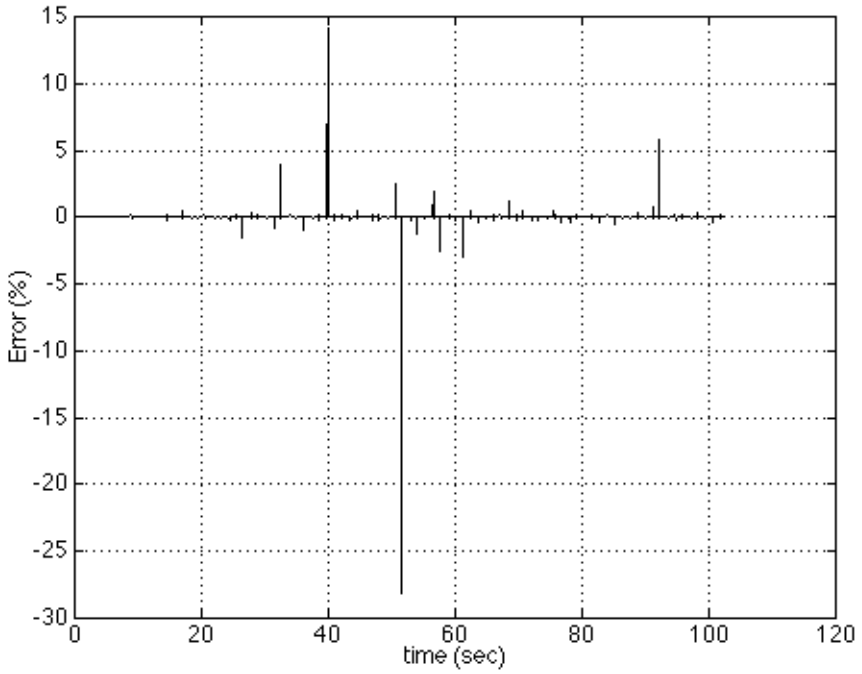

Figure 4.7: Percentage error in identified control surface pitch response

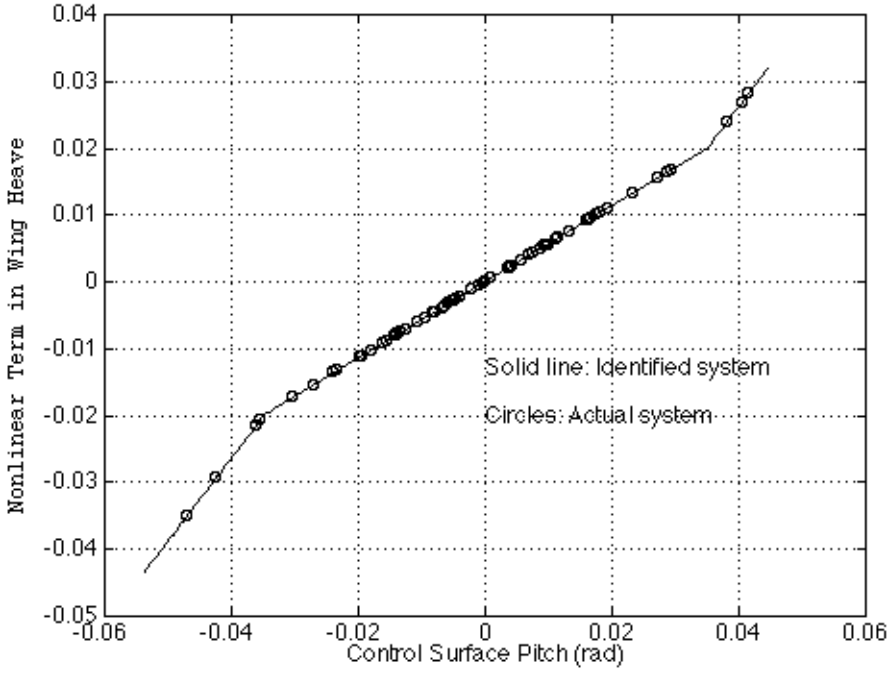

Figure 4.8: True and identified bilinear term in wing heave

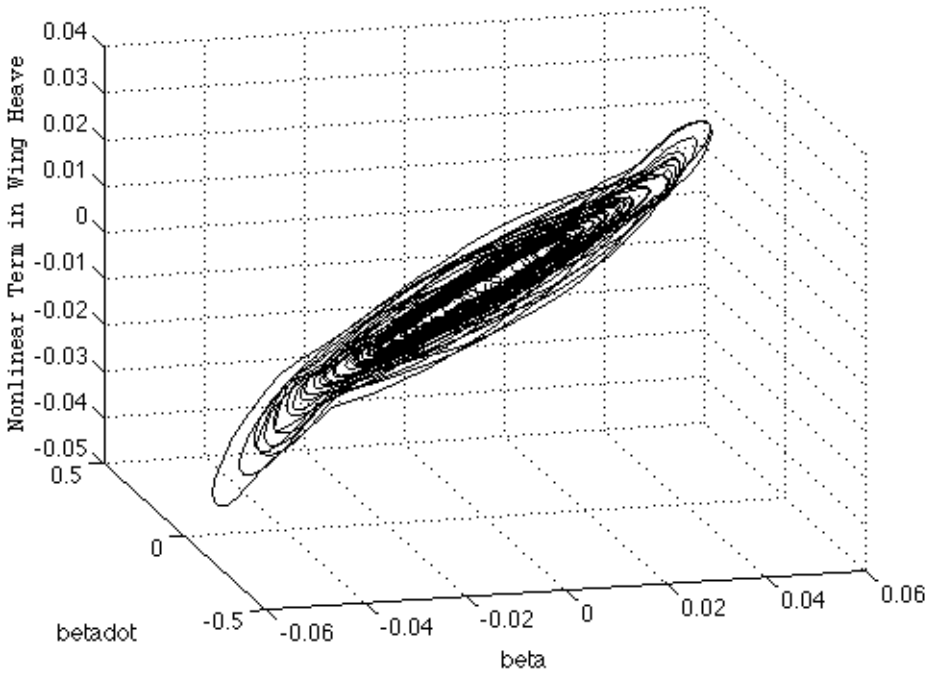

Figure 4.9: Wing heave bilinear surface

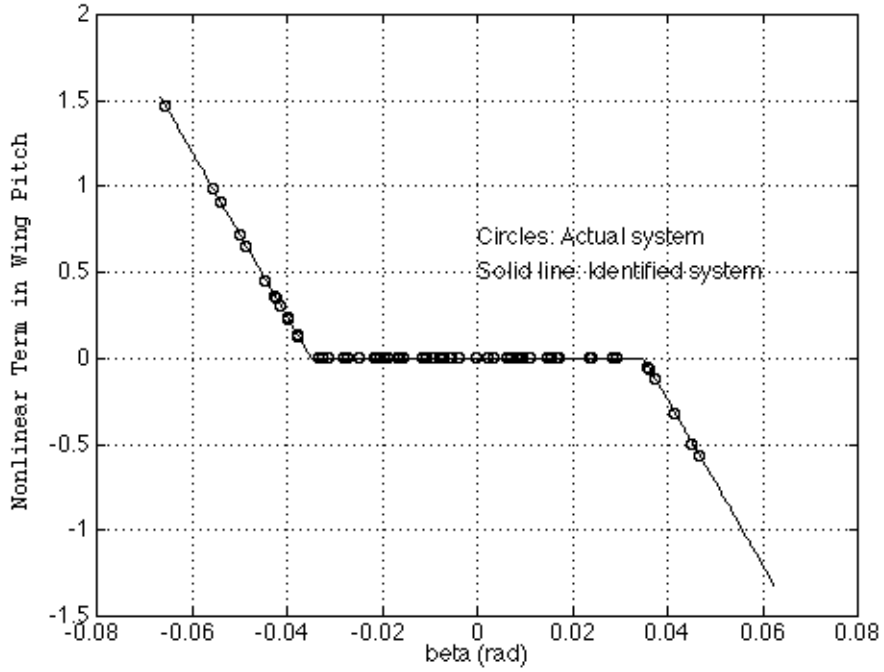

Figure 4.10: True and identified nonlinear term in wing pitch for freeplay

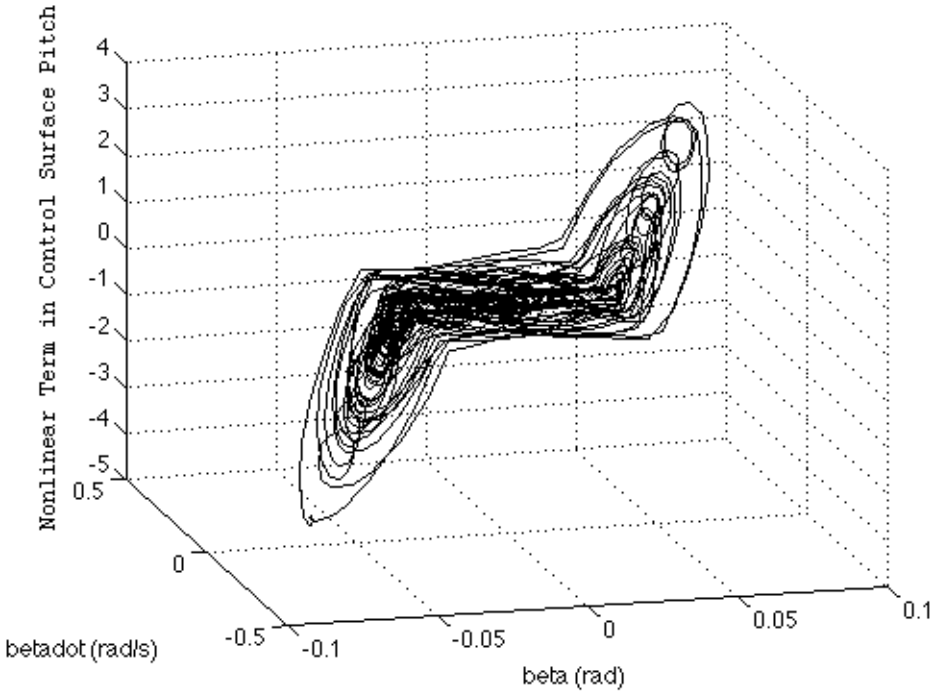

Figure 4.11: Wing pitch freeplay surface

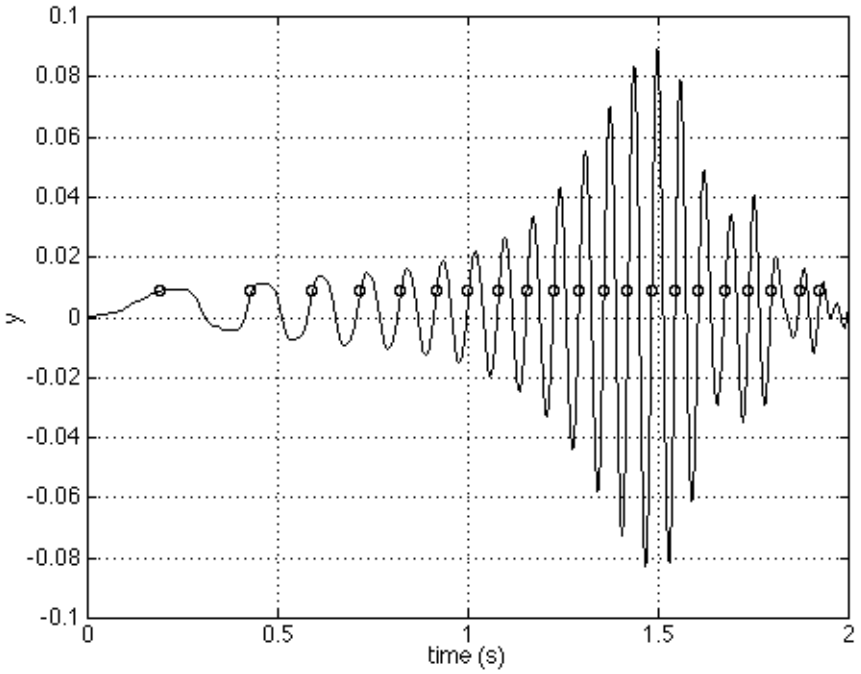

Figure 4.12: Constant level response points used in identification of hysteresis

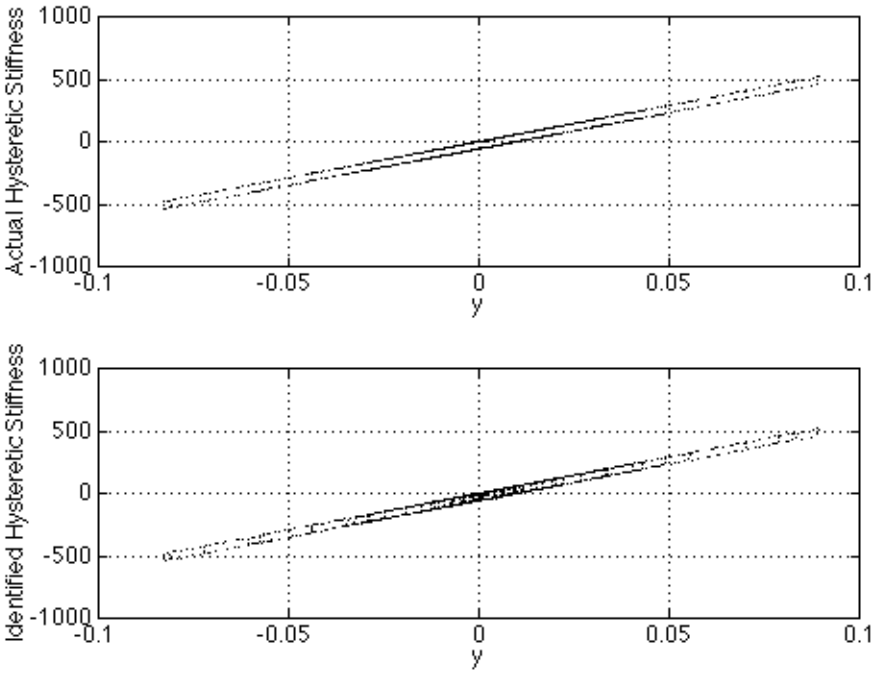

Figure 4.13: True and identified hysteretic stiffness

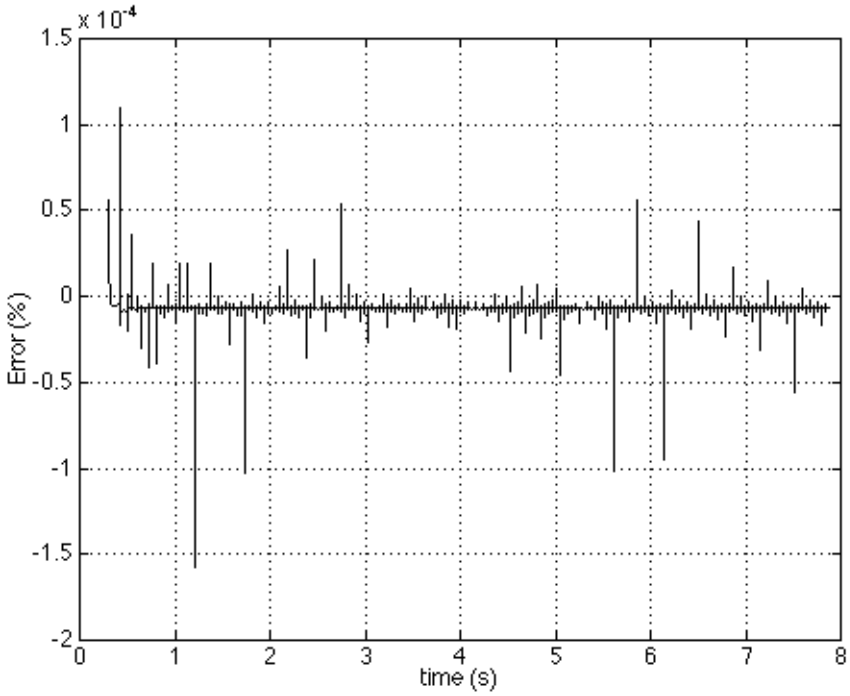

Figure 4.14: Percentage error in identification of hysteretic nonlinear term

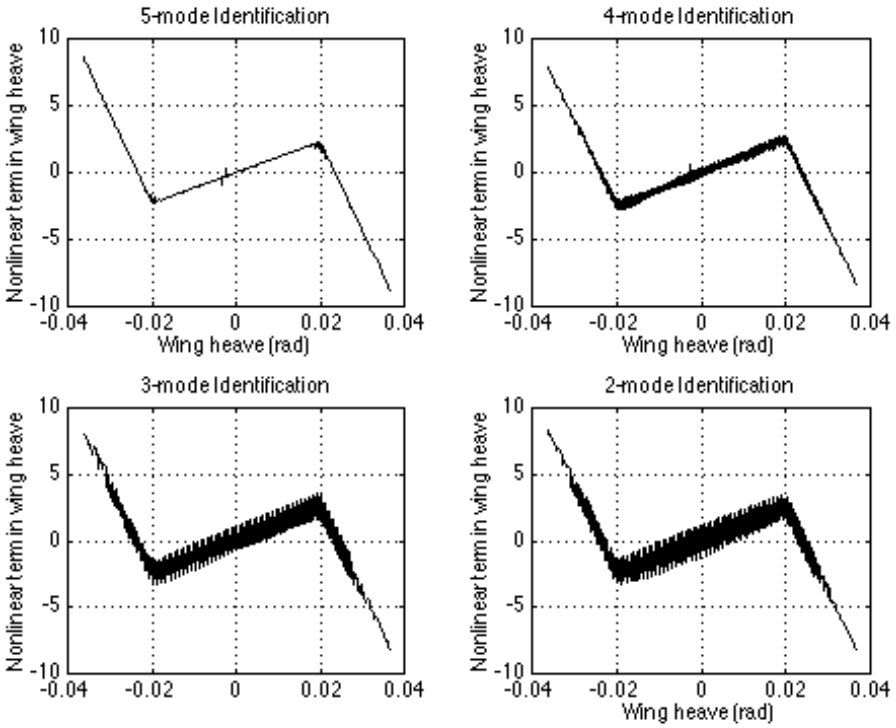

Figure 4.15: Identification of a 5-dof system with 5, 4, 3 and 2-mode models)

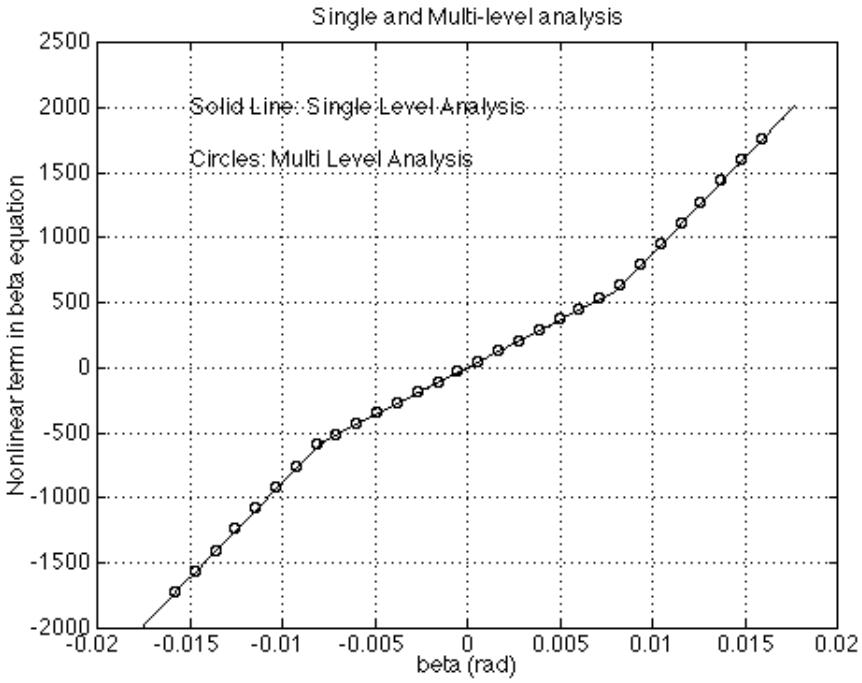

Figure 4.16: Comparison of 1-level and multi-level identification, no noise

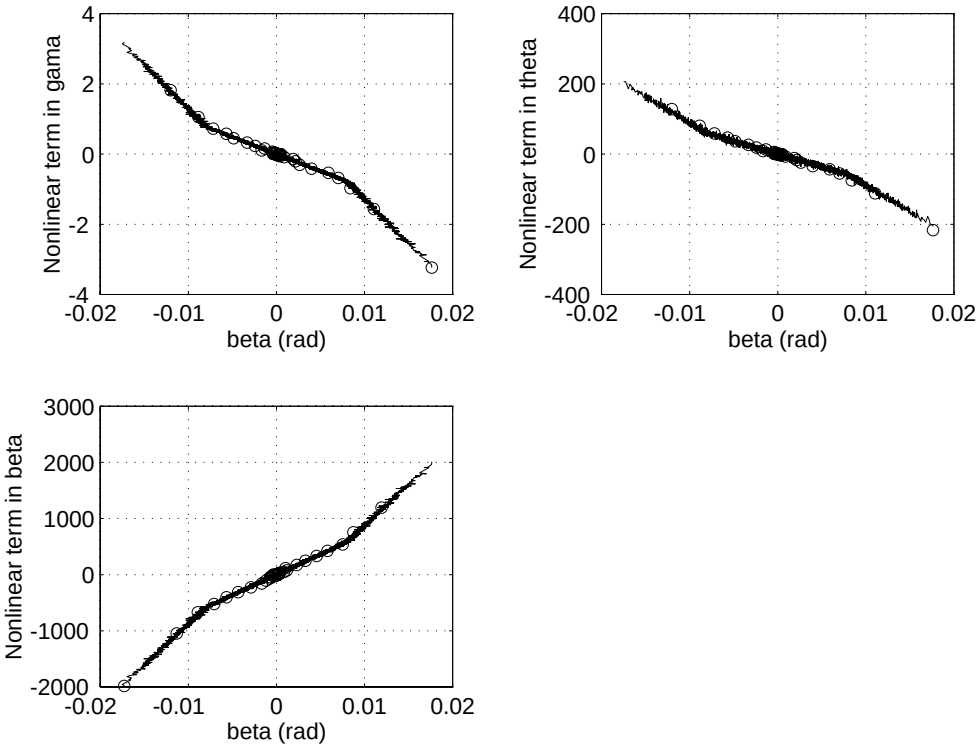

Figure 4.17: Quality of identification in the presence of 5% rms noise

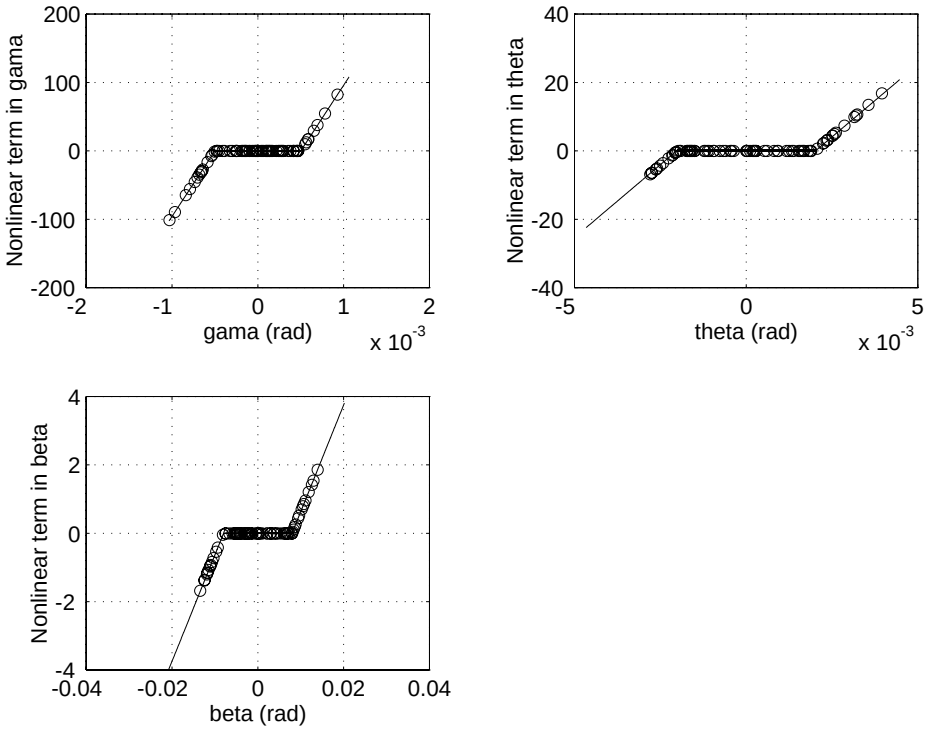

Figure 4.18: Identification of a system with three nonlinearities

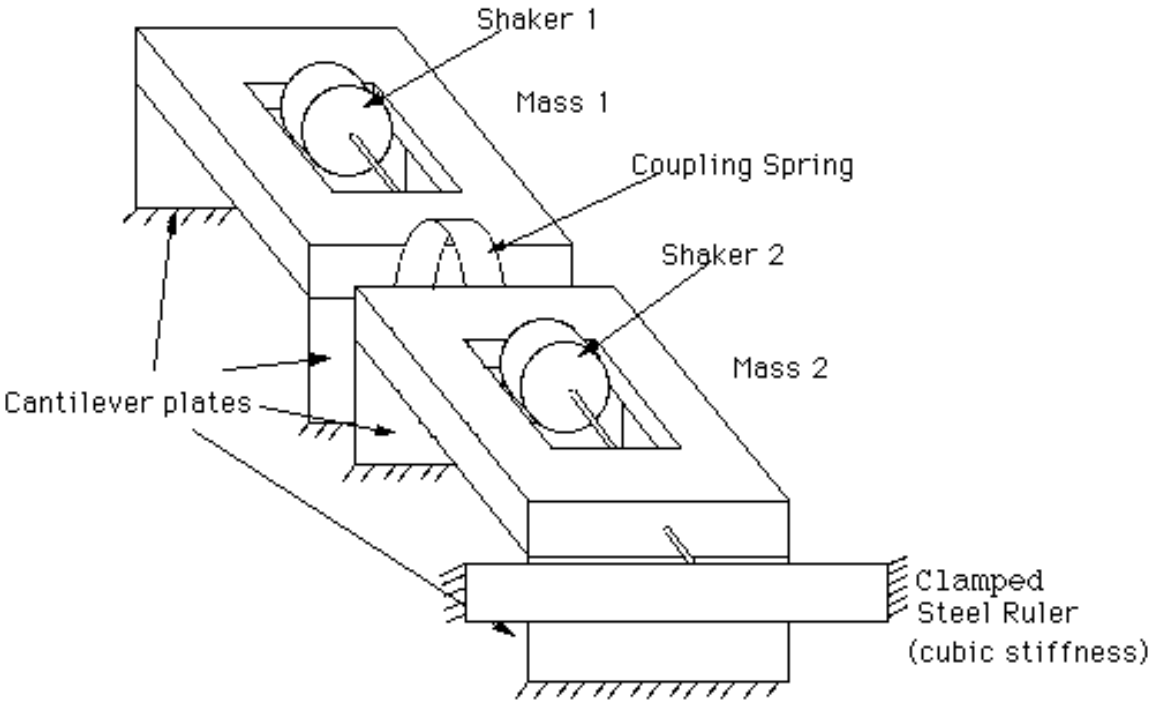

Figure 4.19: Experimental 2 DOF system layout

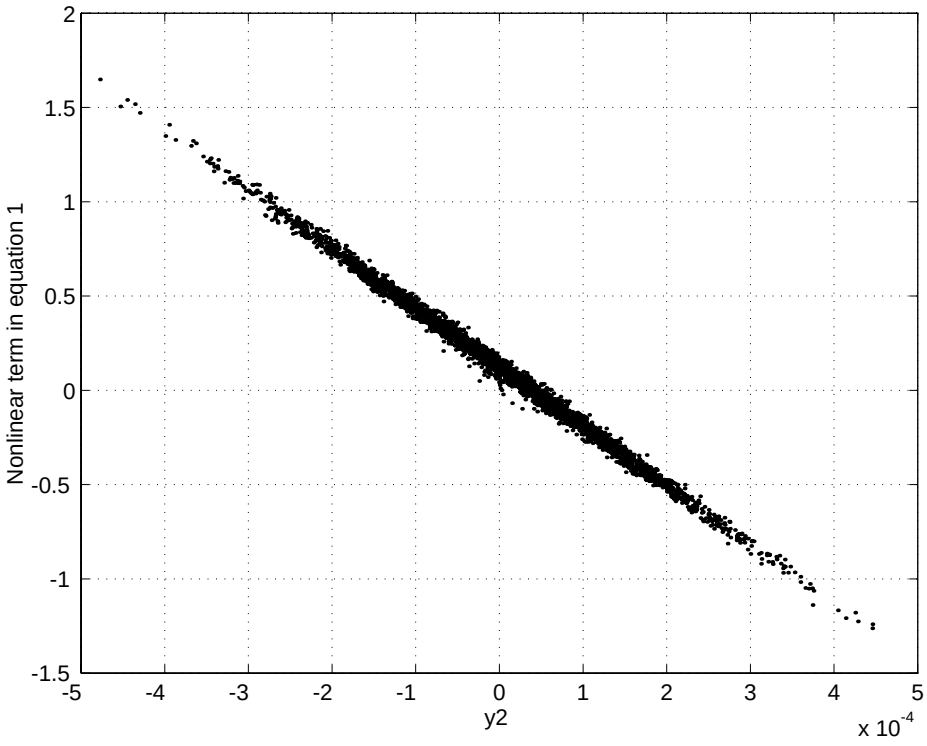

Figure 4.20: Linearised identification of 2DOF experimental system, mass 1

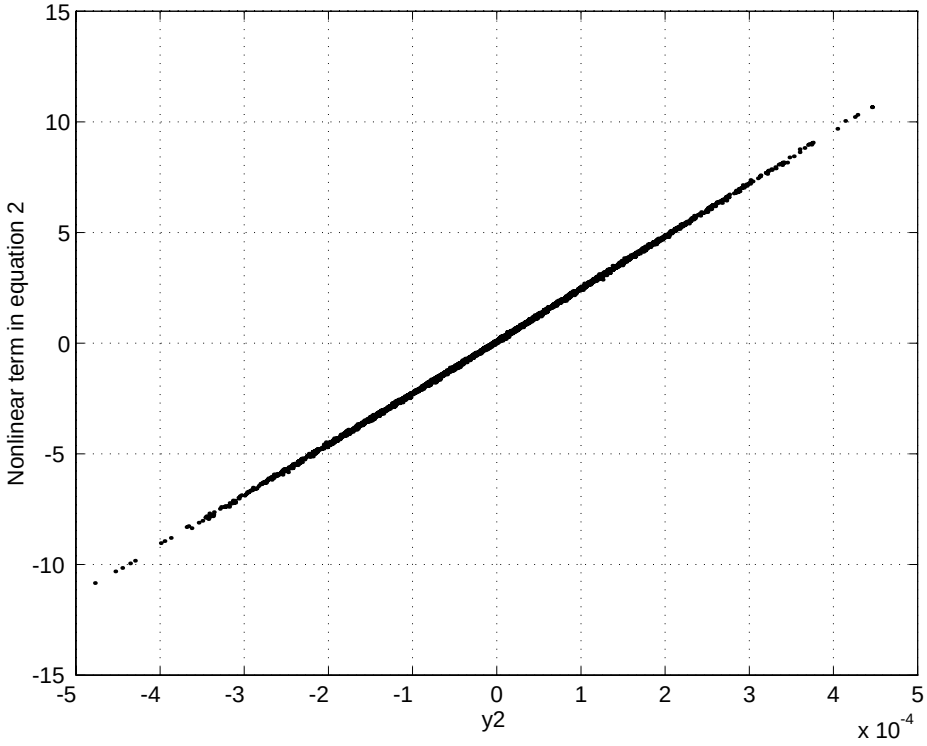

Figure 4.21: Linearised identification of 2DOF experimental system, mass 2

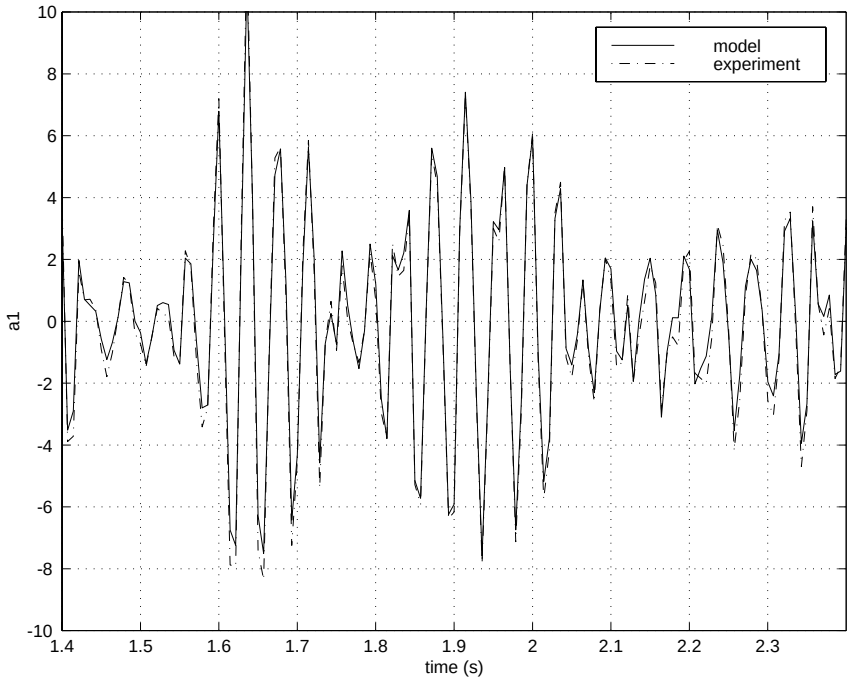

Figure 4.22: Comparison of experimental and identified responses, mass 1, linearised

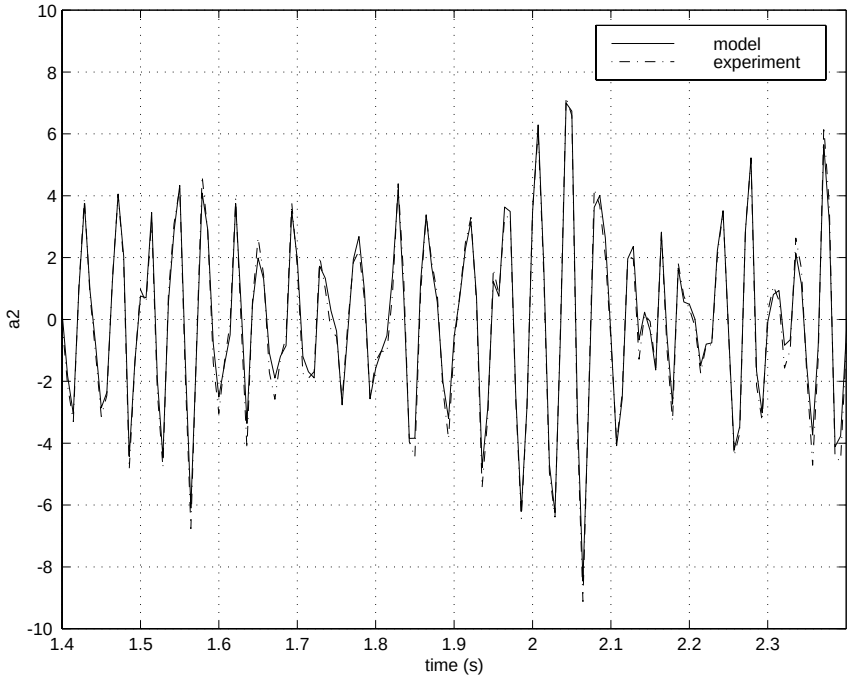

Figure 4.23: Comparison of experimental and identified responses, mass 2, linearised

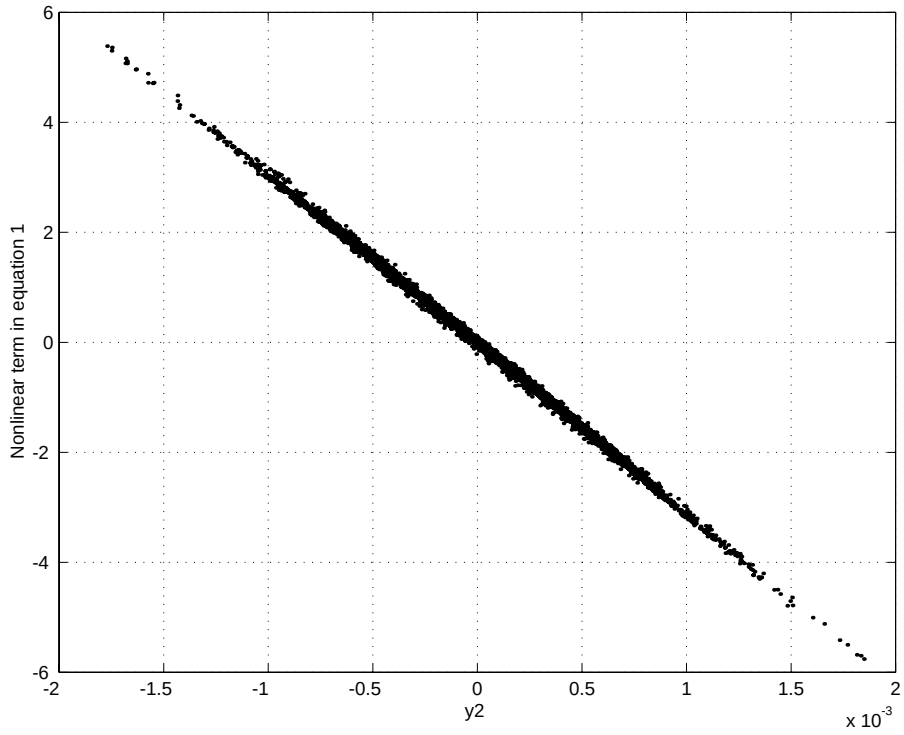

Figure 4.24: Nonlinear term in equation 1

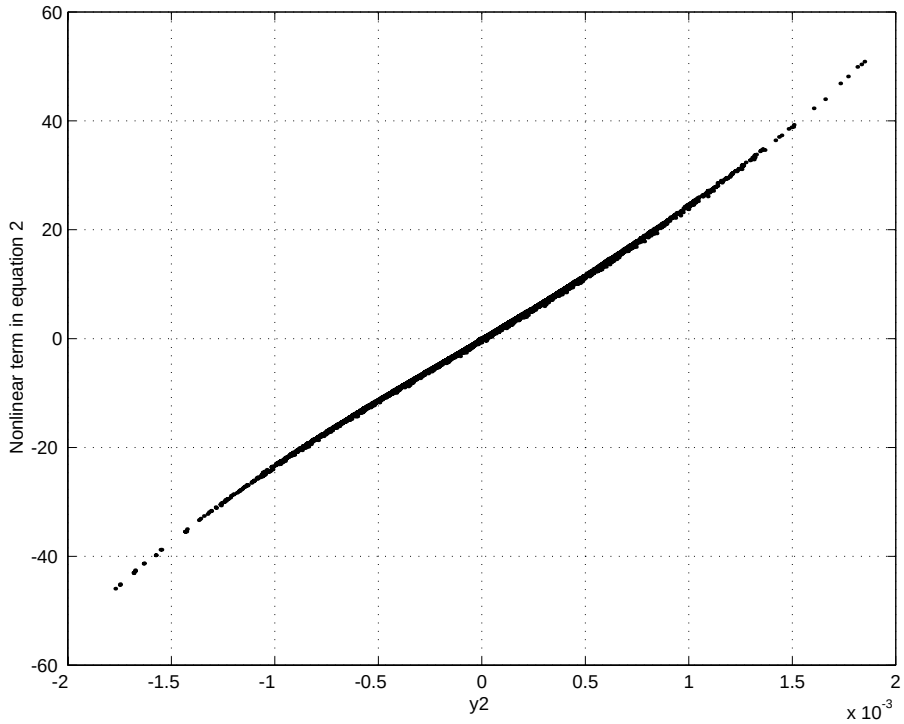

Figure 4.25: Nonlinear term in equation 2

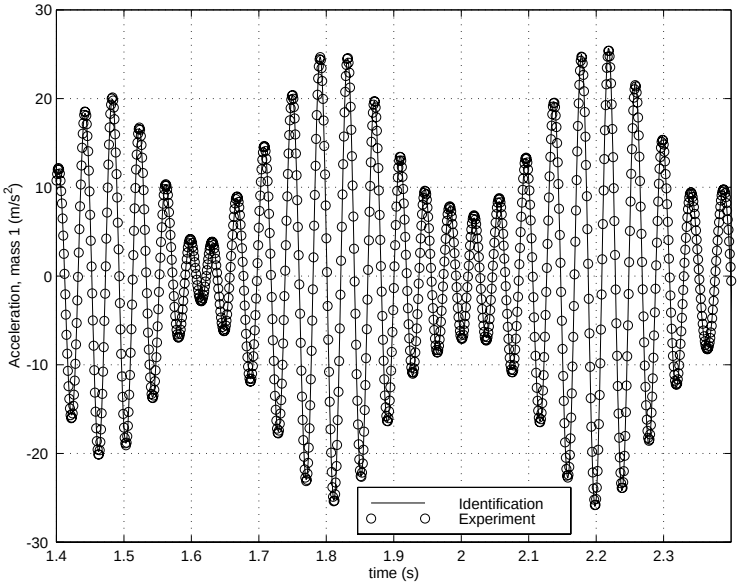

Figure 4.26: Comparison of experimental and identified (CL) responses, mass 1

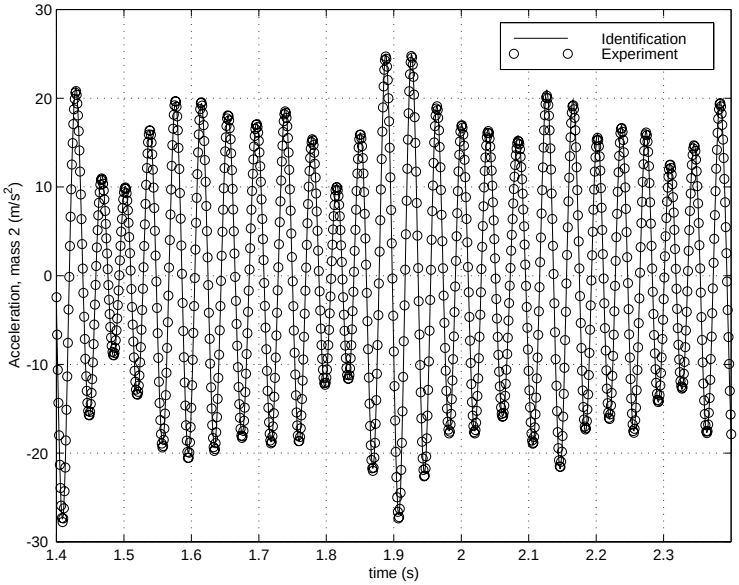

Figure 4.27: Comparison of experimental and identified (CL) responses, mass 2

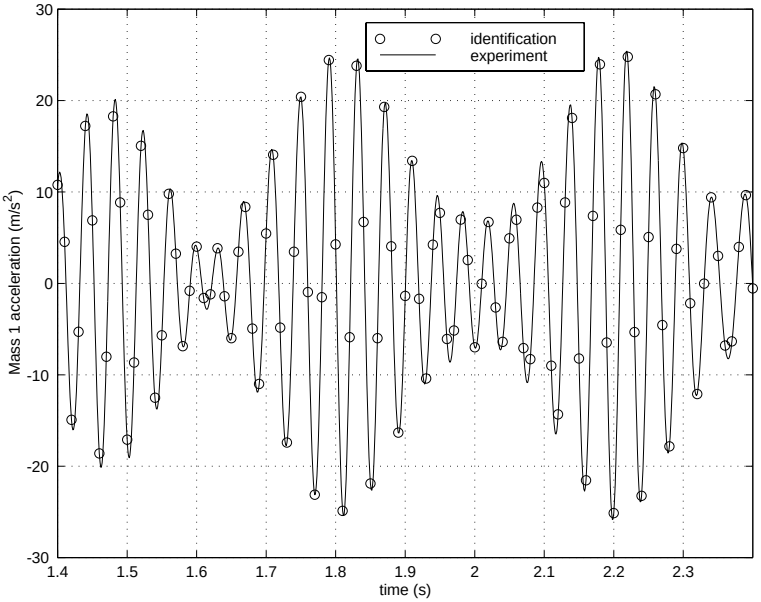

Figure 4.28: Comparison of experimental and identified responses (NARMAX)

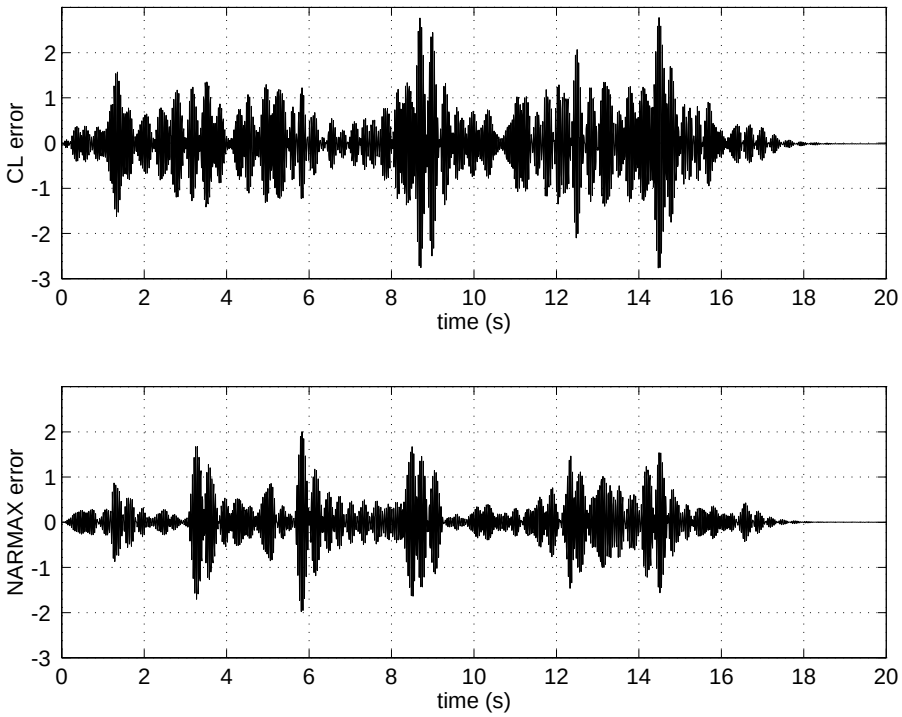

Figure 4.29: Comparison of CL and NARMAX error

Chapter 5

Gust Load Response of Nonlinear Aircraft

5.1 Introduction

Atmospheric turbulence affects negatively the performance of aircraft (both military and civil) in various ways. A few of these are:

- A Need to avoid regions of severe atmospheric turbulence.
- Ride roughness can cause discomfort and accidents to both crew and passengers.
- The shortening of aircraft life time due to metal fatigue and increased need for aircraft inspection.
- Possible temporary or total loss of aircraft control with severe consequences. Reference [64] describes a number of incidents where aircraft sustained significant structural damage or even crashed as a result of encounters with Clear Air Turbulence (CAT).

For a more detailed description of all the hazards caused by atmospheric turbulence see [65], which focuses on the special case of military aircraft and the introduction to [8].

Since very early in the history of aviation, aircraft designers have been aware of the dangers associated with loads caused on airplane structures by atmospheric turbulence. Consequently there has a been a sustained effort to calculate these loads and to set suitable airworthiness requirements for design loads. References [66] and [64] describe the evolution of both methods for modelling atmospheric turbulence and of setting requirements.

Of particular recent interest is the calculation of the load response of an airplane when it contains non-linearities in either the structure or in the control system. There are various methods for predicting the load response of linear aircraft (as will be described later) to atmospheric turbulence, however, non-linear aircraft cause a greater challenge because they preclude superposition.

The first part of this chapter will focus on a description of the turbulent atmosphere, and the second part will focus on gust-analysis methods for non-linear aircraft. All methods are compared on two simulated aircraft, a simple one, commonly known as the Noback aircraft, and a more complex model, called the "universal" A310 model.

5.2 Turbulent gusts and their mathematical description

In general, atmospheric turbulence can be modelled by either of two categories:

- Continuous turbulence
- Discrete gusts

5.2.1 Continuous turbulence

The structure and properties of continuous turbulence varies with the altitude of the flight-path. In general, the lower the altitude, the more complicated the structure is [8]. To better explain this, it is necessary to briefly describe some aspects of the engineering simplifications that are used to model turbulence. First of all, it should be noted that the main difficulty with turbulence modelling is the 'closure problem', that is, the fact that there are less describing equations than unknowns. This necessitates various assumptions to be made about the structure of turbulence.

It is very useful to visualize turbulence as a group of interacting eddies or structures of varying size and kinetic energy. Then, the largest eddies are responsible for the transport of momentum and kinetic energy, which is provided by the mean flow. Some energy is passed on to successively smaller eddies until it is dissipated into heat by viscosity [67]. The size of the largest eddies, which is called the integral length-scale of turbulence, is what determines a lot of the properties and the suitable simplifications that can be applied to a given flow. At high altitude, the turbulent length-scales encountered are large. This means that the turbulent velocity over a passing airplane is constant, i.e. that only turbulent translation is important; rotation and strain are negligible. This allows a wealth of simplifications to be applied; The flow is treated as:

- frozen
- homogeneous
- isotropic and
- self-similar.

The frozen flow assumption is that turbulent velocities do not change during the time of passage of the aircraft [8]. A visual example of this is clouds which

take a long time to change shape or position, much longer than it takes for an airplane to pass through them. Homogeneity means that the mean turbulent kinetic energy present in each of the three translational velocity components is equal. Isotropic turbulence means that the structure of turbulence is independent of orientation, so that all average values (velocity, kinetic energy etc.) related to the eddies do not change under rotations or reflections of the coordinate system [67]. Self-similarity implies that velocity fluctuations at differing length scales are related by a simple scaling up or scaling down transformation. Self-similarity only holds true for intermediate length scales. At the bottom of the range (where energy is dissipated by viscosity) and the top (where most of the turbulent transport occurs) it is irrelevant. These simplifications allow the modeling of the spectrum of the turbulent flow using simple mathematical models like the Dryden or the Von Karman spectra. Since experimental evidence favours the latter [68], this report will not deal with the former. The Von Karman spectrum is given by [8], [69]

$$\begin{aligned} \Phi_{11}(\omega) &= \sigma_g^2 \frac{L}{\pi} \frac{1}{\left[1+\left(1.339\omega\frac{L}{V}\right)^2\right]^{\frac{5}{6}}} \\ \Phi_{22}(\omega) &= \Phi_{33}(\omega) = \sigma_g^2 \frac{L}{2\pi} \frac{1+\frac{8}{3}\left(1.339\omega\frac{L}{V}\right)^2}{\left[1+\left(1.339\omega\frac{L}{V}\right)^2\right]^{\frac{11}{6}}} \end{aligned} \tag{5.1}$$

where $\Phi_{11}(\omega)$ is the longitudinal spectrum, $\Phi_{22}(\omega)$ is the transverse spectrum, L is the length scale of turbulence and V is the horizontal airspeed, V is the free-stream velocity of the aircraft, ω is the angular frequency and σ_g is the turbulence intensity given by

$$\sigma_g^2 = \bar{u^2} = \bar{v^2} = \bar{w^2}$$

Hence, the turbulent spectrum is fully defined with the determination of L, V and σ_g. The turbulent length scale can be calculated using either the area

under a correlation curve or a fit to spectrum. These two methods give very different results, the problem being aggravated by the choice of experimental data used for the calculations. A value that is usually acceptable is $L = 762m$ $(2500\ ft)$, (U.S. Air Force specifications [8]). The same specification requires that the highest value of σ_g is $2.1m/sec$ for Clear Air Turbulence or $6.4m/sec$ for storm turbulence. $\Phi_{22}(\omega)$ is plotted in figure 5.1 for $\sigma_g = 2.1$ m/s.

It should be noted at this point that empirical evidence [64] suggests that structural loads due to transverse velocity perturbations are more significant than those due to longitudinal ones. Hence, most gust loads calculations use the $\Phi_{22}(\omega)$ spectrum.

As a result of the assumption mentioned earlier, continuous atmospheric turbulence is most often assumed to be a stationary Gaussian process with the Von Karman spectrum. Mathematically, it can be modelled as a white noise signal of unity variance passed through a filter with Von Karman characteristics. Such a filter is [70]

$$G(s) = \sigma_g \sqrt{\frac{L}{\pi V}} \frac{[1 + 2.618\left(\frac{L}{V}\right)s][1 + 0.1298\left(\frac{L}{V}\right)s]}{[1 + 2.083\left(\frac{L}{V}\right)s][1 + 0.823\left(\frac{L}{V}\right)s][1 + 0.0898\left(\frac{L}{V}\right)s]} \tag{5.2}$$

where s is the Laplace variable. Instead of using a filter, the white noise signal can be convoluted with the Frequency Response Function representation of the transverse Von Karman spectrum [71]

$$G(\omega) = \sqrt{\frac{L}{\pi V}} \frac{1 + \sqrt{\frac{8}{3}}\left(1.339 i\omega \frac{L}{V}\right)}{\left(1 + 1.339 i\omega \frac{L}{V}\right)^{\frac{11}{6}}} \tag{5.3}$$

The procedure would then be to take the Fourier transform of the signal, multiply by $G(\omega)$ and then take the inverse Fourier transform.

The analysis described above is adequate for high altitude turbulence with moderate to severe turbulent intensity. For low altitudes a different approach

must be followed since the assumptions mentioned above can not be as readily made. But even at high altitudes, for extreme turbulence intensity, the analysis breaks down [69], [72]. The cause of this is that, for these extreme cases, the assumption of self-similarity is no longer valid. The behaviour of the flow changes from self-similar to intermittent (patches of laminar and turbulent flow) with decreasing scale. For this special case a fractal method of analysis was proposed in [72].

This work will not deal with the topic of low altitude gust response, since the problem is further complicated by changes in the aircraft configuration (flaps, landing gear etc), which are beyond the scope of this project.

5.2.2 Discrete gusts

Discrete gusts are isolated steep gradients in the horizontal or vertical air-speed. They usually occur at the edges of thermals, wakes of mountains and temperature inversions [8]. Even though they are highly structured compared to the chaotic background turbulence, they are assumed to exhibit some turbulent characteristics. They are usually approximated by simple mathematical functions like steps, ramps, impulses and $1 - cos$ or combinations of these.

Discrete gusts can be viewed as parts of a continuous turbulence 'signal' even though they stand out from the rest of the background turbulence. Even in the case of pure continuous turbulence without significant discrete events, there are certain parts of the turbulent signal felt by the aircraft which cause the highest loads on the structure. Consequently, when seeking to calculate worst-case loads on aircraft, it makes sense to search for these discrete patches of extreme turbulence rather than treat extreme turbulence as a stationary random process [73].

Accordingly, most recent methods for predicting gust loads on nonlinear aircraft are based on seeking the discrete gust, or family of discrete gusts that will cause the largest response. Discrete gusts can be modelled in many ways. The most common are

- Ramp gusts
- 1-cosine gusts
- Sections of a white-noise signal
- Spectral gusts

All these gust models are so-called one-dimensional models. In general, a turbulent event will consist of velocity fluctuations in the vertical, lateral and longitudinal directions. However, a particular load on an aircraft is usually associated with one of these components whose variation over the aircraft can be neglected. As a consequence, the search for worst-case gusts centres on such one-dimensional models. Figure 5.2 shows examples of ramp, 1-cosine and white noise gusts. Figure 5.3 shows all four spectral gusts [74].

Ramp Gusts

Ramp gusts are ramp variations in gust velocity caused by discrete pulses in the velocity gradients. The model arises from the reasoning that peaks in aircraft response to a gust depend more on increments in velocity gradient than the actual magnitude of the gust velocity itself [75]. Important quantities describing a ramp gust are the total duration of the pulse, Δt, and the maximum value of the velocity gradient. Combinations of smooth ramp gusts can be employed to describe the self-similar variation of a turbulent velocity component.

1-cosine Gusts

1-cosine gusts are the most straightforward description of the extreme variation of a turbulent velocity component. The velocity gradient first increases, then decreases back to its original value or vice-versa. Consecutive 1-cosine gusts can be used to describe a more complex variation in a velocity component. This particular discrete gust model will be further analysed later in the section on the Statistical Discrete Gust (SDG) method.

Sections of a white-noise signal

The rationale behind this particular model is based on the model of continuous turbulence. Certain sections of a white noise turbulent excitation will cause a peak response in an aircraft load. It stands to reason that these sections will contain some of the characteristics present in a "worst case" discrete gust. Hence, a discrete gust is modelled as a section of a white noise signal leading up to a high peak in the aircraft load response. The magnitude of the peak load response will depend on the chosen value for the turbulence intensity, σ_g.

Spectral Gusts

All three of the models described above are either deterministic functions of time or position or random functions. As such, they do not contain the appropriate characteristics that describe turbulent events. Spectral gusts are designed to contain these characteristics, such that their power spectral density is close to the power spectral density of atmospheric turbulence. They are evaluated by taking the inverse Laplace transform of existing gust filters, either the Von-Karman or the Dryden filter [76]. Spectral gusts evaluated from the Von-Karman filter are given by

$$u_G(t) = \pm c_0 \sqrt{\frac{TV}{L}} e^{\frac{-t}{T_0}} \left(\frac{t}{T_0}\right)^{-\frac{1}{6}} \left(1 - c_1 \frac{t}{T_0}\right) \tag{5.4}$$

where $c_0 = \frac{5/6\sqrt{8/3}}{\Gamma(11/6)}$, $c_1 = 6/5\left(1 \pm \sqrt{3/8}\right)$ and $\Gamma(11/6) = 0.9407, T_0 = 1.339\frac{L}{V}$, V is the free-stream velocity, $T = \frac{L}{V}$ and L is the length-scale of atmospheric turbulence. Equation 5.4 defines four spectral gust shapes due to the $\pm$ signs. All four of these shapes are shown in figure 5.3. Spectral gusts will also be treated in a later section on the Spectral Gust Method.

5.3 Methods for nonlinear gust load prediction

There are two main categories of gust load prediction methods for nonlinear aircraft. The first is stochastic methods which rely on generating long turbulence-like excitation signals and looking for peak values in the load response of the aircraft. The second category is deterministic methods which rely on deterministically identifying the one single discrete gust shape that will cause an adverse load response.

Gust load prediction methods attempt to calculate design and correlated loads. A design load is a load which has a finite but low probability of being exceeded, usually given by airworthiness requirements. A correlated load is the value of a load, say z, when another load, say y, assumes its design value.

5.3.1 Probability of Exceedence Criteria

The Probability of Exceedence Criteria (PEC) method [77] is an extension of the Power Spectral Density method (PSD) for nonlinear aircraft. The PEC is stochastic and attempts to calculate design loads. The procedure is as follows [78] & [77]:

1. The flight conditions at which the design loads are to be evaluated are

prescribed and values of U_σ and b_2 are determined from the airworthiness requirements (b_2 is a coefficient used in the expression for the probability that the load will exceed the design load - its variation with altitude can be found in [68]).

2. A representative value of the rms gust intensity, σ_{wr}, is computed using

$$\sigma_{wr} = b_2 \sqrt{\frac{1 + \sqrt{1 + 4(U_\sigma / b_2)^2}}{2}} \tag{5.5}$$

3. An input white noise signal with σ_{wr} is generated, passed through a gust pre-filter and fed into the nonlinear aeroelastic model. The resulting load time history for load y is used to calculate the probability that the design load will be exceeded in a turbulent flow-field of intensity σ_{wr} using

$$P(y > y_d, \sigma_{wr}) = \frac{1}{\sqrt{2\pi}\bar{A}\sigma_{wr}} \int_{y_d}^{\infty} \exp\left(-\frac{y^2}{2\bar{A}^2\sigma_{wr}^2}\right) dy d\sigma_{wr} \tag{5.6}$$

where $\bar{A} = \sigma_y / \sigma_{wr}$.

4. The design load is defined as the value of the load for which

$$P(y > y_d, \sigma_{wr}) = \frac{1}{2} erfc\left(\frac{U_\sigma}{\sqrt{2}\sigma_{wr}}\right) \tag{5.7}$$

where $erfc$ is the error function complement.

Instead of calculating the probability distribution of load y, it is possible to obtain the design load by estimating the number of exceedences, N, of this load given by [79]

$$N = \frac{T_{tot}}{dt} P(y > y_d, \sigma_{wr})$$

where T_{tot} is the total length of the simulation (in seconds) and dt is the time step. Then, the array containing the load response y is sorted from higher to

lower values and the design load is the Nth element of the sorted array. If N is not an integer, linear interpolation can be used to obtain the design load. This procedure is demonstrated in figure 5.4, where the PEC method is applied to the A310 model (see Appendix H).

According to [77], this procedure only gives an estimate of the nonlinear design load which may be substantially different to the real value. The estimate can be improved by repeating the procedure for two values of σ_w at which the value of the following quantity is the same

$$\exp\left(-\frac{\sigma_w^2}{2b_2^2}\right) erfc\left(\frac{U_\sigma}{\sqrt{2}\sigma_w}\right)$$

Then, the design loads obtained for these two values of gust intensity can be combined with the initial estimate such that

$$y_d = 0.5y_d(\sigma_{wr}) + 0.25y_d(\sigma_{w1}) + 0.25y_d(\sigma_{w2}) \tag{5.8}$$

In reference [79], it is suggested that, instead of three simulations with three different values of σ_w, only one simulation with $\sigma_w = U_\sigma/2.5$ can be performed. The results will be adequate in the altitude range of 22,000ft-35,000ft since, in this range, the value of σ_{wr} is very close to $U_\sigma/2.5$. This latter approach is also adopted in the present work since it is suggested that increasing the total simulation length at one value of σ_w improves the quality of the design load predictions by a larger amount than increasing the number of simulations at different values of σ_w.

The correlated loads can be obtained using

$$P(z > z_c | y = y_d) = 0.5 \tag{5.9}$$

i.e. the probability of load z to be higher than the correlated load, z_c, when load y assumes its design value is 0.5. This is implemented by extracting the value of z at all the time instances were $y = y_d$. The probability distribution of these

values is then calculated and the correlated load is obtained as the load whose probability is 0.5. As with the design load, the correlated loads can be obtained using the number of exceedences instead of the probability distribution.

Since the PEC input to an aeroelastic model is stochastic turbulence, modelled as white noise, in order for the method to work accurately, long simulation times are needed so that the variance of the input is as close as possible to σ_w and its mean is almost zero. However, the advantage that this method has over some of the less computationally demanding discrete gust methods is that the airworthiness requirements concerned are more uniformly defined [68].

Application of the Method and Examples

The method was applied to the Noback and A310 aircraft models (see Appendix H). The design values of the loads for the two models are given in table 5.1.

Noback aircraft	
Load1	Load2
$10.83 m/s^2$	$6.33 m/s^2$
A310 aircraft	
Load2	Load3
$2.8711 \times 10^6 lb.ft$	$2.4608 \times 10^5 lb.ft$

Table 5.1: Design loads by the PEC method for the Noback and A310 models

5.3.2 Matched Filter based 1-Dimensional search

Matched Filter Theory (*MFT*) was originally developed as a tool used in radar technology [70]. The main objective of the method is the design of a filter such that its response to a known input signal is maximum at a specific time, which makes it suitable for application to gust response problems. The method can only be applied to linear systems because it makes use of the principle of superposition

which does not apply to nonlinear systems. However, by applying a search procedure, it can be adapted to provide results for nonlinear aircraft. The method is deterministic.

Brief Description of the Method

The technique is quite simple and consists of the following steps [70],[71], also graphically depicted in figure 5.5

1. A unit impulse of a certain strength K_g is applied to the system.
2. The unit impulse passes through a pre-filter describing gust turbulence (usually the Von Karman Gust pre-filter).
3. The pre-filtered input is fed into the aircraft model and the response of the various loads is obtained (e.g. wing root bending and torsional moments).
4. The response of the load whose design value is to be estimated is isolated, reversed in time, normalized by its own energy and multiplied by U_σ, the design gust velocity (which is determined by airworthiness requirements [68]).
5. The resulting signal is the input that maximizes the response of the chosen load for this particular impulse strength, K_g. It is then fed back into the system (first the Gust pre-filter, then the aircraft model) in order to obtain the response of the load whose design value is to be estimated and also the responses of the other loads (which are termed the correlated loads).
6. The procedure is repeated from step 1 with a different K_g

The characterization of the method as one-dimensional refers to the variation of K_g. The end result is a graph of peak load versus initial impulse strength. The maximum of this function is the design load and the gust input that causes it is

termed the Matched Excitation Waveform. It must be mentioned at this point that the method does not guarantee that the maximum load for a nonlinear aircraft will be obtained. As was found in [60], the variation of peak load with initial impulse strength for some types of nonlinearities (e.g. freeplay and bilinear stiffness) does not display a global maximum (instead it slowly asymptotes to a certain value). This fact is corroborated by [78].

Application of the Method and Examples

The method is here applied to the Noback and the A310 models. The Matlab implementation of the MFB 1-D method was kindly supplied by Dr W.J. Vink of the NLR, National Aerospace Laboratory, Holland.

Figure 5.6 shows the variation of design loads with increasing linearized gain for the Noback aircraft. Figure 5.7 shows the variation of design loads with increasing linearized gain for the A310 aircraft. The design values of the loads for the two models are given in table 5.2.

Noback aircraft	
Load1	Load2
$10.720 m/s^2$	$6.541 m/s^2$
A310 aircraft	
Load2	Load3
$2.824 \times 10^6 lb.ft$	$2.373 \times 10^5 lb.ft$

Table 5.2: Design loads by the MFB 1-D for the Noback and A310 models

Figures 5.8- 5.9 show the design load variations for the two Noback aircraft loads with the respective gust velocity variations. Figures 5.10- 5.11 show the design load variations for two of the four A310 aircraft loads with the respective gust velocity variations.

5.3.3 Deterministic Spectral Procedure

This method was first proposed by Jones [80]. In its most general form it is based on the assumption that there exists a single deterministic input function that causes a maximum response in an aircraft load. It states that a design load on an aircraft can be obtained by evaluating the load response to a family of deterministic gust inputs with a prescribed constraint. In practice, this implies a search for the worst case gust, subject to the constraint that the energy of the gusts investigated is constant. The method is deterministic. The procedure consists of the following steps:

1. A model input shape in the time-domain is generated.
2. The input shape is parameterized to produce a set of describing coefficients
3. The coefficients are used to generate the input waveform
4. The energy of the input is constrained by dividing the signal by its rms value
5. The constrained waveform is fed into a turbulence pre-filter and next through the nonlinear aircraft system
6. The aircraft load response is assessed. If it has not been maximized the coefficients that generate the input are changed and the process is repeated from step 3.

This iterative procedure requires a constrained optimization scheme, to ensure that the maximum load has been obtained, and a model input shape. The optimization scheme proposed in [80] is simulated annealing [81]. Another approach, proposed in [71] is to convert the constrained optimization problem to an unconstrained one by means of the Kreisselmeier-Steinhauser function.

As for the generation of the initial input shape, two approaches have been proposed. In [75] a white noise gust model is used. The problem with this approach is that it is more difficult to parameterize a random signal than a deterministic one. In [71] the MFT 1-dimensional search results are proposed as the input to the DSP loop which results in what is called the MFT multi-dimensional search procedure.

The parameterization process is probably the most crucial aspect of the DSP method. Input waveforms have to be described by a minimum number of coefficients to minimize computational cost but this description has to be as accurate as possible. Again, two popular procedures can be found in the literature. The first one [75] is to fit the waveform by a number of half-sinusoid (or cosinusoid) functions. The other approach is to fit the waveform using a set of Chebyshev polynomials [71]. In the same reference, a Fourier series approach was considered but it was found to be much more computationally expensive. One further approach has been tried by the present author, namely the use of a sum of exponentially decaying sinusoids. This requires much fewer coefficients than any of the other methods mentioned above, however, when used in conjunction with the matched-filter based scheme can only be successfully applied to linear systems. The waveform fitted is the output of the system (reversed and normalised) and, in the case of a nonlinear system, can not be fitted in such a way.

The most common implementation of the DSP method is the Multi-Dimensional Matched Filter Based method which is described next.

5.3.4 Multi-Dimensional Matched Filter Based Method

The Multi-Dimensional Matched Filter Based (*MD-MFB*) method [82], [71] for gust load prediction for nonlinear aircraft is a practical application of the Deterministic Spectral Procedure proposed by Jones in [80]. It was designed to provide

a more computationally efficient alternative to the Stochastic Simulation Based approach. Reference [71] shows how the method provides almost identical results to those obtained by use of the SSB but with less computational effort. The method is deterministic.

Brief description of the method

The MD-MFB approach revolves around the fact that the usual design envelope analysis can be reformulated as an exactly equivalent time-domain worst-case analysis. In other words, the search for a worst-case gust load in the presence of a turbulence field of prescribed intensity is equivalent to the search for a design load [75]. Hence, the simplest possible procedure for determining the worst-case load is to simulate very long patches of turbulence and to look within the load response of the aeroelastic system in question for the design load. This is the stochastic simulation approach and is, generally, regarded as computationally impractical.

The worst-case load problem can be simplified by noting that the significant part of a long turbulent signal that causes the maximum load is short and can be approximated as a discrete gust. Hence the MD-MFB method searches for the single discrete worst-case gust waveform thus avoiding the need for long simulation times.

The implementation of the method is as follows, also depicted graphically in figure 5.12:

1. An initial guess for the worst-case gust waveform (or *matched excitation waveform*) is obtained by use of the 1-dimensional MFB procedure.

2. The initial guess is parameterized. In the present application the parameterization scheme used is Chebyshev Polynomials (see appendix E).

3. The values of the various parameters are changed and the resulting waveform is fed into the aeroelastic system (including a turbulence pre-filter as described earlier).

4. The resulting maximum load is compared to the previous value for the worst-case gust load and is accepted or rejected according to some optimization procedure. The optimization procedure used for the present application is Simulated Annealing [81] (see appendix F). The procedure is repeated, i.e. the parameters are changed again resulting in a new gust waveform which is then used as an input to the system, until the worst-case gust load is obtained.

Application of the Method and Examples

Once the initial gust waveform has been parameterized, it is reconstituted from its parameters and fed into the aeroelastic system under consideration to provide the initial value for the design load. Since the simulated annealing algorithm works best when used on minimization problems, the cost function used in equation F.1 is chosen to be the inverse of the maximum load. Then the procedure is as follows:

1. One of the N Chebyshev weights is randomly chosen

2. A random number between 0 and 1 determines whether the weight is going to be increased or decreased with equal probability, i.e. if the number is less than 0.5 then the weight will be decreased and vice versa.

3. A different random number between 0 and 10 determines how much the weight is going to be varied by.

4. The new waveform is calculated, fed into the system and the new cost function evaluated.

5. Equation F.1 is applied and the new state is either accepted or rejected.

6. Steps 1-5 are repeated until a given number of states has been accepted or rejected. Then the temperature is decreased by a set amount and steps 1-6 are repeated.

7. The optimization process is terminated when the ratio of the number of rejected states to that of accepted states reaches a certain low value. The last accepted state defines the worst-case gust load and the corresponding gust waveform is the worst-case gust input.

It is obvious that the correct application of the algorithm depends on a number of settings namely the initial value of the temperature, the temperature decrement, the number of states to be evaluated between temperature decrements and the termination criterion. As a consequence, the application of the method is very laborious and needs to be repeated until the best settings are found. Additionally, as mentioned earlier, the procedure needs to be repeated for a certain number of initial gust waveforms.

However, it is argued here that since the initial guess is already the result of an optimization procedure, the application of the MD-MFB can be simplified. It can be assumed that the initial design load is already close to the global maximum and hence a small initial value for the temperature can be used. As a consequence, mainly improved states are accepted and the number of accepted states is limited, hence accelerating the occurance of the termination criterion. Additionally, the need for repeating the procedure with different initial conditions is eliminated. After a number of applications of the method to the Noback aircraft, it was found that the biggest improvement on the design load was approximately 4.9% of the initial guess and was obtained by using a relatively high initial temperature. Using a low initial temperature the best improvement obtained was 4.4% but with huge savings in computational cost.

Figures 5.13- 5.15 show the results of a sample application of the MD-MFB method. Figure 5.13 shows the convergence history of the procedure, culminating in an improvement of around 4.2% on the design load. Figure 5.14 shows the initial and worst-case gust waveform. The initially 'noisy' shape of the latter is due to the randomness in the optimization procedure. Since that part of the waveform is not critical as far as the design load is concerned, it remains more or less random. Figure 5.15 shows the initial and optimized load response of the Noback aircraft. Note that, despite the fact that the system is nonlinear, the maximum load occurs very close to the point where the excitation waveform reaches a maximum. It can also be seen that the initial noise in the optimized gust waveform causes a very subdued response. The design loads predicted by the MFB M-D method for both aircraft models considered here, are tabulated in table 5.3.

Noback aircraft	
Load1	Load2
$11.46 m/s^2$	$7.017 m/s^2$
A310 aircraft	
Load2	Load3
$2.826 \times 10^6 lb.ft$	$2.379 \times 10^5 lb.ft$

Table 5.3: Design loads by the MFB-MD method for the Noback and A310 models

A notable disadvantage of the multi-dimensional search is the fact that a large number of coefficients is needed in order to parameterize high frequency waveforms. This was especially a problem for the A310 model, where load 3 contains relatively high frequencies. The most important side-effect of this was that numerical difficulties with convergence were encountered, of the same type as those reported in [78].

5.3.5 Statistical Discrete Gust Method

The Statistical Discrete Gust Method (*SDG*) has been introduced as a method that employs a better description of atmospheric turbulence than the Power Spectral Density method for extreme gusts on linear aircraft [73], [77], [83]. This description is based on families of discrete 1-cosine ramp gusts. The present description of the SDG methodology is based on a similar description in [77]. It should be noted that the method was developed as an attempt to bridge the gap between continuous turbulence and discrete gusts methodologies and is being continuously refined, most recently with the use of wavelets. The SDG calculates design loads.

Brief Description of the Method

Figure 5.16 shows a single discrete gust, as used by the SDG method. Initially, its velocity increases in a 1-cosine fashion until, at a distance H, it levels out to the value U which is given by

$$U = U_0 H^{1/3} \tag{5.10}$$

if H is less than L, the length-scale of turbulence, and

$$U = U_0 L^{1/3}$$

if $H \geq L$. The value of U_0 is decided by the equivalence of the design value of σ_g in the continuous turbulence PSD analysis to the SDG analysis as [83]

$$U_0 = \frac{\sigma_g}{10.4}$$

where σ_g is obtained from the airworthiness requirements [68].

For extreme turbulence the scaling of equation 5.10 changes to

$$U = U_0 H^{1/6} \tag{5.11}$$

This is how the SDG methodology can bridge the gap between continuous turbulence and discrete gusts. Continuous turbulence is assumed to be self-similar, which is where the 1/3 scaling law comes from. Self-similarity can be modelled as a stretching transformation. In the time-domain, if the time axis is stretched by a certain amount, h, the dependent variable, say $y(t)$, will be stretched by $h^{-\lambda}$. The similarity parameter λ can be chosen such that the function $h^{-\lambda}y(ht)$ is statistically independent of h. This value for λ can be obtained by considering the spectrum, $\Phi(\omega)$ of the process $y(t)$, when stretched by h, which in reference [69] is shown to satisfy

$$h^{-(2\lambda+1)}\Phi(\omega/h) = \Phi(\omega) \tag{5.12}$$

In the special case where the process $y(t)$ is turbulent, the Von Karman spectrum applies, i.e.

$$\begin{aligned}
\Phi_{11}(\omega) &= \sigma_g^2 \frac{L}{\pi} \frac{1}{\left[1 + \left(1.339\omega\frac{L}{V}\right)^2\right]^{\frac{5}{6}}} \\
\Phi_{22}(\omega) &= \Phi_{33}(\omega) = \sigma_g^2 \frac{L}{2\pi} \frac{1 + \frac{8}{3}\left(1.339\omega\frac{L}{V}\right)^2}{\left[1 + \left(1.339\omega\frac{L}{V}\right)^2\right]^{\frac{11}{6}}}
\end{aligned} \tag{5.13}$$

Simple algebra shows that the limit of both $\Phi_{11}(\omega)$ and $\Phi_{22}(\omega)$ as ω tends to infinity (which defines the inertial subrange where self-similarity applies) is

$$\lim_{\omega\to\infty}(\Phi) = A\omega^{-5/3}$$

where A is a proportionality constant. Equation 5.12 becomes

$$h^{-(2\lambda+1)} A \left(\frac{\omega}{h}\right)^{-5/3} = A\omega^{-5/3}$$

For this expression to be satisfied, h must vanish from the left-hand-side, or

$$-2\lambda - 1 = -\frac{5}{3}$$

Hence for continuous, self-similar turbulence, $\lambda = 1/3$, as in equation 5.10.

Discrete gusts are extreme events for which self-similarity breaks down. They are larger-scale and more ordered events than the background turbulence within which they are contained. The similarity parameter for such events is given by, [73]

$$\lambda = \frac{1}{3} - \frac{3 - D}{3}$$

where D is termed the active volume of turbulence and has values $2 < D \leq 3$. For $D = 3$ the standard self-similar value, $\lambda = 1/3$, is obtained. For a value of $D = 2.5$, the extreme turbulence similarity parameter is obtained, $\lambda = 1/6$, as in equation 5.11. Hence, with a simple change in the scaling law, the SDG method can be made also applicable to extreme turbulent events like discrete gusts.

At a particular value for the gust-length, H, the nonlinear aeroelastic system under consideration will exhibit a maximum load response. The maximum value of this maximum response, $\bar{\gamma}_1$ is an estimate for the design load, y_{d1}. A second estimate is obtained using a pair of gusts as shown in figure 5.17. Here, there are three parameters that govern the gust shape, H_1, H_2 and the spacing between the two gusts, S. The values of these parameters are varied until the maximum, $\bar{\gamma}_2$, is obtained. Another two estimates for the design load are calculated using two pairs of gusts and four pairs of gusts. Finally, four design loads are calculated using

$$\begin{aligned} y_{d1} &= p_1 \bar{\gamma}_1 U_0 \\ y_{d2} &= p_2 \bar{\gamma}_2 U_0 \\ y_{d3} &= p_3 \bar{\gamma}_3 U_0 \\ y_{d4} &= p_4 \bar{\gamma}_4 U_0 \end{aligned} \tag{5.14}$$

with $p_1 = 1.0$, $p_2 = 0.81$, $p_3 = 0.57$ and $p_4 = 0.40$. For highly damped systems the first two design values are more important, for slightly damped ones the last two design values predominate.

For linear systems, estimating the maximum response due to SDG gusts is simple since superposition can be employed. For nonlinear systems this estimation can only be performed by means of an optimization scheme, especially for the longer gust-shapes. The optimization scheme chosen was again Simulated Annealing.

Application of the Method and Examples

The application of the SDG method can be divided into four steps, depending on the number of 1-cosine gusts present in each family of gusts.

- Step 1. One single 1-cosine gust
- Step 2. One pair of 1-cosine gusts
- Step 3. Two pairs of 1-cosine gusts
- Step 4. Four pairs of 1-cosine gusts

Each step can be performed separately. In the first and second steps, since only one and three parameters, respectively, determine the shape of the gust, it is more efficient not to use any optimization algorithms but to search the entire parameter space. This calculation is not as expensive as it sounds since, for a vertical gust, reference [83] suggests that the gust length should be between 30 and 500 ft. In the third and fourth steps, since the number of parameters is significantly higher, optimization has to be employed.

As mentioned earlier the Simulated Annealing procedure requires an initial guess for the gust shape that will cause the maximum response and ,consequently,

for the maximum response itself. In contrast with the application of the algorithm with the MFB method, when Simulated Annealing is applied to the SDG method, the initial guess can only be a set of random values for the various parameters that control the gust shape. Hence, in general, the initial guess will not be close to the gust causing maximum response, which can imply longer computation times. The procedure is as follows

1. Initial guess for the gust shape gives initial cost function
2. A random number decides whether one of the gust lengths, H, or one of the gust spacings, S will be altered.
3. A random number decides which of the gust lengths or spacings will be altered.
4. A random number between 0 and 1 determines whether the parameter is going to be increased or decreased with equal probability, i.e. if the number is less than 0.5 then the parameter will be decreased and vice versa.
5. A different random number between 0 and 1 determines how much the weight is going to be varied by (from 0% to 100% of the original value).
6. The new gust waveform is calculated, fed into the system and the new cost function evaluated.
7. Equation F.1 is applied and the new state is either accepted or rejected.
8. Steps 1-5 are repeated until a given number of states has been accepted or rejected. Then the temperature is decreased by a set amount and steps 1-6 are repeated.
9. The optimization process is terminated when the ratio of the number of rejected states to that of accepted states reaches a certain low value. The

last accepted state defines the worst-case gust load and the corresponding gust waveform is the worst-case gust input.

Preliminary applications of the SDG method to the Noback aircraft have revealed that the design values obtained by the single gust and single pair of gusts families give quite adequate results, while the optimization applications delivered only slight if not negligible increases in the design load. Figure 5.18 shows the evolution of maximum loads with increasing gust length for the SDG step 1. The maximum load for the centre of gravity acceleration caused by aileron action only is 6.4 which implies (using equation 5.14) that the design load predicted by step 1 is 6.4. The critical gust waveform and load responses are shown in figures 5.19 and 5.20.

The application of step 2 is depicted in figures 5.21- 5.22 which show critical gust waveform and resulting load response for the total acceleration, respectively. The maximum load is 8.4, for which, $y_{d2} = 6.8$. Hence step 2 has given an improvement in the design load.

Figure 5.23 shows the convergence history for the application of step 3. The basic feature of the Simulated Annealing algorithm is evident in this figure, i.e. that the jumps in cost functions accepted become smaller as the temperature increases. The maximum load obtained was 8.4 which is equivalent to $y_{d3} = 4.8$. The corresponding critical gust profiles and load response are shown in figures 5.24-5.25.

The convergence time history for step 4 is shown in figure 5.26. The number of accepted states is much higher than for step 3, reflecting the increased complexity of the optimization problem. The maximum load obtained is again 8.4. This corresponds to $y_{d4} = 3.4$. As a consequence steps 3 and 4 do not deliver any improvements to the design load predicted by step 2.

5.3.6 Indirect Deterministic Power Spectral Density Method

The Indirect Deterministic Power Spectral Density method (*IDPSD*) [84], [85], is derived from the Design Envelope Analysis [68] of the continuous Power Spectral Density method. For linear aircraft it yields design loads equal to those obtained by the PSD method but using a deterministic input, in a similar way to the linear MFT method. For nonlinear systems it can be extrapolated to a 1-dimensional search procedure, equivalent to the MFB 1-D search but involving a linearized representation of the system. The method is deterministic.

Brief Description of the Method

The IDPSD procedure is very similar to the MFB 1-D method with two main differences. Firstly, the IDPSD method uses a different gust filter and, secondly, the initial excitation is applied to a linearized version of the system whose output is then reversed, normalized and fed into the nonlinear system. Hence, the MFB 1-D method consists of a filtered impulse of variable strength fed into the nonlinear system, the resulting gust waveform being fed into the same system. In the IDPSD method, an initial input of constant strength is fed into a linearized system, called the first system, whose nonlinear element has been replaced by a variable gain. The resulting waveform forms the input to the nonlinear system, called the second system. The search procedure consists of varying the linear gain until the response of the second system is maximized. The IDPSD scheme is shown graphically in figure 5.27.

The input to the first system is given by $U_\sigma V(t)$, where U_σ is the design gust velocity and $V(t)$ is the Fourier Transform of the two-sided Von Karman Spectrum, $\Phi_{ww}(\omega)$, given by

$$\Phi_{ww}(\omega) = \frac{L}{V}\frac{1+\frac{8}{3}(1.339\omega\frac{L}{V})^2}{\{1+(1.339\omega\frac{L}{V})^2\}^2} \tag{5.15}$$

where ω is the radial frequency, L is the turbulence length-scale and V is the aircraft velocity [85]. This input can be alternatively defined as the Auto-Correlation function pertaining to $\Phi_{ww}(\omega)$ i.e.

$$V(t) = R_{ww}(t) = \frac{1}{2\pi}\int_{-\infty}^{+\infty} \Phi_{ww}(\omega)e^{j\omega t}d\omega \tag{5.16}$$

Equation 5.16 can be expressed in a more practical form as the Auto-Correlation function of the filtered MFB impulse,

$$V(t) = \frac{\overline{u_g(\tau)u_g(\tau+t)}}{\overline{u_g(\tau)^2}} \tag{5.17}$$

where u_g is the MFB filtered impulse gust velocity, the overbars denote averaging and τ is an integration variable. Figure 5.28 shows $U_\sigma V(t)$ obtained both by equations 5.15 and 5.17. The solid line is the Fourier Transform result and differs from the Auto-Correlation result (dotted line) in that it takes negative values away from the peak. As a consequence the Auto-Correlation result was preferred for the present work.

The IDPSD Method procedure is as follows:

1. $U_\sigma V(t)$ is formed, say using equation 5.17.

2. The input is fed into the linearized aircraft model with linear gain K and the response of the various loads is obtained (e.g. wing root bending and torsional moments).

3. The response of the load whose design value is to be calculated is isolated, convoluted by $V(t)$, normalized by its own energy and multiplied by U_σ, the design gust velocity.

4. The resulting signal is the input that maximizes the response of the chosen load for this particular linearised gain, K. It is then fed into the nonlinear

system in order to obtain the response of the load whose design value is to be calculated and also the responses of the correlated loads.

5. The procedure is repeated from step 2 with a different K.

Reference [84] suggests that the values of the linearized gain should be between 0 and 1.

Application of the Method and Examples

The Matlab implementation of the IDPSD method was kindly supplied by Dr W.J. Vink of the NLR, National Aerospace Laboratory of Holland. Figure 5.29 shows the variation of design loads with increasing linearized gain for the IDPSD aircraft. Figure 5.30 shows the variation of design loads with increasing linearized gain for the A310 aircraft. The design values of the loads for the two models are given in table 5.4.

Noback aircraft	
Load1	Load2
$11.03 m/s^2$	$6.72 m/s^2$
A310 aircraft	
Load2	Load3
$2.826 \times 10^6 lb.ft$	$2.465 \times 10^5 lb.ft$

Table 5.4: Design loads by the IDPSD method for the Noback and A310 models

Figures 5.31- 5.32 show the design load variations for the two Noback aircraft loads with the respective gust velocity variations. Figures 5.33- 5.34 show the design load variations for the two of the four A310 aircraft loads with the respective gust velocity variations.

5.3.7 Stochastic Simulation Based Method

The Stochastic Simulation Based method (*SSB*) models continuous turbulence as white noise input with a Von Karman spectrum, in the same way as the PEC

method. Hence, the SSB is stochastic and can predict calculate design loads, correlated loads and worst-case gusts, given a target value for the design load. The procedure is as follows [86]:

1. A Gaussian white noise signal with unity variance is generated and fed through a gust pre-filter, such as equation 5.2. The output of the filter is a time history of continuous turbulence data. The object is to identify segments of this time history that lead up to peak loads.

2. A number of long time-domain simulations are performed

3. The load time histories obtained from the simulations are analysed. Instances in time are isolated where the load exhibits a peak near a prescribed value or within a specified range. Then standard durations of time data leading up to the peak values are extracted, lined up in time and averaged. The result is 'averaged-extracted' time-histories of the excitation waveform (input to the gust filter), gust profile (section of turbulence data) and load. These have been shown to be directly equivalent to results obtained by the MFB methods [86] (see later section), if the value of the turbulence intensity (σ_g) is selected appropriately.

To ensure that there is an adequate number of extracted samples so that the final waveforms are as smooth as possible, very long simulations are required (1000 seconds are suggested in [86]). Long simulation times also ensure that the white noise input has a variance very close to unity and a mean very close to zero. Finally, the extraction and averaging process must take place separately for positive and negative peak load values.

The stochastic simulation method, as outlined here cannot be used on its own since it requires a target load to be specified, around which it will search for peaks in the load response. This target load value can be supplied by another

method. The authors of [86] used the MFB multi-dimensional search procedure to obtain the target design load value and picked peaks in the SSB load output within ±8% of that value. Of course, the object of their work was to show that the MFB results are equivalent to stochastic results. In a straightforward design loads calculation it would be extremely wasteful to use two of the most computationally expensive methods to produce the same results twice.

However, it is suggested here that the SSB method can be used to supplement results obtained by the Probability of Exceedence Criteria method. As mentioned earlier, the PEC method will only produce values for the design and correlated loads. It will not calculate time-variations of the loads or the gust velocity. The SSB, on the other hand can produce design and correlated load responses and critical gust waveforms. Hence, the PEC method can be used to yield a target value for the design load to be subsequently used with the SSB method.

Application of the SSB Method and Examples

The application of the SSB method is here illustrated on the A310 model (see Appendix H). Plots of the design, correlated loads and gust shapes are shown which were obtained using target loads from the PEC and the MFB 1-D methods. In both cases, total of 40 200-second-long simulations were performed, each one containing 8192 time-steps. Peaks were chosen which fell within ±2.5% of the target loads. The value of the turbulence intensity was chosen to be $U_\sigma/2.5$, as with the PEC method. Figure 5.35 shows the averaged-extracted load 2 variation with time together with the critical gust waveform. Figure 5.36 shows the averaged-extracted load 3 variation and gust shape. Figure 5.37 shows the correlated loads obtained using the two different target loads. The design values of the loads for the two aircraft models are given in table 5.5.

Noback aircraft	
Load1	Load2
$10.81 m/s^2$	$6.31 m/s^2$
A310 aircraft	
Load2	Load3
$2.8641 \times 10^6 lb.ft$	$2.4595 \times 10^5 lb.ft$

Table 5.5: Design loads by the SSB method for the Noback and A310 models

5.3.8 Comparison between the methods

Since the absolutely correct design load cannot be obtained for a nonlinear system, one of the methods has to be used as a benchmark. The benchmark for the comparison of the different methods reported in this work was chosen to be the Matched Filter Based 1-Dimensional search method. This choice was dictated by the relative simplicity of the method and by the fact that it is less computationally expensive than the other methods. However, the term "benchmark" does not imply that the design loads predicted by the MDB 1-D method are taken to be the best estimates but that there is no separate subsection on the MFB 1-D.

The graphical comparisons between the methods presented in this section are based on the following figures (unless otherwise stated).

- Figures 5.38- 5.39 show a direct comparison of maximum load variations and worst-case gust velocities obtained by the SSB, IDPSD and MFB 1-D method for the Noback aircraft model.

- Figure 5.40 compares correlated loads obtained by the three methods for the Noback model.

- Figures 5.41- 5.42 compare the load and gust shape predictions of the three methods on the A310 model.

- Figure 5.43 compares correlated loads obtained by the three methods for the Noback model.

SSB method

Despite the presence of a fair amount of noise in the SSB results, it is obvious that the agreement between its results and those of the two deterministic methods is very good. The only exception is the critical gust shape for Load2 of the Noback model (figure 5.39). The SSB result for this test-case agree more closely with the IDPSD Method results than with those calculated using the MFB 1-D.

The good agreement between the two deterministic methods and the SSB however, heavily depends on the choice of the value of the turbulence intensity, σ_g. The authors of [87] suggest that, in order to compare the two methods the value of the turbulence intensity used with the MFB scheme should be

$$\sigma_g = U_\sigma$$

where U_σ is the design gust velocity. For the SSB method, the suggested value is

$$\sigma_g = U_\sigma/3$$

As mentioned earlier, the turbulence intensity used during the course of this work was

$$\sigma_g = U_\sigma/2.5$$

This value, suggested in [79], was preferred to the $U_\sigma/3$ because it agrees more closely with the representative, σ_{wr} (see section 5.3.1), value at normal civil aircraft cruising altitudes.

IDPSD method

The agreement between the IDPSD and the MFB 1-D methods is, generally, very good. For the particular case of the worst-case gust for Load2 of the Noback aircraft (figure 5.40), the agreement breaks down to a certain extent. The figure

shows that the gust shape estimated using the IDPSD lies between the SSB and MFB 1-D gusts.

Since both the Noback and MFB 1-D methods are deterministic methods estimating worst-case gusts there is no problem with scaling the turbulence intensity value in order to get agreement between the two methods.

MFB Multi-Dimensional Search

Table 5.6 shows a comparison of results from the 1-dimensional and the multi-dimensional MFB searches, obtained from the Noback and A310 models. The table confirms what is claimed in [78] and [71], that the 1-dimensional search provides a very good estimate of the design load. The design loads for the Noback model have been improved upon by the MFB M-D method by up to 6.8%. However, for the A310 model, the improvement is almost negligible. The fact that the multi-dimensional search is much more computationally expensive but only delivers a small improvement in the final result suggests that the 1-dimensional search is more suitable, especially in the case of the gust-load prediction for a full aircraft, where the design loads need to be predicted at a very large number of stations over the whole aircraft.

Load	MFB 1-D	MFB M-D	% Improvement
Noback Load1	10.73 m/s^2	11.46 m/s^2	6.8
Noback Load2	6.55 m/s^2	7.02 m/s^2	6.7
A310 Load1	2.8242×10^6 $lb.ft$	2.8261×10^6 $lb.ft$	0.1
A310 Load2	2.3736×10^5 $lb.ft$	2.3793×10^5 $lb.ft$	0.2

Table 5.6: Comparison of design loads by the MFB-MD and MFB 1-D methods for the Noback and A310 models

Comparative Results

Tables 5.7 and 5.8 show design and correlated load predictions obtained by the SSB, MFB 1-D, PEC, SDG and IDPSD methods for both the aircraft models

under investigation. There are two sets of results for the SSB method, one obtained using the MFB design load as the target load and one using the PEC design load. The IDPSD method tends to predict slightly more conservative results than the MFB 1-D method. In the case of the Noback model the IDPSD results are closest to those obtained from the MFB M-D method. Since the SSB and PEC are stochastic, their design load predictions change slightly every time the calculations are performed. Consequently, there is no definitive way of determining whether these predictions are generally more or less conservative than the results obtained with the other two methods. However, it can be seen that the SSB results based on MFB target loads agree more closely with the MFB 1-D results and the SSB results based on PEC target loads agree more closely with the PEC results.

Another crucial conclusion drawn from the tables is that the design load predictions of the methods agree more closely with each other than the correlated load predictions. In reference [79] this phenomenon is also noted. Additionally, the author of [79] shows the cause of the phenomenon to be that the theoretical standard deviation of the design load will generally be smaller than the theoretical standard deviation of the correlated loads. It is not known, however, why this should also be the case with the deterministic methods.

Method	Design Load 1	Correlated Load 2	Design Load 2	Correlated Load 1	Number of flops	CPU time (s)
IDPSD	11.04	-2.00	6.72	-1.82	4492533	35.41
MFB 1-D	10.73	-2.77	6.55	-0.23	130633	16.07
MFB M-D	11.46	-2.77	7.02	-0.23	Variable	Variable
PEC	10.83	-2.24	6.33	-1.03	34005961	88.08
SDG	11.98	-3.23	5.98	-1.45	Variable	Variable
SSB(MFB)	10.73	-2.58	6.57	-1.80	67884692	185.13
SSB(PEC)	10.81	-2.31	6.31	-1.30	68054593	198.29

Table 5.7: Comparison of design and correlated loads predicted by various methods for Noback a/c (all loads in m/s^2)

Method	Design Load 2	Correlated Load 3	Design Load 3	Correlated Load 2	Number of flops	CPU time
IDPSD	2.8264×10^6	-5.5646×10^4	2.4649×10^5	-7.1880×10^5	2237174	24.45
MFB 1-D	2.8242×10^6	-5.1097×10^4	2.3736×10^5	-5.9080×10^5	66310	18.73
MFB M-D	2.8261×10^6	-5.1097×10^4	2.3793×10^5	-5.9080×10^5	Variable	Variable
PEC	2.8711×10^6	-4.4959×10^4	2.4608×10^5	-8.5987×10^5	34086207	100.93
SDG	2.7919×10^6	-4.1455×10^4	2.2386×10^5	-6.7905×10^5	Variable	Variable
SSB(MFB)	2.8229×10^6	-4.9609×10^4	2.4145×10^5	-6.6719×10^5	69251847	275.21
SSB(PEC)	2.8641×10^6	-5.6184×10^4	2.4595×10^5	-7.4691×10^5	69111494	274.85

Table 5.8: Comparison of design and correlated loads predicted by various methods for A310 (all loads in $lb.ft$)

The tables also compare the computational expense of the SSB, MFB 1-D, PEC and IDPSD methods. All the tests were performed on a PowerTower Pro 225, PowerMacintosh compatible computer with a 225 MHz 604e processor running MacOS 8.1, using Matlab Student Edition, version 4.1. Neither the CPU time nor the number of floating point operations (*flops*) figures are absolute. CPU time depends on the computer used and the software installed and the number of flops performed depends on the programming and on the routine that counts the flops. The Matlab manual makes it clear that its flop counting routine does not count all the flops. It specifically states that "It is not feasible to count absolutely all floating point operations, but most of the important ones are counted". Nevertheless there is a clear pattern to the results in the tables. The least computationally expensive method is the MFB 1-D and the most computationally expensive one is the SSB, with the IDPSD and PEC methods lying somewhere in between. The CPU time and number of flops for the multi-dimensional MFB and SDG methods are labeled "variable" in the table since the method relies on a directed random search. Hence, the duration of the calculations is different every time the procedure is applied, but always much longer than the duration of any of the other methods.

5.4 Figures

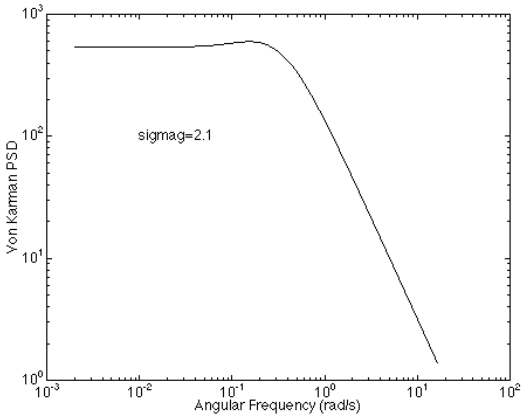

Figure 5.1: Von Karman Power Spectral Density (transverse)

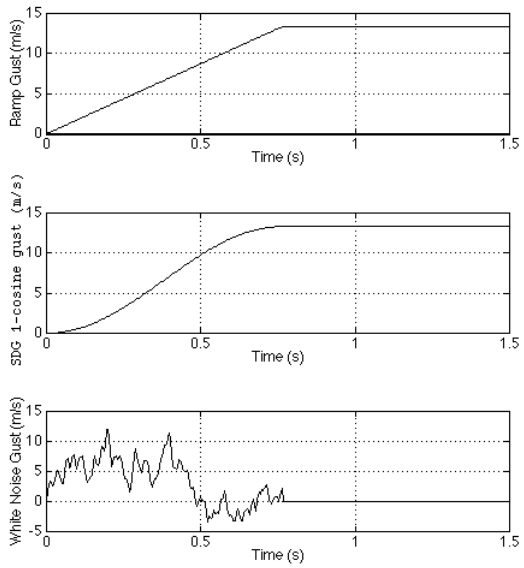

Figure 5.2: Examples of ramp, 1-cosine and white noise gusts

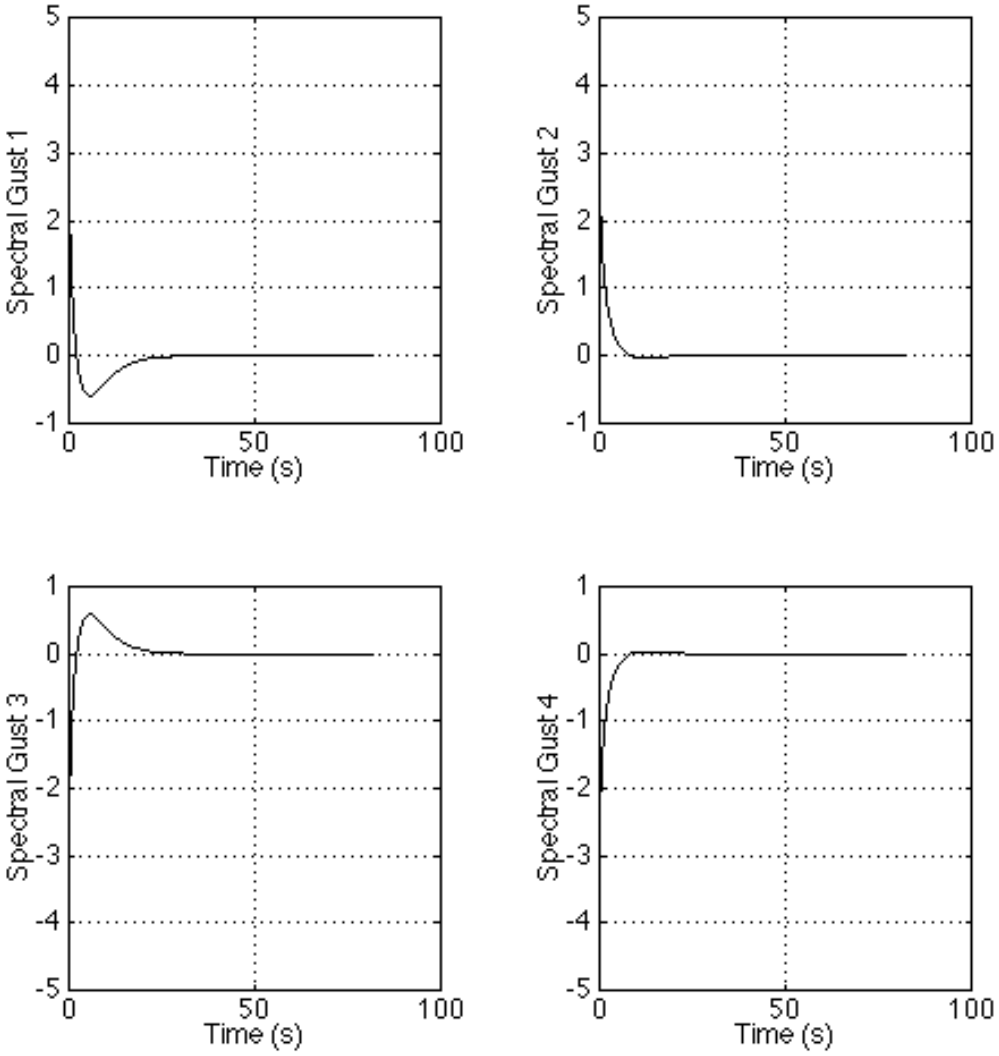

Figure 5.3: The four spectral gusts

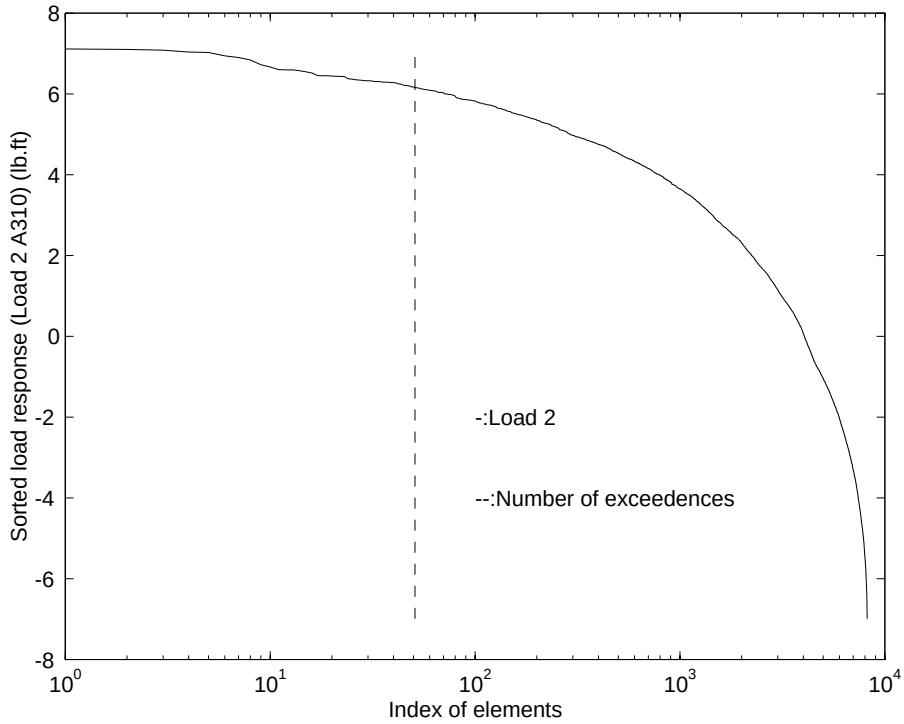

Figure 5.4: Selecting the design load with the PEC method

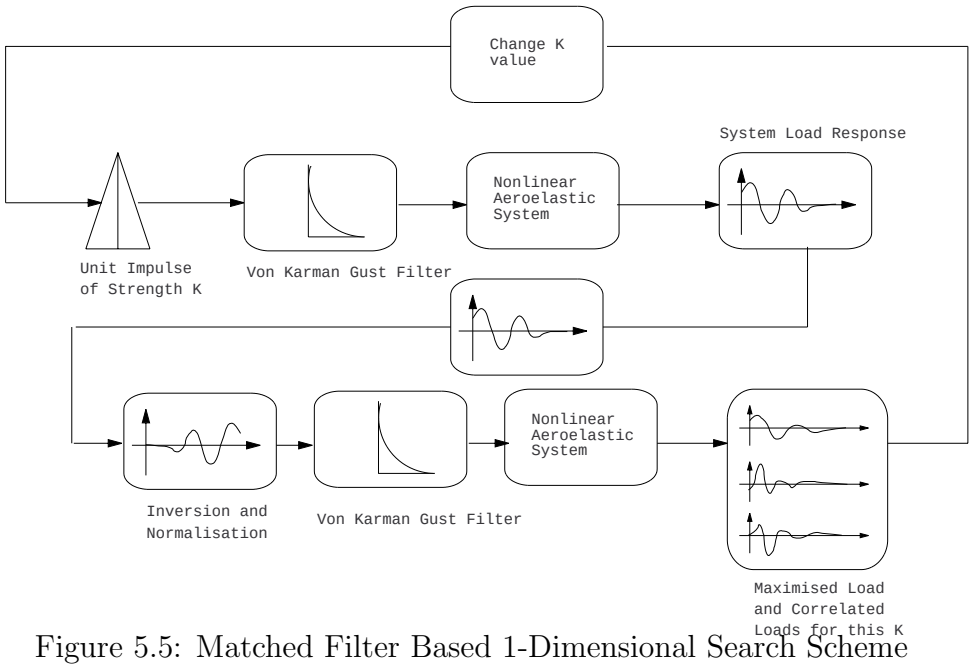

Figure 5.5: Matched Filter Based 1-Dimensional Search Scheme

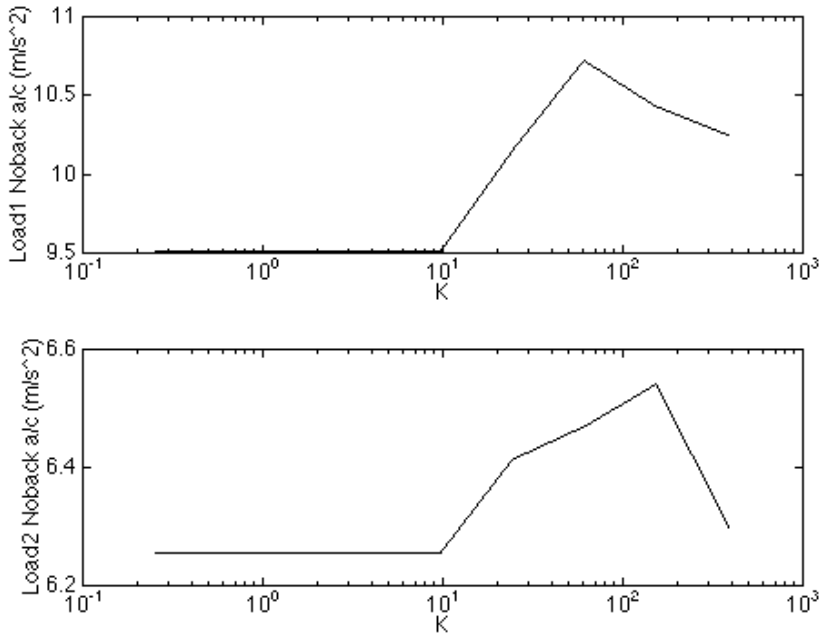

Figure 5.6: Variation of Maximum Loads with Impulse Strength for Noback aircraft, using MFB 1-D

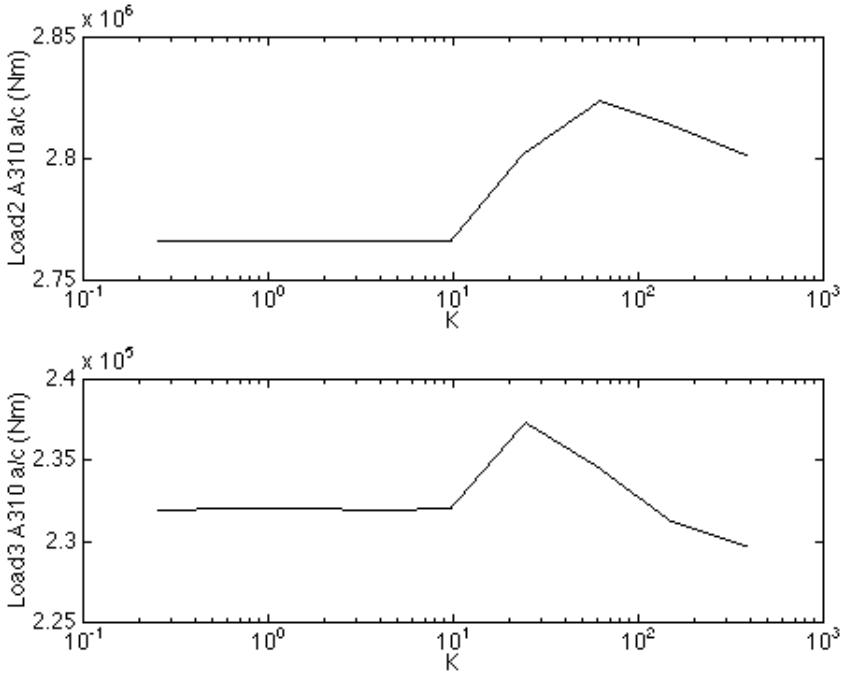

Figure 5.7: Variation of Maximum Loads with Impulse Strength for A310 aircraft, using MFB 1-D method

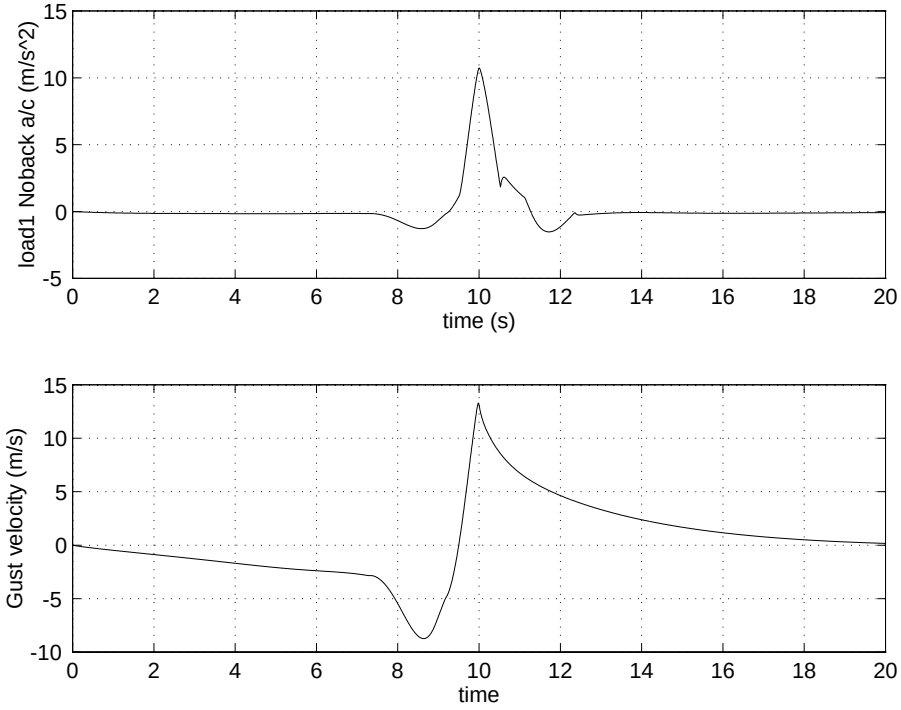

Figure 5.8: Design Load1 and critical gust shape for Noback a/c by MFB 1-D

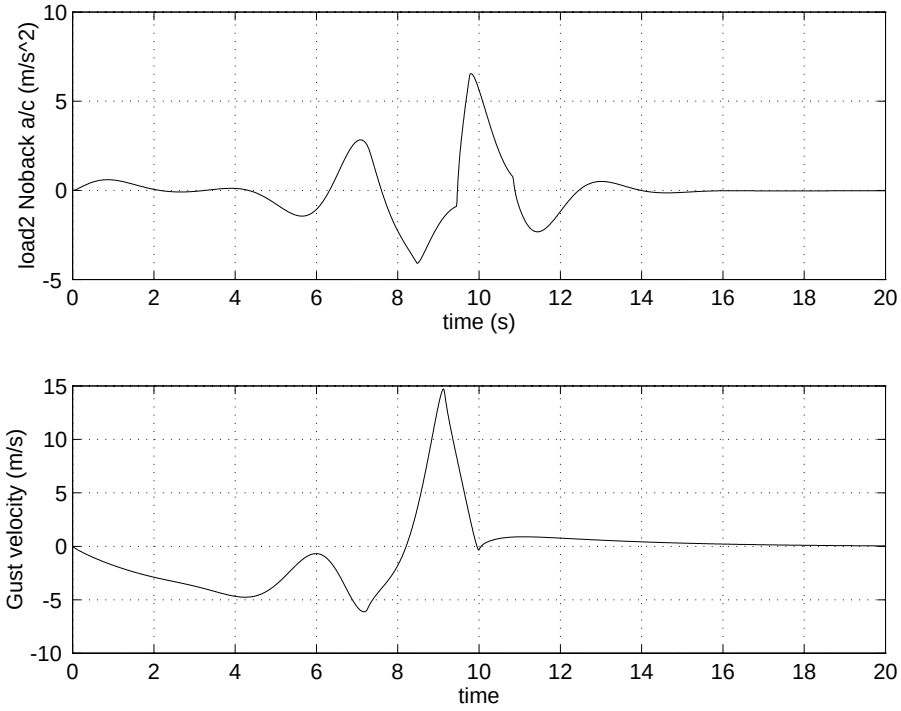

Figure 5.9: Design Load2 and critical gust shape for Noback a/c by MFB 1-D

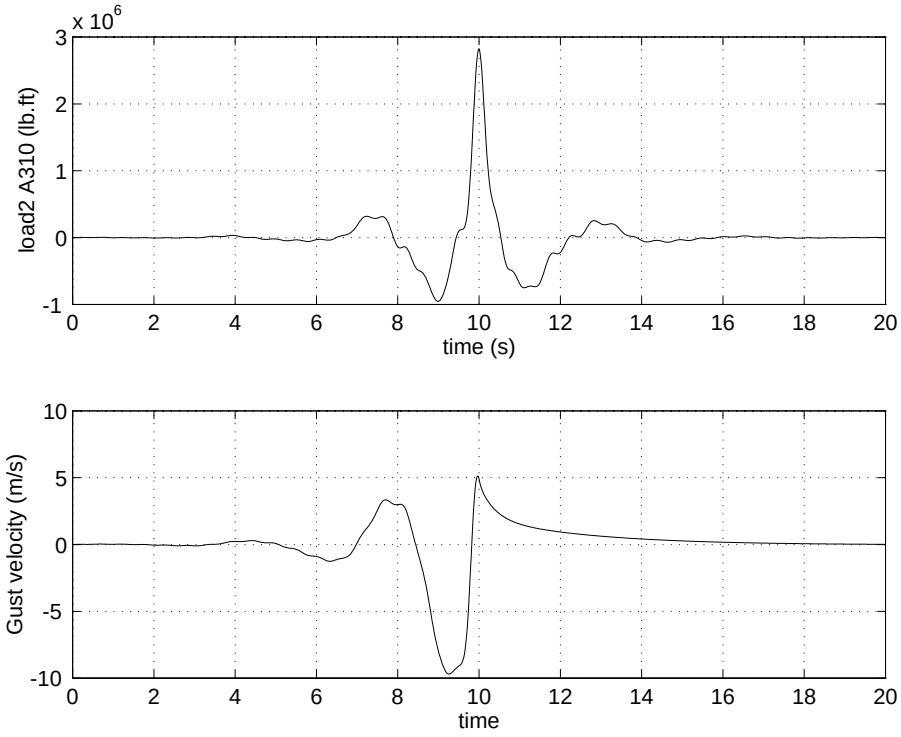

Figure 5.10: Design Load2 and critical gust shape for A310 by MFB 1-D

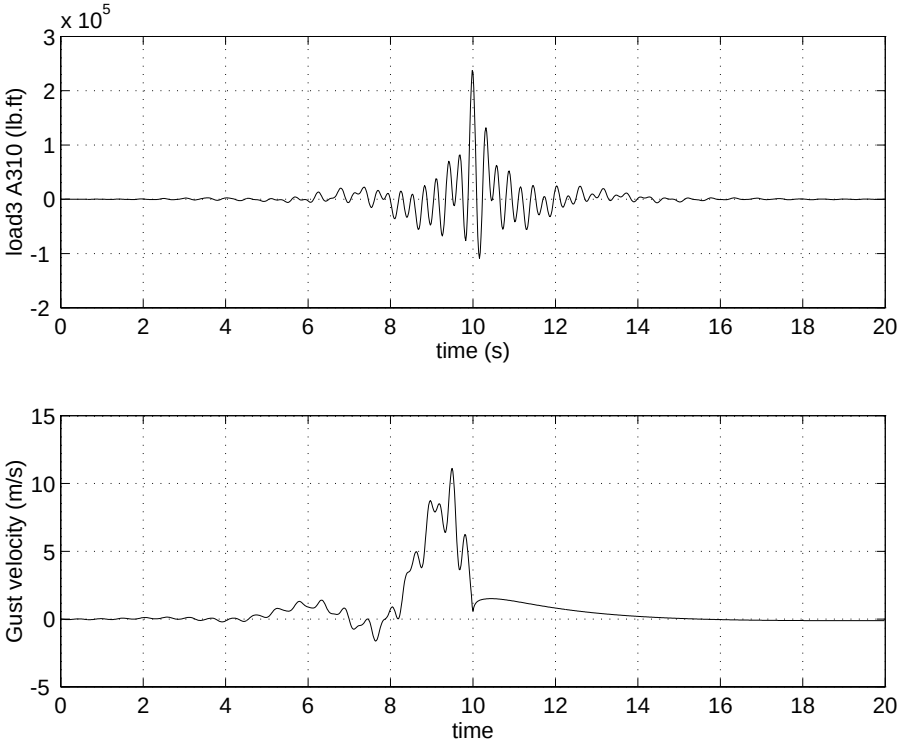

Figure 5.11: Design Load3 and critical gust shape for A310 by MFB 1-D

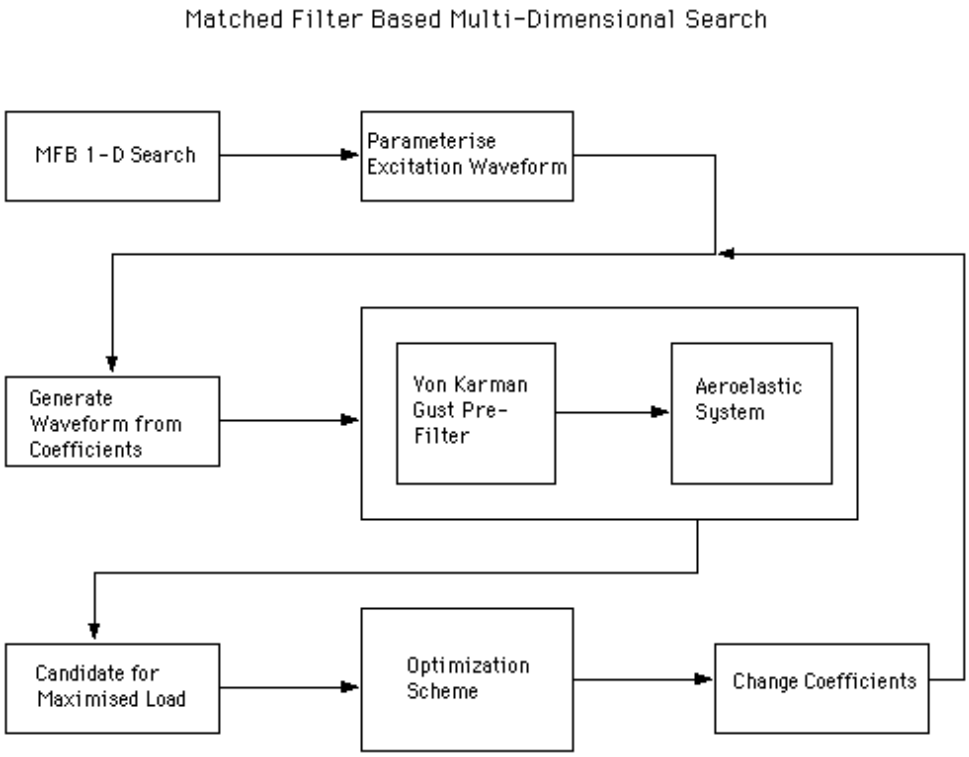

Figure 5.12: Matched Filter Based Multi-Dimensional Search scheme

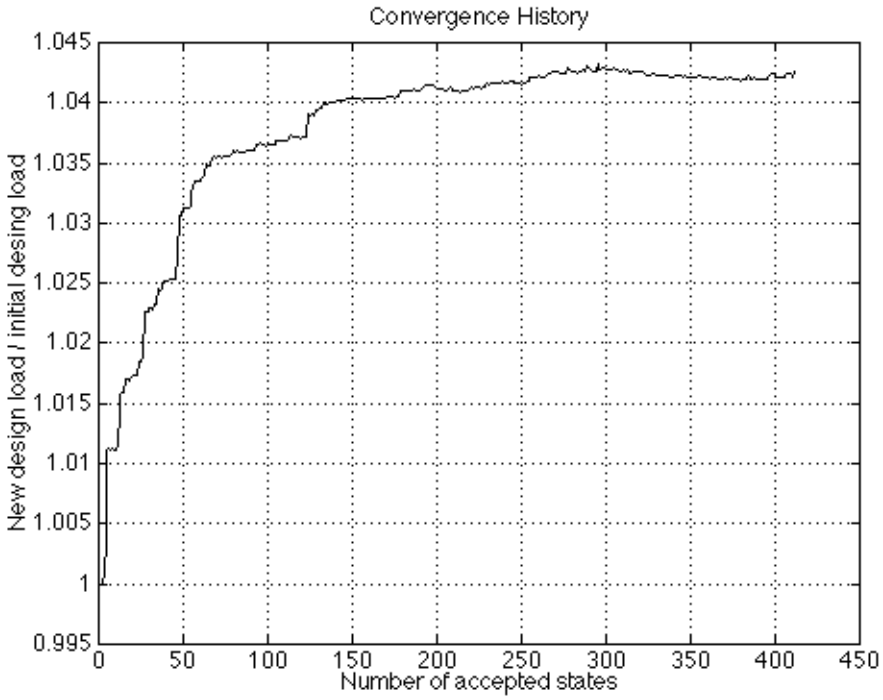

Figure 5.13: Convergence History of MD-MFB method

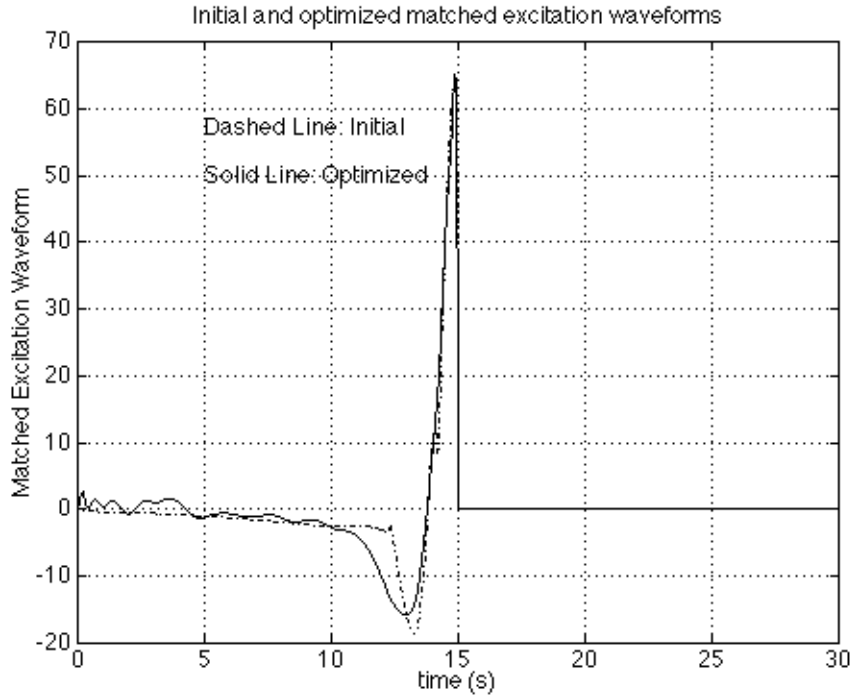

Figure 5.14: Comparison of Initial and Optimized Matched Excitation Waveforms

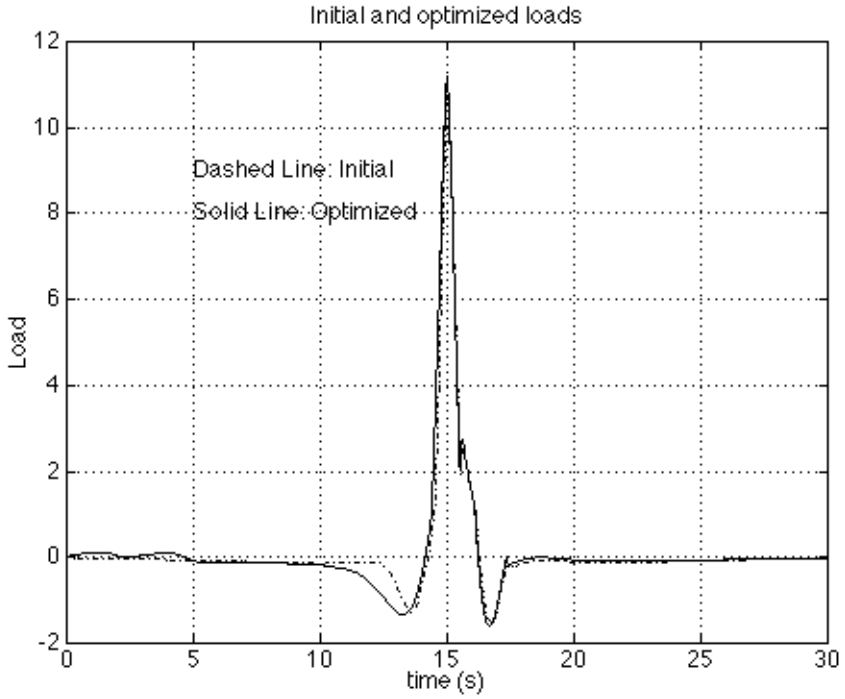

Figure 5.15: Comparison of Initial and Optimized Load Responses

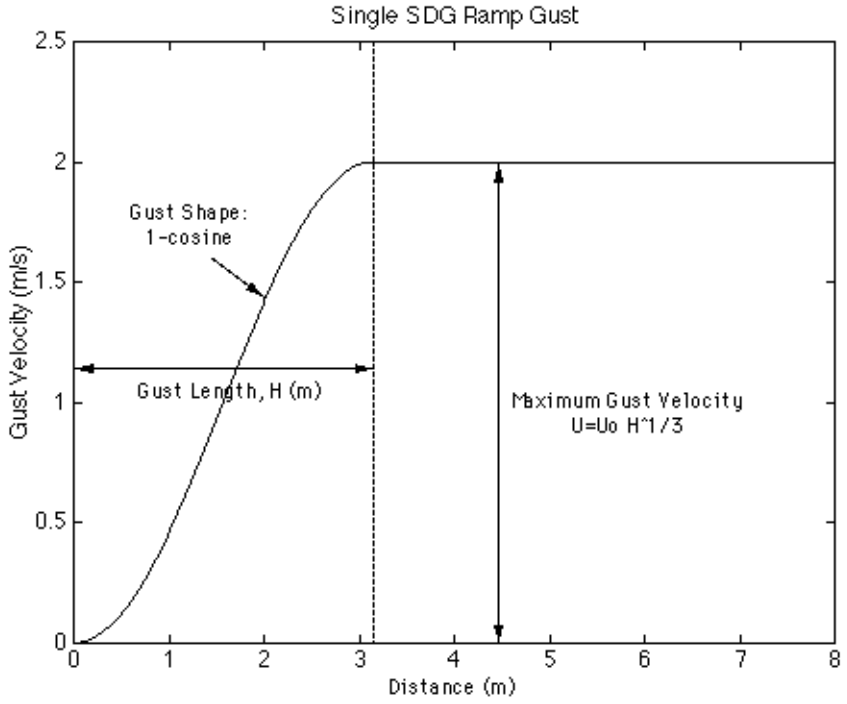

Figure 5.16: Single Statistical Discrete Gust

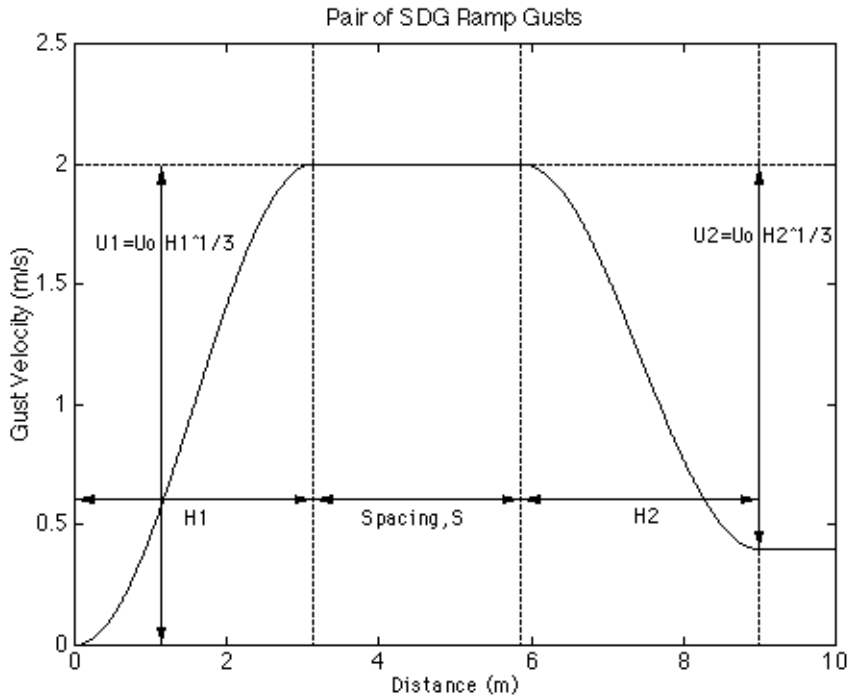

Figure 5.17: Pair of Statistical Discrete Gusts

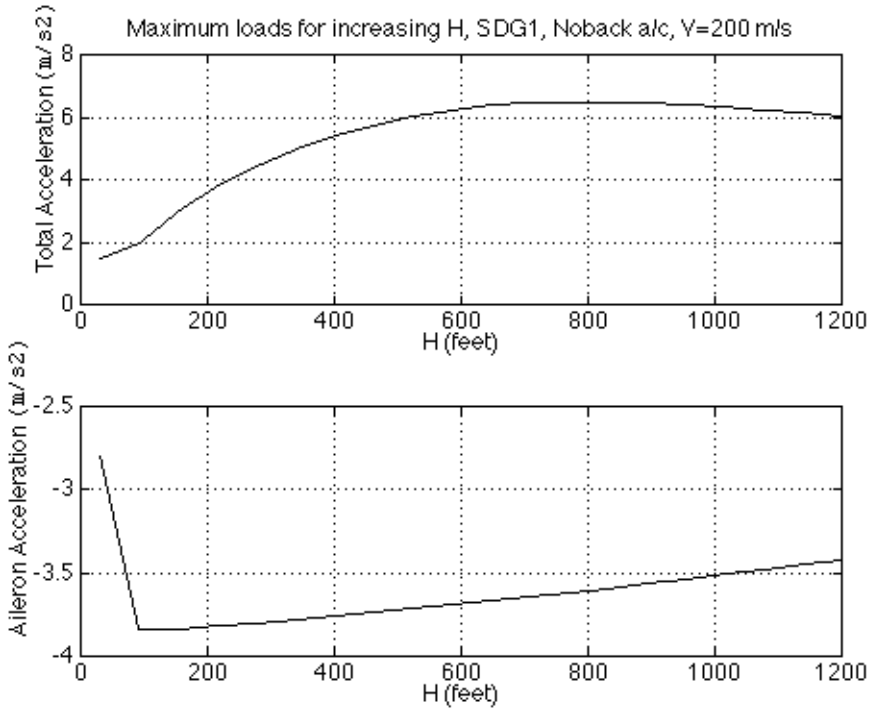

Figure 5.18: Variation of Maximum Load with Gust Length, SDG step 1

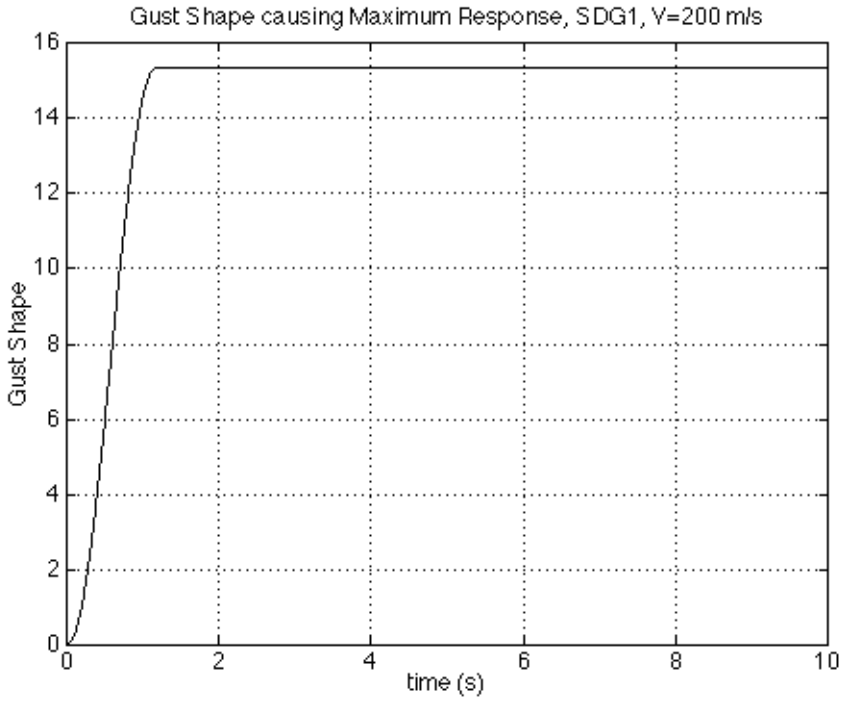

Figure 5.19: Critical Gust Waveform, SDG step 1

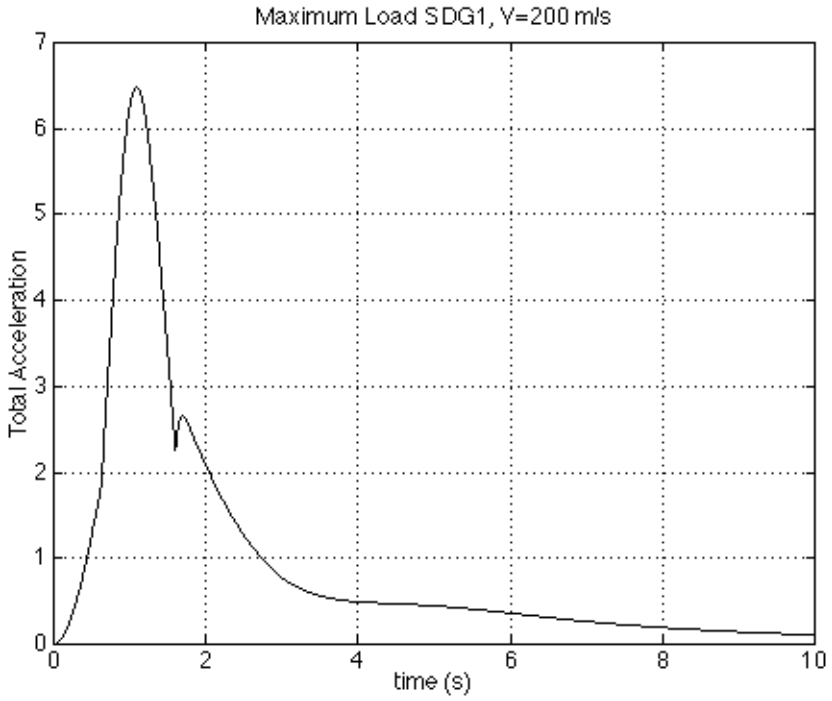

Figure 5.20: Maximum Load Response (Total Acceleration), SDG step 1

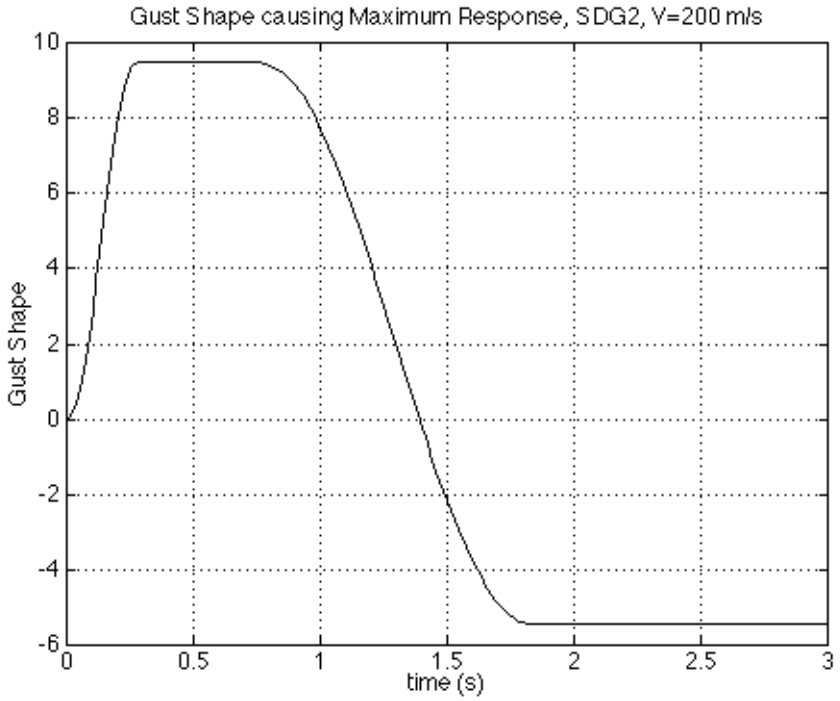

Figure 5.21: Critical Gust Waveform, SDG step 2

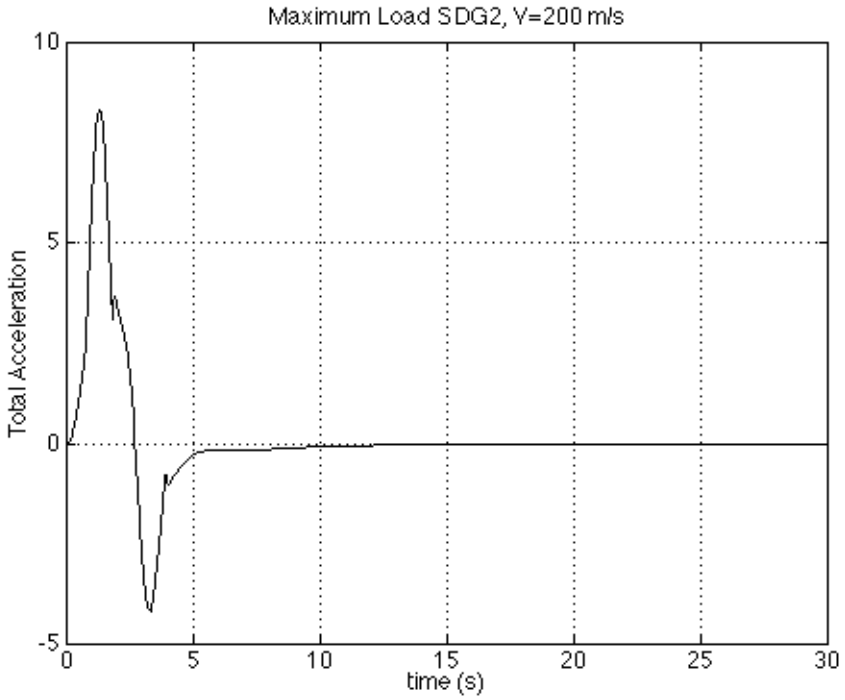

Figure 5.22: Maximum Load Response (Total Acceleration), SDG step 2

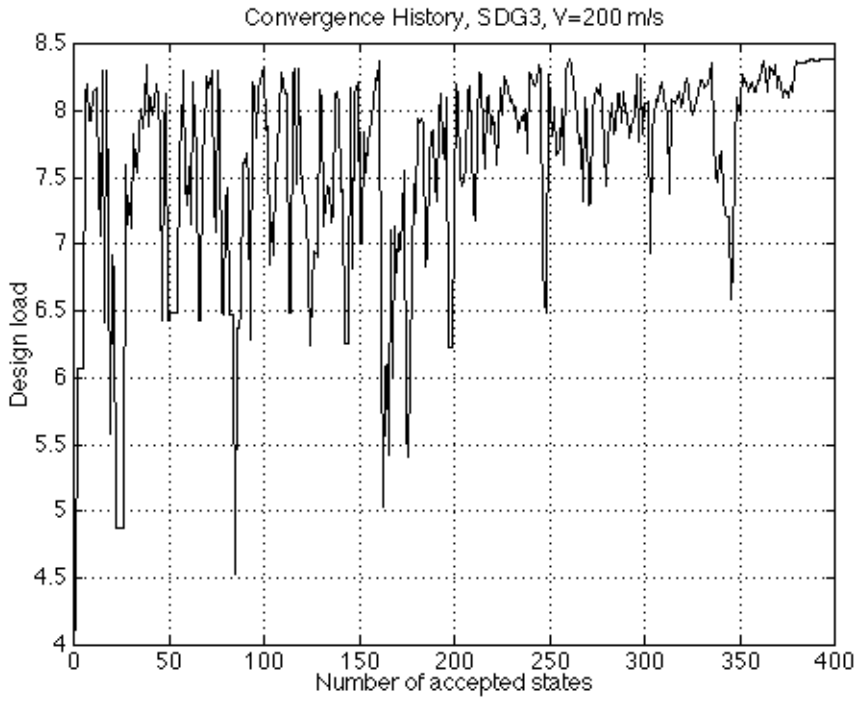

Figure 5.23: Convergence History for SDG step 3

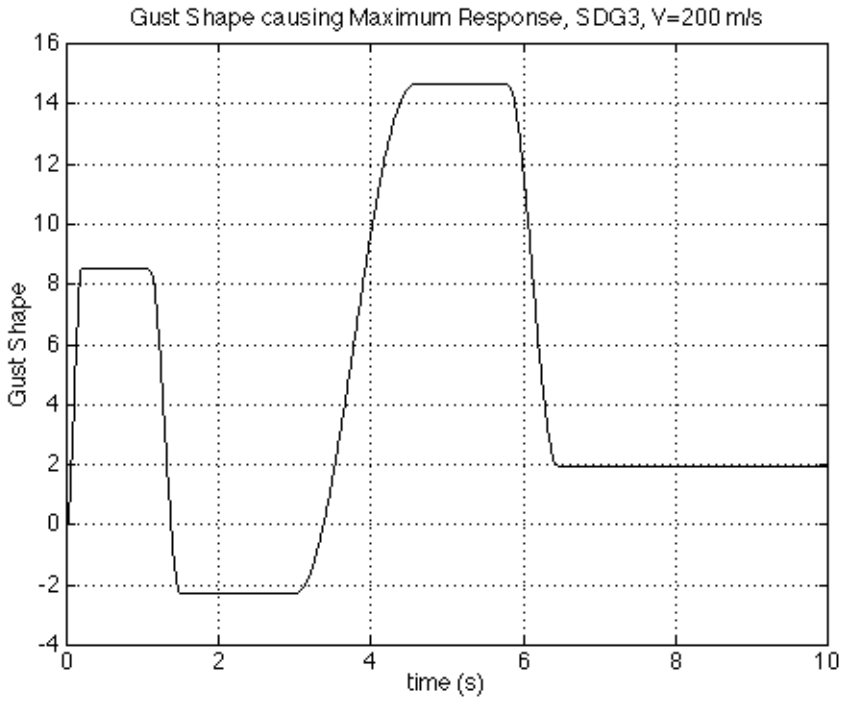

Figure 5.24: Critical Gust Waveform, SDG step 3

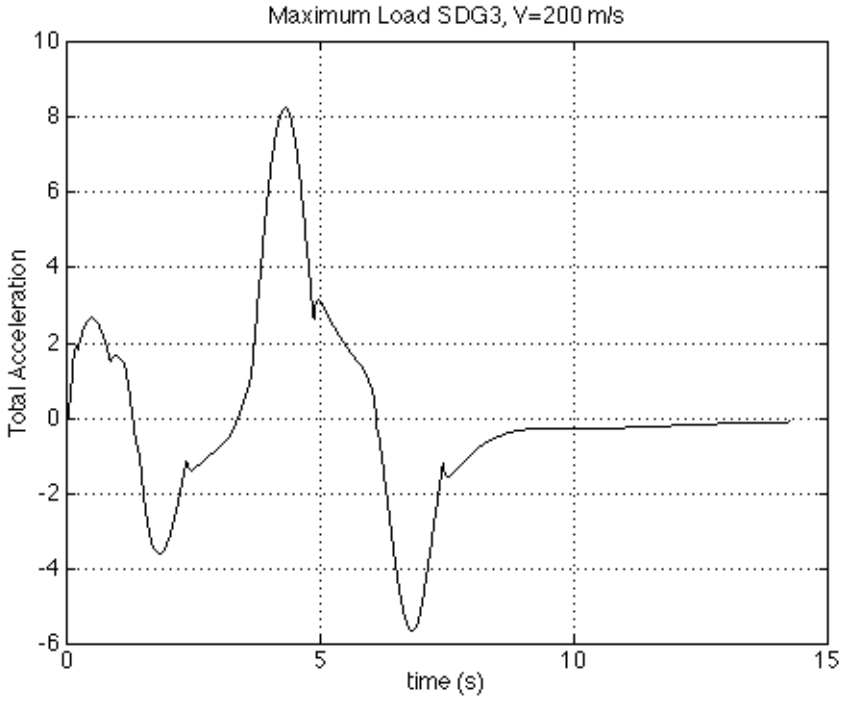

Figure 5.25: Maximum Load Response(Total Acceleration), SDG step 3

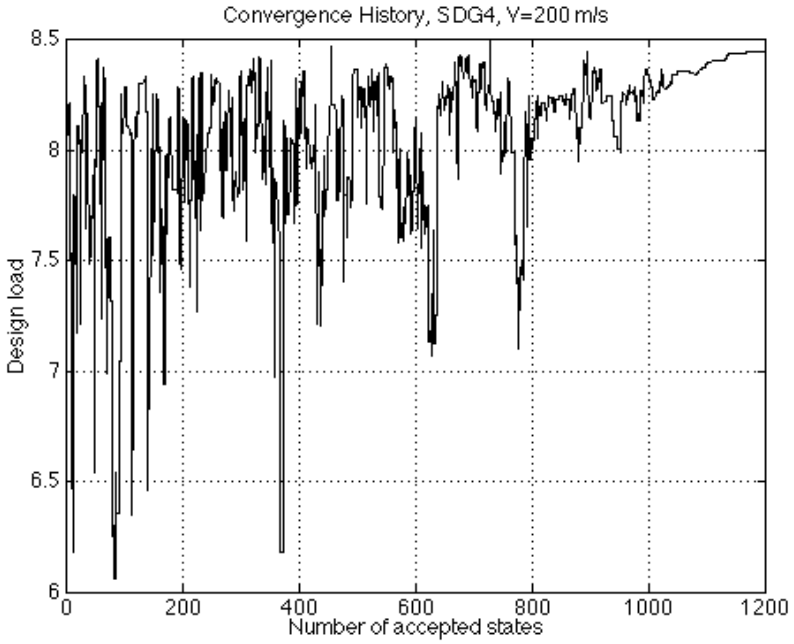

Figure 5.26: Convergence History for SDG step 4

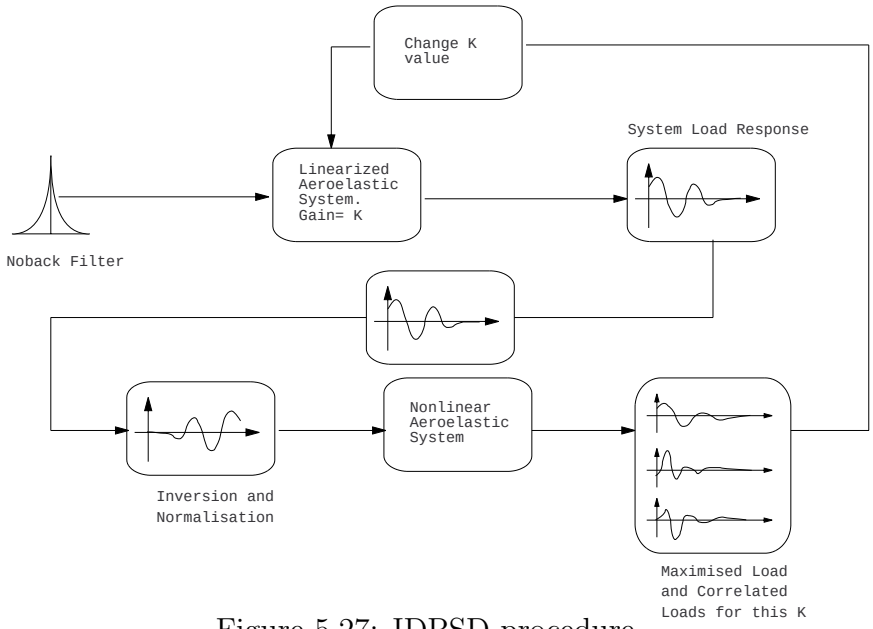

Figure 5.27: IDPSD procedure

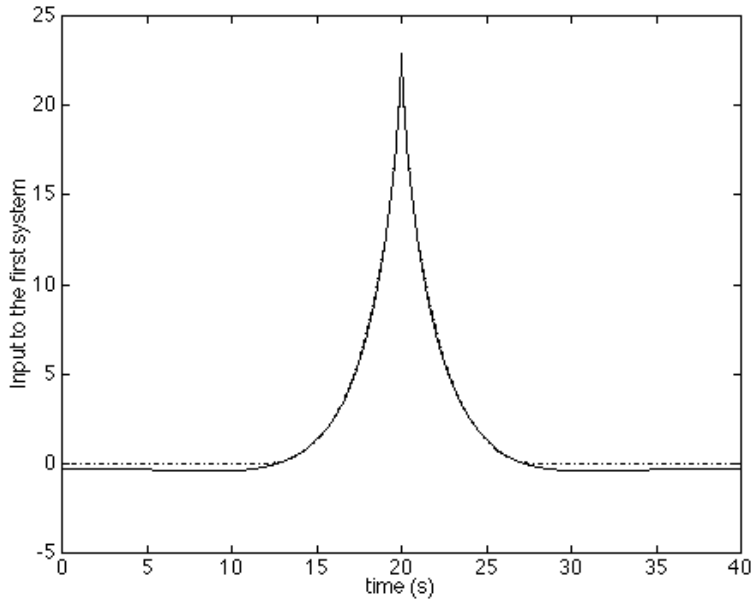

Figure 5.28: Fourier Transform and Auto-Correlation Representations of the IDPSD Gust Input

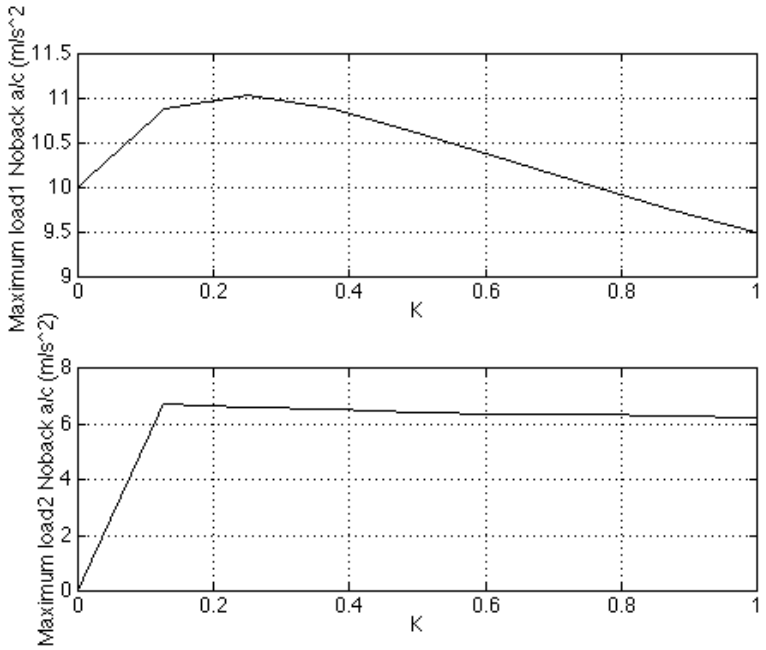

Figure 5.29: Variation of Maximum Loads with Linearized Gain for Noback aircraft, using IDPSD method

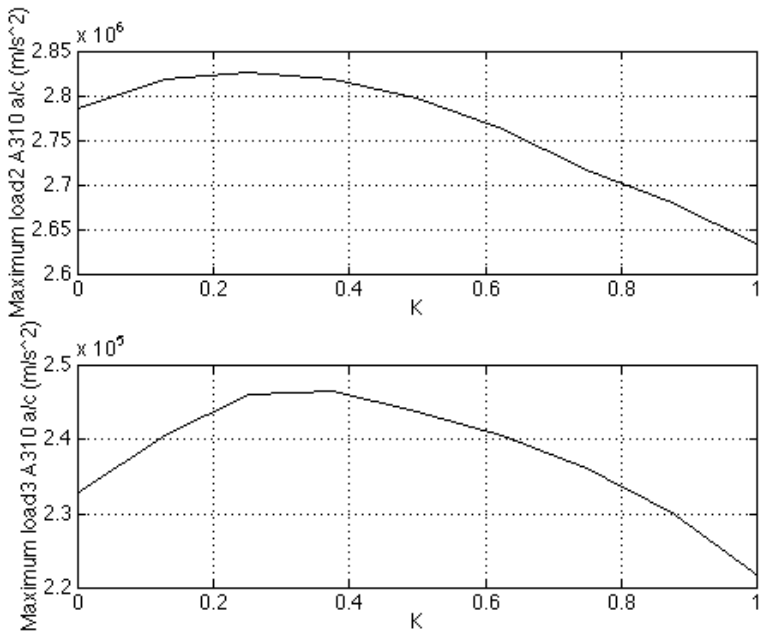

Figure 5.30: Variation of Maximum Loads with Linearized Gain for A310 aircraft, using IDPSD method

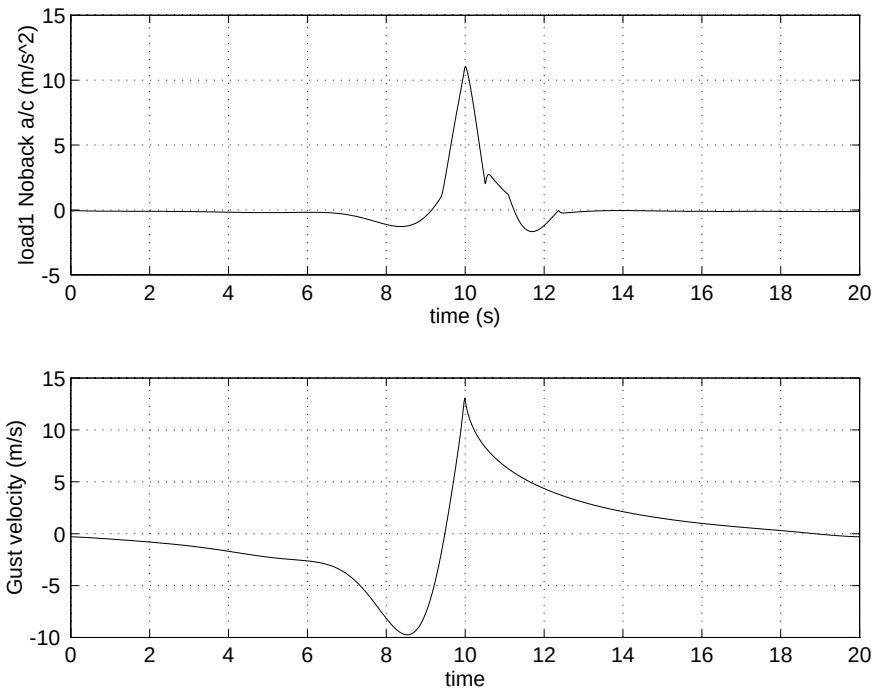

Figure 5.31: Design Load1 and critical gust shape for Noback a/c by IDPSD Method

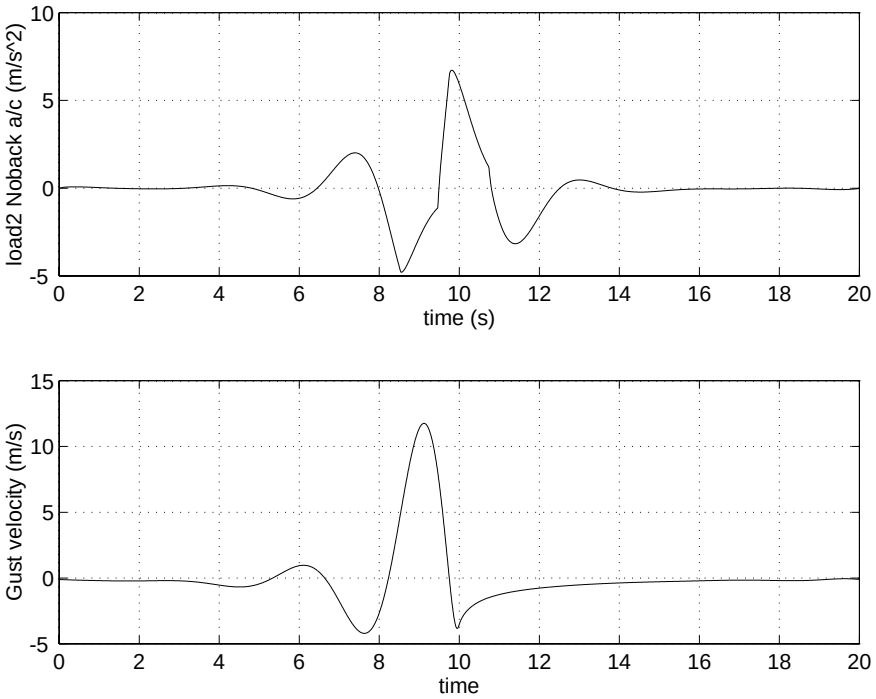

Figure 5.32: Design Load2 and critical gust shape for Noback a/c by IDPSD Method

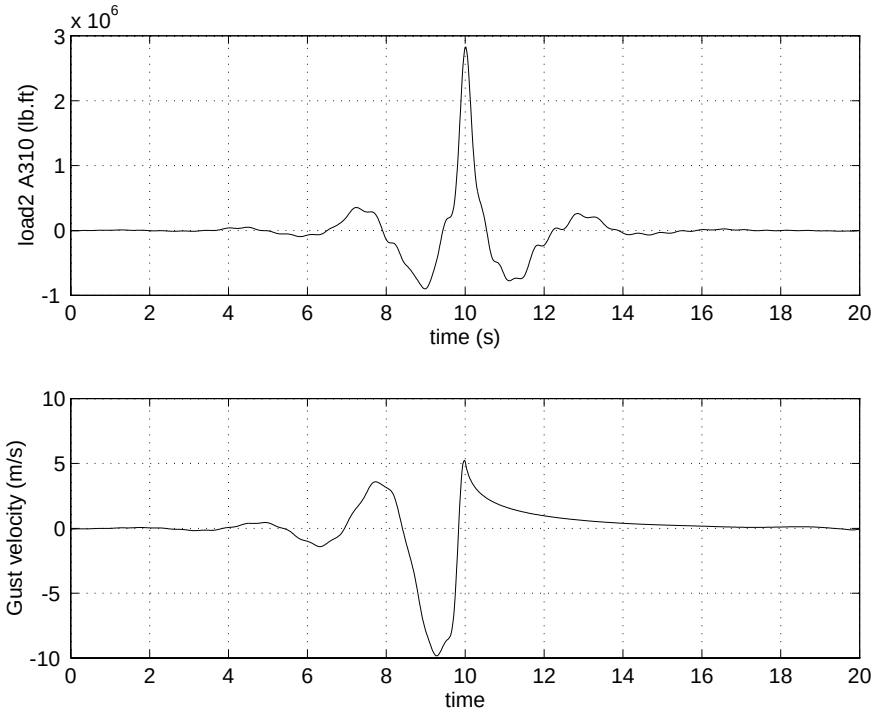

Figure 5.33: Design Load2 and critical gust shape for A310 by IDPSD Method

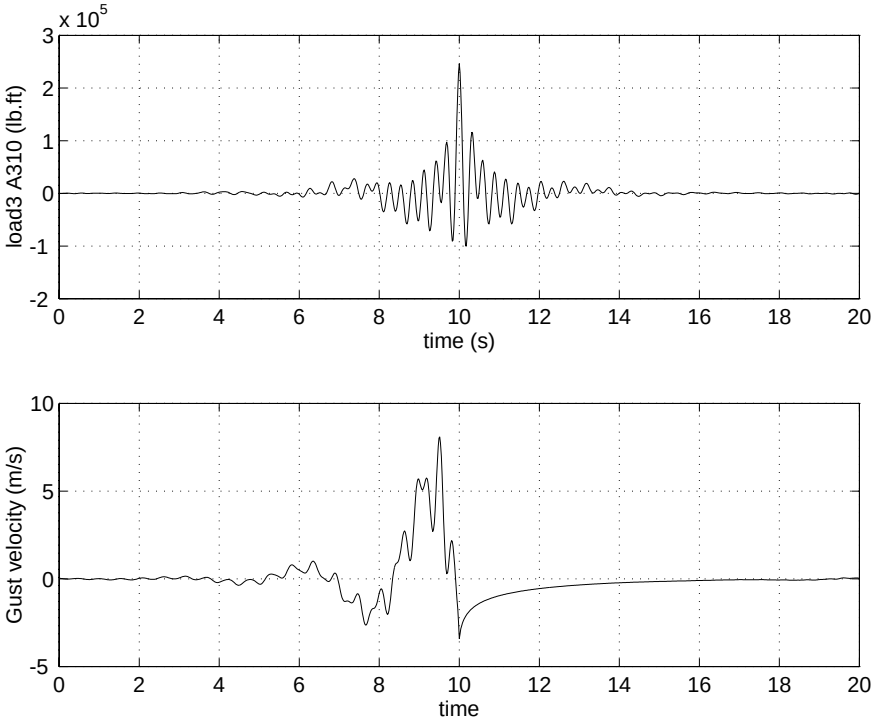

Figure 5.34: Design Load3 and critical gust shape for A310 by IDPSD Method

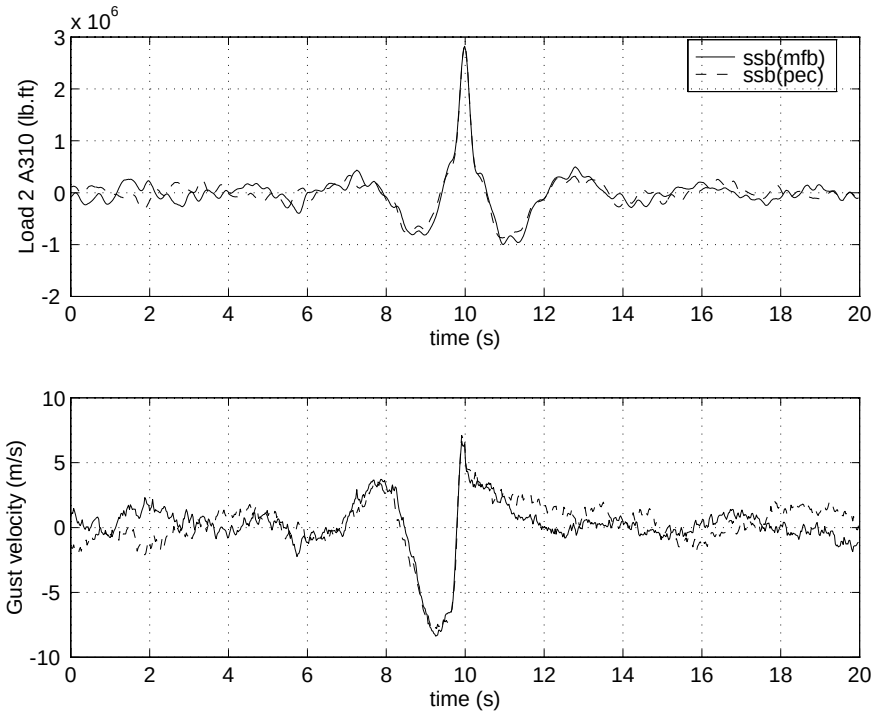

Figure 5.35: Design Load 2 and critical gust for A310 model using the SSB method

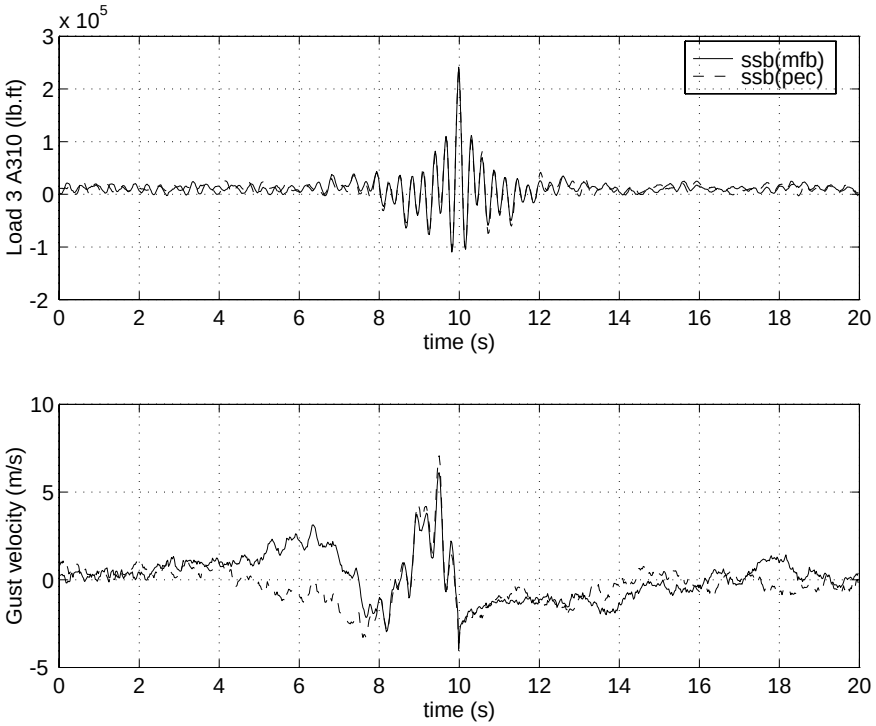

Figure 5.36: Design Load 3 and critical gust for A310 model using the SSB method

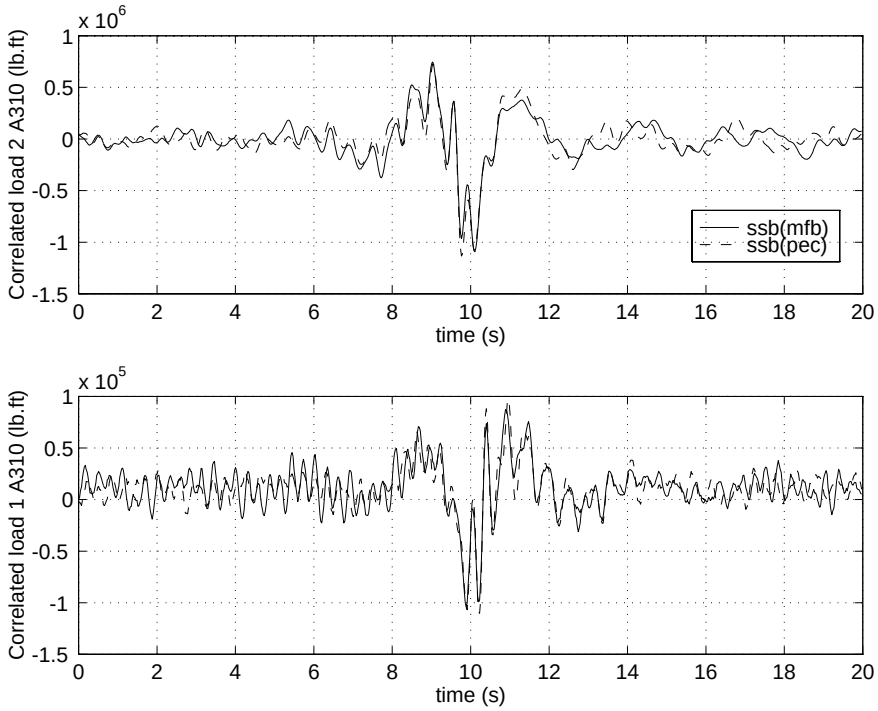

Figure 5.37: Correlated loads (for Load 2 and Load 3) for A310 model using the SSB method

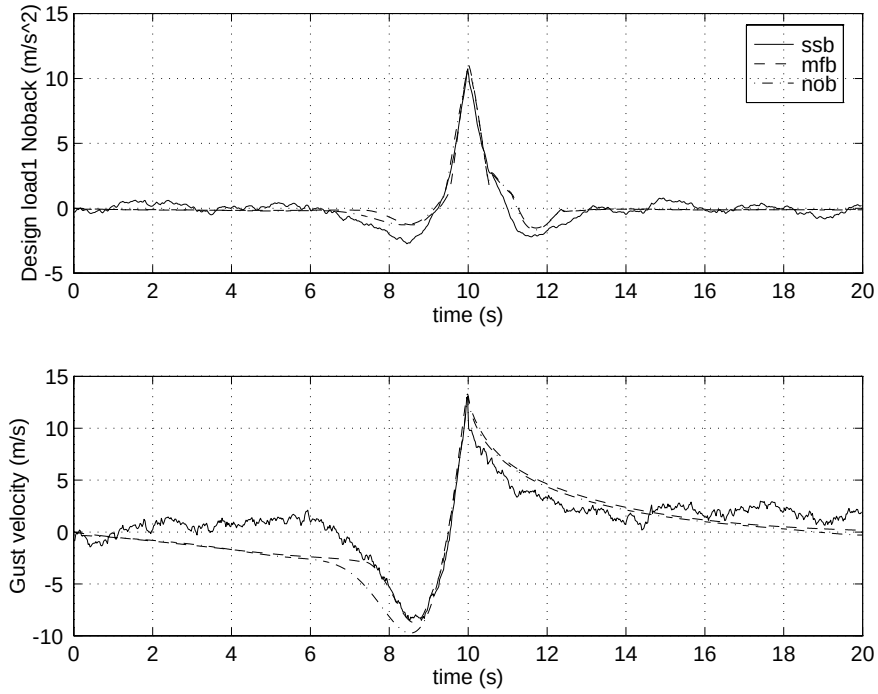

Figure 5.38: Comparison between SSB, MFB 1-D and IDPSD for Noback a/c Load 1 (Design load and gust shape)

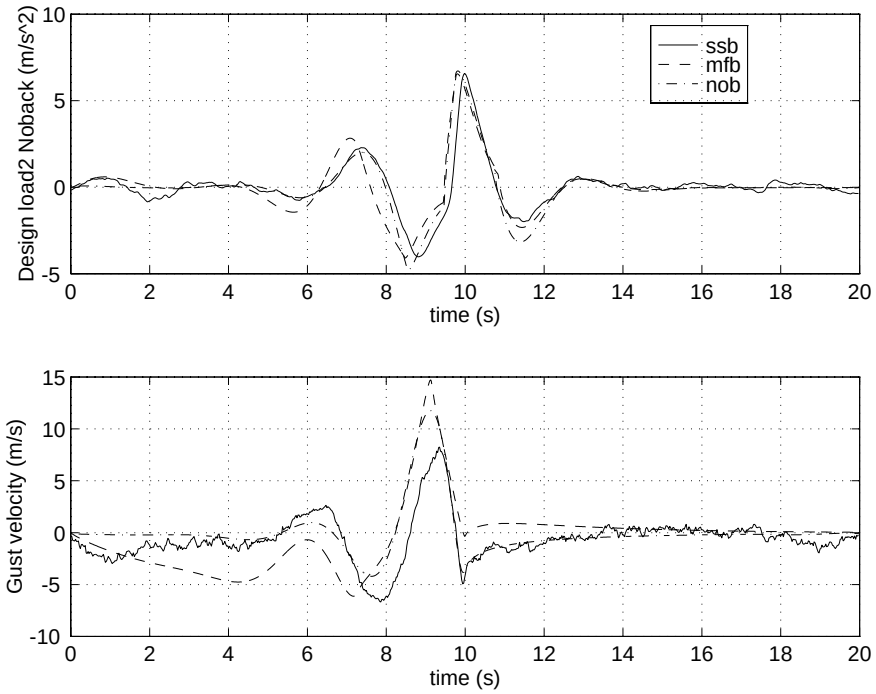

Figure 5.39: Comparison between SSB, MFB 1-D and IDPSD for Noback a/c Load 2 (Design load and gust shape)

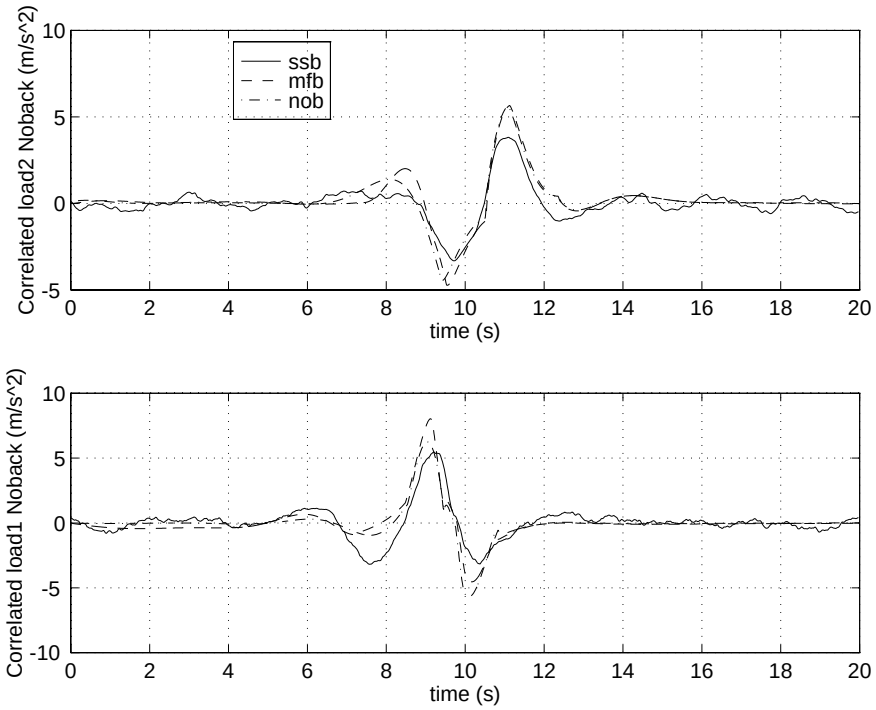

Figure 5.40: Comparison between SSB, MFB 1-D and IDPSD for Noback a/c (Correlated loads)

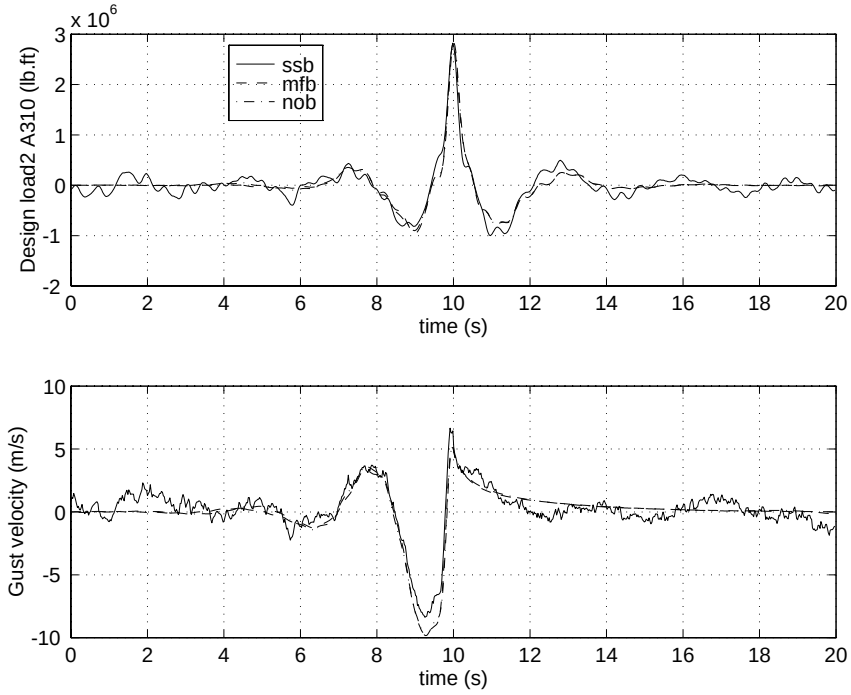

Figure 5.41: Comparison between SSB, MFB 1-D and IDPSD for A310 Load 2 (Design load and gust shape)

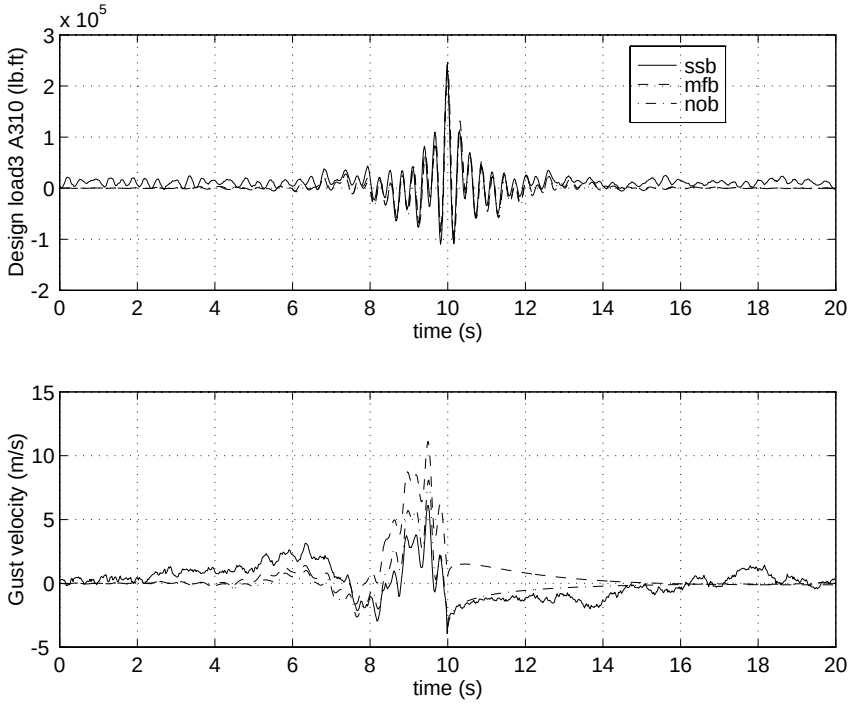

Figure 5.42: Comparison between SSB, MFB 1-D and IDPSD for A310 Load 3 (Design load and gust shape)

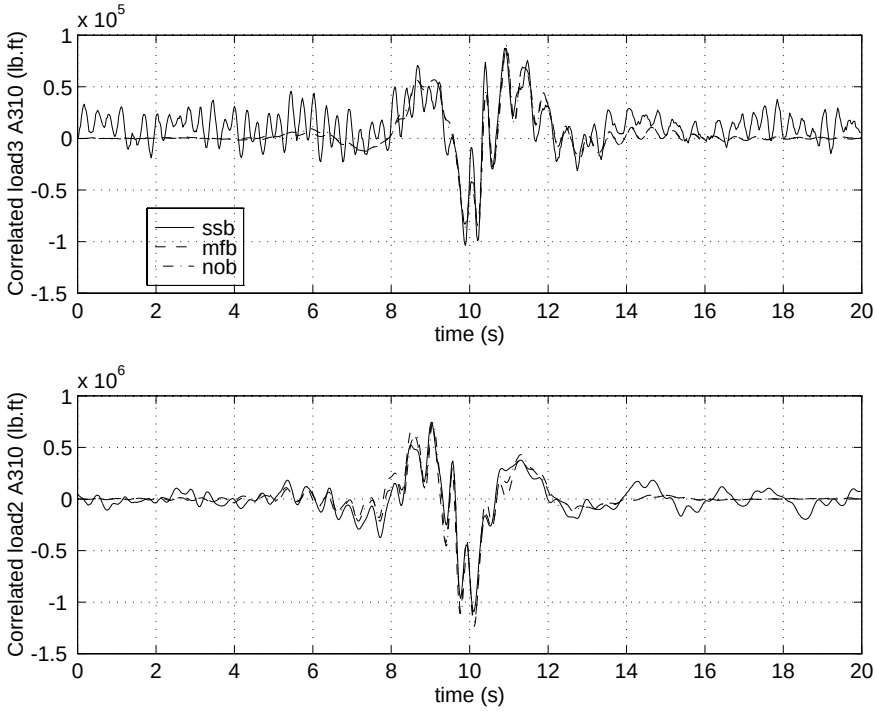

Figure 5.43: Comparison between SSB, MFB 1-D and IDPSD for A310 (Correlated loads)

Chapter 6

Conclusions

This work has considered a number of different aspects of the modelling of nonlinear aeroelastic systems. Improvements have been made in the identification of nonlinear systems and also in the control of Limit Cycle Oscillations. Original comparisons of flutter prediction and gust load prediction techniques on nonlinear aeroelastic systems have been made.

In chapter 2 six different linear flutter prediction methods were tested on a mathematical representation of an aeroelastic system and their performance was evaluated. The criteria used in this evaluation were the quality of predictions and method complexity. The Nissim & Gilyard and the Steady State Identification methods were found to consistently provide the most reliable predictions for the simple Hancock model however, they failed completely for the larger Sim-2 model. The Flutter Margin method can yield acceptable results when applied to an aeroelastic system whose flutter mechanism is known but it requires flight tests to be carried out at relatively high subcritical airspeeds in the presence of high levels of noise corruption. The Damping Fit and Envelope Function method were found to give the best results for the Sim-2 model. The ARMA-based method was found to suffer in the presence of measurement error, mainly because of the inaccuracy of the ARMA fitting procedure.

The linear flutter prediction approaches where also applied to nonlinear systems in order to evaluate their performance in the presence of nonlinearities. It was found that all of the methods can provide flutter predictions of varying accuracy for a slightly nonlinear system. Highly nonlinear systems however, cause some of the methods to fail, especially in the presence of limit cycles. The Steady-State Identification technique was found to produce the best results because of its tendency to linearise the system response. None of the methods were found to be able to predict limit cycles with the possible exception of the SSI method after further development.

In chapter 3, the current state of the art in the investigation of nonlinear aeroelastic systems was presented. Most recent research is in the process of generating data rather than analysing and explaining them. By using basic bifurcation theory and the Harmonic Balance method, a preliminary analysis of the behaviour of a simple, simulated, nonlinear system was attempted. The analysis confirmed a number of conclusions that have been reached by other researchers. Specifically, the strong dependence of nonlinear behaviour on initial conditions was confirmed as well as the partitioning of the multi-dimensional phase-space of nonlinear systems caused by singularities such as limit cycles. These are two very important problems encountered in the field of nonlinear vibrations since, despite the improved performance of modern computers, it is still not feasible to calculate the response of a nonlinear aeroelastic system at every possible (or significant) combination of initial conditions and airspeed.

The analysis presented in chapter 3 has, however, led to a simple control scheme for taming, or even suppressing, LCOs. Nevertheless, the effectiveness of this scheme depends on the stability of the various point and line singularities in the phase-space of a given nonlinear system. For a more mathematical analysis of the feasibility of LCO control see [88].

The simulated aeroelastic system investigated also exhibits chaotic oscillations at particular combinations of initial conditions and airspeed. Poincaré plots and Lyapunov exponents were used to confirm that the behaviour was chaotic.

In chapter 4 two identification methods for nonlinear systems were presented. The NARMAX method was used to introduce the concept of nonlinear system identification and to demonstrate its feasibility on aeroelastic systems. An aeroelastic version of the NARMAX approach was introduced, based on expressing the NARMAX coefficients as polynomial fractions, evaluated at a number of airspeeds.

A new method for identification of nonlinear aeroelastic systems was proposed, based on the restoring force method. The main thrust of the technique consists of curve fitting the system at time instances where the response of a degree of freedom and, hence, the non-linearity dependent on it, has a constant value. The method was demonstrated on a simple single-degree-of-freedom system and then applied to a multi-degree of freedom system representing a rigid wing, yielding in both cases models whose response was in very good agreement with that of the actual systems. The method was found capable of identifying a wide range of nonlinearities including discontinuous and hysteresis-type nonlinear functions. Finally, the method was applied successfully to an experimental 2 DOF system with cubic nonlinearity.

In chapter 5, five methods for predicting design gust loads for nonlinear aircraft were compared on two simulated gust response models. The methods included two stochastic techniques, the PEC and SSB and three deterministic ones, the MFB 1-D and multi-D, the IDPSD and the SDG. For nonlinear aircraft, there exists no approach that will yield the 'correct' design loads. In reference [74] it is proposed that a stochastic simulation, given a 'specific' turbulent patch, can

be assumed to yield the true design load. This proposal however, is an assumption designed to facilitate the foundation of an 'International Cooperative Effort' to validate deterministic gust methods, rather than an attempt at calculation of correct design loads. Hence, in the present work, more emphasis was given on conservatism rather than absolute accuracy. For the simple Noback aircraft, the MFB multi-D yielded the most conservative results, whereas for the Airbus model, the PEC method was more conservative. Another important aspect of the comparison was computational effort. The MFB 1-D was found to be the cheapest method to apply.

All the developments summarized above are seen as a stepping stone towards the modelling and identification of full scale nonlinear aircraft.

6.1 Suggestions for further work

The work presented in this thesis is by no means complete. Aeroelasticity seems to be an inexhaustible source of interesting but complicated problems to be solved. In this section, some avenues of further research into the topics investigated in the present thesis are presented.

Robust flutter prediction methods from flight test data, such as the μ method presented in [89] and [90] seem to hold much promise for the future. The investigation of flutter prediction techniques presented in chapter 2 could be widened to include robust approaches. Then, the criteria for the comparison of methods should also include the size of the test matrix for flutter clearance, since the promise of robust flutter prediction is to reduce these matrices [90].

The verdict on the linearisation of nonlinear systems presented in this work was that linearisation can work for systems with mild nonlinearities but will generally fail for highly nonlinear systems. The problem with this verdict is that, unless nonlinear identification is performed, it can be impossible to know whether

the nonlinearities present in a system are mild or not. However, since nonlinear identification of real aircraft is still not feasible, linearisation will be a necessity for the near future. Hence, there is scope for the development of a procedure that could indicate the confidence margin of linearised flutter predictions.

The CL method for identification of nonlinear systems, presented in chapter 4, can be improved in two ways. Firstly, more extensive experimental verification should take place, especially on continuous systems with distributed nonlinearity. Theoretically, the method should work for such a system, by identifying it as a series of discrete elements attached to discrete nonlinearities. However, this approach requires some type of mass appropriation to be carried out first, as discussed in section 4.3.7. Another approach for the identification of systems with many nonlinearities, that could potentially dispense with the need for mass appropriation, is the design and use of excitation signals that excite only one of the nonlinearities at a time.

The evaluation and comparison of gust load prediction methods presented in chapter 5 could be improved by including the latest version of the Statistical Discrete Gust method which employs wavelets to simulate discrete gusts [91]. Additionally, the response of aircraft to other than lateral gusts should be researched, as in [92] which investigated the effects of side gusts. Such an investigation would be a stepping stone towards gust load prediction involving gusts impacting on aircraft from all directions.

References

[1] M. W. Kehoe. A historical overview of flight flutter testing. In *AGARD-CP-566*, May 1995.

[2] J. E. Cooper. Parameter estimation methods for flight flutter testing. In *AGARD-CP-566*, May 1995.

[3] G. J. Hancock, J. R. Wright, and A. Simpson. On the teaching of the principles of wing flexure-torsion flutter. *Aeronautical Journal*, 89(888):285–305, October 1985.

[4] Ll. T. Niblett. The fundamentals of body-freedom flutter. *Aeronautical Journal*, pages 373–377, November 1986.

[5] T. E. Noll, B. Perry III, and M. W. Kehoe. A quarter century of NASA wind-tunnel and flight experiments involving aeroservoelasticity. In *AGARD-CP-566*, May 1995.

[6] E. Breitbach. Effects of structural nonlinearities on aircraft vibration and testing. Report R-665, AGARD, January 1978.

[7] D. Graham and D. McRuer. Retrospective essay on nonlinearities in aircraft flight control. *Journal of Guidance*, 14(6):1089–1099, 1991.

[8] B. Etkin. Turbulent wind and its effect on flight. *Journal of Aircraft*, 18(5):327–345, 1981.

[9] S. J. Price, H. Alighanbari, and B. H. K. Lee. The aeroelastic behaviour of a two-dimensional airfoil with bilinear and cubic structural nonlinearities. *Journal of Fluids and Structures*, 9:175–193, 1995.

[10] T. J. Barnes. Manual on the flight of flexible aircraft in turbulence; Chapter IV. Report AG-317, AGARD, May 1991.

[11] M. Géradin and D. Rixen. *Mechanical vibrations*. John Wiley & Sons, 1997.

[12] N. H. Zimmerman and J. T. Weissenburger. Prediction of flutter onset speed based on flight testing at subcritical speeds. *Journal of Aircraft*, 1(4):190–202, 1964.

[13] S. J. Price and B. H. K. Lee. Evaluation and extension of the Flutter-Margin method for flight flutter prediction. *Journal of Aircraft*, 30(3):395–402, 1993.

[14] E. J. Routh. *Advanced part of a treatise on the dynamics of a system of rigid bodies*, volume II. MacMillan, 5th edition, 1930.

[15] M. Dickinson. CF-18 Flight flutter test (FFT) techinques. In *AGARD-CP-566*, May 1995.

[16] R. M. Bennett. Application of Zimmerman Flutter-Margin criterion to a wind-tunnel model. Technical Memorandum 84545, NASA, 1982.

[17] J. E. Cooper, P. R. Emmett, J. R. Wright, and M. J. Schofield. Envelope Function - A tool for analyzing flutter data. *Journal of Aircraft*, 30(5):785–790, 1993.

[18] D.R. Gaukroger, C.W. Skingle, and K.H. Heron. An application of system identification to flutter testing. *Journal of Sound and Vibration*, 72(2):141–150, 1980.

[19] E. Nissim and G. B. Gilyard. Method for experimental determination of flutter speed by parameter identification. Report AIAA-89-1324-CP, AIAA, 1989.

[20] W. Eversman and A. Tewari. Consistent rational-function approximation for unsteady aerodynamics. *Journal of Aircraft*, 28(9):545–552, 1991.

[21] K. A. Stroud. *Engineering mathematics*. MacMillan, 2nd edition, 1970.

[22] Y. Matsuzaki and Y. Ando. Estimation of flutter boundary from random responses due to turbulence at subcritical speeds. *Journal of Aircraft*, 18(10):862–868, October 1981.

[23] P. N. James, P. Souter, and D. C. Dixon. A comparison of parameter estimation algorithms for discrete systems. *Chemical Engineering Science*, 29:539–547, 1974.

[24] J. E. Cooper. Comparison of some time-domain-system identification techniques using approximate data correlations. *Journal of Modal Analysis*, pages 51–57, April 1989.

[25] Y. Matsuzaki and H. Torii. Response characteristics of a two-dimensional wing subjected to turbulence near the flutter boundary. *Journal of Sound and Vibration*, 136(2):187–199, 1990.

[26] S. F. Shen. An approximate analysis of nonlinear flutter problems. *Journal of the Aerospace Sciences*, pages 25–32, January 1959.

[27] Z. C. Yang and L. C. Zhao. Analysis of limit cycle flutter of an airfoil in incompressible flow. *Journal of Sound and Vibration*, 123(1):1–13, 1988.

[28] S. J. Price, B. H. K. Lee, and H. Alighanbari. Postinstability behaviour of

a two-dimensional airfoil with a structural nonlinearity. *Journal of Aircraft*, 31(6):1395–1401, 1994.

[29] D. S. Woolston, H. L. Runyan, and T. A. Byrdsong. Some effects of system nonlinearities in the problem of aircraft flutter. Technical Note TN 3539, NACA, October 1955.

[30] D. S. Woolston, H. L. Runyan, and R. E. Andrews. An investigation of effects of certain types of structural nonlinearities on wing and control surface flutter. *Journal of the Aeronautical Sciences*, pages 57–63, January 1957.

[31] N. Minorsky. *Introduction to non-linear mechanics*. J.W. Edwards, 1947.

[32] N.Kryloff and N.Bogoliuboff. *Introduction to Nonlinear Mechanics (a free translation by S.Lefschetz)*. Princeton University Press, 1947.

[33] R. M. Laurenson and R. M. Trn. Flutter analysis of missile control surfaces containing structural nonlinearities. *AIAA Journal*, 18(10):1245–1251, 1980.

[34] S. C. McIntosh Jr., R. E. Reed, and W. P. Rodden. Experimental and theoretical study of nonlinear flutter. *Journal of Aircraft*, 18(12):1057–1063, 1981.

[35] E. H. Dowell. Flutter of a buckled plate as an example of chaotic motion of a deterministic autonomous system. *Journal of Sound and Vibration*, 85(3):333–344, 1982.

[36] C. L. Lee. An iterative procedure for nonlinear flutter analysis. *AIAA Journal*, 24(3):833–840, 1986.

[37] R. M. Laurenson, A. J. Hauenstein, J. L. Gubser, and R. P. Briley. Effects of structural nonlinearities on limit cycle response of aerodynamic surfaces. Report 86-0899, AIAA, 1986.

[38] L. O. Brase and W. Eversman. Application of transient aerodynamics to the structural nonlinear flutter problem. *Journal of Aircraft*, 25(11):1060–1068, 1988.

[39] L. C. Zhao and Z. C. Yang. Chaotic motions of an airfoil with non-linear stiffness in incompressible flow. *Journal of Sound and Vibration*, 138(2):245–254, 1990.

[40] A. J. Hauenstein, R. M. Laurenson, W. Eversman, G. Galecki, and K. Qumei. Chaotic response of aerosurfaces with structural nonlinearities. Report AIAA-90-1034-CP, AIAA, 1990.

[41] A. J. Hauenstein, J. A. Zara, W. Eversman, and K. Qumei. Chaotic and nonlinear dynamic response of aerosurfaces with structural nonlinearities. Report AIAA-92-2547-CP, AIAA, 1992.

[42] D. M. Tang and E. H. Dowell. Flutter and stall response of a helicopter blade with structural nonlinearity. *Journal of Aircraft*, 29(5):953–960, 1992.

[43] O. Tanrikulu and M. Imregun. Forced harmonic response analysis of nonlinear structures using describing functions. *AIAA Journal*, 31(7):1313–1320, 1993.

[44] F. C. Moon. *Chaotic and fractal dynamics - An introduction for applied scientists and engineers.* John Wiley & Sons, 1992.

[45] M. Holden, R. E. J. Brazier, and A. A. Cal. Effects of structural nonlinearities on a tailplane flutter model. In *Proceeding of the CEAS International Forum on Aeroelasticity and Structural Dynamics*, Manchester, UK, 1995.

[46] I. Lee and S. H. Kim. Aeroelastic analysis of a flexible control surface with structural nonlinearity. *Journal of Aircraft*, 32(4):869–874, 1995.

[47] S. H. Kim and I. Lee. Aeroelastic analysis of a flexible airfoil with a freeplay non-linearity. *Journal of Sound and Vibration*, 193(4):823–846, 1996.

[48] M. D. Conner, D. M. Tang, E. H. Dowell, and L.N. Virgin. Nonlinear behaviour of a typical airfoil section with control surface freeplay: a numerical and experimental study. *Journal of Fluids and Structures*, 11:89–109, 1997.

[49] T. O'Neil and T. W. Strganac. Aeroelastic response of a rigid wing supported by nonlinear springs. *Journal of Aircraft*, 35(4):616–622, 1998.

[50] J. E. Marsden and M. McCracken. *The Hopf Bifurcation and its applications*. Springer-Verlag, 1976.

[51] N. Minorsky. *Non-linear oscillations*. Van Nostrand Company PLC, 1962.

[52] R. L. Devaney. *An introduction to chaotic dynamical systems*. Addison-Wesley, 1990.

[53] A. Wolf, J. B. Swift, H. L. Swinney, and J. A. Vastano. Determining Lyapunov exponents from a time series. *Physica D*, 16:285–317, 1985.

[54] S. A. Billings and K. M. Tsang. Spectral analysis for nonlinear systems, part I: Parametric nonlinear spectral analysis. *Mechanical Systems and Signal Processing*, 3(4):319–339, 1989.

[55] S. Chen and S. A. Billings. Representations of non-linear systems: the NARMAX model. *International Journal of Control*, 49(3):1013–1032, 1989.

[56] S. J. Gifford and G. R. Tomlinson. Recent advances in the applications of functional series to non-linear structures. *Journal of Sound and Vibration*, 135(2):289–317, 1989.

[57] K. Worden. Characterisation of nonlinear systems using time data. In *Structural Identification: Dynamic Methods and Diagnostics, ISMES*, Bergamo, Italy, October 1992.

[58] S. A. Billings, M. J. Korenberg, and S. Chen. Identification of nonlinear output-affine systems using an orthogonal least squares algorithm. *International Journal of Systems Science*, 16:1339–1568, 1988.

[59] G. Dimitriadis and J. E. Cooper. A method for identification of non-linear multi-degree-of-freedom systems. *Proceedings of the Institute of Mechanical Engineers, Part G*, 212:287–298, 1998.

[60] J. E. Cooper and G. Dimitriadis. Prediction of maximum loads due to turbulent gusts using nonlinear system identification. In *Proceedings of the CEAS International Forum on Aeroelasticity and Structural Dynamics, Volume II*, pages 71–78, Rome, Italy, June 1997.

[61] M. Simon and G. R. Tomlinson. Use of the Hilbert transform in modal analysis of linear and non-linear structures. *Journal of Sound and Vibration*, 96(4):421–436, 1984.

[62] E. F. Crawley and A. C. Aubert. Identification of nonlinear structural elements by force-state mapping. *AIAA Journal*, 24(1):155–162, 1986.

[63] M. Ajjan Al-Hadid and J. R. Wright. Estimation of mas and modal mass in the identication of non-linear single and multi degree of freedom systems using the force-state maping approach. *Mechanical Systems and Signal Processing*, 6(4):383–401, 1992.

[64] J. R. Fuller. Evolution of airplane gust loads design requirements. *Journal of Aircraft*, 32(2):235–246, 1995.

[65] J. C. Houbolt. Special effects of gust loads on military aircraft. Report 798, AGARD, May 1994.

[66] H. I. Flomenhoft. Brief history of gust models for aircraft design. *Journal of Aircraft*, 31(5):1225–1227, 1994.

[67] H. Tennekes and J. L. Lumley. *A first course in turbulence*. MIT Press, 1972.

[68] F. M. Hoblit. *Gust loads on aircraft: Concepts and applications*. AIAA Education Series, 1988.

[69] G. W. Foster and J. G. Jones. Analysis of atmospheric turbulence measurements by spectral and discrete-gust methods. *Aeronautical Journal*, pages 162–176, May 1989.

[70] A. S. Pototzky and T. A. Zeiler. Calculating time-correlated gust loads using matched filter and random process theories. *Journal of Aircraft*, 28(5):346–352, 1991.

[71] R. C. Scott, A. S. Pototzky, and B. Perry III. Computation of maximized gust loads for nonlinear aircraft using Matched-Filter-Based schemes. *Journal of Aircraft*, 30(5):763–768, 1993.

[72] J. G. Jones, G. W. Foster, and A. Haynes. Fractal properties of inertial-range turbulence with implications for aircraft response. *Aeronautical Journal*, pages 301–308, October 1988.

[73] J. G. Jones. Statistical-Discrete-Gust Method for predicting aircraft loads and dynamic response. *Journal of Aircraft*, 26(4):382–392, 1989.

[74] J. B. De Jonge and W. J. Vink. Evaluation of deterministic spectral gust

methods. Technical Publication TP 94368 U, NLR, National Aerospace Laboratory, Holland, 1994.

[75] G. Rosenberg, D. A. Cowling, and M. Hockenhull. The deterministic spectral procedure for gust response analysis of nonlinear aircraft models.

[76] H. Lusebrink and J. Brink-Spalink. Treatment of non-linear systems by timeplane-transformed C.T. methods. Report 798, AGARD, May 1994.

[77] R. Noback. S.D.G., P.S.D. and the nonlinear airplane. Technical Publication TP 88018 U, NLR, National Aerospace Laboratory, Holland, 1988.

[78] P. J. Goggin. Comparison of stochastic and deterministic nonlinear gust analysis methods to meet continuous turbulence criteria. Report 798, AGARD, May 1994.

[79] W. J. Vink. A stochastic simulation procedure compared to deterministic methods for psd gust design loads. Technical Publication TP 98240, NLR, National Aerospace Laboratory, Holland, 1998.

[80] J. G. Jones. Formulation of Design Envelope criterion in terms of Deterministic Spectral Procedure. *Journal of Aircraft*, 30(1):137–139, 1993.

[81] E. Aarst and J. Korst. *Simulated annealing and Boltzman machines*. John Wiley & Sons, 1989.

[82] R. C. Scott, A. S. Pototzky, and B. Perry III. Maximized gust loads for a nonlinear airplane using matched filter theory and constrained optimization. Technical Memorandum 104138, NASA, 1991.

[83] D. L. Hull. Design limit loads based upon statistical discrete gust methodology. Report 798, AGARD, May 1994.

[84] R. Noback. The Deterministic Power-Spectral-Density method for nonlinear systems. Technical Publication TP 92342 U, NLR, National Aerospace Laboratory, Holland, 1992.

[85] R. Noback. The Deterministic Power-Spectral-Density method for linear systems. Technical Publication TP 92062 U, NLR, National Aerospace Laboratory, Holland, 1992.

[86] R. C. Scott, A. S. Pototzky, and B. Perry III. Similarity between methods based on matched filter theory and on stochastic simulation. Report AIAA-92-2369-CP, AIAA, 1992.

[87] R. C. Scott, A. S. Pototzky, and B. Perry III. Matched-Filter and Stochastic-Simulation-Based methods of gust loads prediction. *Journal of Aircraft*, 32(5):1047–1055, 1995.

[88] F. Mastroddi and L. Morino. Limit-cycle taming by nonlinear control with applications to flutter. *Aeronautical Journal*, 100(999):389–396, November 1996.

[89] R. C. Lind and M. J. Brenner. Robust flutter margin analysis that incorporates flight data. Technical Report Draft, NASA, 1997.

[90] M. J. Brenner, R. C. Lind, and D. F. Voracek. Overview of recent flight flutter testing research at NASA Dryden. Technical Memorandum 4792, NASA, 1997.

[91] J. G. Jones, G. W. Foster, and P. G. Earwicker. Wavelet analysis of gust structure in measured atmospheric turbulence. *Journal of Aircraft*, 30(1):94–99, 1993.

[92] I. A. Olwi. Aerodynamic characteristics of aircraft under side gust. *Journal of Aircraft*, 33(5):901–905, 1996.

[93] A. M. Kuethe and C. Y. Chow. *Foundations of aerodynamics - basis of aerodynamic design*. John Wiley & Sons, 1986.

[94] R. H. Scanlan and R. Rosenbaum. *Introduction to the study of aircraft vibration and flutter*. The MacMillan Company, 1951.

[95] G. Dimitriadis. Implementation and comparison of three methods of modelling the effect of the aerodynamic forces on the aeroelastic behaviour of a simple wing. Master's thesis, University of Manchester, Aerospace Department, October 1995.

[96] The Mathworks Inc., editor. *The student edition of SIMULINK*. Prentice-Hall, 1996.

[97] The Mathworks Inc., editor. *The student edition of MATLAB*. Prentice-Hall, 1995.

[98] C. F. Gerald and P. O. Wheatley. *Applied numerical analysis*. Addison-Wesley, 5th edition, 1990.

Appendix A

Hancock model with control surface

The mathematical model chosen to investigate nonlinear aeroelastic behaviour was a rectangular wing of flat plate section, of thickness t, with a control surface. It is based on the Hancock model [3] i.e. it is assumed to be rigid and is attached to a rigid wall at its root via two rotational springs, one in the pitch and one in the yaw direction. It has one extra degree of freedom, the control surface pitch. A diagram of the wing can be seen in figure A.1.

The first part of the modeling of the flutter equations involved writing the displacement of the wing-control surface assembly in the z-direction in terms of the displacements in the y and x directions and the angles γ, θ and β, as defined in figure A.1. The diagram in figure A.2 shows this procedure in more detail. According to this diagram (and the middle diagram in figure A.1) the vertical displacement of the main wing, z_w (for $x < x_c$) is given by (assuming that all displacement angles are small)

$$z_w(x, y) = y\gamma + (x - x_f)\theta$$

and the vertical displacement of the control surface, z_c (for $x > x_c$) is given by:

$$z_w(x,y) = y\gamma + (x - x_f)\theta + (x - x_h)\beta$$

The equations of motion for the system were arrived at by use of Lagranges equation:

$$\frac{d}{dt}\left(\frac{dT}{d\dot{q}_i}\right) + \frac{dV}{dq_i} = Q_i \tag{A.1}$$

where T is the kinetic energy, V is the potential energy, Q_i are the generalised forces applied to the system (in this case aerodynamic forces) and q_i are the generalised displacements (in this case γ, θ and β). Terms that are equal to zero have been omitted from the equation.

For this system the kinetic energy is given as the sum of the kinetic energies of the main wing and the control surface, i.e.

$$T = T_w + T_c = \frac{1}{2}\int_0^s \int_0^{x_c} \dot{z}_w^2 dm + \frac{1}{2}\int_0^s \int_{x_c}^c \dot{z}_c^2 dm$$

Substituting for z_w and z_c yields the following expression for the kinetic energy.

$$T = \frac{\dot{\gamma}^2}{2} I_\gamma + \frac{\dot{\theta}^2}{2} I_\theta + \frac{\dot{\beta}^2}{2} I_\beta + \dot{\gamma}\dot{\theta} I_{\gamma\theta} + \dot{\gamma}\dot{\beta} I_{\gamma\beta} + \dot{\theta}\dot{\beta} I_{\theta\beta} \tag{A.2}$$

where,

$$\begin{aligned} I_\gamma = \int_0^s \int_0^c y^2 dm \quad &, \quad I_{\gamma\theta} = \int_0^s \int_0^c y\,(x - x_f)\,dm \\ I_\theta = \int_0^s \int_0^c (x - x_f)^2\,dm \quad &, \quad I_{\gamma\beta} = \int_0^s \int_c^{x_c} y\,(x - x_h)\,dm \\ I_\beta = \int_0^s \int_c^{x_c} (x - x_h)^2\,dm \quad &, \quad I_{\theta\beta} = \int_0^s \int_c^{x_c} (x - x_h) \end{aligned}$$

The potential energy is given by

$$V = \frac{1}{2} K_\gamma \gamma^2 + \frac{1}{2} K_\theta \theta^2 + \frac{1}{2} K_\beta \beta^2 \tag{A.3}$$

where K_γ, K_θ and K_β are the stiffnesses of the springs restraining motion in the γ, θ and β directions respectively.

By substituting equations A.2 and A.3 into A.1 the following expression for the equations of motion is obtained:

$$\begin{pmatrix} I_\gamma & I_{\gamma\theta} & I_{\gamma\beta} \\ I_{\gamma\theta} & I_\theta & I_{\theta\beta} \\ I_{\gamma\beta} & I_{\theta\beta} & I_\beta \end{pmatrix} \begin{Bmatrix} \ddot{\gamma} \\ \ddot{\theta} \\ \ddot{\beta} \end{Bmatrix} + \begin{pmatrix} K_\gamma & 0 & 0 \\ 0 & K_\theta & 0 \\ 0 & 0 & K_\beta \end{pmatrix} \begin{Bmatrix} \gamma \\ \theta \\ \beta \end{Bmatrix} = \begin{Bmatrix} Q_\gamma \\ Q_\theta \\ Q_\beta \end{Bmatrix} \tag{A.4}$$

The aerodynamics of the flat plate with control surface airfoil were modeled according to references [93] and [94] and then, using steady strip theory, they were generalised for the whole wing. The effect of the control surface is to displace the lift curve of the airfoil in the horizontal direction, as seen in figure A.3. So, for a positive (nose up) control deflection, the lift curve is displaced upwards, as shown below. The main effect this has on the behaviour of the airfoil is that for zero angle of attack, it produces lift, ΔC_l. Accordingly, for zero angle of attack, there is a moment around the aerodynamic centre, $\Delta C_{m_{ac}}$. In other words, the lift coefficient of the wing with control surface deflection is given as the superposition of the lift coefficient without deflection and ΔC_l. Similarly for the moment coefficient around the aerodynamic centre with the difference that this quantity is zero for symmetrical wing sections, therefore the total moment coefficient is equal to $\Delta C_{m_{ac}}$. These two incremental quantities can be evaluated using the method described in [93], resulting in (where α is the angle of attack)

$$\begin{aligned} C_l &= 2\pi\alpha + \Delta C_l = 2\pi\alpha + \left[2(\pi - \theta_h) + 2\sin\theta_h\right]\beta \\ C_{m_{ac}} &= 0 + \Delta C_{m_{ac}} = \left[\frac{1}{2}\sin\theta_h(\cos\theta_h - 1)\right]\beta \end{aligned} \tag{A.5}$$

where (x_h being the position of the hinge axis, as defined in figure A.2),

$$\theta_h = \cos^{-1}\left(1 - \frac{2x_h}{c}\right)$$

However, the moment coefficient around the aerodynamic centre is not very useful in this instance since the wing is attached to the wall at its flexural axis. Therefore the moment coefficient has to be evaluated around the flexural axis too. This is accomplished by taking moments about the flexural axis and obtaining

$$M_{fa} = M_{ac} + ecL$$

or,

$$C_{m_{fa}} = C_{m_{ac}} + eC_l$$

where e is the ratio of the distance between the flexural and aerodynamic axes. Hence,

$$C_{m_{fa}} = 2\pi e\alpha + \left\{ [2(\pi - \theta_h) + 2\sin\theta_h]\, e + \left[\frac{1}{2} \sin\theta_h (\cos\theta_h - 1) \right] \right\} \beta \qquad \text{(A.6)}$$

In order to complete the aerodynamic modeling it is necessary to determine the value of the control surface moment coefficient around the hinge axis. This can be calculated by evaluating the pressure distribution around the control surface only and then summing it while taking moments about the hinge axis. However this is a very laborious process and if the method of [93] is used, it involves calculating the integrals of infinite series.

Two alternative approaches were identified and tried. The first one was to solve for the flow around the wing section using the vortex panel method in a manner similar to the procedure in [95]. This produced good results and also gave an insight into the aerodynamic intricacies of the model. Figure A.4 shows a typical pressure distribution around a flat plate with control surface deflection. The control causes a second peak in pressure near the hinge axis which accounts for the increase in lift. However, this is again a complicated procedure and does take up a lot of useful computing time. As a consequence, a third approach was used, found in [94]. It yields the following result.

$$C_{m_{ha}} = -\frac{T_{12}}{2}\alpha - \frac{T_{12}T_{10}}{2\pi}\beta \tag{A.7}$$

where,

$$\begin{aligned} T_{10} &= \sqrt{1-d^2} + \cos^{-1} d \\ T_{12} &= \sqrt{1-d^2}(2+d) + \cos^{-1} d(2d+1) \\ d &= 2\frac{x_h}{c} - 1 \end{aligned}$$

The easiest way of incorporating results (5), (6) and (7) into the equations of motion is to express the three coefficients as follows.

$$\begin{aligned} C_l &= a_1\alpha + a_2\beta \\ C_{m_{fa}} &= b_1\alpha + b_2\beta \\ C_{m_{ha}} &= c_1\alpha + c_2\beta \end{aligned} \tag{A.8}$$

where,

$$\begin{aligned} a_1 &= 2\pi & a_2 &= [2(\pi-\theta_h) + 2\sin\theta_h] \\ b_1 &= 2\pi e & b_2 &= \left\{[2(\pi-\theta_h) + 2\sin\theta_h]\, e + \left[\tfrac{1}{2}\sin\theta_h(\cos\theta_h - 1)\right]\right\} \\ c_1 &= -\frac{T_{12}}{2} & c_2 &= -\frac{T_{12}T_{10}}{2\pi} \end{aligned}$$

Taking a small strip dy of the wing, the total lift on it, dL is given by

$$dL = \frac{1}{2}\rho V^2 c C_l dy = \frac{1}{2}\rho V^2 c(a_1\alpha + a_2)\beta dy$$

where V is the free stream velocity. The angle of attack, α, is the sum of the geometrical angle of attack, θ, and the dynamic angle of attack caused by the vertical movement of the wing. Hence,

$$\alpha = \theta + \frac{\dot{\gamma} y}{V}$$

Similarly, the other two aerodynamic coefficients for the strip dy can be formed and the three coefficients can then be expressed as

$$\begin{aligned} dL &= \frac{1}{2}\rho V^2 c\left[a_1\left(\theta+\frac{\dot{\gamma}y}{V}\right)+a_2\beta\right]dy \\ dM_{fa} &= \frac{1}{2}\rho V^2 c^2\left[b_1\left(\theta+\frac{\dot{\gamma}y}{V}\right)+b_2\beta\right]dy \\ dM_{ha} &= \frac{1}{2}\rho V^2 c^2\left[c_1\left(\theta+\frac{\dot{\gamma}y}{V}\right)+c_2\beta\right]dy \end{aligned} \tag{A.9}$$

Furthermore the work done by the aerodynamic force and moments on the wing is given by

$$\delta W = -\int_0^s dLy\delta\gamma + \int_0^s dM_{fa}\delta\theta + \int_0^s dM_{ha}\delta\theta \tag{A.10}$$

where the negative sign is due to the fact that γ is defined positive downwards whereas L is positive upwards. Finally, the equations of motion can be completed by writing the generalised forces Q_i in terms of the work done on the wing as follows.

$$Q_\gamma = \frac{\partial(\delta W)}{\partial(\delta\gamma)}, \qquad Q_\theta = \frac{\partial(\delta W)}{\partial(\delta\theta)}, \qquad Q_\beta = \frac{\partial(\delta W)}{\partial(\delta\beta)}$$

Combining the expressions above with equations A.1, A.4 and A.9 gives the full equations of motion for the wing with control surface model in a free stream of velocity V.

$$\begin{pmatrix} I_\gamma & I_{\gamma\theta} & I_{\gamma\beta} \\ I_{\gamma\theta} & I_\theta & I_{\theta\beta} \\ I_{\gamma\beta} & I_{\theta\beta} & I_\beta \end{pmatrix}\begin{Bmatrix} \ddot{\gamma} \\ \ddot{\theta} \\ \ddot{\beta} \end{Bmatrix} + \frac{1}{2}\rho V sc \begin{pmatrix} \frac{s^2 a_1}{3} & 0 & 0 \\ -\frac{scb_1}{2} & 0 & 0 \\ -\frac{scc_1}{2} & 0 & 0 \end{pmatrix}\begin{Bmatrix} \dot{\gamma} \\ \dot{\theta} \\ \dot{\beta} \end{Bmatrix} + \begin{pmatrix} K_\gamma & 0 & 0 \\ 0 & K_\theta & 0 \\ 0 & 0 & K_\beta \end{pmatrix}\begin{Bmatrix} \gamma \\ \theta \\ \beta \end{Bmatrix}$$

$$+\frac{1}{2}\rho V^2 sc \begin{pmatrix} 0 & \frac{sa_1}{2} & \frac{sa_2}{2} \\ 0 & -\frac{cb_1}{2} & -\frac{cb_2}{2} \\ 0 & -\frac{cc_1}{2} & -\frac{cc_2}{2} \end{pmatrix}\begin{Bmatrix} \gamma \\ \theta \\ \beta \end{Bmatrix} = \begin{Bmatrix} 0 \\ 0 \\ 0 \end{Bmatrix} \tag{A.11}$$

In order to improve the accuracy of the model, two more terms were added to approximate aerodynamic unsteadiness. These terms were the first order aerodynamic derivatives around θ and β. The final form of the equations of motion

is as follows:

$$\begin{pmatrix} I_\gamma & I_{\gamma\theta} & I_{\gamma\beta} \\ I_{\gamma\theta} & I_\theta & I_{\theta\beta} \\ I_{\gamma\beta} & I_{\theta\beta} & I_\beta \end{pmatrix} \begin{Bmatrix} \ddot{\gamma} \\ \ddot{\theta} \\ \ddot{\beta} \end{Bmatrix} + \frac{1}{2}\rho V sc \begin{pmatrix} \frac{s^2 a_1}{3} & 0 & 0 \\ -\frac{scb_1}{2} & -c^2 M_{\dot{\theta}} & 0 \\ -\frac{scc_1}{2} & 0 & -c^2 M_{\dot{\beta}} \end{pmatrix} \begin{Bmatrix} \dot{\gamma} \\ \dot{\theta} \\ \dot{\beta} \end{Bmatrix} +$$

$$\begin{pmatrix} K_\gamma & 0 & 0 \\ 0 & K_\theta & 0 \\ 0 & 0 & K_\beta \end{pmatrix} \begin{Bmatrix} \gamma \\ \theta \\ \beta \end{Bmatrix} + \frac{1}{2}\rho V^2 sc \begin{pmatrix} 0 & \frac{sa_1}{2} & \frac{sa_2}{2} \\ 0 & -\frac{cb_1}{2} & -\frac{cb_2}{2} \\ 0 & -\frac{cc_1}{2} & -\frac{cc_2}{2} \end{pmatrix} \begin{Bmatrix} \gamma \\ \theta \\ \beta \end{Bmatrix} = \begin{Bmatrix} 0 \\ 0 \\ 0 \end{Bmatrix} \quad \text{(A.12)}$$

To make the study of the model more complete it was decided to excite the main wing by an external force which could be applied anywhere on the wing, vertically and at given x and y-positions. The work done by such a force is given by

$$\delta W = F\left[y_{ff}\delta\gamma + (x_{ff} - x_f)\delta\theta\right]$$

where F is the magnitude of the force and (x_{ff}, y_{ff}) is the position of the forcing function. Therefore, the generalised forces in the γ and θ coordinates (the control surface is not excited and there is no generalised force in the β coordinate) are

$$Q_\gamma = \frac{\partial(\delta W)}{\partial(\delta\gamma)} = F y_{ff}$$
$$Q_\gamma = \frac{\partial(\delta W)}{\partial(\delta\theta)} = F(x_{ff} - x_f)$$

As a consequence, the right hand side of the equations of motion changes to:

$$\begin{Bmatrix} F y_{ff} \\ F(x_{ff} - x_f) \\ 0 \end{Bmatrix}$$

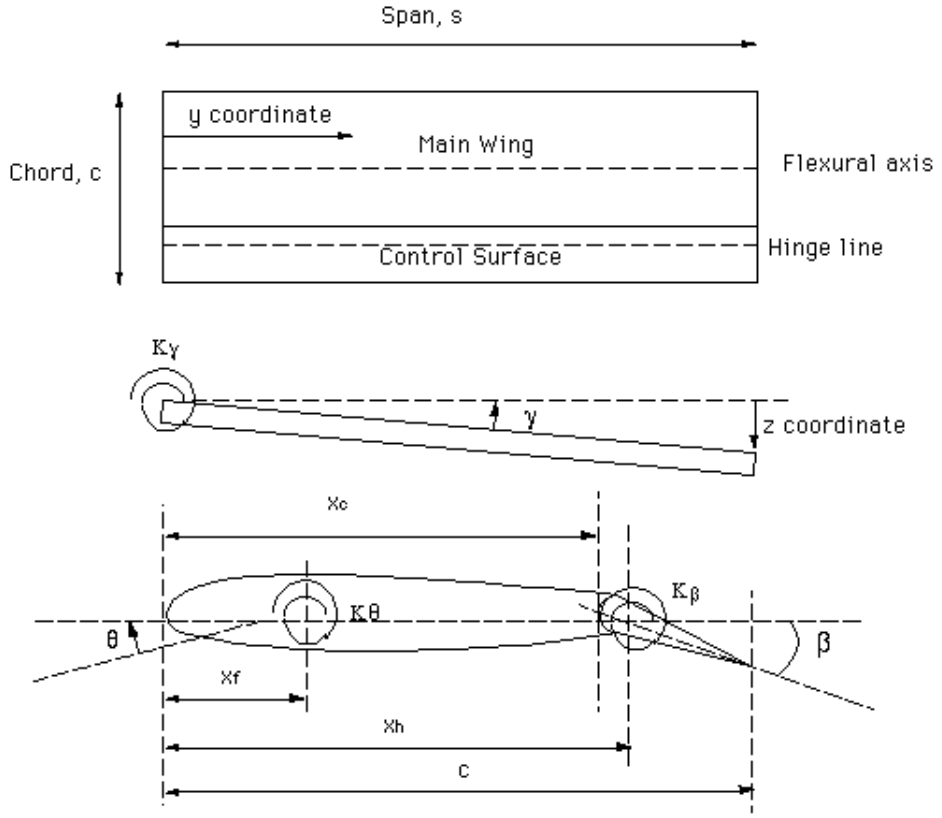

Figure A.1: Diagram of the Hancock wing with control surface

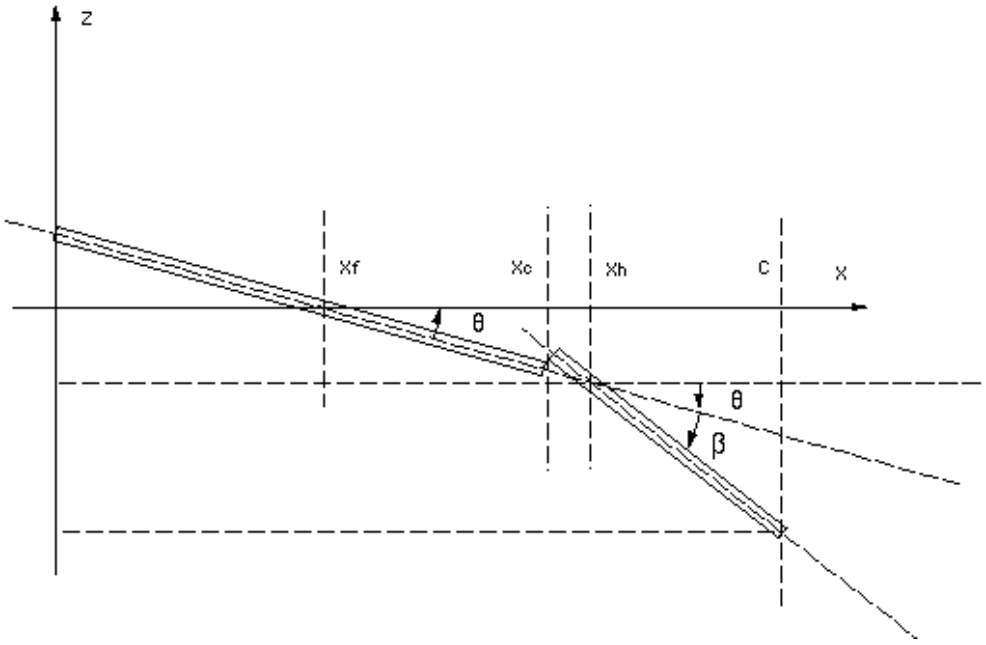

Figure A.2: Flat plate wing section

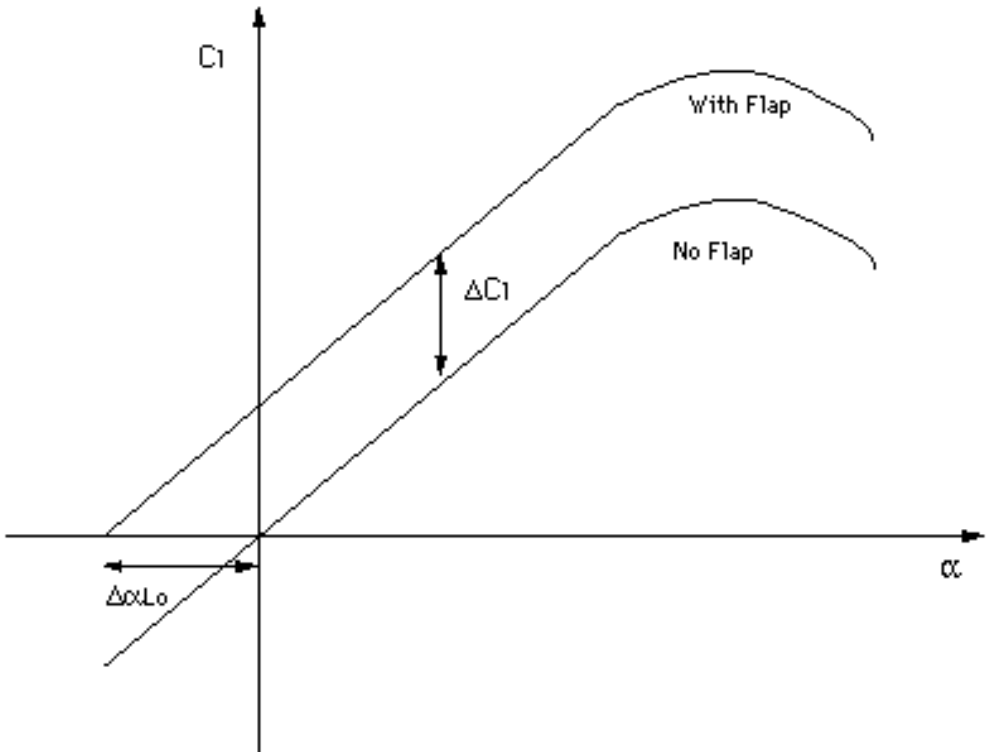

Figure A.3: Effect of control surface

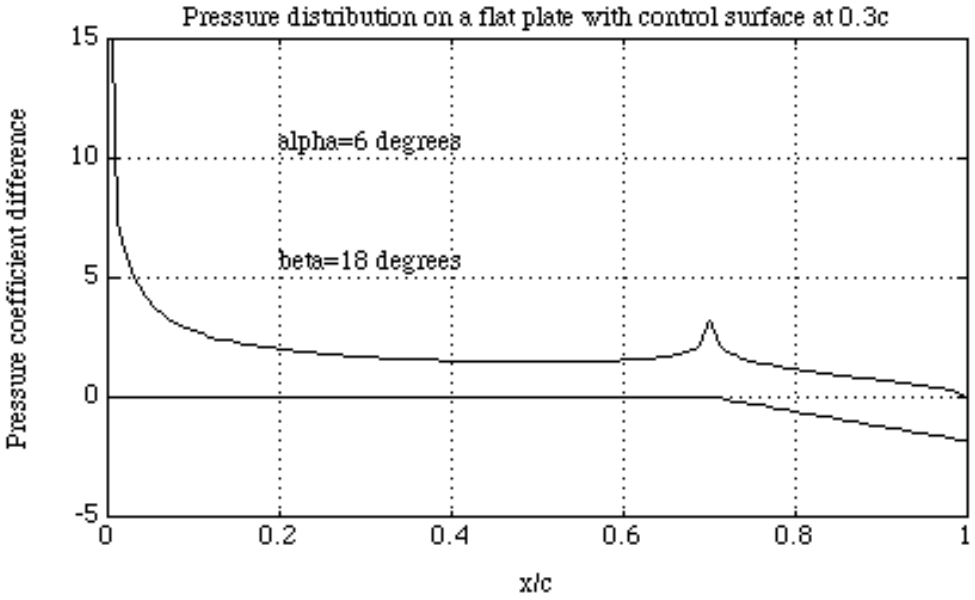

Figure A.4: Pressure distribution over a flat plate with control surface

Appendix B

The eigenvalue method

The equations of motion for a linear aeroelastic system without excitation can be solved using the eigenvalue method. The method works by reducing the second order problem to a first order one and then evaluating the eigenvalues of the resulting matrix. For a demonstration of the procedure consider the following equations of motion.

$$M\ddot{q} + C\dot{q} + Kq = 0 \tag{B.1}$$

where M is the mass matrix, C is the damping matrix, K is the stiffness matrix and q is the displacement vector. If equation B.1 is combined with

$$M\dot{q} - M\dot{q} = 0$$

the following system is produced.

$$\begin{pmatrix} 0 & M \\ M & C \end{pmatrix} \begin{Bmatrix} \ddot{q} \\ \dot{q} \end{Bmatrix} + \begin{pmatrix} -M & 0 \\ 0 & K \end{pmatrix} \begin{Bmatrix} \dot{q} \\ q \end{Bmatrix} = \begin{Bmatrix} 0 \\ 0 \end{Bmatrix}$$

This system of equations can be simplified by multiplying throughout by the inverse of the first matrix, resulting in

$$\begin{pmatrix} I & 0 \\ 0 & I \end{pmatrix} \begin{Bmatrix} \ddot{q} \\ \dot{q} \end{Bmatrix} + \begin{pmatrix} -M^{-1}C & -M^{-1}K \\ I & 0 \end{pmatrix} \begin{Bmatrix} \dot{q} \\ q \end{Bmatrix} = \begin{Bmatrix} 0 \\ 0 \end{Bmatrix}$$

which can be rewritten as

$$-\dot{p} + Qp = 0 \tag{B.2}$$

by setting,

$$p = \left\{ \begin{array}{c} \dot{q} \\ q \end{array} \right\}, \quad Q = \left(\begin{array}{cc} -M^{-1}C & -M^{-1}K \\ I & 0 \end{array} \right)$$

The system has now been reduced to a first order eigenvalue problem. It can be easily solved by letting $p = Pe^{\lambda t}$. The solution yields as many pairs of complex conjugate solutions as there are modes in the system. By writing

$$\{-\lambda I + Q\} Pe^{\lambda t} = 0$$

and then solving for λ the following eigenvalues are obtained

$$\lambda_{1,2,\ldots,2(m)-1,2(m)} = -\zeta\omega \pm i\omega\sqrt{1-\zeta^2}$$

where ζ is the damping ratio, ω is the natural frequency of the motion and m is the number of modes. A number of very important pieces of information can be deduced from these two parameters. The damping coefficient determines whether the motion is stable or not. Positive damping coefficient implies stable motion whereas negative implies flutter. The critical flutter speed occurs when one of the damping ratios is equal to zero. The natural frequencies determine exactly how unstable the system is and which two modes are coupling to cause flutter. For more details on the eigenvalue method see reference [95].

Appendix C

Pinpointing the flutter velocity

The most commonly used flutter criterion for a known linear aeroelastic system is the zero damping criterion. A number of approaches can be used in order to determine at which exact velocity the damping in at least one of the modes of the system becomes zero, when the equations of motion are known. Throughout the present work, quasi steady aerodynamic models are used, in which case there is no need for frequency matching. This simplifications enables the use of the following algorithm:

1. The procedure starts at a velocity at which the system is known to be stable. This velocity could be V=1 m/s but, in order to save computing time higher velocities can be used. The eigenvalues of the system (and, hence, the natural frequencies and damping ratios of each mode) are calculated at this velocity using the eigenvalue method. Then, all the dampings are checked to make sure that none of them are equal to or less than zero.

2. The velocity is increased by a set amount, ΔV (10 m/s is most convenient). The damping ratios are again evaluated and checked.

3. If all the dampings are greater than zero the velocity is again increased and the procedure returns to step 2. If one of the dampings is less than zero, the

velocity is decreased by ΔV and ΔV itself is divided by 10. The velocity is increased by the new ΔV and the procedure continues from step 2.

4. When a velocity is reached at which the damping is positive but less than a required small value (which depends upon the desired accuracy), the procedure stops and the the current velocity is taken to be the flutter velocity.

Other procedures could be used but this approach is most convenient since, in general, more than one modes of an aeroelastic system will flutter, at different velocities. The flutter velocity, however, is the first velocity at which the zero damping criterion is reached and the method described above will always pinpoint this particular velocity.

Appendix D

Finite difference solution

The equations of motion of a system (whether linear of nonlinear) can be integrated numerically to give the complete time history of the system for a particular set of airspeed, initial conditions, and excitation force. This can be done using various methods, two of which were used with this project. The first method was the Runge-Kutta method, applied by means of a computer package called Simulink [96], operating within the MATLAB [97] environment. This method is of high order (fifth) accuracy and can be applied easily using Simulink but the package itself allows very little control over the solution procedure and makes it very difficult to identify what has, or may have, gone wrong. For this reason, an alternative method of solution was sought in the form of finite differences [98]. This method is of lower accuracy than the Runge-Kutta method (second order) but is very stable and easy to apply. The basis of the finite difference method is to write functions as the first term of their Taylor expansion. Thus, derivatives can be approximated in terms of their previous and/or currant and/or future values. The Taylor expansion of a discretized function of time, f, at time instance $j+1$ in terms of f_j is

$$f_{j+1} = f_j + \Delta t \dot{f}_j + \frac{\Delta t^2}{2} \ddot{f}_j + ... \tag{D.1}$$

where Δt is the time step. If terms of order Δt^2 and higher are ignored then

$$\dot{f}_j = \frac{f_{j+1} - f_j}{\Delta t} \tag{D.2}$$

This expression is called the forward difference representation of $\dot{f}$ and is of first order accuracy. If the Taylor expansion of f is written for $-\Delta t$

$$f_{j-1} = f_j - \Delta t \dot{f}_j + \frac{\Delta t^2}{2} \ddot{f}_j + ... \tag{D.3}$$

and 2nd order terms are ignored as previously, the backward difference representation of $\dot{f}$ is obtained

$$\dot{f}_j = \frac{f_j - f_{j-1}}{\Delta t} \tag{D.4}$$

which is again of 1st order accuracy. If equations D.1 and D.3 are subtracted then the central difference representation can be obtained

$$\dot{f}_j = \frac{f_{j+1} - f_{j-1}}{2\Delta t} \tag{D.5}$$

which is of 2nd order accuracy (since the 2nd order terms are not ignored but cancel each other out). Finally, if equations D.1 and D.3 are added, the central difference representation of $\ddot{f}$ can be obtained as

$$\ddot{f}_j = \frac{f_{j+1} - f_j + f_{j-1}}{\Delta t^2} \tag{D.6}$$

Consequently, by discretizing a function and expressing $f(t)$ as f_j, expressions for its first and second derivatives can be obtained, albeit with numerical errors, the order of which depends on the type of finite difference representations used.

For dynamical systems, central differences are most suitable because of their higher accuracy. The equations of motion for such a system are

$$\mathbf{M}\ddot{\mathbf{q}} + \mathbf{C}\dot{\mathbf{q}} + \mathbf{K}\mathbf{q} = \mathbf{F}$$

where $\mathbf{M}$ is the mass matrix, $\mathbf{C}$ is the damping matrix, $\mathbf{K}$ is the stiffness matrix, $\mathbf{F}$ is the excitation vector and $\mathbf{q}$ is the vector of generalised coordinates. After discretization, these equations can be rewritten using equations D.5 and D.6 as

$$\mathbf{M}\frac{\mathbf{q}_{j+1} - \mathbf{q}_j + \mathbf{q}_{j-1}}{\Delta t^2} + \mathbf{C}\frac{\mathbf{q}_{j+1} - \mathbf{q}_{j-1}}{2\Delta t} + \mathbf{K}\mathbf{q}_j = \mathbf{F}_j$$

Moving all j and $j-1$ terms to the right hand side

$$\left(\frac{\mathbf{M}}{\Delta t^2} + \frac{\mathbf{C}}{2\Delta t}\right)\mathbf{q}_{j+1} = \mathbf{F}_j + \left(\frac{\mathbf{M}}{\Delta t^2} - \mathbf{K}\right)\mathbf{q}_j + \left(-\frac{\mathbf{M}}{\Delta t^2} + \frac{\mathbf{C}}{2\Delta t}\right)\mathbf{q}_{j-1} \tag{D.7}$$

Hence, equation D.7 can be solved at every step j to obtain $\mathbf{q}_{j+1}$ provided that $\mathbf{q}_j$ and $\mathbf{q}_{j-1}$ are known. This is called a time-marching solution. For the scheme to work, the values of $\mathbf{q}_1$ and $\mathbf{q}_2$ must be known. The initial conditions will yield $\mathbf{q}_1$ but $\mathbf{q}_2$ can only be obtained using a forward difference representation of the equations of motion at $j = 1$, assuming that all the second derivatives are zero at that particular instance. Hence, using equation D.2,

$$\frac{\mathbf{C}}{\Delta t}\mathbf{q}_2 = \mathbf{F}_1 + \mathbf{K}\mathbf{q}_1 + \frac{\mathbf{C}}{\Delta t}\mathbf{q}_1 \tag{D.8}$$

Nonlinear systems can also be solved using the time-marching finite difference scheme, however, only in the case where the nonlinear functions in a given system depend only on $\mathbf{q}$ (i.e. nonlinear stiffness), so that the nonlinearity is moved to the right-hand side of equation D.7. If the nonlinear function depends on $\dot{\mathbf{q}}$ (nonlinear damping) then the first derivatives have to be expressed as backward differences, which creates numerical difficulties since the second derivatives have

to be expressed as central differences. These difficulties can be overcome however, this is beyond the scope of the present work since only stiffness nonlinearities were solved by finite differences.

Appendix E

Chebyshev Polynomials

Chebyshev polynomials approximate a function, $f(x)$, by a series of weighted orthogonal polynomials given by [98]

$$\left.\begin{aligned} T_{n+1}(x) &= 2xT_n(x) - T_{n-1}(x) \\ T_0(x) &= 1 \\ T_1(x) &= x \end{aligned}\right\} \tag{E.1}$$

Then, the function can be written as

$$f(x) = \frac{a_o}{2} + \sum_{i=1}^{\infty} a_i T_i(x) \tag{E.2}$$

and the weights, a_i are obtained, due to the orthogonality property, using

$$a_i = \frac{2}{\pi} \int_{-1}^{1} \frac{f(x)T_i(x)}{\sqrt{1-x^2}} dx \tag{E.3}$$

The integration needs to be performed carefully since the integrand becomes infinite at the integration limits.

The sum in equation E.2 is infinite but, in practice, only a small number of polynomials is enough to approximate the function. For example, figures E.1 and E.2 show how the quality of a fit is improved by increasing the number of polynomials from 30 to 40. Hence the parameters describing the function are the

weights $a_o, \ldots, a_N$. Reference [82] recommends Chebyshev Polynomials for the parameterization of gust waveforms indicating that less parameters are required than if Fourier Series were used.

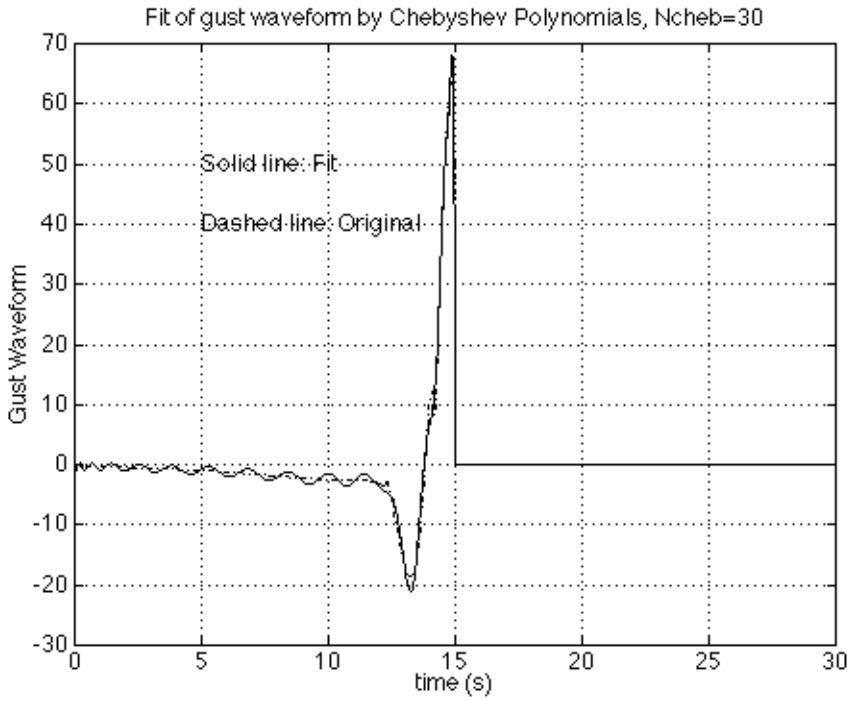

Figure E.1: Gust Waveform Fit by 30 Chebyshev Polynomials

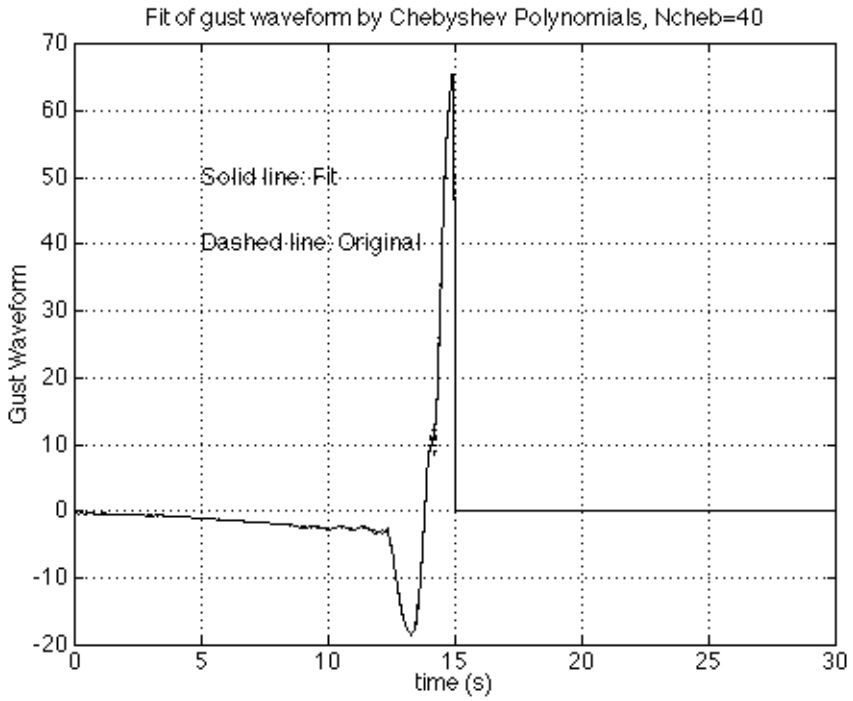

Figure E.2: Gust Waveform Fit by 40 Chebyshev Polynomials

Appendix F

Simulated Annealing

Simulated Annealing [81], [60]is an optimization process approximating the way alloys are annealed, i.e. heated up and then left to cool down naturally so that the energy of their crystal structure is minimized. Once the parameter space of a particular optimization problem is defined, the simulated annealing algorithm alters randomly one or more parameters and produces the corresponding cost function that is to be optimized. Then the algorithm determines whether the new state is to be accepted or rejected by applying the condition

$$J = \exp\left(-\frac{c_{new} - c_{old}}{T}\right) \geq rand \tag{F.1}$$

where c_{new} is the cost function of the new state, c_{old} is the cost function of the previous state, T is a relaxation coefficient termed the temperature and $rand$ is random number between 0 and 1. The criterion is written for the case of a minimization problem. The role of the temperature is to allow the system to exit local optima and move towards the global optima. When the temperature is high, worse states can be accepted as well as better ones. As the temperature decreases less 'bad' states are accepted and the system is moved towards its global optimum.

More specifically, the application of the Simulated Annealing method to a minimization problem starts with a high temperature value. Minimization implies that the cost function, c, needs to be minimized. There are three possible cases

1. If the cost function of a new state, c_{new}, is less than the cost function of the previous state, c_{old}, then, from equation F.1, $J > 1$ and the new state will be accepted since $rand$ assumes values between 0 and 1.

2. If the cost function of a new state is equal to the cost function of the previous state, $J = 1$ and the new state is accepted.

3. If the cost function of a new state is greater than the cost function of the previous state, $0 < J < 1$, and the new state is only accepted if $J > rand$. At the start of the procedure the temperature is high which means that J will often be greater than $rand$ and a lot of worse cases will be accepted. As the temperature decreases, J also decreases, meaning that gradually fewer worse cases will be accepted.

It should be noted that the algorithm is not guaranteed to deliver the absolute optimum. This would only be possible with an exhaustive search of the parameter space. However, its capability to avoid local optima means that the final state will be very close to the global optimum. The best guarantee that the optimum has been reached is to repeat the procedure from different initial states and to choose the most common final state.

Appendix G

Sim-2 aeroelastic model

The Sim-2 model is a mathematical aeroelastic model that describes the behaviour of a 4-engined civil transport. The model contains the equations of motion for the aircraft in the form of structural and aeroelastic modal mass, stiffness and damping matrices. There are two sets of matrices, one for symmetric modes (21 flexible and 3 rigid body) and one for antisymmetric modes (20 flexible and 3 rigid body). The symmetric and antisymmetric behaviors are uncoupled and can be solved separately. In physical space, the aircraft can be excited at 17 excitations positions shown in figure G.1.

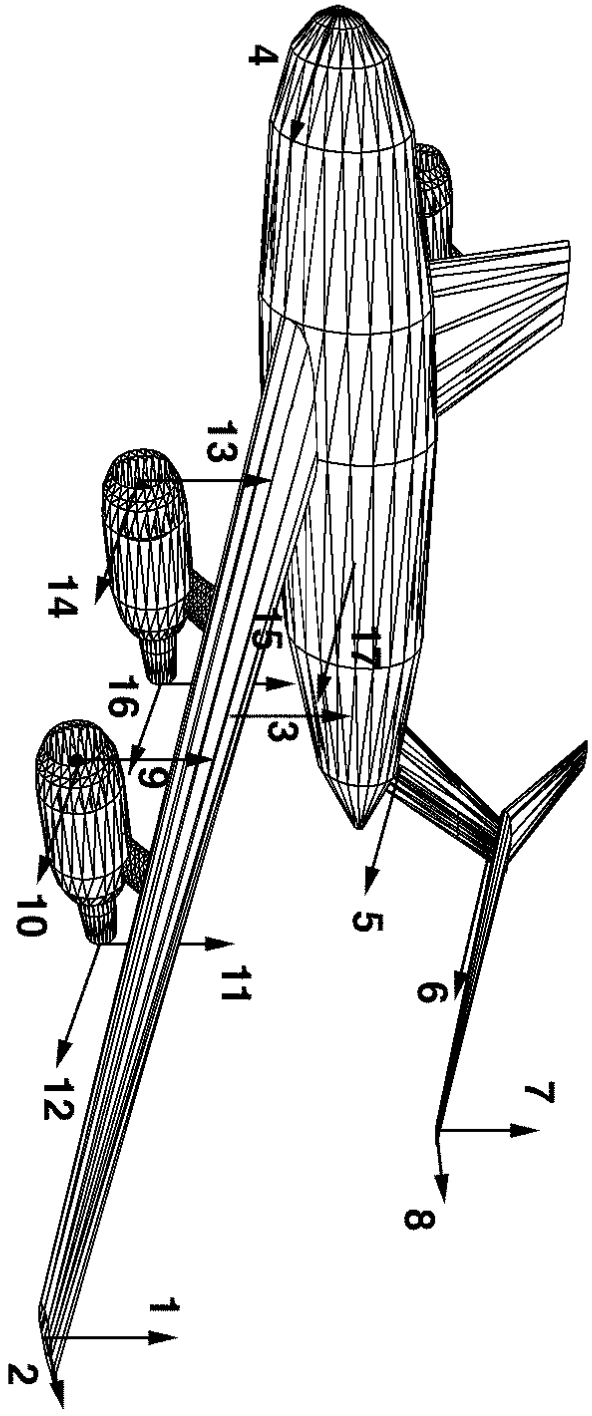

Figure G.1: Sim-2 aeroelastic model

Appendix H

Gust load response models

Two simulated symmetrical aircraft models were used in this research, both of which were kindly provided by Dr W.J. Vink of the National Aerospace Laboratory, NLR, in Holland. Descriptions of the models can also be found in [79]. The first model, commonly known as the Noback aircraft, is a simple, 2-dof model of a large transport aircraft with a load alleviation system. The two degrees of freedom are pitch and heave and the load alleviation system feeds back the centre of gravity acceleration to aileron deflection. The model has two load outputs:

- load 1: Centre of gravity acceleration (m/s^2)
- load 2: Centre of gravity acceleration caused by aileron action only (m/s^2)

A Simulink block diagram of the Noback aircraft is shown in figure H.1.

The second model represents a A310 aircraft with two rigid-body degrees of freedom, pitch and heave, and three symmetric flexible degrees of freedom. The control system of the aircraft feeds back the centre of gravity acceleration to the ailerons and the spoilers. The deflections of both the ailerons and the spoilers are limited between 0 and 10 degrees. The model has four load outputs:

- load 1: Engine lateral acceleration (ft/s^2)

- load 2: Wing bending moment ($lb.ft$)
- load 3: Wing torsion ($lb.ft$)
- load 4: Load factor (ft/s^2)

A Simulink block diagram of the A310 model is shown in figure H.2.

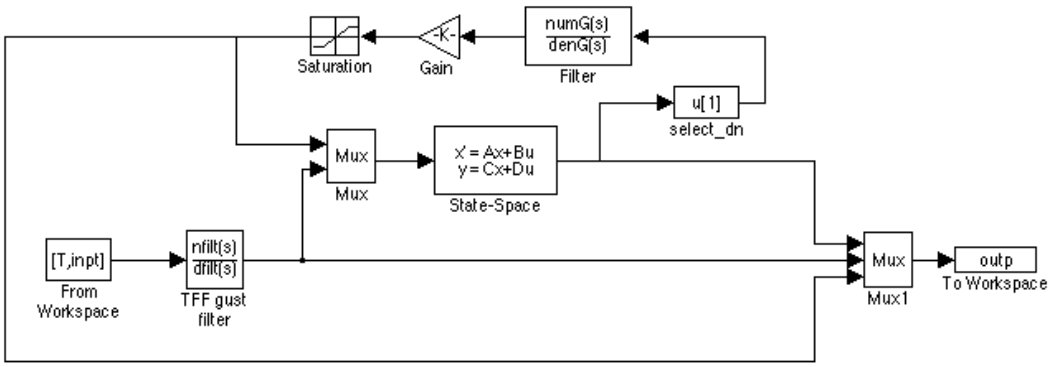

Figure H.1: Simulink diagram of nonlinear Noback Aircraft

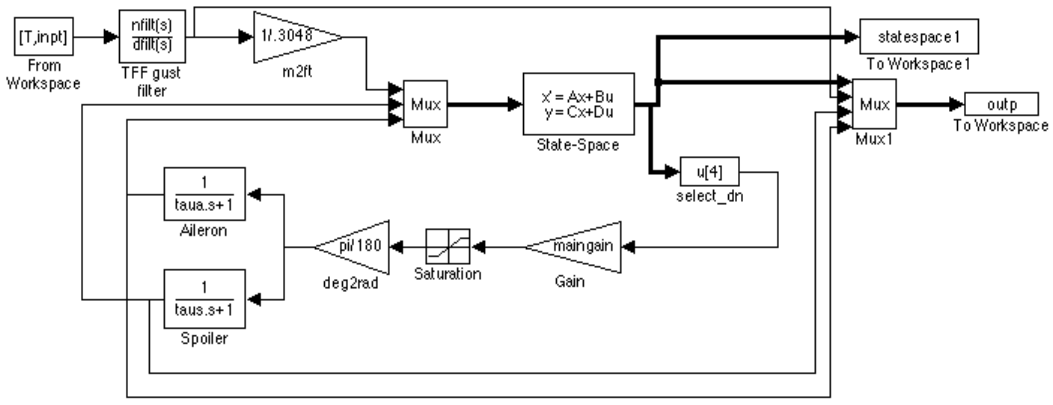

Figure H.2: Simulink diagram of nonlinear A310 aircraft